COLLECTIVE MECHANOCHEMICAL GROWTH OF CARBON NANOTUBES

by

Mostafa M. K. M. A. Bedewy

A dissertation submitted in partial fulfillment
of the requirements for the degree of
Doctor of Philosophy
(Mechanical Engineering)
in the University of Michigan
2014

Doctoral Committee:

Associate Professor A. John Hart, Chair
Assistant Professor Allen Po-Chih Liu
Professor Michael J. Solomon
Adjunct Associate Professor Eric A. Stach, Purdue University and
Brookhaven National Laboratory

DEDICATION

I dedicate this work to my wife, my soul mate, and my best friend, Mai, without whom the completion of this work would have been impossible.

ACKNOWLEDGMENTS

The exciting and eventful journey of my PhD started with a phone interview back in 2008. On the other end of the line was a young, energetic and obviously very smart new faculty. Little did I know, he would be my boss for years. Now, I consider myself very lucky to have worked with Professor A. John Hart for the past five years, and I would like to take this opportunity to express my sincere appreciation and gratitude to him for his excellent guidance and continued support. When I become a professor, my future students should also be grateful to John because if I ever do or say something nice to them, odds are I learned it from John!

I would like to thank my PhD committee members Doctor Eric Stach, Professor Allen Liu, and Professor Michael Solomon for their time and efforts. I really value their inputs and appreciate their support.

I was fortunate to have collaborated with many outstanding researchers over the course of my PhD research. I would like to thank Doctor Arthur R. Woll for his keenness on making sure that our experiments work out as planned at the Cornell

High Energy Synchrotron Source (CHESS). Thanks are also due to Doctor Eric Meshot, Doctor Erik Polsen for being such helpful lab-mates and good friends. I also enjoyed working closely with Brittan Farmer and want to thanks him for being fun to work with. At the Brookhaven National Laboratory, I had the pleasure of working closely with Doctor Eric Stach and Doctor Dmitri Zakharov, and I want to express great appreciation to them for their dedication and friendliness.

While working in the Mechanosynthesis group, I got the chance to meet, interact with, and learn from a set of exceptional scientists and brilliant students. I thank you all for creating such a positive atmosphere in the lab. It was a great pleasure to work with all of you.

I have been blessed with a wonderful group of friends here in Ann Arbor, without whom, those five years would have never been that enjoyable. Thank you all for being part of my life.

I cannot find adequate words to thank and acknowledge my lovely family. I can't imagine how my life would have been without their nonstop love and support. Thanks for being there for me every step along the way.

TABLE OF CONTENTS

LIST OF FIGURES

ABSTRACT

Hierarchically ordered carbon nanotubes (CNTs) are promising for integration in high-performance structural composites, electrical interconnects, thermal interfaces, and filtration membranes. These and other applications require CNTs that are monodisperse, well aligned, and densely packed. Moreover, because more than 1 billion CNTs per square centimeter grow simultaneously in a typical chemical vapor deposition (CVD) process, understanding the collective chemical and mechanical effects of growth is key to engineering the properties of CNT-based materials. This dissertation presents tailored synthesis processes, characterization techniques, and mathematical models that enable improved control of the morphology of as-grown CNT "forests."

First, a comprehensive characterization methodology, combining synchrotron X-ray scattering and attenuation with real-time height kinetics, enabled mapping the spatiotemporal evolution of CNT diameter distribution, alignment and density. By this method, the forest mass kinetics were measured and found to follow the S-shaped Gompertz curve of population growth. Dividing a forest into subpopulations revealed size-dependent activation-deactivation competition. Additionally, in situ transmission electron microscopy (TEM) showed that the

kinetics of CNT nucleation are S-shaped. Based on these findings, a collective growth model is proposed, wherein randomly oriented CNTs first nucleate then self-organize and lift-off during a crowding stage, followed by a density decay stage until self-termination when the density drops below the self-supporting threshold.

Next, further X-ray data analysis enabled modeling the mechanics of entangled CNTs and proved that mechanical coupling is not only responsible for the self-organization into the aligned morphology, but is also an important limiting mechanism as significant forces ensue from diameter-dependent CNT growth rates. A custom-built CVD system was used for mechanical manipulation of growing CNTs, leading to insights that external forces modulate the reaction kinetics. Last, a mathematical model describing the synergetic chemical coupling among growing CNT micropillars predicted height variations, and enables the design of CNT catalyst patterns for improved uniformity.

The insights in this dissertation contribute to the fundamental understanding of self-organized CNT growth, enabling improved manufacturing and metrology. The models and techniques for studying population behavior of nanofilaments may also be applied to other systems, such as inorganic nanotubes, nanowires, and biofilaments.

CHAPTER 1: INTRODUCTION

1.1. The Origin and Definition of Nanotechnology

Nanotechnology is not merely creating and utilizing material structures at the nanoscale (1-100 nm), but it is rather an ability to monitor and manipulate matter at this small scale. This requires a deep understanding of the properties and interactions that arise uniquely from the size and surface characteristics of nanostructures. For hundreds – or perhaps thousands – of years (Figure 1), the unique properties of nanostructured materials have been harnessed, albeit without recognizing the nanoscale building blocks responsible for these properties. In those times and until very recently, the know-how for creating these materials primarily depended on an empirical approach for developing and optimizing the required material processing methods. For example, the marvelous red and purple colors of stained glass windows, such as the north rose window of the Notre Dame Cathedral built in the 13th century (Figure 1), owe their richness to the presence of gold nanoparticles.[1] Another example is the sharp patterned blades of the Damascus sword (saber) made in the period between the 13th and the 18th centuries. These blades were recently shown to have carbon nanotubes and cementite nanowires embedded in their steel microstructure.[2] In these cases, however, the remarkable

material properties were the result of experimentation with high temperature processing of materials, without the benefit of sophisticated tools that enable insights into the chemical and morphological changes caused by the successive heat treatment steps.

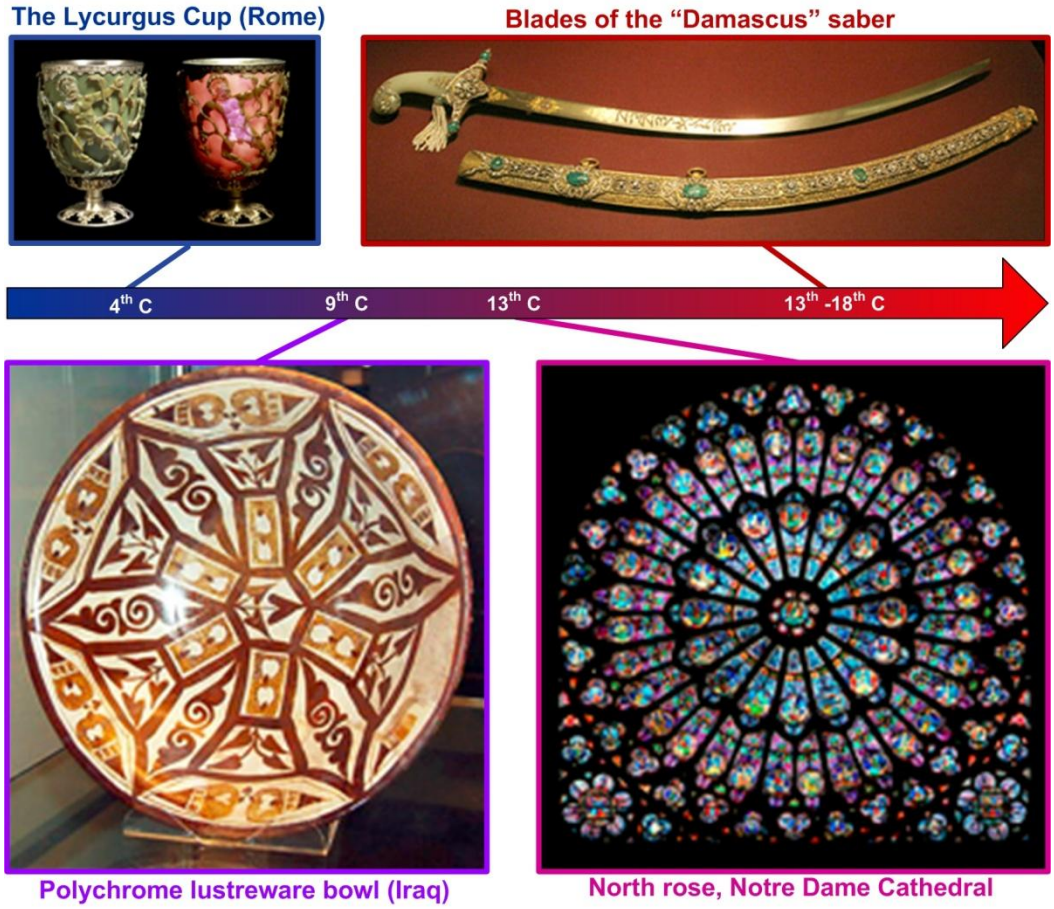

Figure 1. Ancient nanostructured functional materials.

True science and engineering at the nanoscale became accessible only after the development of material characterization techniques capable of probing length scales

ranging from atomic to the microscale, as well as the development of controllable methods capable of engineering nanostructures. The emerging field of "Nanotechnology" is motivated by the scientific progress in recognizing the unique physical, chemical, mechanical, thermal and electrical properties of nanomaterials[3] that result from the large surface-area-to-volume ratio of nano-sized particles as well as their unique molecular designs. Hence, a great deal of scientific research is currently being directed towards creating and improving the means by which these nanoscopic materials are synthesized, characterized, and assembled, for integration into high impact applications.

1.2. Promising Applications of Nanomaterials

The utilization of the size-dependent properties of nanostructures (Figure 2) such as zero-dimensional (0D) nanoparticles/clusters, one-dimensional (1D) nanofilaments and two-dimensional (2D) sheets/films is sought after for many applications. In addition, the collective behavior of a large number of these nanoscale building blocks is also promising in cases where the overall properties of an assembly of nanostructures depend on both the properties of individual nanostrucutres as well as the interactions and coupling phenomena between them.

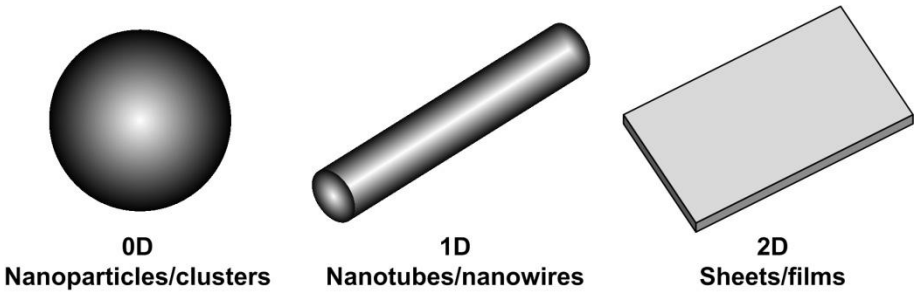

Figure 2. Nanoscale building blocks.

It is important at this point to classify applications of nanomaterials into three categories (Figure 3).

Category 1: Applications based on an individual nanostructure

This category includes those applications that are designed to exploit the unique nanoscale properties of an individual nanostructure. For example, an individual carbon nanotube (CNT) has been shown to operate as a radio.[4, 5]

Category 2: Applications based on discrete number of nanostructures

This category includes applications that require precise organization of a discrete number of particles into a structure that exhibits unique collective properties. For example, high performance sensors can be fabricated by utilizing Fano resonance of plasmonic discrete metal NP clusters.[6]

Category 3: Applications based on a large number of nanostructures

This category includes applications that are based on the utilization of collective properties of a large number of nanostructures in parallel, where the resultant

transport property, for instance, is more than the sum of its components. For example, populations of carbon nanotubes (CNTs) have been shown to be promising as electric interconnects,[7-9] and structural fibers.[10, 11] Another example is the utilization of large-area and defect-free nanoparticle crystal layers as antireflective coatings for enhancing efficiency of thin-film photovoltaic cells.[12, 13]

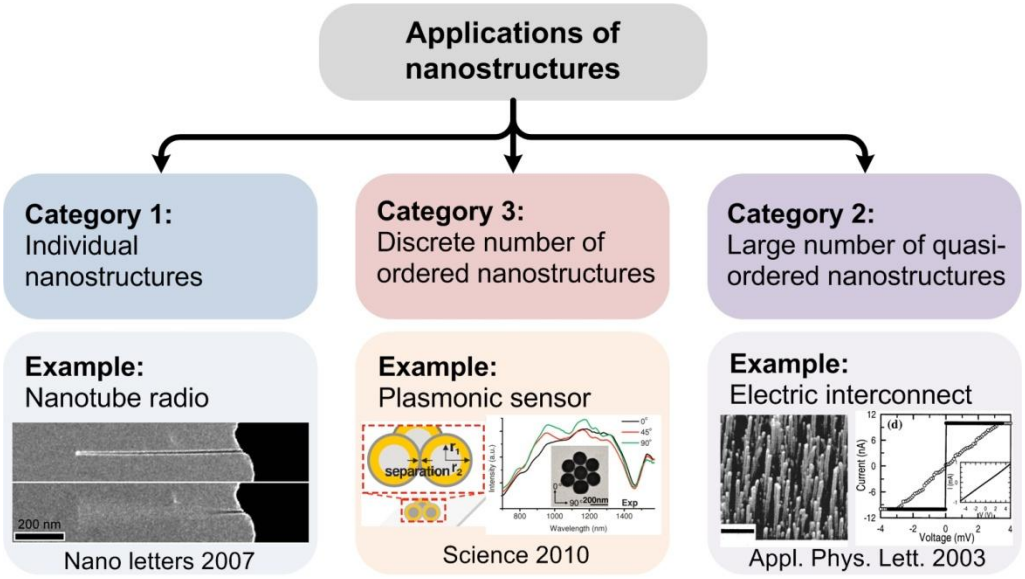

Figure 3. Schematic showing different categories of nanomaterial applications. Nanotube radio is adapted from reference 4. Plasmonic sensor is adapted from reference 6. Electric interconnect is adapted from reference 8.

1.3. Nanomanufacturing

In order to realize these applications, contributions are needed towards developing fabrication methods capable of satisfying the length-scale and the order requirements, ranging from precise placement of individual nanostructures and

clusters thereof to the bulk assembly of larger three-dimensional ensembles. Moreover, integrating these nanomaterials into economically viable products that can be mass produced in a "true" manufacturing process is often a roadblock.

Nowadays, "Nanomanufacturing" can be defined as the field of designing and developing "advanced" manufacturing processes to produce functional materials and devices (products) having dimensional and morphological features in the nanoscale (generally 1 – 100 nm). It is a rapidly growing field of research and is increasingly becoming a major thrust of advanced manufacturing initiatives. In fact, advanced manufacturing has been recently identified by the US President's Council of Advisors on Science and Technology (PCAST) and the President's Innovation and Technology Advisory Committee (PITAC) as key to the nation's economy and national security.[14] The synergetic benefits between two largely separate disciplines, i.e. nanoscale science and manufacturing engineering, are occupying an ever greater part of manufacturing research. This is manifested in the increasing percentage of publications related to manufacturing that are also related to the nanoscale (reached 30% in 2012).

It is important to make a distinction here between nanomanufacturing and nanofabrication. The later simply means the "making" of nanoscale materials using any process such as synthesis, growth, deposition, assembly, etching, etc. On the other hand, manufacturing implies much more than just fabrication. It implies

repeatability, scalability, quality control, cost effectiveness, energy efficiency and sustainability.

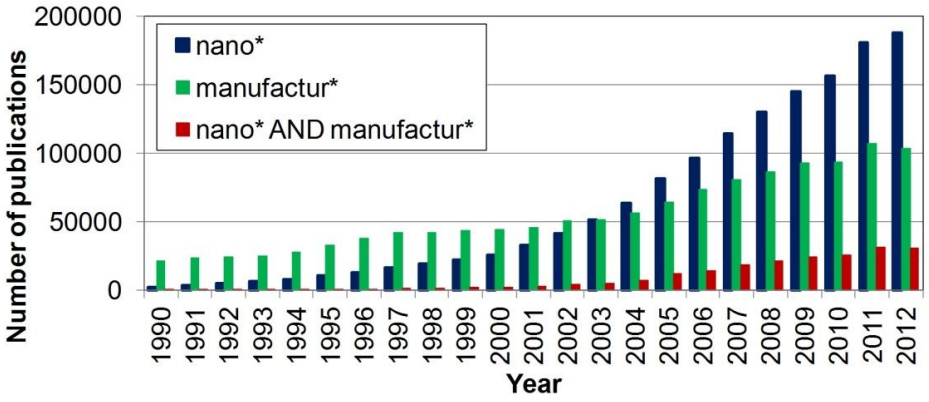

Figure 4. Chronological evolution of the number of publications on nanomanufacturing. Data collected from Web of Knowledge database using the enquiry in the legend as topic.

1.4. Bottom-Up vs. Top-Down Fabrication

Historically, efforts towards nanofabrication focused on miniaturization and scaling down of traditional fabrication techniques such as conventional and non-conventional material removal methods. The creation and demand of the semiconducting industry gave rise to the well-established microfabrication technology, which is primarily based on the controllable addition (deposition, implantation or doping) and/or removal (micromachining or etching) of material by a plethora of chemical and physical techniques.[15] Although some state-of-the-art microfabrication equipment are capable of controlling feature dimensions (e.g. film

thickness or line-width) down to the nanoscale, such as physical vapor deposition of thin films and electron-beam lithography of patterns, they have inherent limitations on the design of materials produced, as they represent a top-down approach. However, truly probing the possibilities of both structuring material at nanoscale and integrating these nanostructures into macroscopic applications is a manufacturing challenge, especially that viability of commercialization heavily depends on developing economic technologies for large scale production of functional nanostructures. In general, top-down fabrication techniques fail to satisfy two seemingly contradicting requirements in a cost-effective manner: smaller resolution and large scale production, in addition to the stringent requirement on accuracy and complexity dictated by the applications. Hence, the idea of a bottom-up approach, such as self-organization of nanoscale building blocks,[16] soon became attractive for manipulating nanostructures, and is currently sought after for expanding the capabilities and applications of nanomanufacturing.

Manufacturing functional devices/systems that are based on bottom-up fabrication is schematically depicted in Figure 5. First, the nanoscale building blocks are "made" by physical/chemical synthesis techniques. Then, these nanostructures can either be integrated directly into a functioning devices or be assembled into larger systems before integration into devices. The fundamentally bottom-up processes of synthesis and self-assembly could be achieved either in a fluid (solution of gas-phase) or on a solid substrate. Eventually, placing an individual

nanostructure, or ensembles thereof, in a precisely ordered fashion by a controllable method leads to the integration into functional devices. In some systems, the synthesis and the assembly steps may be combined, and in other cases the assembly and the integration steps can be combined. It is important to note here that combining bottom-up processing with top-down fabrication is also promising for directing self-assembly and on-chip integration steps by microfabricated topographies or lithographically patterned chemistries for instance.

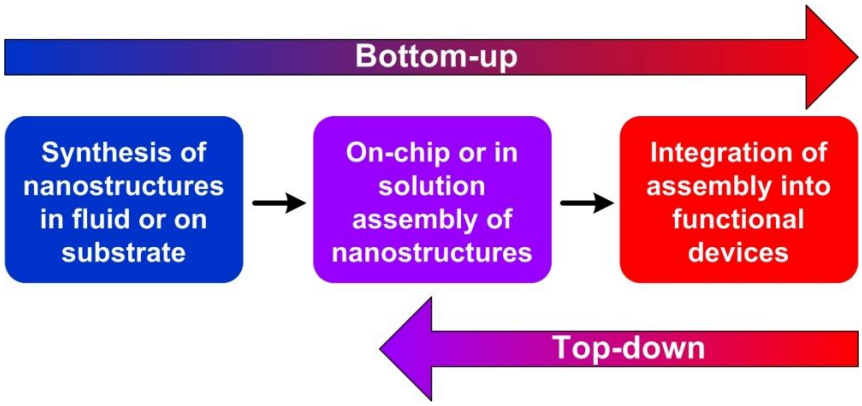

Figure 5. Bottom-up nanomanufacturing of functional devices.

1.5. Science and Technology of Nanomanufacturing

Research in nanomanufacturing generally aims at addressing all challenges blocking realization of products based on nanomaterials. On the one hand, fundamental scientific contributions (*basic research*) are required for understanding the nanofabrication processes, and for developing lab-scale methods/instruments to precisely control the process and deterministically design the fabricated material

morphology and properties. This science aspect of nanomanufacturing is heavily dependent on developing/utilizing advanced characterization techniques for studying the evolution of morphology during processing (*in situ*), as well as the correlation of the morphological evolution to real-time process kinetics (*operando*). On the other hand, these scientific findings pave the way for developing high-throughput, cost-effective and energy-efficient production technologies (*applied research*) that scale-up the lab process into either a continuous or batch production process. Ultimately, both fundamental and translational research are required to overcome roadblocks towards commercialization. Figure 6 schematically depicts the two main domains to research on nanomanufacturing: science contributions, and technology development.

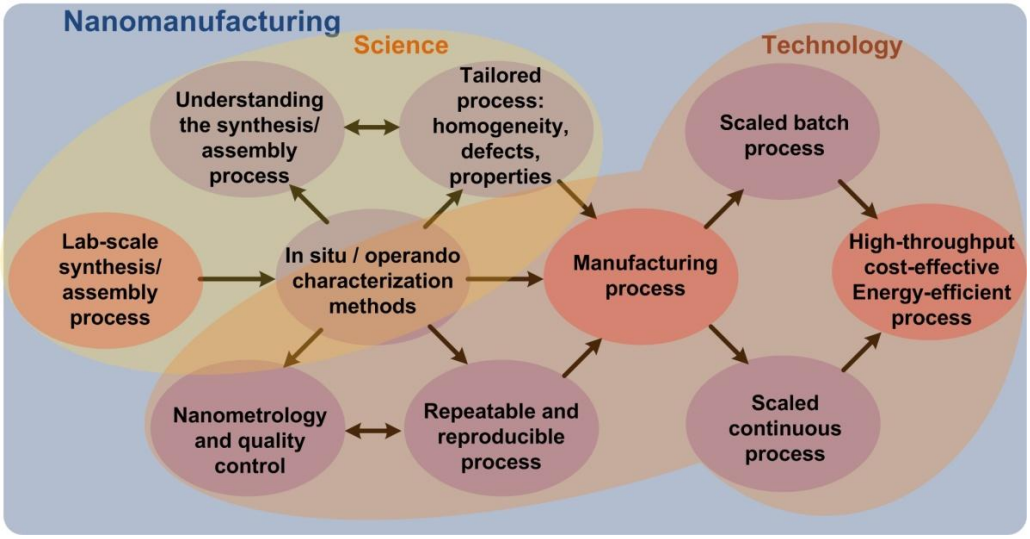

Figure 6. Schematic showing the science and technology aspects of Nanomanufacturing.

1.6. Manufacturing Hierarchical Carbon Nanotubes

This dissertation addresses the challenges facing the manufacturing of hierarchical carbon nanotube (CNT) materials. CNTs are made of sheets of graphene seamlessly wrapped into cylinders (Figure 11). If a CNT is made of only one graphene sheet, it is called a single-walled nanotube (SWNT), and if it is made of multiple sheets, it is called a multiwalled nanotube (MWNT). Although the nanotube structure was first reported over 20 years ago, CNTs are still considered promising for many applications owing to their unique properties (such as high mechanical strength as well as excellent electrical and thermal conductivities).[17, 18] In fact, *nano-scale carbon materials* was identified in the 2011 PCAST report as an area where technological development could have transformative potential.[14]

Commercial production of CNTs has rapidly increased over the past few years, reaching more than 2000 tons/year in 2011.[18] Nevertheless, the majority of products containing CNTs utilize large numbers of randomly oriented CNTs as additives to a matrix to improve the overall properties of the mixture. Examples include adding CNTs to a polymer to render it conductive for use as electrostatic shields, or adding CNTs to a resin matrix to improve the mechanical properties for use as structural composites. On the other hand, many emerging applications will be based on ordered CNT structures such as CNT forests and yarns (Figure 8).

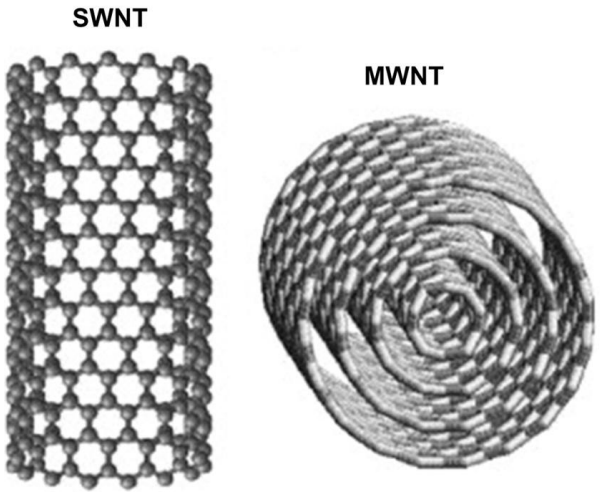

Figure 7. Schematic of single-walled and multiwalled carbon nanotubes (SWNTs and MWNTs). Adapted from reference [19].

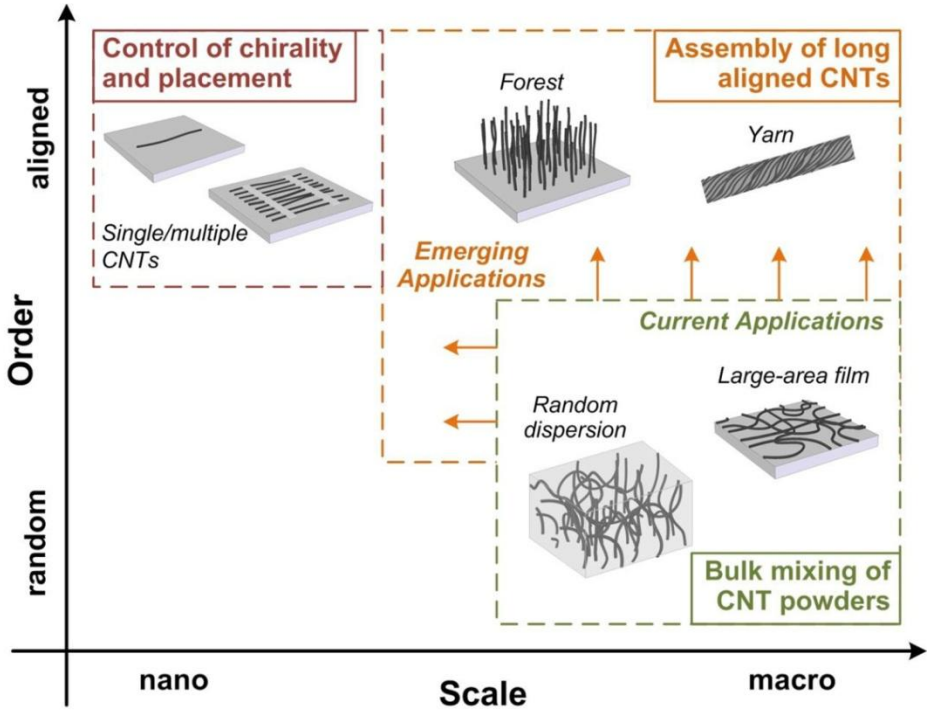

Figure 8. Schematic showing the current trend in shifting from CNT applications that are based on bulk mixing of CNT powder to emerging applications that rely on ordered structures such as CNT forests. Adapted from reference 18.

In particular, this dissertation focuses on macroscopic structures that are composed of self-aligned CNTs forming a hierarchical morphology, referred to herein as "CNT forest", shown in Figure 9. Potential applications of CNT forests (Figure 10) include integration in high-performance structural composites,[11] electrical interconnects,[7, 9] thermal interfaces,[20] filtration membranes,[21] gas sensors,[22-24] and oil-sorbent materials,[25] to name a few.

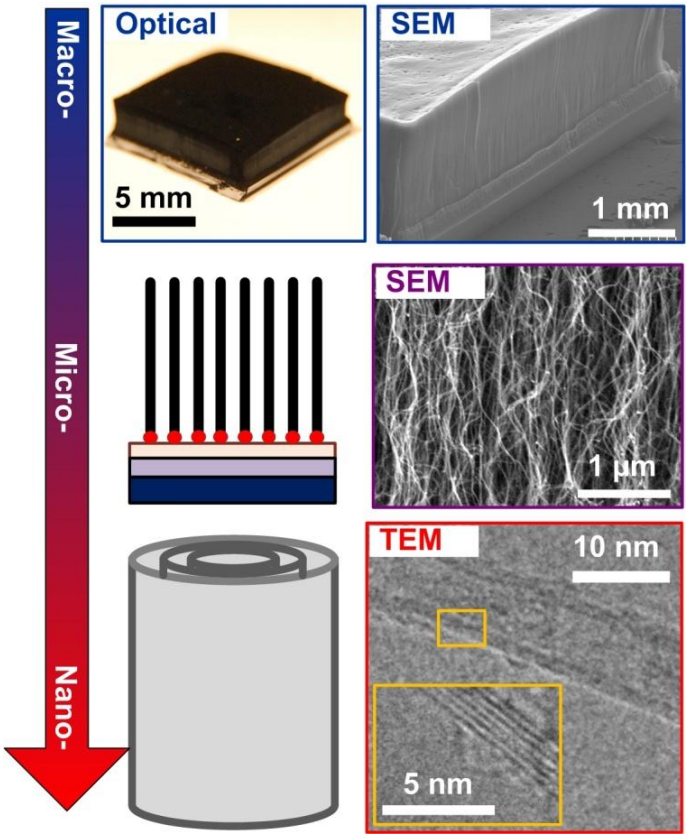

Figure 9. Hierarchical structure of CNT forests.

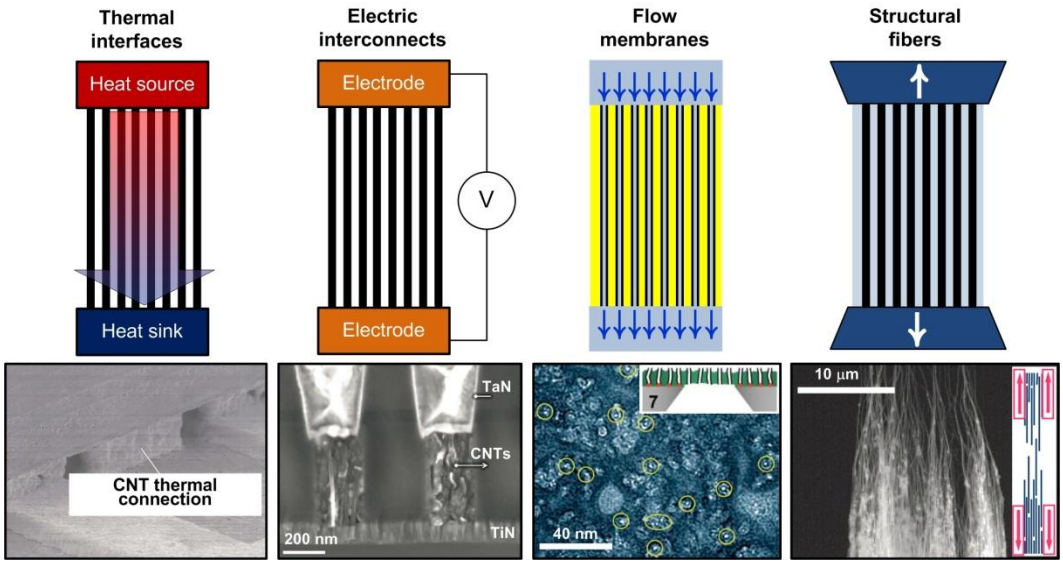

Figure 10. Some promising applications of ordered CNT ensembles. Thermal interface image adapted from http://www.fujitsu.com. Interconnect image adapted from reference 26. Flow membrane image adapted from reference 27. Structural fiber image adapted from reference 28.

CNT forests are typically grown by chemical vapor deposition (CVD) owing to its scalability and versatility for producing high quality CNTs. This dissertation focuses on the CVD growth of CNT forests catalyzed by substrate-bound catalyst nanoparticles. In CVD (Figure 11), a hydrocarbon gas decomposes and dissociates at the surface of a catalyst nanoparticle, where carbon atoms diffuse onto the catalyst surface and/or into the bulk of the nanoparticles. After that, a cap of self-organized graphitic carbon starts to form on the curved catalyst surface, followed by lift-off of the tubular CNT structure. In this process, the catalyst nanoparticles are typically made of transition metals such as iron and nickel, and are usually supported on a thin support layer.[29-34] In order to grow CNT forests, substrates having high density

catalyst nanoparticles (Fe nanoparticles in this work) on a support layer (Al_2O_3 thin film in this work) are placed inside a CVD reactor. Upon introducing the hydrocarbon gas (C_2H_4 and/or C_2H_2 in this work), CNTs grow from seeding nanoparticles simultaneously to self-organize into a forest.

1.7. Scope and Outline of this Dissertation

The promising applications of CNT forests, shown in Figure 10, require CNTs with high monodispersity, a high degree of alignment, and close-packing. However, as shown in Figure 11, the actual morphology of a typical CVD-grown forest is very different from this ideal picture, depicted schematically in Figure 10, or in many proof-of-concept publications. Work in this dissertation enabled revealing the collective growth behavior leading to the hierarchical forest structure shown in Figure 11.

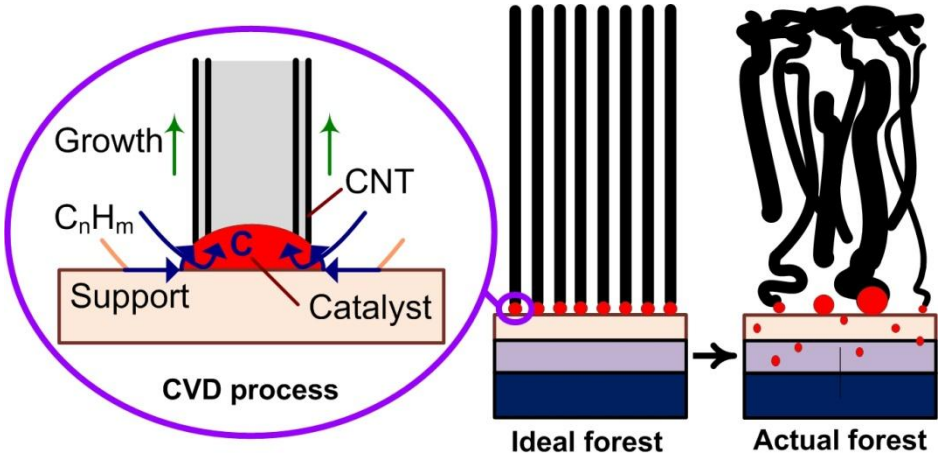

Figure 11. Schematic of CVD-grown forest, showing the deviation of actual forest morphology from the ideal picture.

Actual CNT forests have a hieratical morphology of CNTs that are highly entangled and intertwined. There is a wide distribution of CNT diameters and lengths. The tortuosity also varies, where some CNTs within the same population are straighter than others. Only a small fraction of nanoparticles bear CNTs and the rest are inactive. The same forest may have SWNTs and MWNTs having different numbers of walls. In addition to all these global differences, there is also a spatial variation of density, diameter distribution, and alignment across a typical CVD-grown forest. Since a large number of CNTs grow simultaneously in a typical CVD process (more than 10^9 CNTs/cm^2), understanding the collective chemical and mechanical effects of growth is key to overcoming the fundamental limiting mechanisms of growth.

This dissertation presents tailored synthesis processes, characterization techniques, and mathematical models that **enable both revealing the spatiotemporal evolution of the collective CNT population growth and achieving improved control on the morphology of hierarchical CNT structures synthesized by CVD**. Below is a brief description of the following chapters.

Chapter 2 elucidates the population dynamics of CNTs growing in a forest by CVD, through the development of a new comprehensive characterization methodology. By combining Synchrotron X-ray scattering and attenuation with real forest height kinetics, the spatiotemporal evolution of diameter distribution,

alignment and density are mapped during growth. Using a mathematical model of population growth to describe the forest mass kinetics provided insights into activation and deactivation behavior.

Chapter 3 reveals the diameter-dependent nature of growth activation and deactivation within large CNT populations. This is achieved by developing an approach for further analysis of the data produced by the methodology presented in chapter 2, to obtain the mass kinetics of CNT subpopulation having a narrow diameter range. This technique enabled quantitatively describing the catalytic lifetimes as a function of CNT diameter.

Chapter 4 explains and mathematically models the synergetic chemical coupling effects arising among neighboring CNT micropillars growing in arrays. The model is validated by comparison to experimental results, and can predict the spatial variation of CNT micropillar height. The model is also used to inform the design of microscale catalyst patterns for engineering the morphological and geometric uniformity of as-grown micropillars.

Chapter 5 presents a mechanical model for the tangled CNT morphology comprising tortuous CNTs that are pinned to each other at contact. Internal forces ensuing from the mismatch between the apparent forest growth rate and the diameter dependent growth rates of individual CNTs, are estimated based on the

calculated stiffness of curved beams. X-ray characterization of CNT morphology is used as input to this model for correlating the evolution of forces and densities.

Chapter 6 shows that reaction kinetics of CNT growth by CVD can be modulated by mechanical forces, highlighting the mechanochemical nature of growth. This chapter presents an experimental study using a custom-built CVD reactor that enable *in situ* mechanical manipulation of growing forest, while measuring the real-time growth kinetics.

Chapter 7 reveals the nucleation and self-organization of CNTs during the early growth stages by *in situ* studies using environment transmission electron microscopy (E-TEM). Results show that the kinetics of nanoparticle formation are S-shaped, and elucidate the importance of mechanical coupling in building the self-aligned structure during CNT crowding.

Chapter 8 summarizes the contributions and findings of this dissertation, as well as future outlook to areas of research that can build on the present work. Also, this chapter lists other complementary contributions, which are not directly related to chapters of this dissertation, and the author has made largely through collaborations. These include the utilization of X-ray based characterization techniques for interrogating the morphology of CNTs grown from nanocomposite catalysts, alumina-coated CNTs, and electrostatically manipulated CNTs. In addition, the

author contributed to research on the convective self-assembly of nanoparticles into 2D and 3D structures.

CHAPTER 2: POPULATION GROWTH DYNAMICS OF CARBON NANOTUBES[1]

2.1. Summary

Understanding the population growth behavior of filamentary nanostructures, such as carbon nanotubes (CNTs), is hampered by the lack of characterization techniques capable of probing statistical variations with high spatial resolution. Presented in this chapter is a comprehensive methodology for studying the population growth dynamics of vertically aligned CNT forests, utilizing high-resolution spatial mapping of synchrotron X-ray scattering and attenuation, along with real-time height kinetics. CNT alignment and dimensions are mapped within CNT forests, revealing broadening and focusing of size distributions during different stages of the process. Then, the number density and mass density of the CNT population are calculated versus time, which are true measures of the reaction kinetics. Results show that the mass-based kinetics of a CNT population is accurately represented by the S-shaped Gompertz model of population growth, although the forest height and CNT length kinetics are essentially linear. Hence,

[1] Significant portions of this chapter are reprinted with permission from reference 35. Bedewy, M.; Meshot, E. R.; Reinker, M. J.; Hart, A. J., Population Growth Dynamics of Carbon Nanotubes. *ACS Nano* 2011, 5, 8974-8989. Copyright 2011 American Chemical Society.

competition between catalyst activation and deactivation govern the rapid initial acceleration and slow decay of the CNT number density. The maximum CNT density (i.e., the overall catalyst activity) is limited by gas-phase reactions and catalyst-surface interactions, which collectively exhibit autocatalytic behavior. Thus, this chapter presents a comprehensive picture of CNT population growth which combines both chemical and mechanical cooperation. These findings are relevant to both bulk and substrate-based CNT synthesis methods, and provide general insights into the self-assembly and collective growth of filamentary nanostructures.

2.2. Introduction and Literature Review

Engineering of materials comprising highly ordered nanostructures requires an understanding of the collective behavior of individual nanostructures in a large population. While many destructive and non-destructive techniques can be employed for measuring the geometry and dimensions of individual nanostructures, there are fewer methods capable of interrogating large populations thereof. The importance of acquiring and understanding statistical information arises from the fact that a macroscopic assembly of nanostructures typically consists of an extremely large number of individual nanoscale elements. For instance, a 1 cm^2 substrate area of an array of vertically aligned carbon nanotubes (CNTs), a so called "forest," typically contains more CNTs than there are humans on earth. In this and many other examples, there is a profound gap between measurements of individual nanostructures, and measurements of the bulk properties of materials. This gap

spans the challenge of obtaining representative statistics on the size and/or the distribution of nanostructures throughout a physical space, which limits essential insights into the causes of variation in the final material properties. Advances in population-based analysis of nanostructures will also be necessary for use of statistical methods to analyze and control the quality of nanostructured materials and their production, much like is commonplace in traditional manufacturing operations.

CNT forests are a model system for investigating the population dynamics of nanostructure synthesis, and are an attractive material design that potentially enables the utilization of the properties of billions of CNTs in parallel. Importantly, it has recently come to light that typical CNT forests have a complicated and spatially non-uniform morphology, including gradients (e.g., from top to bottom) of alignment, diameter, and packing density.[36-40] These variations depend on the multivariate conditions used for CVD growth. Nevertheless, many investigations of CNT forest properties have assumed a perfectly uniform morphology. In many cases such ideal morphology is needed to optimize functional properties; hence, a more detailed understanding of the morphology is needed to accurately model mechanical, thermal, electrical, and other properties that depend on hierarchical network effects[41-43]. Highly uniform ensembles of monodisperse CNTs are needed for electrical interconnects,[7, 9] filters,[21] gas sensors,[22-24] and structural composites[11]. Also, consistent morphology is required for post-synthesis processing such as the

spinnability of CNTs from forests into yarns and sheets,[44, 45] which was shown to depend on the CNT areal density and bundle organization within a forest.[46]

An accurate picture of the internal structure of CNT forests is also essential for understanding how to control the growth process to approach the ideal structure. In fact, the kinetic picture of how a population of CNTs evolves with time during synthesis is still largely incomplete. The CNTs within a forest nucleate from a population of catalyst nanoparticles having a distribution of sizes and shapes, whose morphology was shown to evolve during growth,[39, 47] resulting in a distribution of CNT sizes, and likely a polydispersity of growth rates. Based on our recent observation that the number and mass density of CNTs change during growth and considerably decay (by almost an order of magnitude) towards termination,[36] the apparent forest height kinetics measured *in situ*[48-54] or *ex situ*,[55-57] must be complemented by a measure of the mass kinetics. The discrepancy between forest height kinetics and mass kinetics further explains the abruptness of forest growth self-termination[36], which we[51] and others[53, 58-62] have observed.

Several *in situ* and *ex situ* methods for nondestructively measuring CNT forest height have been developed, such as optical photography and videography,[50, 53] optical interference,[48] single-slit laser diffractography,[63] time-resolved reflectivity,[49] and cycling of growth conditions to form marks that are visible in electron microscopy.[56, 57] Methods of accurate and nondestructive mass measurements are fewer, and generally use a microbalance either *in situ*,[64] or *ex situ*,[36, 65] which is limited

by the resolution of the balance and cannot be used for spatial mapping. Alternatively, the changes in contrast from *ex situ* Z-contrast transmission electron microscopy (Z-STEM) images, as well as changes in the estimated effective extinction coefficient from time-resolved optical reflectivity (TRR) were used to infer information about CNT forest density.[66] Although these methods can be used for spatial profiling, they can only provide relative measures of density, and cannot give absolute density values.

In addition, *in situ* Raman Spectroscopy has been used to infer CNT growth kinetics from real-time monitoring of the area under the G-band.[67-70] Because the CNT-laser coupling strength depends on the structure, diameter, and number of walls of a CNT, it is unlikely that the G-band intensity is directly proportional to the total mass of a polydisperse CNT population.[71] For both single-wall (SWNT) and multi-wall (MWNTs) CNTs, the line shape of the G-band is a superposition of multiple peaks which depend on the CNT chirality, conductivity, and charge transfer with the surroundings.[71, 72] Further, for a typical millimeter-sized CNT forest, Raman spectroscopy cannot be reliably used to get population measurements because the laser beam cannot fully penetrate the forest. The presence of non-CNT graphitic deposits can also contribute to the G-band intensity. Hence, Raman studies require either a single CNT or a relatively limited number thereof to give relative mass measurements, and require small diameter SWNTs to give structural information about size and chirality.

It has been previously showed that small angle X-ray scattering (SAXS)[73, 74] and ultra-small angle X-ray scattering (USAXS)[75] can provide precise measurements of the diameter, bundle size, and alignment of CNTs within a forest. This chapter presents a comprehensive non-destructive characterization methodology for CNT materials, which enables identification of the population kinetics of the CNT growth process. This method combines high resolution spatially resolved X-ray scattering and intensity attenuation measurements after growth, with real-time measurements of CNT forest height during growth. The spatial and temporal evolution of the mass density, number density, and cumulative CNT areal density are analyzed with unprecedented accuracy from the initial CNT self-organization stage until growth termination. Based on these findings, growth of a CNT forest can be explained as a time-varying population. This population behavior results from a statistical ensemble of individual particles and CNTs having polydisperse reaction behavior, contrasting previous studies that explained CNT forest growth kinetics based on models for a single particles and/or CNTs.[49, 58, 76, 77] Population growth models indicate that CNT synthesis exhibits an autocatalytic and cooperative nature, and that the maximum density of CNTs is limited by the process conditions. Finally, surface analysis of the catalyst gives insights into how competition between catalytic activation and deactivation rates prevent indefinite growth of CNTs using current CVD methods.

2.3. Methods

Forests of vertically aligned CNTs are grown using either a hot-wall reactor (tube furnace), or a substrate heated cold-wall reactor that is equipped with real-time height monitoring. Figure 12 shows the schematics and time-temperature-flow sequences for the two different reactors that were used for carbon nanotube (CNT) forest synthesis by chemical vapor deposition (CVD). Source gases of He (99.999%, PurityPlus), H_2 (99.999%, PurityPlus), and C_2H_4 (99.999%, PurityPlus) were used. During growth in the cold-wall reactor, the heated substrate is operated at T_s, while the thermal decomposition of the incoming gas mixture is determined by preheating upstream of the reactor at temperature T_p. First, a five-minute purging step is carried out to purge out air from the tube as a preparation step for introducing H_2; during this step, the preheater is ramped to the setpoint T_p= 1050°C. Then, a three-minute gas-mixing step is carried out to stabilize the gas atmosphere before heating. After that, the temperature is rapidly increased to T_s = 775°C in a period of approximately ten seconds. In both types of CVD reactors, custom labVIEW interfaces were used to control process variable, such as temperature and gas flow rates. For the cold-wall reactor the substrate temperature was measured by an infrared sensor (Exergen 2ACF-K-HIE). Digital mass flow controllers (Aalborg GFC 17, response time = 2 s) were used to control and measure gas flow rates. Real-time forest height is measured using a non-contact laser displacement sensor (LK-G152, Keyence) which is mounted above the cold-wall reactor as described earlier.[51, 54] The substrate is a

multi-layer catalyst thin film (1 nm Fe / 10 nm Al_2O_3 / 300 nm SiO_2) deposited by e-beam evaporation on 0.5 mm thick <100> 4-inch silicon wafer.

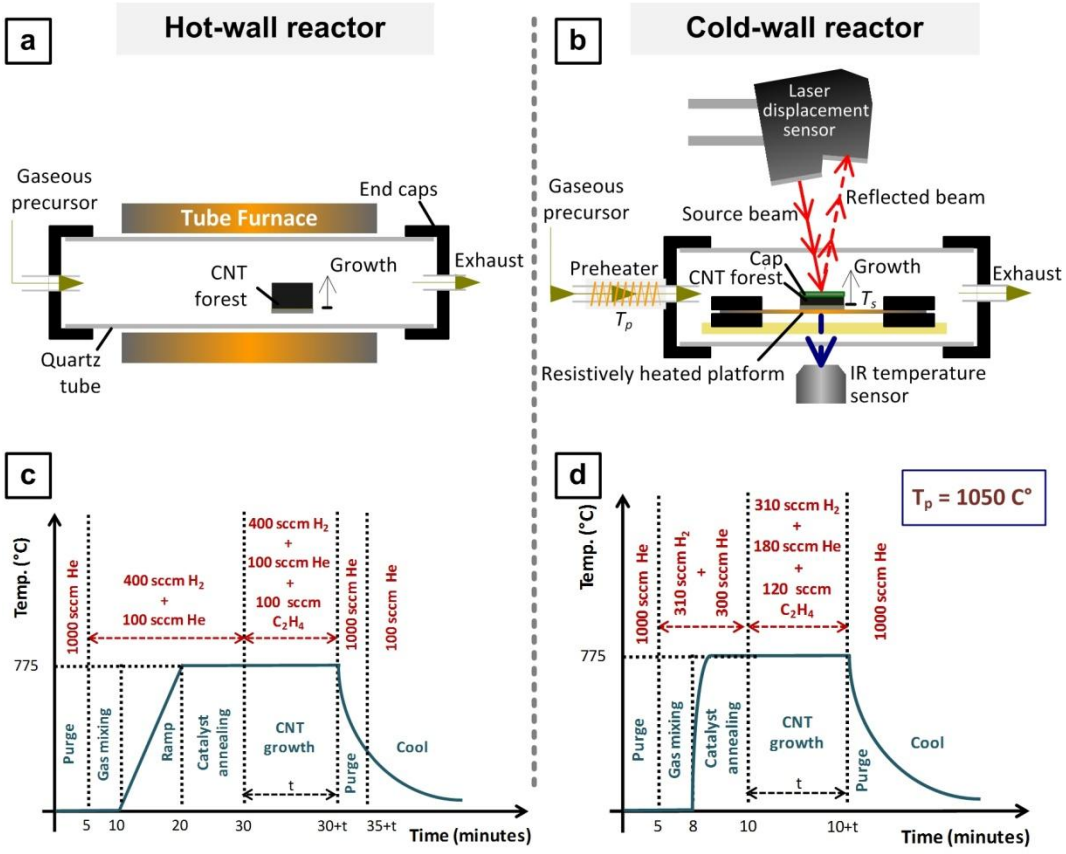

Figure 12. Details of CNT synthesis: Schematics of the (a) hot-wall reactor (tube furnace) and (b) cold-wall reactor; Process sequence for growth of CNTs forests in the (c) hot-walled reactor and the (d) cold-walled reactor for growth time *t*.

For X-ray scattering measurements, the CNT forest is placed on a motorized stage in the beam path of the G1 beamline at Cornell High Energy Synchrotron

Source (CHESS). A beam energy of 10 +/- 0.1 keV (wavelength ≈ 0.13 nm) is selected with synthetic multilayer optics (W/B4C, 27.1 Å d-spacing), and the beam is focused down to ≈10 μm using a single-bounce monocapillary that was fabricated at CHESS. The sample is aligned according to the procedure explained in Figure 13. A bare Si substrate is first placed on a metal holder having a ground top surface, as shown in Figure 13a. The motorized sample stage is then used to scan the vertical direction (z-axis) to find the edge by recording the respective intensity reading at each position and selecting the middle point (Figure 13b). Then, the tilt angle θ (around y-axis) is scanned to find the position of maximum intensity, which corresponds to the surface orientation that is parallel to the direction of the X-ray beam (Figure 13c). As a result, the error in tilt angle is expected to be less than 0.01°.

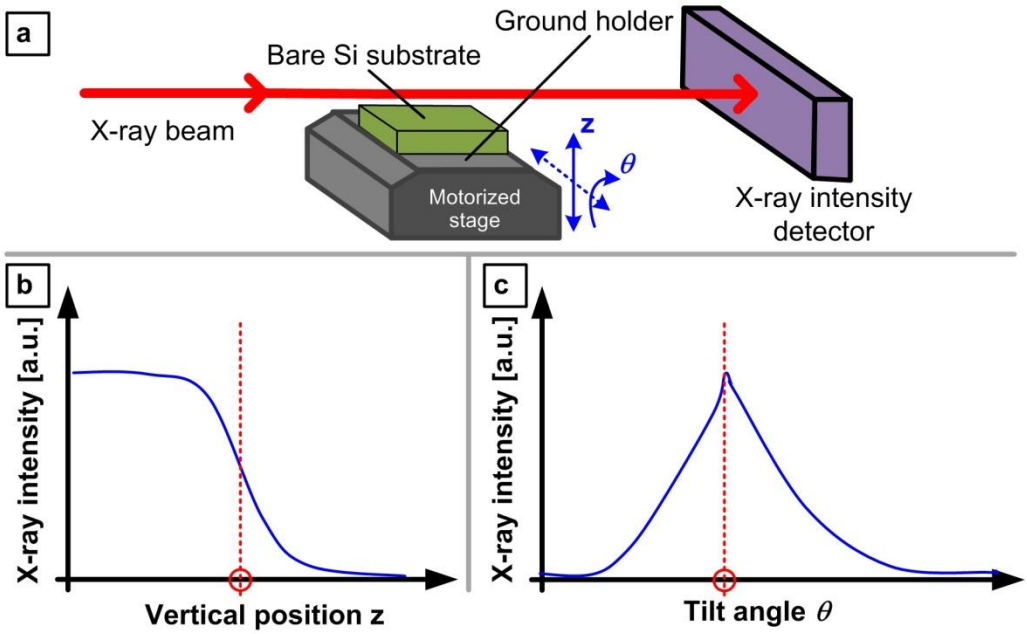

Figure 13. Sample alignment procedure: (a) Schematic of the alignment procedure; (b) Scan of X-ray intensity versus vertical position; (c) Scan of X-ray intensity versus tilt angle θ.

Figure S2 shows the intensity readings from the X-ray sensors placed upstream and downstream of the CNT forest. The downstream X-ray intensity measurements are normalized to the upstream measurements in order to eliminate the effect of the drift in synchrotron intensity with time. Then the Beer-Lambert-Bouguer law is applied to calculate the mass density of each slice in the CNT forest, based on the total mass attenuation coefficient of carbon (graphite) at the X-ray energy of 10 KeV ($\approx 3\ cm^2/g$)[78].

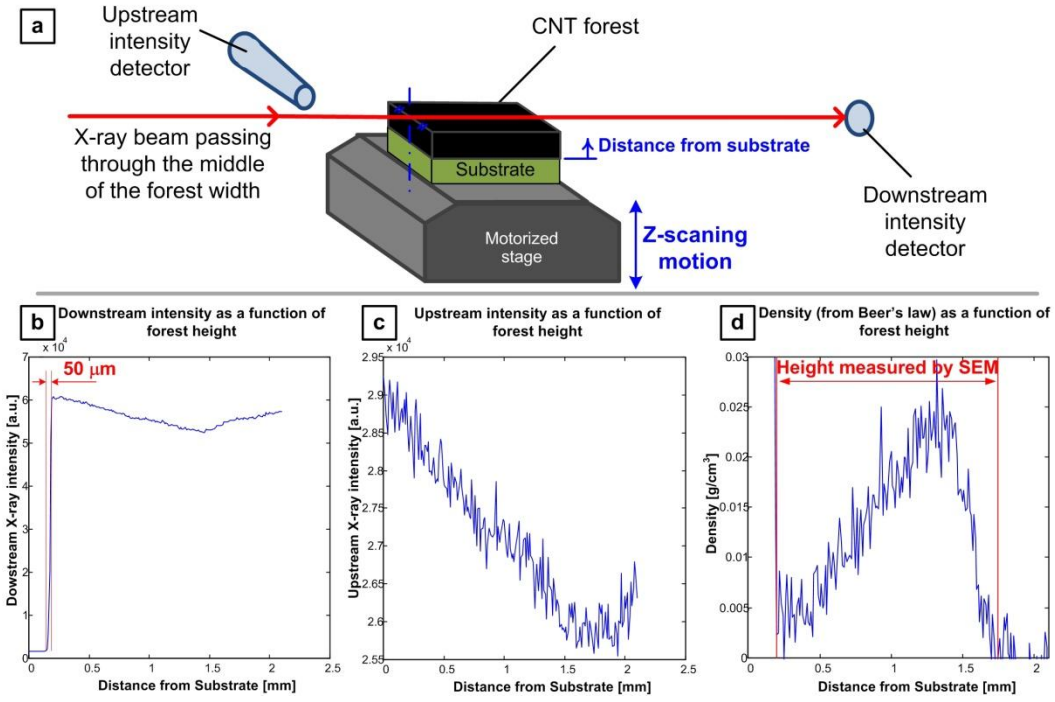

Figure 14. X-ray attenuation results for the sample grown in the cold-wall reactor: (a) Schematic of the sample configuration showing that the focused X-ray beam passes through the middle portion of the forest (away from the sample corners); (b) Evolution of the X-ray intensity measured downstream of the CNT forest sample (using the beam-stop diode shown in Figure 21a), as a function of distance from the bottom substrate. The 50 μm span for intensity increase as the beam crosses the top-edge of the Si-substrate results from two main sources: angular misalignment of the sample (about y-axis) and beam divergence; (c) Evolution of the X-ray intensity measured upstream of the CNT forest sample (using the florescence detector shown in Figure 21a), as a function of distance from the bottom substrate; (d) Evolution of the mass density of each slice in our CNT sample, as a function of distance from the bottom substrate.

A standard sample of silver behenate powder (d_{001} = 58.380 Å) is used to calibrate the pixel-to-q ratio. Line-scans from the 2D SAXS patterns are fitted using

a mathematical model for log-normally-distributed hollow cylinders (Figure 15). These scans are obtained by integration of intensities (I) within +/- 10º from the reference direction of the inverse space parameter q, chosen to be the direction of maximum intensity ($I(q) = \int_{-\pi/18}^{\pi/18} I(q,\theta)d\theta$).

The mathematical model used to fit the SAXS line-scans considers the scattering intensity of hollow cylinders (Figure 15) having the same inner radius (R_i) and outer radius (R_o) as a CNT, with the ratio c = R_i /R_o. The probability density function (PDF) used is for a log-normal distribution of diameters. The scattering intensity is modeled as $I(q) = A$ F(q) $S(q)$, where F(q) is the intraparticle form factor, S(q) is the interparticle structure factor, and A is an adjustable constant that accounts for instrumental and other experimental factors. We set S(q) = 1 because particle-particle scattering occurs at far lower q values than of interest for determining the CNT diameter. The CNT forest is therefore modeled as a population of non-interacting hollow cylinders.

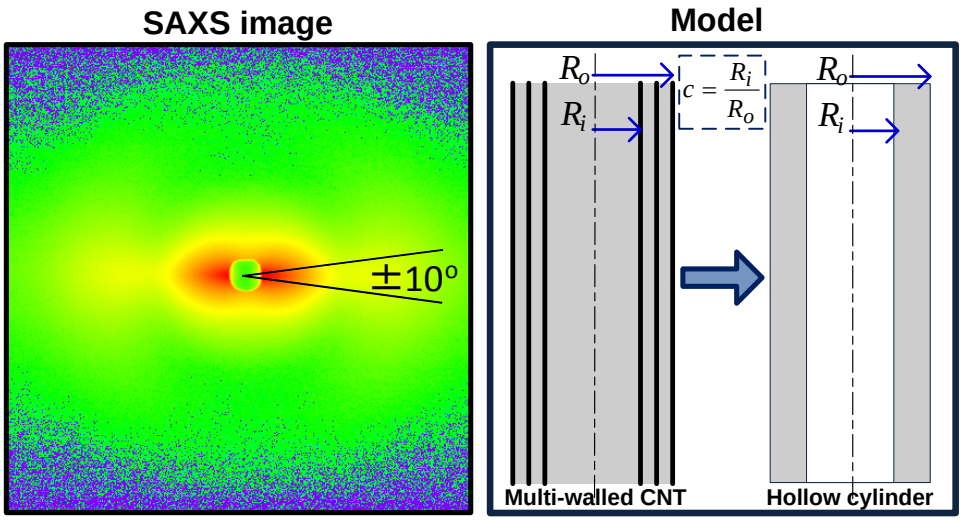

Figure 15. Typical SAXS image used to in the diameter fitting: the model of hollow cylinders having the same inner radius (R_i) and outer radius (R_o) as a CNT, with the ratio c = R_i / R_o.

The form factor for a rod-like particle can be expressed as $F(q) = \frac{L\pi}{q} I_C(q)$, where L is the length of a CNT, $I_C(q)$ is the cross-section scattering function of a cylinder, and q is the scattering vector. $I_C(q)$ is

$$I_C(q) = \frac{\int_0^\infty P(R) f^2(q,R) dR}{\int_0^\infty P(R) dR}, \qquad \text{Eq. 2.1}$$

where P(R) is the distribution function of cylinder radii. For a hollow cylinder,

$$f(q,R,c) = \Delta\rho R_o \frac{2\{J_1(Rq) - cJ_1(cRq)\}}{qR(1-c^2)}. \qquad \text{Eq. 2.2}$$

J_1 is the spherical Bessel function of the first kind, $\Delta\rho$ is the difference in scattering density distribution between the CNT and the surrounding medium (air), and R is the CNT radius. We choose a lognormal distribution to account for polydispersity in CNT radii, such that:

$$P(R) = \frac{1}{R\sigma\sqrt{2\pi}} \exp\left[\frac{-(\ln R - \mu)^2}{2\sigma^2}\right]. \quad \text{Eq. 2.3}$$

The parameters μ and σ are related to the mean ($\overline{R}$) and variance (σ_R) of the CNT radius as

$$\mu = \ln \overline{R} - \frac{1}{2}\ln\left(1 + \frac{\sigma_R^2}{\overline{R}^2}\right), \text{ and} \quad \text{Eq. 2.4}$$

$$\sigma^2 = \ln\left(1 + \frac{\sigma_R^2}{\overline{R}^2}\right). \quad \text{Eq. 2.5}$$

In order to automate the process of fitting for hundreds of scattering images, an algorithm was developed to select the fitting range of each scan and determine an approximate location of the peak based on the locations of the inflection points around the peak. As shown in Figure 16, the experimental data points of a linescan within a predetermined range (q = 0.45 – 1.6) are first fitted with a 9th order polynomial equation that matches the data almost exactly. This fitted polynomial equation is then differentiated twice to identify a local maximum, as well as the two

infliction points that typically straddle the peak point. Then either the local maximum is used as the peak location if it is present, and in case that there is no well-defined peak, the arithmetic mean of the two q locations of the inflection points is used instead. The starting and end points for the selected fitting range are then selected based on a predetermined factor that entails how much of the (maximum intensity – peak intensity) is included in the fitting range in case of the start point, and how much of the (peak intensity – minimum intensity) is included in the fitting range in case of the end point (see the two horizontal dashed red lines). The start and end of fitting range are then selected based on the intersection of those two horizontal red lines with the data. For all the fits in this paper the factors used for determining the start and the end points were 0.8 and 0.7, respectively.

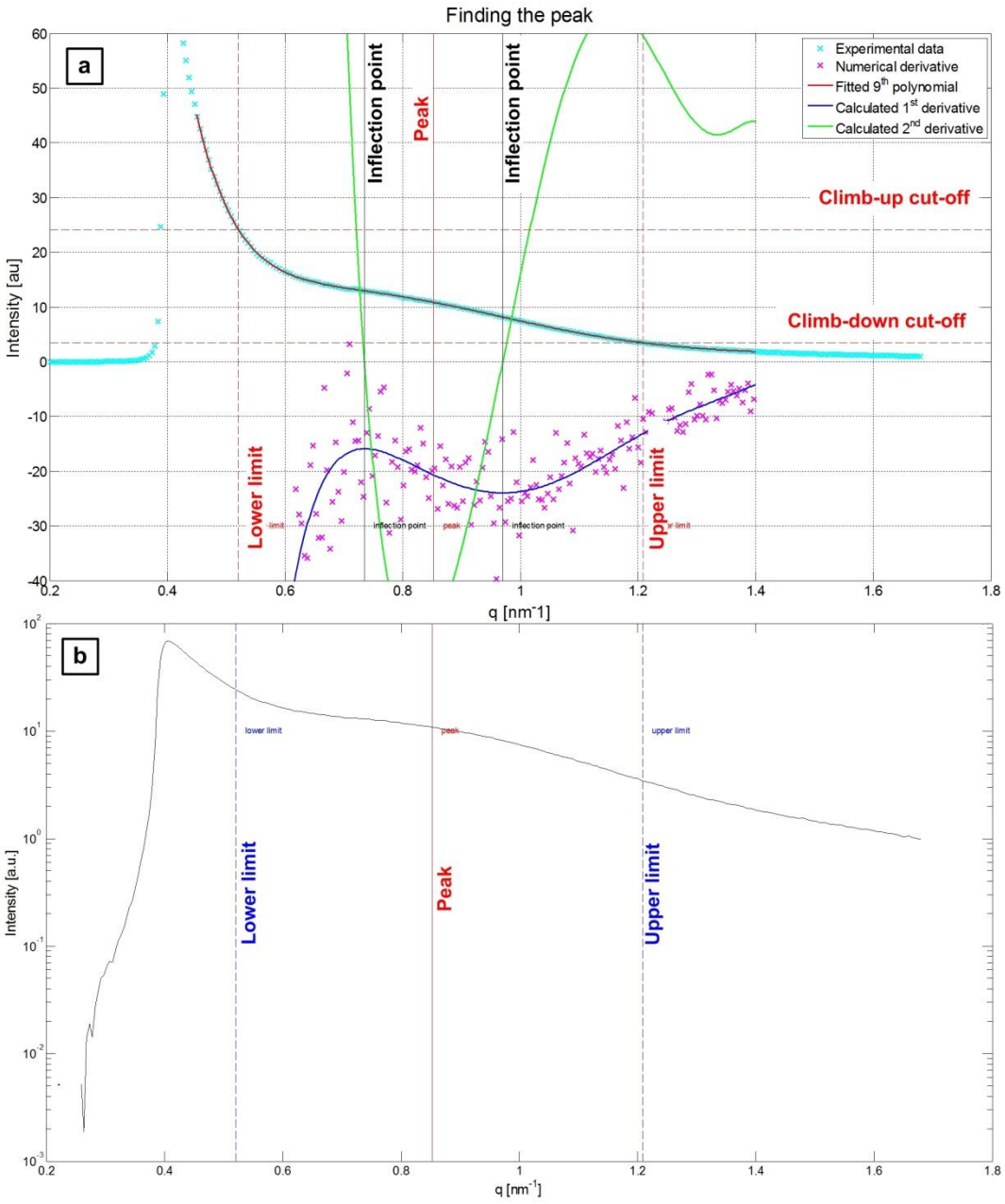

Figure 16. (a) Range-/peak-finding algorithm; (b) Semi-log plot of the experimentally-obtained linescans, along with the peak and fitting limits obtained from the algorithm.

The fitting code used an iterative approach in searching for the best fit within this selected fitting range. By including the low q part of the data, a good fit was achieved that selects a probability density function (PDF) for diameter distribution as well as for the ratio c = ID/OD, where ID is the inner diameter of the multi-walled CNT and OD is the outer diameter of the multi-walled CNT. As can be seen in Figure 17, the correct choice of c results in a better fit of the slope of the low q part of the linescans. The slope is generally steeper for smaller values of c.

X-ray photoelectron spectroscopy (XPS) was carried out at room temperature on the substrate-bound catalyst for ≈ 5×5 mm samples. In all cases, samples were exposed to the atmosphere before putting them in the high-vacuum XPS chamber. A Kratos Axis Ultra X-ray Photoelectron Spectrometer was used with a monochromatic X-ray source (Al kα X-ray radiation). The pass energy of the analyzer is 160 eV for the Survey scans and 20 eV for the core scans. The anode voltage was set to 15 kV, and emission current to 6 mA (X-ray power ≈ 90 Watt). CasaXPS software (Version 2.3.14) was used to process the spectra. All samples were placed together on the same sample holder and spectra were collected back-to-back during the same run for comparative purposes (Figure 18). The carbon 1s peak is used to obtain an offset correction factor of +3.2 eV, based on the commonly used value of 285 eV for the carbon peak (Figure 19).

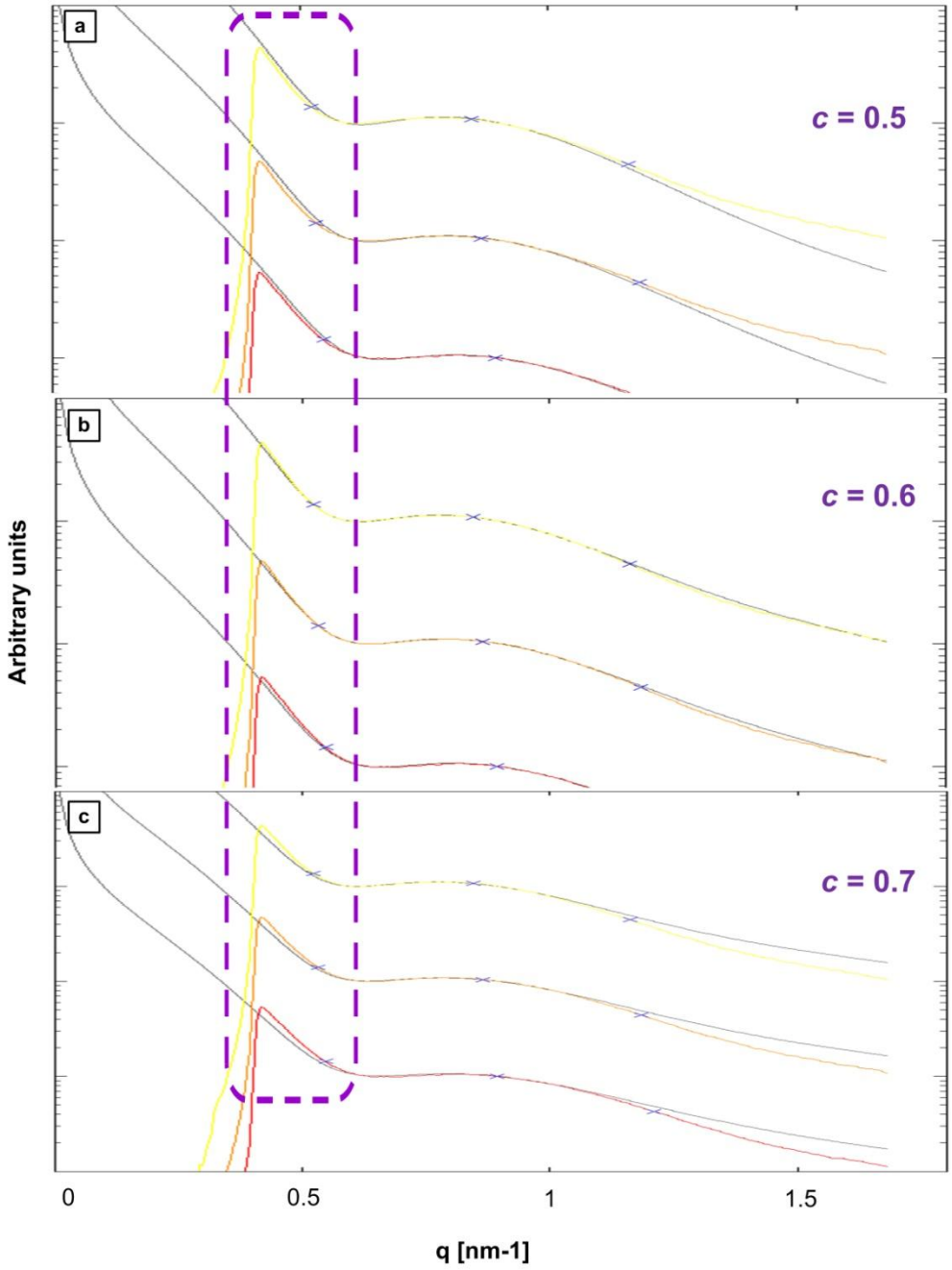

Figure 17. SAXS model fits for linescans of three forest slices along forest height with fixing value of the fitting parameter c to (a) 0.5, (b) 0.6, and (c) 0.7.

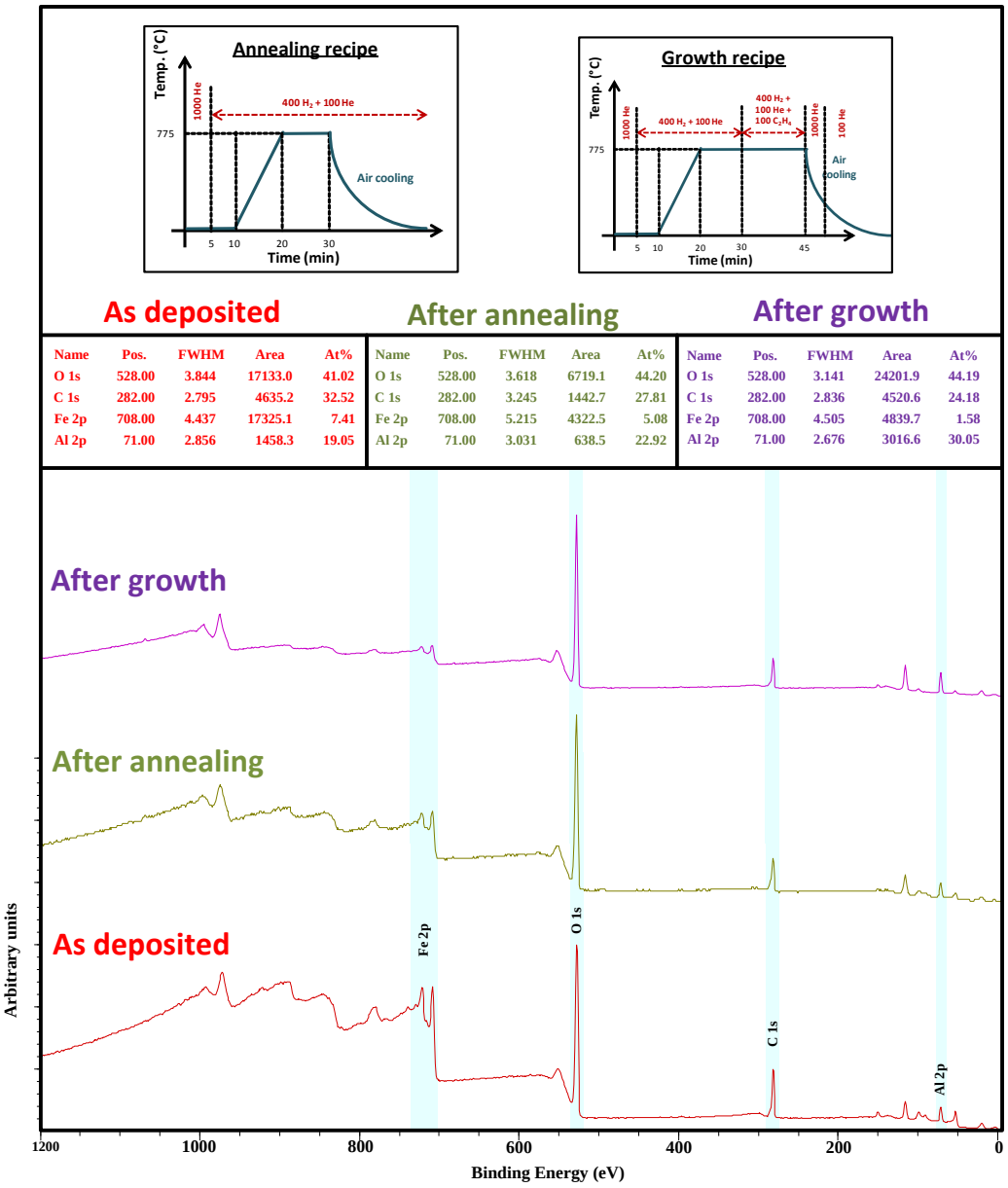

Figure 18. XPS survey spectra for three samples collected together in the same run. The three samples were substrates for CNT forest growth. The first sample is the as-deposited multi-layer thin film catalyst (1 nm Fe/ 10 nm Al_2O_3/ 300 nm SiO_2 / 500 μm Si); the second sample was annealed according to the recipe in the inset; the third sample was after growth according to the recipe in the inset, and then the forest was delaminated.

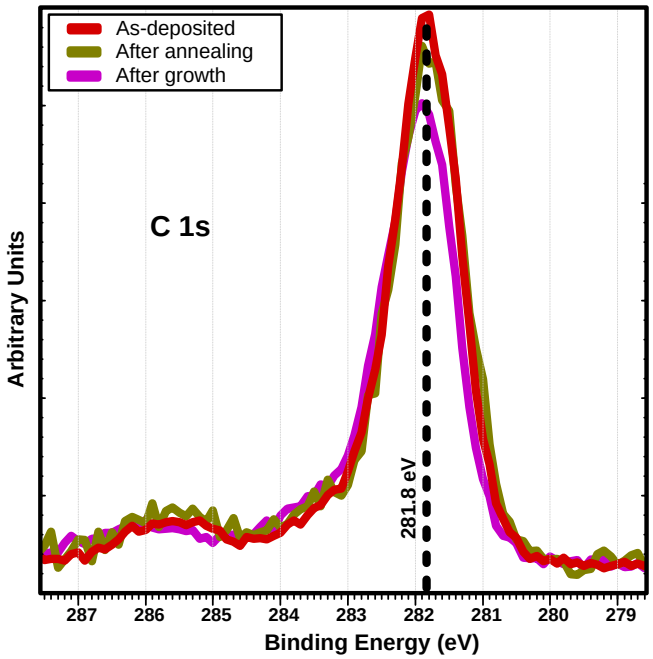

Figure 19. XPS core spectra for C 1s peaks for different samples (as deposited, after annealing, after growth). Peak position at ≈ 281.8 eV, is used to calibrate the binding energy value by using the commonly used value of 285 eV, i.e. a shift of + 3.2 eV is applied to the spectra in Figure 7.

AFM imaging was done using MultiMode AFM, Nanoscope IIIa controller in tapping mode, and WSxM 3.0 Beta 12.1 software was used to view results.[79] A Matlab code was developed to further process AFM images in order to count the particle number density based on an algorithm that finds the local maxima of the intensity map representing the AFM image (Figure 20).

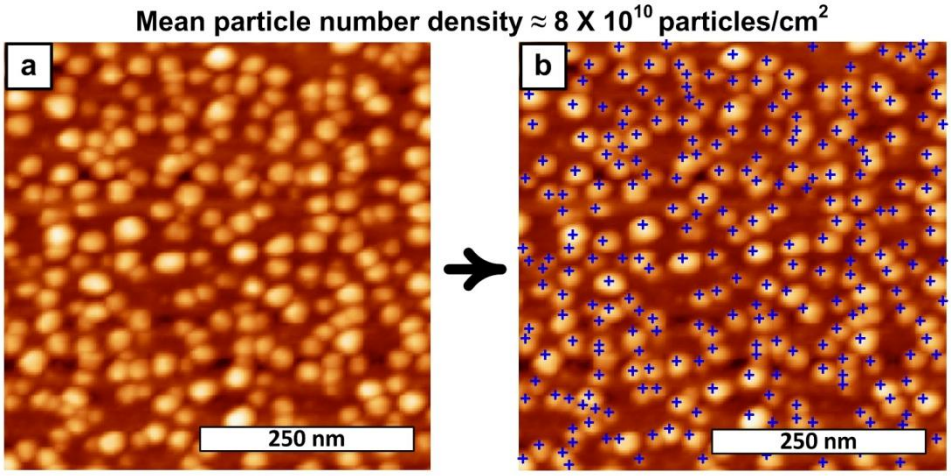

Figure 20. (a) AFM image of a sample annealed in the cold-wall reactor according to the recipe in Figure 12; (b) applying an algorithm that counts the particles by identifying local maxima in an intensity map from the AFM image.

2.4. Results and Discussion

The methodology for CNT population analysis presented in this chapter begins with high-resolution spatial mapping of the forest using synchrotron X-ray scattering. We place an already-grown CNT forest on a motorized stage in the beam path of a synchrotron X-ray beam that is focused using monocapillary optics, as shown in Figure 21a. By scanning the forest from top to bottom at increments of 10 μm, which is approximately equal to the beam size, the forest is discretized into a stack of differential volumes that is referred to as "slices". Two different types of data are acquired for each slice: (1) X-ray scattering patterns, collected using a 2D area detector; and (2) X-ray intensity, collected using diode detectors placed

upstream and downstream to the CNT forest. We also measure the CNT forest height versus time *in situ* during growth (see methods section). Both the *in situ* and *ex situ* data are inputs to the quantitative analysis procedure shown in Figure 21b.

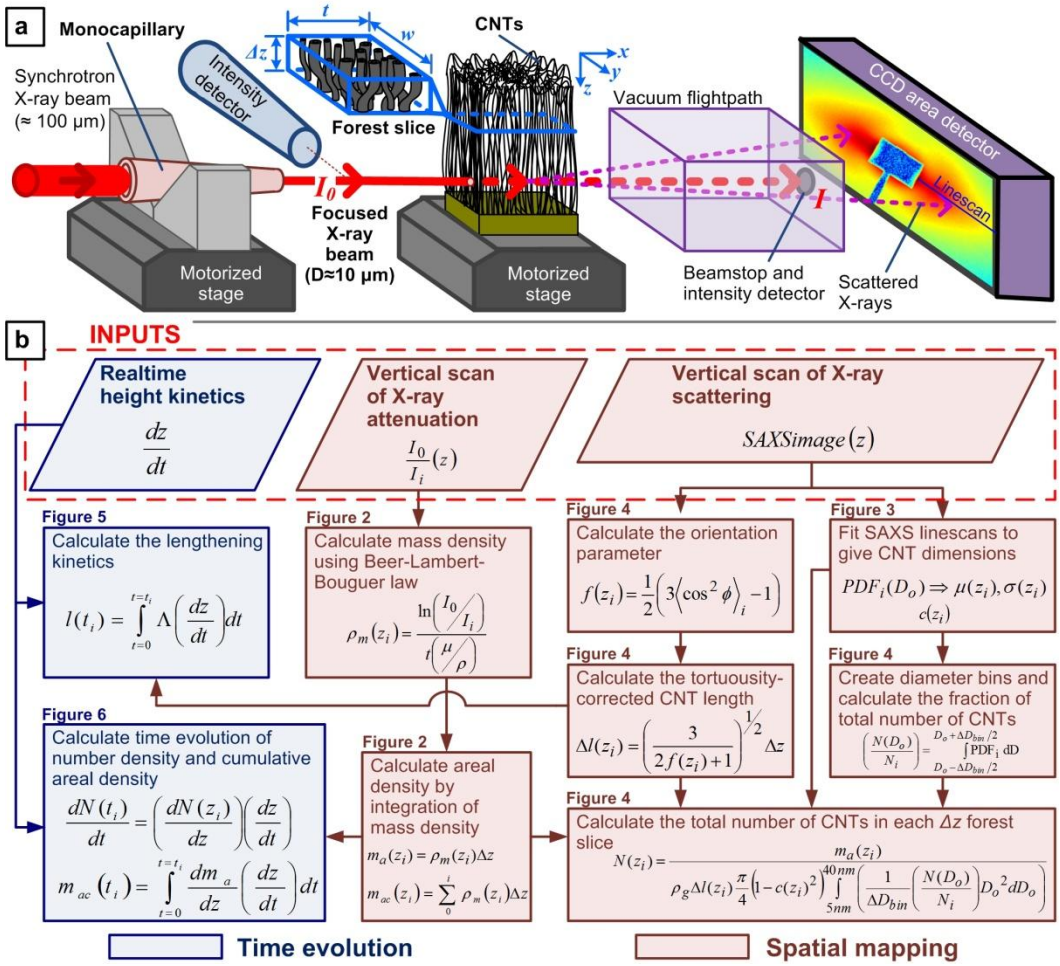

Figure 21. Method of X-ray mapping and analysis of CNT populations: (a) schematic of experimental setup for simultaneous spatially resolved synchrotron X-ray mass attenuation and scattering measurements; (b) Quantitative analysis procedure incorporating real-time CNT height measurements with X-ray data to give mass and number density kinetics. The figure labels above each box indicate where the respective results are shown.

First, the measurements of X-ray intensity are used to calculate the local mass density of the CNT forest within the beam path, according to the Beer-Lambert-Bouguer law.[80, 81] This relates the density of a material to the X-ray intensity attenuation due to both scattering and absorption, such that

$$\rho_m(z_i) = \frac{\ln\left(I_0 / I_i\right)}{t\left(\mu / \rho\right)}. \qquad \text{Eq. 2.6}$$

Here $\rho_m(z_i)$ is the local mass density obtained from each forest slice (index i), defined as the mass of CNTs in each slice (dm_i) per unit volume ($dv = t \times w \times dz$); z is the distance from the top of the forest to the forest slice; t is the CNT forest depth in the direction of the X-ray beam; I_0 is the X-ray intensity upstream of the CNT forest; I is the X-ray intensity downstream of the CNT forest; and μ/ρ is the total mass attenuation coefficient. The index is counted starting at the top of the forest, *i.e.*, for a 2 mm forest, $i = 200$ at the base.

The Beer-Lambert-Bouguer law is applicable for a homogeneous medium. This assumption is valid for the CNT forest because the waviness of the CNTs is on a much smaller length scale than the beam, and the variations in morphology (discussed later) occur over a much larger length scale. Throughout this analysis, it is also assumed that the forest is homogeneous in the X-Y plane, *i.e.*, along the direction of the X-ray beam, which was validated in previous work.[73]

For X-rays with energies below 100 keV, absorption is the primary contribution to X-ray attenuation, compared to both elastic and inelastic scattering. Hence, using the absorption mass attenuation coefficient instead of the total mass attenuation coefficient would have only resulted in a small error in the density calculation. Further, because there is only a small amount of absorption compared to the overall X-ray intensity, *i.e.*, $I_0 \approx I_i$, noise in the measurements leads to an apparent fluctuation in the calculated vertical profile of density. We estimate that the signal-to-noise ratio (SNR) of density measurements is equal to ≈ 2. The SNR is calculated as the ratio between the mean and the standard deviation (Figure 14). Nevertheless, due to the high spatial resolution of this mapping technique, this noise is inconsequential when the local density measurements are integrated as discussed later.

Using the mass density $\rho_m(z_i)$ of each slice with thickness ($\Delta z = 10$ μm) and relating the slice mass (m_i) to the unit cross forest sectional area ($a = t \times w$), we calculate the areal mass density of each slice,

$$m_a(z_i) = \rho_m(z_i)\Delta z \,. \qquad \text{Eq. 2.7}$$

Next the cumulative areal density (m_{ac}, total CNT mass per unit area) versus position in the forest is calculated by summing the areal density of all slices,

$$m_{ac}(z_i) = \sum_0^i \rho_m(z_i)\Delta z \,. \qquad \text{Eq. 2.8}$$

The areal mass density per slice represents how much CNT mass was created for that specific 10 μm of the forest, and the cumulative areal density represents the mass of the CNT forest above (and including) the indexed slice.

X-ray mapping of tall CNT forests (up to 2 mm) grown in both cold-wall (heated substrate, Absolute Nano SabreTube) and hot-wall (heated tube, Thermo-Fisher MiniMite) systems was performed. Each forest was discretized into up to 200 slices with 10 μm thickness. As shown in Figure 23, the mass density varies throughout the forest: it increases in a closely linear trend from the top surface ("crust") of the forest until it reaches a maximum and brief plateau, then it decays gradually towards the bottom of the forest. The formation of a tangled crust at the start of growth is well-known; however, this density map reveals a subsequent "crowding" stage where the CNT density increases substantially as new CNTs begin to grow even long after the forest self-organizes and starts to thrust upward. The distance of this density increase (≈300) is significantly larger than the non-uniformity of the top surface of the forest, which we estimate to be less than 100 μm (Figure 22). Also, the employed alignment procedure (Figure 13), utilizing X-ray intensity scans ensures that the sample tilt (about y-axis) is within ≈ 0.01° of the substrate plane. Hence, the slope of the density increase predominately represents the kinetics of the crowding stage, i.e., the rate at which new CNTs begin growing from catalyst particles that were inactive during the self-organization stage.

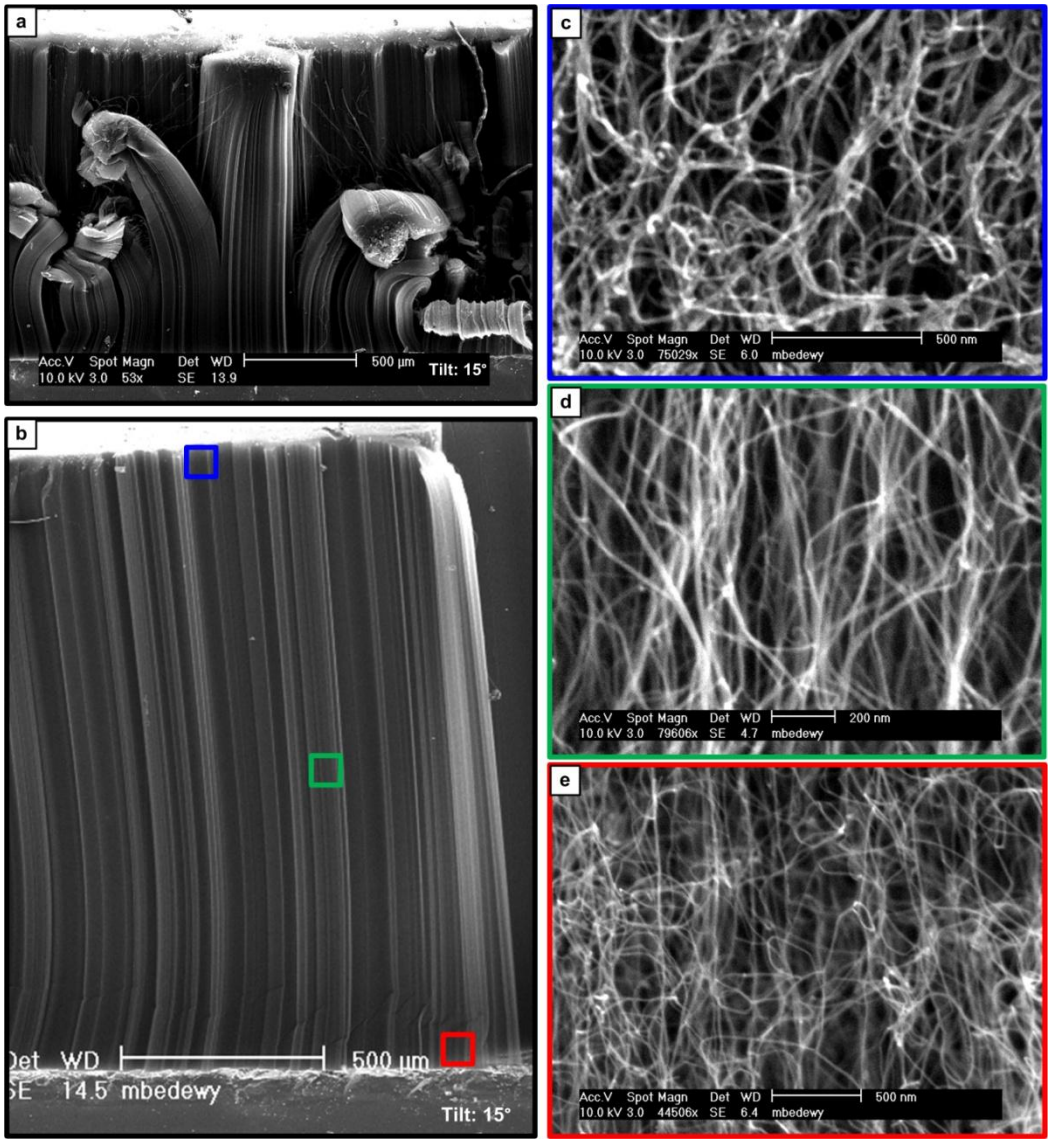

Figure 22. SEM images of the sample grown in the cold-wall reactor: (a) forest sidewall, showing flatness of top-surface in the middle if the forest; (b) forest corner, showing uniformity of the top surface; forest morphology near the top (c); the middle (d); and the bottom (e of the sidewall of the forest, showing the evolution of alignment and qualitative trends of CNT number density.

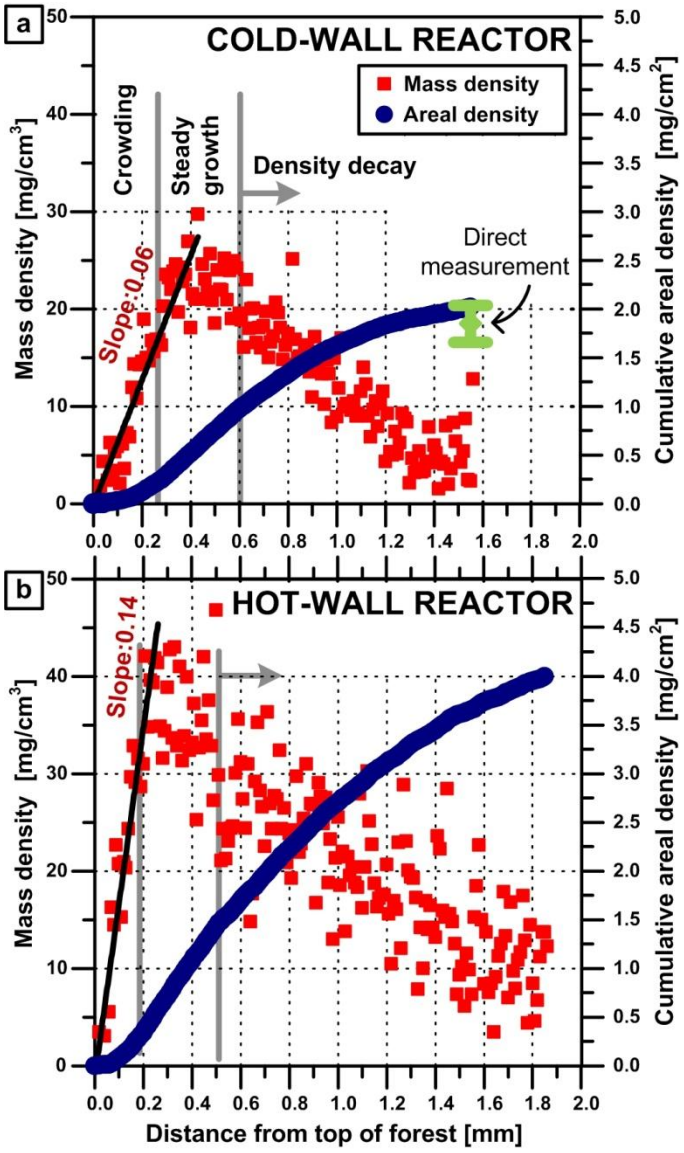

Figure 23. Spatial evolution of mass density and areal density for CNT forests grown in (a) cold-wall reactor with resistively-heated substrate; (b) hot-wall reactor with externally-heated quartz tube.

Results show that the kinetics of crowding depend on the process conditions; therefore, the rate of crowding and the maximum density represent the efficiency of

CNT nucleation from the population of catalyst particles on the substrate. For instance, as can be seen by comparing Figure 23a and b, the slope of CNT density increase for the sample grown in a hot-wall reactor is approximately twice that of the sample grown in a cold-wall reactor. This is attributed to the different process parameters used in the two systems, which are documented in Figure 12. Both samples were annealed at 775 °C in H_2/He; however, the rate of heating and duration of annealing in the cold-wall system was much shorter than the hot-wall system. A long annealing duration may be necessary for catalyst nanoparticles to be fully reduced from a higher oxide state (Fe^{2+} or Fe^{3+}) to a lower one (Fe^{1+} or Fe^{0}) in order to become active[82, 83]. This could also explain why the hot-wall sample has a higher maximum density, indicating that a larger fraction of the catalyst nanoparticles becomes active for CNT growth.

After the maximum density is reached, the density remains approximately constant at this value for a small (≈ 300 μm or less) portion of the forest (< 20 % of the forest height). Hence, only a small portion of the forest is truly uniform, and this observation may highlight the general difficulty of producing highly uniform and tall CNT ensembles even though many CVD methods growing millimeter-scale CNT forests have assumed overall uniformity. Then, after the brief steady growth stage, the density decays due to accumulated deactivation of individual catalyst particles, and proceeds until eventual self-termination. The shape and/or the slope of the decay also depend on the growth conditions, representing variability in the catalyst

deactivation kinetics. Nevertheless, a universal observation in all samples that were tested is that both the initial density at the top of the forest (including the crust) and the final density are approximately one order-of-magnitude below the maximum density. Thus the same critical CNT density forms the self-supporting structure that enables "lift-off" of the CNT forest, and causes collective self-termination at the end of the growth process.

The spatial evolution of the cumulative areal mass density (mg/cm^2) is also shown in Figure 23. The last point on this curve corresponds to the bottom of the forest and therefore represents the total areal density of the sample. For the cold-wall forest, this value is compared to a direct measurement of the CNT forest mass which was measured using a microbalance. Therefore it is confirmed that the calculated density value based on X-ray mass attenuation is very close to the true density. Thermo-gravimetric analysis (TGA), shown in Figure 24, show that the contribution of amorphous carbon and any other low evaporation temperature carbonaceous contaminants are limited to about 10 % of the total mass of this sample (recipe in Figure 12). Hence, the mass measurements are dominated by CNTs rather than carbonaceous impurities.

The cumulative areal density follows an S-shaped curve with increasing distance from the top crust. This shape is explained by the spatial evolution of local mass density along the forest height. The initial acceleration (concave up region) in the cumulative areal density results from the newly identified crowding stage, and the

deceleration (concave down region) results from the density decay stage. The intermediate steady growth stage results in an approximately linear relationship between total mass and vertical position.

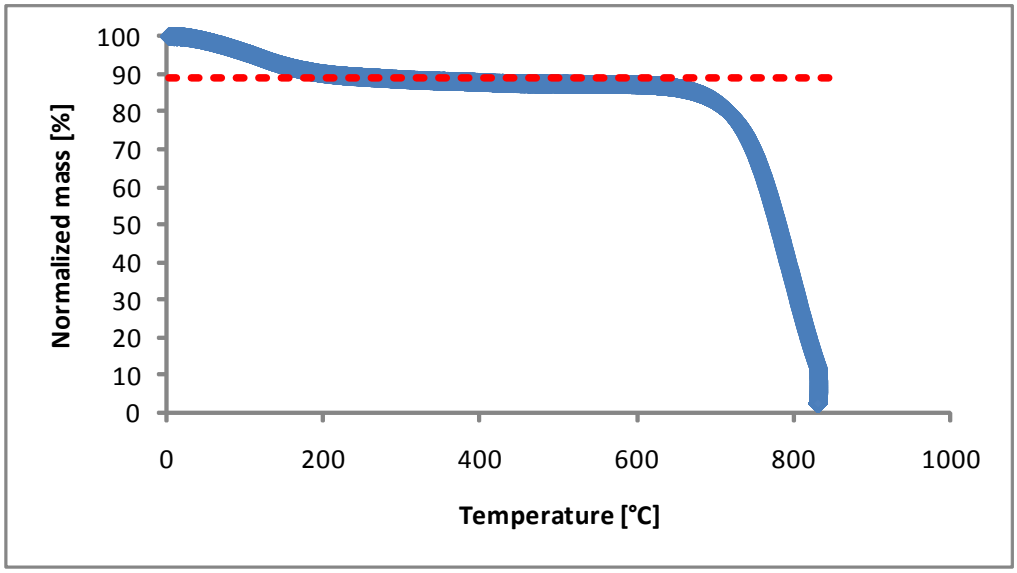

Figure 24. TGA of CNTs from the sample grown in the cold-wall reactor, which is used for all the analysis in the paper. The vertical drop after 800 is due to the setpoint hold, which was preprogrammed for 825 °C.

Now, the analysis of the population dynamics within the forest based on spatial mapping of the CNT diameter and alignment is discussed. This information is necessary to build a comprehensive picture of the forest internal structure, and is needed to calculate the evolution of CNT number density. Then, these results are combined with real-time height kinetics to calculate the time evolution of forest mass

and density. Because real-time height kinetics can only be measured during growth in the cold-wall system, the remainder of analysis in this chapter uses results from the cold-wall growth process.

Although transmission electron microscopy (TEM) has been customarily used for measuring CNT diameters and number of walls,[40] it is painstaking to obtain reliable descriptive statistics from measurements of a limited number of CNTs, compared to the inherent ability of SAXS to probe at least 10^6 CNTs in the beam path. It is also perhaps impossible to do accurate spatial profiling of size distributions using TEM at the high spatial resolution (10 μm) enabled by the capillary optics used with our SAXS setup. Analysis of the radial breathing modes (RBM) using two-wavelength *in situ* Raman spectroscopy has been used to obtain the diameter distribution of single-walled CNTs;[84] however, this is only suitable for SWNTs, or double-wall CNTs (DWNTs), within an incomplete diameter range, and it requires that the CNTs be resonant with the incident laser energy. On the other hand, X-ray scattering methods inherently enable characterization of any CNT based on its dimensions.

Hence, the X-ray scattering 2D image collected on the area detector (Figure 21a) are used to map the CNT size distribution by fitting the peak (or shoulder) observed in a line-scan with a mathematical form factor model for hollow cylinders[54, 73, 74] having a lognormal distribution of diameters (Figure 15). Figure 25a shows the SAXS I-q profiles along with model fits for forest slices selected every 0.1 mm

throughout the forest height. This model-fitting procedure is repeated for each of the 156 slices (images) for the studied forest, resulting in a spatial map with unprecedented resolution compared to previous studies of CNT forest morphology.[36, 40, 54, 74, 85] Because of the large number of images, an automated algorithm was developed for choosing the fitting range based on the key features of the line-scan, as described in the Methods section of this chapter (Figure 16). The blue marks in Figure 25a indicate the lower and upper limits for the fitting range and the peak (shoulder) position determined using this algorithm. A trend of decreasing CNT outer diameter (CNT OD) can be inferred from the position of the peak (or a shoulder in cases in which there is no well-defined peak) relative to the inverse space parameter q, because the peak (or shoulder) position correlates inversely with CNT diameter. The peak moves from $q \approx 0.75$ to 0.9 nm-1 (≈20% increase) from top to bottom of the forest.

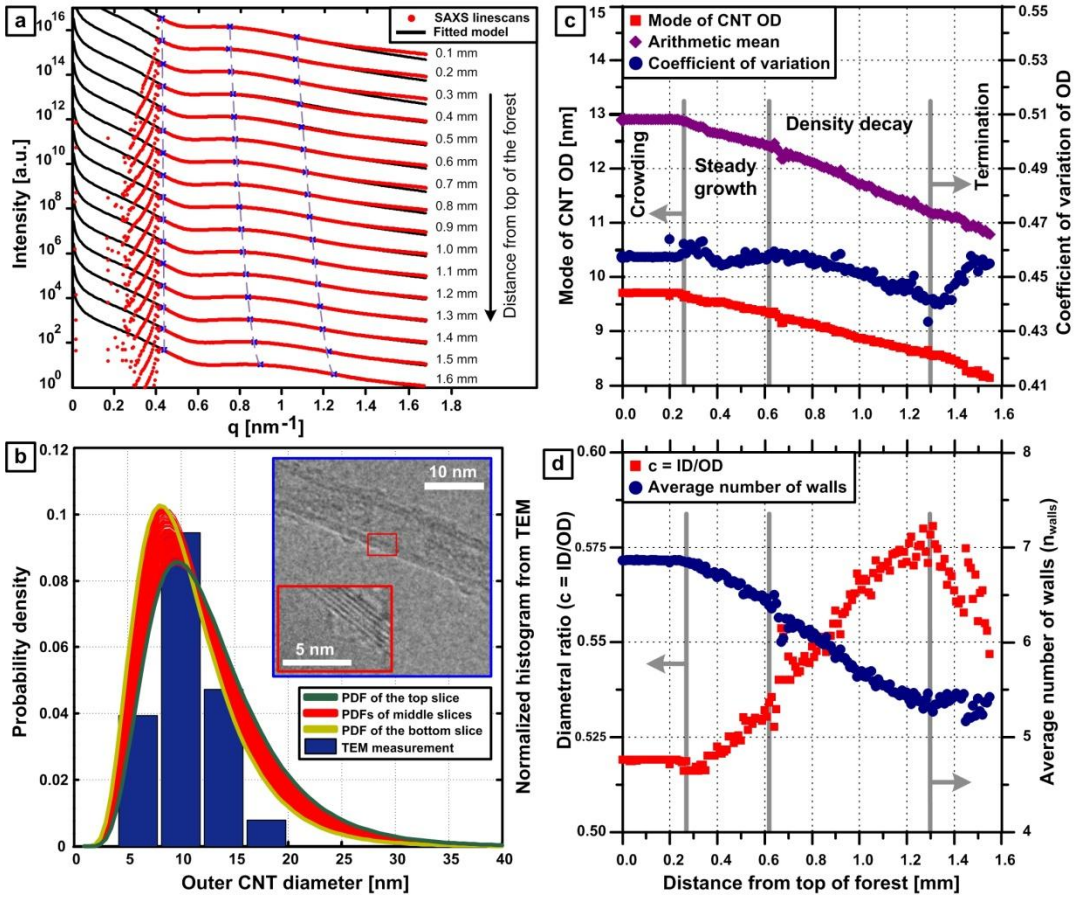

Figure 25. Spatial mapping of CNT dimensions and polydispersity throughout a CNT forest: (a) selected linescans from SAXS images, compared to fits using scattering model (there are nine images between each of the locations shown here); (b) Comparison of the CNT OD distributions (fitted PDFs) to a normalized histogram of measurements from TEM images (example as inset); (c) Mode, arithmetic mean, and coefficient of variation of CNT OD, calculated for each beam position ("slice") in the forest; (d) Diameter ratio *c* and average number of walls for each slice.

As seen in Figure 25, the mathematical model provides excellent fits to the scattering data, throughout the forest. The probability density functions (PDFs) of

CNT OD distribution for each forest slice are laid together in Figure 25b, along with the normalized histogram of CNT OD measurements collected using TEM. There is a good agreement between the diameter values as well as the PDF obtained from SAXS fitting with TEM measurements, validating the accuracy of the SAXS measurement technique.[54, 74] The inset to Figure 25b shows a TEM micrograph of a representative CNT with 6 walls. The smoothness of the spatial trends of CNT dimensions and their variance highlights the precision of our technique, because the mathematical model fit produces a highly confident and accurate result for each slice. Also, the resolution of size measurement is effectively atomic because a scattering model is based on the coherent elastic interactions between X-rays and carbon atoms forming the CNTs. Due to the large number of scatterers (atoms of more than 10^6 CNTs) in the beam path through the CNT forest, high confidence descriptive statistics are obtained.

As shown in Figure 25c, the mode of CNT OD shifts from 9.7 nm to 8.1 nm as growth proceeds (from top to bottom of the forest), which is a 16.5% decrease; and the arithmetic mean shifts from 12.9 to 10.8 nm, which is a 16.3% decrease. The difference between the mode and arithmetic mean highlights the skewness of the log-normal distribution of the CNT population throughout the forest.

In spite of the overall decay in CNT diameter during growth, it is observed that both the CNT OD and its coefficient of variation (CV) are constant during the crowding stage when the CNT number density increases to the maximum. This

shows that the density increase represents an increasing population of active (i.e., CNT-bearing) catalyst particles with an invariant diameter distribution. In other words, there is no preferential nucleation of smaller or larger diameter CNTs within the population under the tested growth conditions (Figure 12). After the crowding stage, the CNT OD decreases until growth stops; and the CV decreases until the onset of the termination stage at which time the CV increases rapidly until growth stops. During the termination stage, the corresponding lowest part (base) of the forest exhibits significant broadening of the diameter distribution. This broadening, along with a continued decrease of the mode and mean OD, may suggest that growth of larger diameter CNTs is halted more abruptly during collective termination. Although the forest height abruptly stops increasing when the CNT density drops below the critical threshold, smaller diameter CNTs may continue to grow and attempt to push up into the forest.[86] This can also explain the shifts in the OD and CV values in the termination region.

Another parameter of the CNT scattering model is the diameter ratio (ι = ID/OD), which is the ratio between the average inner diameter (ID) and outer diameter (OD). This enables calculation of the average number of CNT walls (n_{walls}), shown in Figure 25d. The number of walls is unchanged during crowding, then decreases from ≈ 7 to 5 walls during density decay, and remains fairly constant through the termination stage, as a result of the decay in both the CNT OD and the

diametral ratio (c). These changes can perhaps be linked to the morphological evolution of the catalyst nanoparticles, which is discussed later[39, 87].

Now, the CNT number density profile (*i.e.*, the total number of CNTs at each vertical position) can be calculated by combining the profiles of areal mass density and the measured CNT dimensions. However, owing to the skewness of the lognormal distributions, a single value OD (mean or mode) cannot be used in this calculation, *i.e.*, the average CNT mass of a skewed population is not equal to the mass of CNTs having the average diameter. Hence, the entire PDF must be used to assign the proportion of the population that belongs to a specific narrow bin of diameters, and we must also correct for the CNT tortuosity by calculating the corrected CNT length from alignment and height data for each slice.

Accordingly, the CNT OD range of 5 – 40 nm is divided up into small diameter bins of width $\Delta D_{bin} = 0.5$ nm. Now, the ratio between the number of CNTs within each bin $N(D_o)$ centered at the outer diameter D_o, and the total number of CNTs (N_i) within each forest slice is calculated from the PDF of each slice *i*,

$$\left(\frac{N(D_o)}{N_i}\right) = \int_{D_o-\Delta D_{bin}/2}^{D_o+\Delta D_{bin}/2} \mathrm{PDF_i}\, \mathrm{dD}\,. \qquad \text{Eq. 2.9}$$

Then, to accurately calculate the total volume of the tortuous CNTs within each slice and therefore calculate the mass, we must know the actual CNT length rather than just the height of the slice. So, a height-to-length transformation factor is

calculated based on the CNT alignment within each slice. To quantify the CNT alignment, the orientation parameter (*f*) calculated from azimuthal scans at the *q* location of maximum intensity[36, 38, 73, 74, 88], is used as follows:

$$f(z_i)=\frac{1}{2}\left(3\left\langle\cos^2\phi\right\rangle_i-1\right), \text{ where} \qquad \text{Eq. 2.10}$$

$$\left\langle\cos^2\phi\right\rangle_i=\frac{\int_0^{\frac{\pi}{2}}\left(I_i(\phi)\sin\phi\cos^2\phi\right)d\phi}{\int_0^{\frac{\pi}{2}}\left(I_i(\phi)\sin\phi\right)d\phi}. \qquad \text{Eq. 2.11}$$

Here, ϕ is the angle between the CNT direction and the z-axis direction, $I_i(\phi)$ is the azimuthal intensity distribution of scattered X-rays from the SAXS image of slice *i*.

A transformation factor (Λ) is then calculated to convert the apparent forest height (slice thickness Δz) to the average CNT length (Δl) within that slice,[38]

$$\Delta l(z_i)=\Lambda(z_i)\Delta z, \text{ where} \qquad \text{Eq. 2.12}$$

$$\Lambda(z_i)=\left(\frac{3}{2f(z_i)+1}\right)^{1/2}. \qquad \text{Eq. 2.13}$$

Now, the total number of CNTs within each slice (N) can be calculated by diving the previously calculated (Eq. 2.7) mass of each slice (m_a) by the weighted

average mass of a CNT (m_{CNT}) of the population based on the obtained PDF of CNT OD distribution, and using the corrected average CNT length (Δl) in each slice. This follows as,

$$N(z_i) = \frac{m_a(z_i)}{m_{CNT}(z_i)}, \text{ where} \qquad \text{Eq. 2.14}$$

$$m_{CNT}(z_i) = \rho_g \Delta l(z_i) \sum_{D_o=5nm}^{D_o=40nm} \left(\left(\frac{N(D_o)}{N_i} \right) \frac{\pi}{4} {D_o}^2 \left(1 - c(z_i)^2\right) \right). \qquad \text{Eq. 2.15}$$

Here, the bulk density is taken as the value for graphite, $\rho_g = 2.2\,\text{g/cm}^3$.

The orientation parameter $f(z)$ and the height-to-length transformation factor are shown in Figure 26a. The tangled top "crust" layer is typically no more than a few microns thick; however, the first points of the X-ray map are affected by non-uniformity in the top surface of the forest. As a result, there is an apparent slight decrease of the orientation parameter at the top of the scan, until the beam has passed through the non-uniform region. After this, the orientation parameter increases to a maximum at the end of the steady growth stage, then decreases gradually through the density decay stage, and then decreases rapidly during the termination stage. The transformation factor varies inversely (Eq. 2.13) with the orientation parameter and therefore is greatest at the top and bottom of the forest.

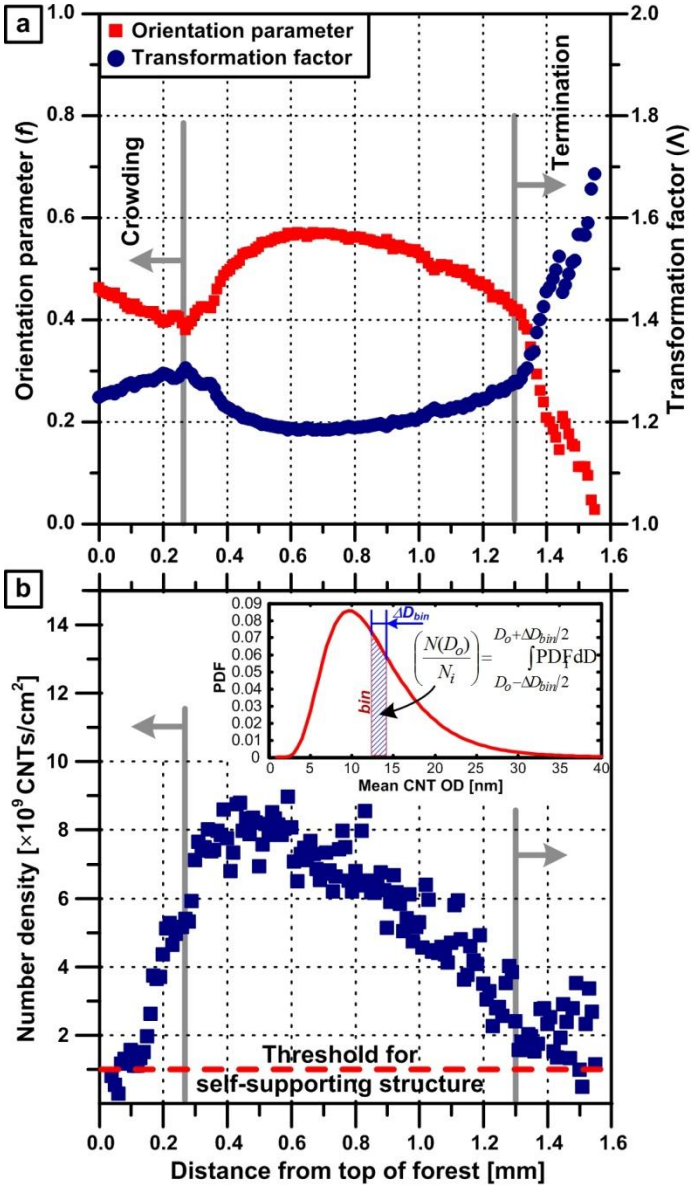

Figure 26. Determination of the CNT population kinetics: (a) Spatial map of the orientation parameter and the height-to-length transformation factor; (b) Spatial map of CNT number density, calculated using the CNT diameter distribution and the tortuosity-corrected average CNT length for each slice. Inset to (b) describes calculation of the total number of CNTs from the PDF of CNT OD for each slice.

The profile of CNT number density versus position, shown in Figure 26b, is now derived. The number density increases during crowding, reaching a maximum of ≈ 9×10^9 CNTs/cm^2, and then decays. The maximum is about an order-of-magnitude higher than the initial density, and then decreases by about an order of magnitude before termination. Compared to the mass density profile (Figure 23a), the number density profile is curvier and less steep due to the diameter change and the tortuosity correction of CNT length. In spite of the noise in the X-ray density measurements, these results suggest that the beginning and ending CNT number density values represent the critical value for the self-supporting structure. The horizontal red line marks the estimated threshold value (≈10^9 CNTs/cm^2) based on a finite element model of post-buckling behavior of CNTs in contact (Figure 27).[36]

These experimental results demonstrate that the decay of the number density of growing CNTs within the forest eventually renders the forest incapable of sustaining a self-supporting morphology, and that abrupt termination of growth occurs when the CNT number density at the base of the forest drops below a critical value. This behavior is captured analytically using a finite element model (ABAQUS), which enables studying the dependence of self-supporting CNT-CNT interactions on the spacing between CNTs within the forest. This model was developed in collaboration with Prof. Wei Lu's group at the University of Michigan.[36] The model considers a pair of CNTs (Figure 27a), modeled as hollow cylinders (d_i = 6 nm, d_o = 10 nm, E = 1 TPa, ν = 0.3), fixed to a rigid top panel and pinned to a bottom substrate. To

simulate the deformation of this two-CNT system, an eigenvalue analysis is first performed to determine the shape of the first buckling mode of an individual CNT, and then the buckled shape is imposed as the starting condition for each CNT in the two-CNT system. Then, the two-CNT system is deformed by applying a downward pressure to the top panel, which is restricted to move only in the vertical direction. The initial buckled shape guarantees that the two CNTs will deform toward each other, and is representative of the actual case where CNTs are inherently tortuous and thus will not behave as perfect columns.

An effective stiffness of the two-CNT system is defined as $K = \sigma/\varepsilon$, where $\sigma = F/d^2$ is the force per unit area (pressure) acting on the top panel, and $\varepsilon = \delta/h$ is the ratio of displacement *(δ)* divided by the initial length *(h)* of the CNTs. By changing the distance between the pair of CNTs in this simple post-buckling mechanical model, we study how the effective stiffness of a CNT forest depends on the CNT number density, as shown in Figure 27b. In a sparse arrangement, CNTs do not contact each other, and consequently, stiffness increases linearly with number density. This linear increase proceeds until a critical value of $\approx 8\times10^8$ CNTs/cm^2, at which point the CNTs contact after deformation, resulting in a nonlinear increase in *K* with increasing number density. This critical value, noted by a vertical line in Figure 5b, is believed to correspond to the threshold CNT number density needed to maintain a self-supporting structure. Although this model simplifies the true structure of a CNT forest, which contains isolated CNTs as well as bundles, the

qualitative insights complement the experimental observations that CNT forest number density and alignment are coupled, and that CNT-CNT contact creates essential mechanical reinforcement.

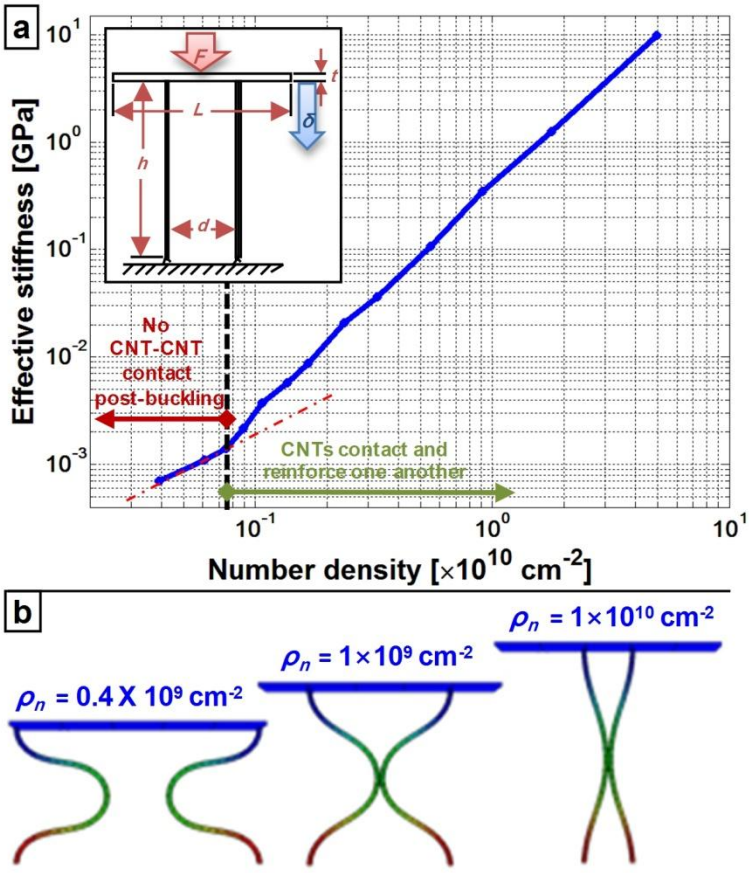

Figure 27. Finite element modeling of CNT buckling and pairwise reinforcement: (a) dependence of the effective stiffness on the areal density of CNTs, with inset showing the model for a pair of CNTs; (b) representative deformed configurations of pairs of CNTs. Reprinted with permission from Reference 36. Copyright 2009 American Chemical Society.

Combining the spatial mapping results with the real-time forest height measurements ($\frac{dz}{dt}$) obtained *in situ* during growth, the time evolution of CNT length, number density, and more importantly, cumulative areal density (mass per unit area) are obtained. The lengthening kinetics $l(t_i)$, the cumulative areal density kinetics $m_{ac}(t_i)$, and the total number density kinetics $N(t_i)$ are calculated,

$$l(t_i) = \int_{t=0}^{t=t_i} \Lambda\left(\frac{dz}{dt}\right) dt \,, \qquad \text{Eq. 2.16}$$

$$m_{ac}(t_i) = \int_{t=0}^{t=t_i} \frac{dm_a}{dz}\left(\frac{dz}{dt}\right) dt \,, \qquad \text{Eq. 2.17}$$

$$\frac{dN(t_i)}{dt} = \left(\frac{dN(z_i)}{dz}\right)\left(\frac{dz}{dt}\right). \qquad \text{Eq. 2.18}$$

In Figure 28, the CNT lengthening kinetics is compared to the height kinetics, showing that the measurements of apparent forest height significantly underestimate the actual CNT length. Owing to the initial increase followed by a decrease in the orientation parameter across the forest, the slightly sublinear curvature of the apparent height kinetics becomes more linear when transformed into true CNT length.[38] Nevertheless, the evolution of forest mass is a more accurate measure of reaction kinetics, as it directly represents the rate at which carbon is incorporated in the growing CNT population. Incidentally, it is observed that, for the same growth

conditions, the areal mass density of CNT forests (i.e., the total mg/cm^2) is more repeatable than the forest height or the volume density (mg/cm^3). In other words, for the same growth time, many grown forests may have a considerable variation in height, but the mass output of each experiment is more consistent (Figure 29).

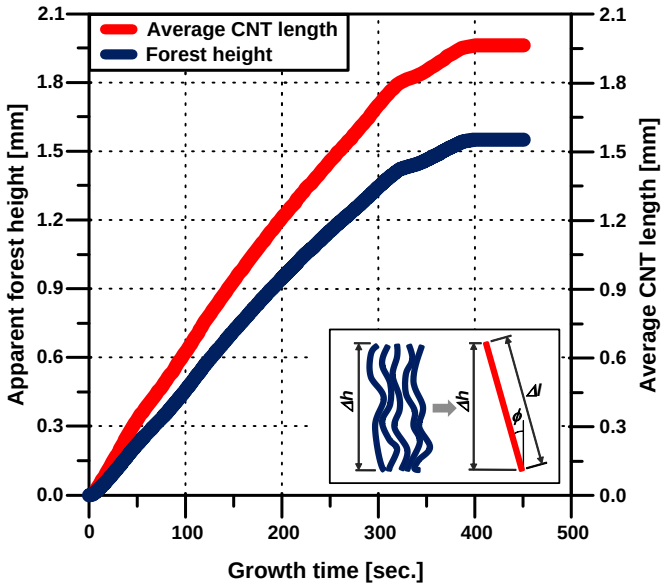

Figure 28. Kinetics of apparent forest height and corrected CNT length. Inset is a schematic of the height-to-length transformation.

Figure 29 shows the mass density vs. forest height for a number of CNT forest samples that were grown in a hot-wall reactor (tube furnace) according to the growth recipe in Figure 12, but for a growth time of 15 minutes (almost half of the time needed for self-termination). Results show considerable non-repeatability in height and mass density, but incidentally show a much narrower variation in their total areal

density (mass per unit substrate area), indicating the CNT mass output is essentially conserved for the same growth conditions, even if forest height varies considerably.

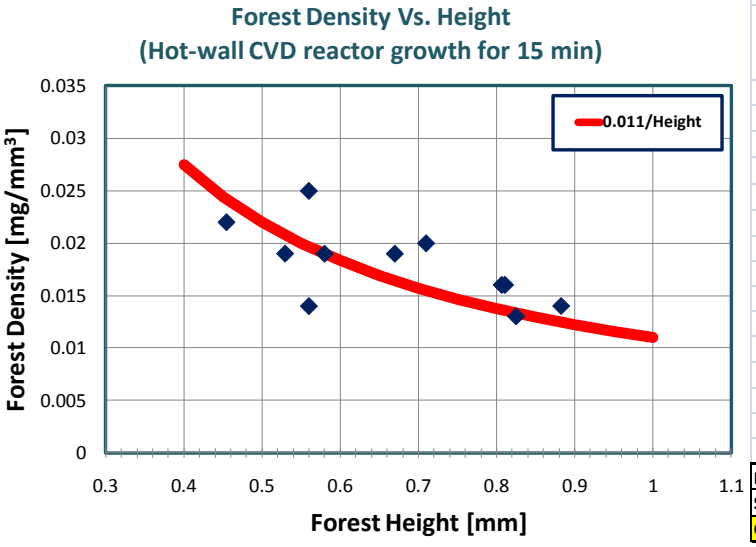

	Summary of results	
	Height (mm)	Mass per unit area (mg/mm2)
	0.807	0.013
	0.811	0.013
	0.825	0.011
	0.883	0.012
	0.455	0.01
	0.53	0.01
	0.45	0.008
	0.446	0.009
	0.406	0.009
	0.58	0.011
	0.56	0.014
	0.56	0.008
	0.71	0.014
	0.67	0.013
Mean	0.621	0.011
SD	0.162	0.002
CoefVAR	0.261	0.192

Figure 29. Forest mass density vs. height of samples grown in the hot-wall reactor for 15 min. Red line represents a line of constant areal density of 0.011 mg/mm^2. The table summarizes the results and presents the mean, standard deviation, and coefficient of variation for height and mass per unit area.

Therefore, the culmination of this comprehensive analysis is a measure of the time evolution of the total cumulative areal density and the total CNT number density, shown in Figure 30. Due to the nearly linear height kinetics, both curves closely resemble the spatial profiles shown in Figure 23 and Figure 26, and the total CNT forest mass versus time is an S-shaped curve. In addition, by processing atomic force microscopy (AFM) images, the mean number density of nanoparticles

is calculated (Figure 20) for samples annealed according to the recipe in Figure 12 to be ≈ 8 x 10^{10} particles/cm^2 (about two orders-of-magnitude higher than the CNT lift-off threshold ≈ 10^9 CNTs/cm^2, identified in Figure 26 and Figure 28). As shown in Figure 30, this results in a calculated catalyst activity that increases from ≈ 1% to about ≈ 11% at the maximum CNT density during the steady growth stage.

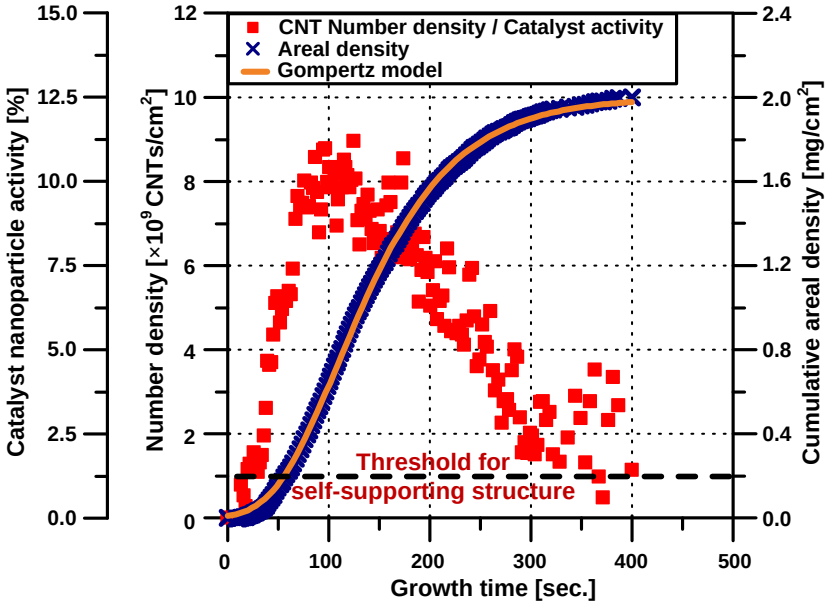

Figure 30. Time evolution of the CNT number density, catalyst activity, and cumulative areal density, which is fitted with the Gompertz population growth model.

The significant spatial variations in CNT morphology during growth confirm that the apparent forest height depends on the interplay between CNT number density, diameter, stiffness, tortuosity, and possibly the hierarchal bundling structure. However, many previous studies that have represented CNT growth kinetics by

forest height, and less commonly by forest mass, have found an S-shaped growth curve. Some have identified its key features including an initial acceleration[64, 69, 70, 89], an inflection point, and a deceleration that concludes in termination[52, 53, 55, 69, 70, 89-91]. In general, growth models for individual CNTs and CNT-particle systems have been used to interpret these stages. The initial acceleration has been explained by the presence of an incubation/induction stage, in which the processes of carburization of the catalyst particles and nucleation of CNTs were proposed to exhibit an autocatalytic nature[70]. The final decelerating part was explained by catalyst deactivation kinetics based on various limiting mechanisms, such as catalyst poisoning, overcoating, evaporation or diffusion.[39, 49, 55, 58, 92] However, the noted discrepancy between CNT forest height and mass, along with the frequent reliance of sparse (i.e., ex situ time points) data to fit height kinetics to different kinetic models without obtaining representative statistics, highlights the importance of obtaining a population-based picture of the growth kinetics. An ideal model of CNT forest growth would therefore consider a distribution of individual growth behaviors, and how these behaviors result in a drastic variation in CNT density throughout the growth process, which results in the observed true kinetic behavior of the population.

To obtain further insight about the S-shaped reaction kinetics, three known models that are ubiquitous to analysis of population growth in natural systems are

investigated: the monomolecular model (Eq. 2.19), the autocatalytic model (Eq. 2.10), and the Gompertz model (Eq. 2.21)[93, 94],

$$m_a(t) = \alpha.\left(1 - e^{-k(t-\tau)}\right), \qquad \text{Eq. 2.19}$$

$$m_a(t) = \frac{\alpha}{1 + e^{-k.(t-\tau)}}, \qquad \text{Eq. 2.20}$$

$$m_a(t) = \alpha.e^{\left(-e^{-k.(t-\tau)}\right)}, \qquad \text{Eq. 2.21}$$

In these models, α is the asymptotic final cumulative mass of growth, k is a reaction rate, and τ is the time origin.

It was found that the Gompertz model is an excellent fit to the CNT mass kinetics in Figure 30. A comparison between all three fits is shown in Figure 31. In fact, only the monomolecular (a.k.a. exponential decay) model was previously used to fit CNT growth data.[55] While the monomolecular model fits the decay part of the cumulative mass kinetics, the model fails to fit the initial accelerating part because it does not have an inflection point. On the other hand, both the autocatalytic and Gompertz models are sigmoidal equations that have inflection points. Further, the autocatalytic curve is symmetric about the inflection point, while the Gompertz is asymmetric. Hence, the Gompertz model fits our data best because the different rates of acceleration (crowding) and deceleration (decay) can be accommodated by the asymmetry of the curve (Figure 30).

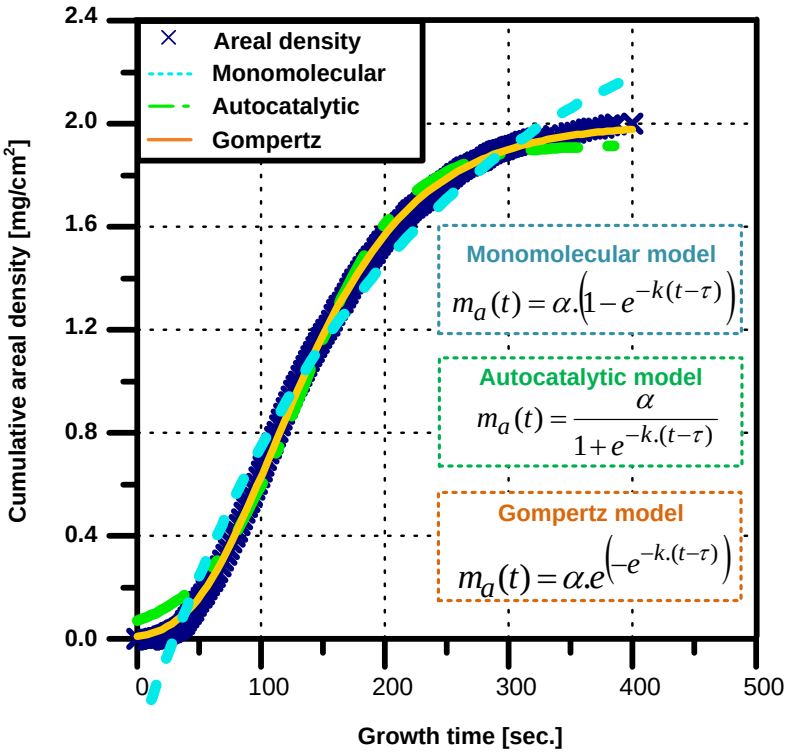

Figure 31. Time evolution of the areal mass density (mass per unit substrate area) with fits from three different models: monomolecular model, autocatalytic model, Gompertz model. Equations are modified to include a y-intercept term added to them in order to find better fits. This is justified by the large SNR that we have, which might mean that our choice of zero is not accurate.

The Gompertz model has been extensively applied to population growth in animal systems,[93] and has been applied to tumor growth[95] and bacterial growth.[96] It has also been recently used to represent the fibrillization kinetics of filamentous aggregates of tau proteins.[97] This analogy can give insights into possible competition among the population of growing CNTs, because tumor growth involves a

population of cells that grows in a confined space, with a limited supply of nutrients. While it is possible that catalyst deactivation and density decay in CNT forest growth analogously result from shortage of necessary growth precursors at the catalyst,[56, 98] this study as well as previous studies[51, 55, 99] show that growth is not strictly governed by the diffusion-limited mathematical model ($h \propto t^{1/2}$). Further, diffusivity through a forest changes during growth because of the evolution of CNT density, indicating that a modification to this model is needed in order to test the hypothesis that growth is purely diffusion-limited.

Alternatively, it is hypothesized here that growth kinetics is essentially a superposition of two different kinetics: activation and deactivation of catalyst nanoparticles. The deactivation rate eventually supersedes the continuous activation rate that dominates during the initial crowding stage. The asymmetry around the inflection point, as well as the catalyst lifetime, may be controlled by changing the growth conditions, affecting this activation-deactivation competition. Thus, the ubiquitous growth-enhancing agents, such as water or ethanol, can result in high overall catalyst activity and lifetime[34, 37, 100-106] by manipulating the rates of activation and deactivation. This may be done by manipulating the gas phase chemistry and influencing migration of catalyst on the substrate. [37]

This interpretation is also consistent with findings that reaction products and intermediates can contribute to the CNT growth rate either by reacting directly with

the catalyst[70, 107, 108] or by co-reacting with other gas species.[109] For instance, the decomposition of hydrocarbon gas (C_2H_4 in our case) may be catalyzed by products or intermediates expelled from the dissociation reactions at the catalyst, even if they are unstable groups or short-lived free radicals. Thermal decomposition and rearrangement of C_2H_4 and H_2 is a multi-step chain of gas-phase reactions yielding a plurality of compounds,[110] and in light of the sigmoid-shaped population kinetics, it is possible that some of these reactions manifest an autocatalytic nature and, depending on the product/compound, contribute to activation or deactivation of CNT growth. For instance, while alkynes have been specifically shown to accelerate CNT growth,[109] PAHs (precursors to soot) are also generated in thermal CVD, and there are many other compounds that are apparently benign. CH_2 was also identified as a possibly active species[111]. Regardless of the exact interplay or competition between these compounds and mechanisms, termination of CNT growth is currently inevitable because the deactivation rate eventually dominates. In fact, this deactivation has been attributed to various mechanisms that are consequential of the gas-phase chemistry such as catalyst poisoning,[55] overcoating with amorphous carbon,[58] or steric hindrance,[70, 112] indicating that manipulating the gas chemistry is an attractive route for controlling deactivation. Another universal observation from our work, as well as others[111], is that carbonaceous deposits on reactor walls from previous growth cycles can improve CNT nucleation and growth, possibly due to the

presence of active species that desorb from the reactor wall surface when the furnace tube is heated.[111]

CNT growth deactivation can also be influenced by morphological evolution of catalyst nanoparticles such as by migration[36, 39, 47] and coarsening.[39, 47, 113] For the CVD system used in this work, it is hypothesized that accumulating CNT deactivation is in large part due to the evolution of the catalyst particles, especially atomic diffusion of the catalyst into and beyond the supporting alumina layer[39, 47]. Indeed, using *ex situ* X-ray photoelectron spectroscopy (XPS), as well as Rutherford backscattering spectroscopy (RBS) (results not shown), we observe significant diffusion of Fe catalyst into the substrate in samples that are processed in the hot-wall reactor. Figure 32a quantified changes in the percentage of surface Fe after annealing and after growth (and delamination of the CNT forest), based on the area under the Fe2p peaks from survey scans (Figure 18). While the Fe concentration after growth and delamination can possibly be affected by mechanical removal of some catalyst particles (i.e., attached to the CNTs), the significant loss of Fe after annealing can only be explained by catalyst diffusion through subsurface layers, because the annealing temperature (775 °C) is not high enough to cause evaporation of the Fe catalyst. Nevertheless, in this base growth process, the catalyst nanoparticles are bound by strong interactions between Fe and Al_2O_3,[47, 114] as demonstrated in literature for similar growth systems by means of backscatter-

electron imaging that showed no traces of metal particles on the top of grown CNT forests[58].

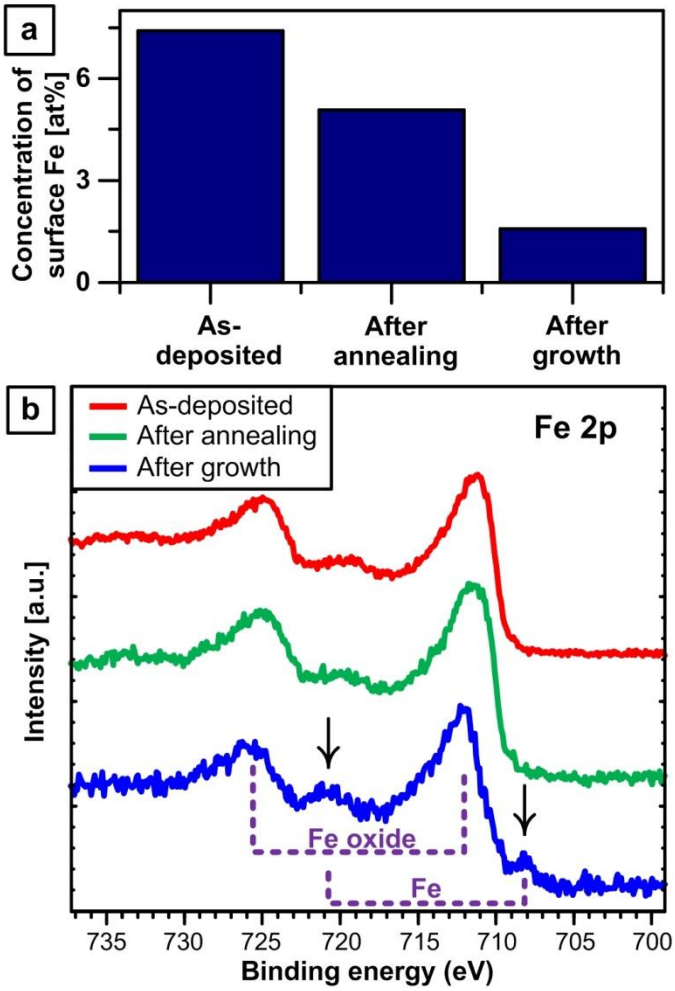

Figure 32. XPS analysis of catalyst evolution during annealing and growth: (a) Atomic concentration of surface Fe based on the areas under the peak of Fe2p peaks of the survey spectra (Figure 18) for three samples (as-deposited, after annealing, and after growth); (b) Comparison of normalized Fe $2p_{1/2}$ & $2p_{3/2}$ peaks for samples as-deposited, after annealing (10 minutes ramp-up to 775 ºC and hold for 10 more minutes), and after growth (for 15 minutes at 775 ºC) and CNT delamination. To

calibrate binding energy values, these spectra were shifted by +3.2 eV based on the measured C 1s peak location (Figure 19).

Figure 32b is a superposition of the Fe2p spectral lines for three different samples (as deposited, after annealing and after growth). All spectra were collected during the same run, and are plotted after applying a correction factor for line positions in order to accurately compare the binding energy values of spectral lines. A correction factor of +3.2 eV is calculated based on the commonly used value of 285 eV for the binding energy of the ubiquitous C 1s peak (Figure 19). Results show that there is no significant change in the binding energy of the Fe $2p_{3/2}$ and $2p_{1/2}$ lines ($2p_{3/2}$ peak remain at about 711.7 eV), indicating that Fe is in essentially the same oxidation state on all three samples. This is likely a combination of F^{2+} and F^{3+} based on the corrected binding energy values[60, 82, 83, 115] and the asymmetry of the peaks. This can be attributed to the ambient oxygen exposure[116] after annealing and after growth which results in oxidation of Fe even if it was reduced to metallic Fe during the high temperature process. Nevertheless, the appearance of a low binding energy Fe $2p_{3/2}$ peak at 708.2 eV indicates that there is some metallic Fe that did not oxidize upon exposure to atmosphere because it is trapped beneath the surface. Notably, after subsequent heating in a reducing environment of H_2/He, this peak becomes more significant, while after heating in air, the peak completely disappears (results not shown). Also, after heating in H_2/He there is no shift in the C1s peak position (Figure 19), and we find that the carbon signal decays while the aluminum

signal increase after growth (Figure 18). These observations indicate that the low binding energy $2p_{3/2}$ peak in fact represents subsurface metallic Fe and not iron carbide or Fe particles encapsulated with graphitic carbon. Because XPS penetrates only a few nanometers into the sample, these findings can only prove the diffusion of Fe to the near subsurface Al_2O_3 layer, although we hypothesize that Fe could also diffuse to the SiO_2 layer.

Based on the population analysis enabled by high-resolution X-ray mapping and the observation of catalyst migration into the substrate, this chapter presents a unified picture of the successive stages of CNT forest growth in Figure 33. This picture begins with the catalyst preparation stage by dewetting of a thin Fe film (1 nm thick) to form nanoparticles. In separate work where we have studied the dewetting process using *in situ* grazing incidence X-ray scattering,[113] we observe that the kinetics of particle formation are very fast, i.e. the Fe film dewets almost immediately when the temperature reaches a certain value during rapid heating. After this, the particle size and shape are fairly stable by the time the hydrocarbon gas is introduced.[113] Hence, the crowding of CNTs during and after self-organization occurs over a much longer timescale than particle formation. Also, as can be seen in Figure 25, the CNT diameter distribution does not change during crowding, indicating that catalyst size evolution is an even longer time scale process. The finding that activation of the catalyst population occurs at an increasing rate evokes thoughts of popcorn (CNTs) popping from a defined population of kernels

(particles).[117] The nucleation kinetics of the CNT population is likely dependent on the hydrocarbon gas decomposition, surface carburization, and other processes, and may reflect an autocatalytic behavior.

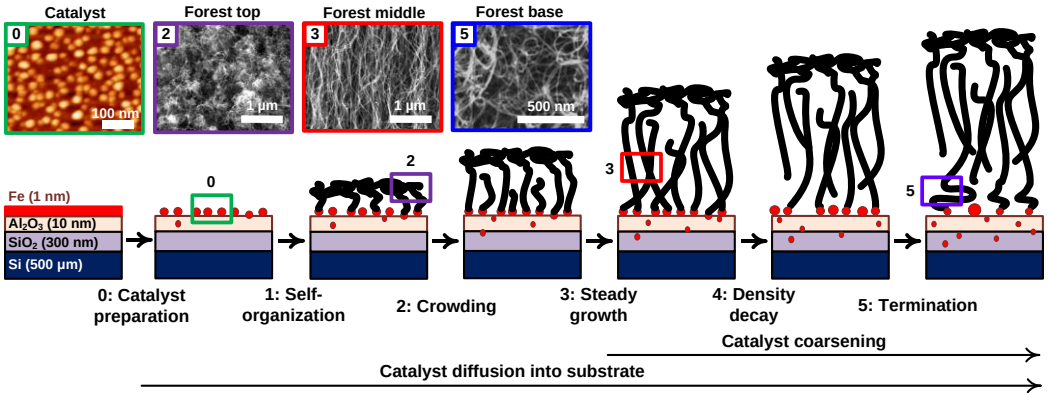

Figure 33. Collective model of catalyst evolution and CNT population dynamics, showing five distinct stages of the forest growth process identified by X-ray mapping, along with AFM image of the catalyst nanoparticles (stage 0, catalyst preparation), and SEM images of the tangled top (stage 2, crowding), aligned middle (stage 3, steady growth), and disordered base (stage 5, termination) of a typical forest grown by thermal CVD. Stage 2 shows how new CNTs begin growing after the forest self-organizes, and Stage 4 shows how the density of CNTs decays until the critical threshold for self-termination is reached.

After the brief steady growth stage that follows crowding, the CNT density decays gradually and for a long duration, resulting in at least an order-of-magnitude decrease in active population of CNT-bearing catalyst particles. The density decay is accompanied by a decrease in the average CNT diameter and a focusing of the diameter distribution. Finally, the collective termination stage is represented by a rapid loss of alignment, and a widening in the CNT diameter distribution as

discussed earlier. Collective termination occurs when the forest is no longer sufficiently dense to maintain a self-supporting structure, although it is likely that some CNTs continue to grow and push upward into the tangled base layer.[86]

In situ[113] and *ex situ*[39, 118] studies showed that the average size of catalyst nanoparticles increases with successive exposure to a hydrogen atmosphere, presumably due to Ostwald ripening. Hence, there is a discrepancy between the evolution of catalyst size (increases) and the evolution of CNT size (decreases). We have also noticed in repeated growth experiments (i.e., growth, delamination, growth) from the same catalyst coated substrate that the CNT forests have larger diameter and lower mass density in subsequent growth cycles. A possible explanation for the decreasing average CNT diameter within a single growth cycle is that larger diameter CNTs stop growing first, i.e., smaller CNTs have a longer catalyst lifetime. A further important point is that not all catalyst particles grow CNTs, and in fact only a small fraction of the catalyst particles may be active depending on the annealing and growth conditions. The catalyst activity measurements shown in Figure 30, indicates that the maximum CNT number density is ≈ 11% of the catalyst particle number density.

Hence, we must consider that the size evolution of catalyst particles that bear CNTs may be considerably different than particles that do not bear CNTs. It is plausible that the presence of a CNT constrains particle migration and atomic diffusion of Fe, and therefore particles with CNTs could have a more stable size

distribution than particles without CNTs. Therefore, the ripening of the overall particle population could be dominated by the large subpopulation of particles that does not bear CNTs. In the limiting case that CNT growth rate does not depend on diameter (which is unlikely based on our recent results), and that CNT-bearing particles do not evolve by Ostwald ripening, the decrease of average CNT diameter with continued growth could be driven solely by a decrease in catalyst size caused by diffusion of Fe atoms into the substrate. While it is widely accepted that the catalyst nanoparticle size determines the CNT diameter,[89, 119, 120] there is no consensus on how an already-nucleated CNT responds to size changes in the catalyst nanoparticle at its root, or how the presence of the CNT affects how the catalyst size changes. Indeed, the catalyst particle is highly dynamic under the thermal and mechanical conditions imposed by CNT growth[87, 121], and further study is required to understand how to stabilize catalyst particles for longer durations and overcome the several competing mechanisms of CNT growth deactivation. And, the distribution of growth behaviors presented by our complete CNT population implies that a particular set of time-invariant growth process parameters may be optimal for only a small subpopulation, whereas the collective growth behavior is dominated by the response of the remainder of the population to the resulting suboptimal process parameters.

2.5. Conclusions

Understanding the population growth dynamics of individual nanostructures such as CNTs is vital to engineer materials comprising assemblies of nanostructures, and to develop accurate models of their scale-dependent properties. This chapter presents a comprehensive methodology for studying the population growth dynamics of vertically aligned CNT forests, utilizing high-resolution spatial mapping of synchrotron X-ray scattering and attenuation, along with real-time height kinetics. This methodology enables non-destructive calculation of the spatiotemporal evolution of absolute CNT mass and number density as well as CNT dimensions (diameter and number of walls). After the CNT forest self-organizes, the density increases during a crowding stage, and then the density decays almost an order of magnitude before self-termination occurs. The S-shaped mass kinetics is accurately fitted with the asymmetric Gompertz model of population growth; hence, CNT synthesis is governed by competing rates of activation and deactivation, and is eventually limited by competing effects of gas-phase chemistry and catalyst evolution. This comprehensive picture of CNT population growth combines both chemical and mechanical cooperation throughout five distinct stages: self-organization, crowding, steady growth, decay, and collective termination.

Although all the X-ray data in this chapter was obtained *ex situ*, the same technique can be applied *in situ* to enable real-time monitoring of population behavior, enabling the control of the outcome by tuning the process parameters *in*

situ either in an open loop or a feedback closed loop system. Such dynamic growth recipes will enable synthesis of CNT forests with highly uniform density or prescribed density gradients; and possibly overcome collective termination to enable growth indefinitely long CNTs. The population-based picture of CNT synthesis can be extended to bulk CNT growth processes from powder catalysts that also represent nanoparticle populations; and is vital for manufacturing uniform CNT materials by post-processing, such as spinning,[46] rolling,[9] and transfer printing[122], which are essential to integration of CNTs into functional materials and devices. Finally, this methodology and insights into the collective growth behavior of filaments can be generalized to study other systems of filamentary nanostructures including inorganic nanowires or biological filaments such as actin.[123]

CHAPTER 3: DIAMETER-DEPENDENT GROWTH KINETICS OF CARBON NANOTUBE POPULATIONS[2]

3.1. Summary

This chapter reveals that the collective growth of vertically aligned carbon nanotube (CNT) forests by chemical vapor deposition (CVD) is governed by the size-dependent catalytic behavior of metal nanoparticles, which can be quantitatively related to the activation and deactivation kinetics of subpopulations of CNTs within the forest. This understanding is established by uniquely combining real-time forest height kinetics with *ex situ* synchrotron X-ray scattering and mass-attenuation measurements. The growing CNT population is divided into subpopulations, each having a narrow diameter range, enabling the quantification of the diameter-dependent population dynamics. Results show that the mass kinetics of different subpopulations are self-similar and are represented by the S-shaped Gompertz model of population growth, which reveals that smaller diameter CNTs activate more slowly but have longer catalytic lifetimes. While competition between growth activation and deactivation kinetics is diameter-dependent, CNTs are held in contact

[2] Significant portions of this chapter are reprinted from Reference 124. Bedewy, M.; Meshot, E. R.; Hart, A. J., Diameter-dependent kinetics of activation and deactivation in carbon nanotube population growth. *Carbon* 2012, 50, 5106-5116. Copyright 2012, with permission from Elsevier.

by van der Waals forces, thus preventing relative slip and resulting in a single collective growth rate of the forest. Therefore, it hypothesized that mechanical coupling gives rise to the inherent tortuosity of CNTs within forests and possibly causes structural defects which limit the properties of current CNT forests in comparison to pristine individual CNTs.

3.2. Introduction and Literature Review

The size-dependent catalytic behavior of metal nanoparticles[125, 126] influences a broad spectrum of technologically important processes, such as the reforming of hydrocarbons[127] and the synthesis of nanotubes and nanowires having controlled dimensions and properties.[128, 129] Knowledge of how reaction rates scale with particle size is required to advance the understanding of underlying reaction steps and to identify the limiting aspects for process control. For particles smaller than ~100 nm, the increase in area-to-volume ratio (Figure 34), gives rise to classical size effects such as reduction of the melting point (Gibbs-Thompson effect). For particles smaller than ~5 nm, even more dramatic scaling of surface energy results from the decrease of the coordination number of surface atoms.[125] As a result of these effects,[129-131] silicon nanowires (SiNWs) grown by chemical vapor deposition (CVD) exhibit diameter-dependent growth rates, which are explained in terms of the diameter dependence of both the chemical potential and supersaturation of the catalyst particle. Because of size effects on catalytic reactions, solubility and

diffusion, individual carbon nanotubes (CNTs) grown by CVD probably exhibit diameter-dependent growth behavior as well.

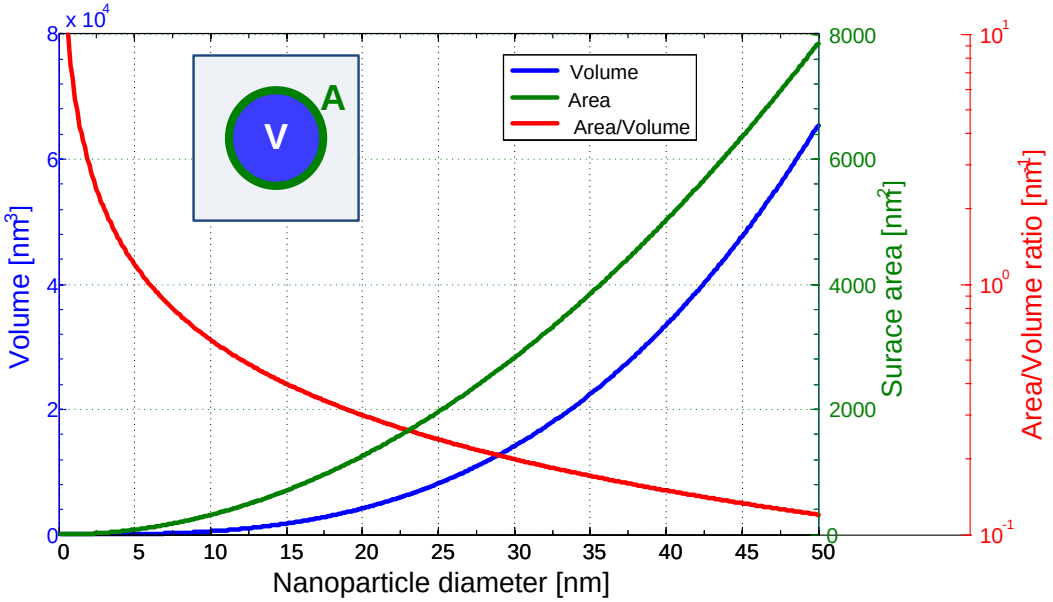

Figure 34. Scaling of volume, surface area and area-to-volume ratio, versus diameter of a spherical nanoparticle.

However, the potential influence of diameter-dependent catalytic behavior on CNT growth is still largely not understood, especially when large populations of CNTs (typically billions of CNTs per cm^2) are grown by CVD from substrate-bound catalyst nanoparticles. Due to the inherent polydispersity of catalyst nanoparticle sizes,[37, 39, 113] the population of CNTs growing from these particles exhibit an intrinsic polydispersity of diameters,[35, 40, 132, 133] and possibly of growth rates as well. Coupled chemical and mechanical phenomena potentially arise as the size-dependent

growth behavior of individual CNTs is combined with interactions among neighboring CNTs due to intermolecular forces. Hence, elucidating these effects is important not only for controlling growth of each CNT individually, but also for understanding how to tailor functional hierarchical structures of CNTs, from bundles to micro- and macroscopic ensembles.

In particular, improved understanding of size-dependent CNT growth behavior would advance engineering of individual-CNT devices such as resonators,[134] flow cells,[135] or even CNT radios.[4, 5] Further, we suggest that understanding the implications of size effects on collective growth is important to enable precise engineering of CNT growth for applications that are based on collective properties of large numbers of CNTs, such as electric interconnects,[7, 9] thermal interfaces,[20] filters,[21] sensors,[22-24, 136] and structural composites.[11] Coupling between the hierarchical structure and the mechanics of CNTs is also important for post-synthesis processing techniques such as the drawing and spinning of CNT yarns and sheets from vertically-aligned as-grown forests.[44-46] Thus, revealing this size dependence in light of mechanical competition is crucial for enabling the capability of truly tailoring the morphological, physical and mechanical properties of hierarchal CNT structures, such as forests, yarns, and sheets.

Although previous studies have shown evidence of diameter dependence of CNT growth kinetics,[54, 137, 138] the size dependence of population growth behavior and the competition between activation and deactivation kinetics among CNTs

growing in a coordinated structure have not been systematically studied before. This is likely due to the challenges in (1) experimentally quantifying the spatiotemporal evolution of the CNT diameter distribution during growth, (2) *in situ* monitoring of growth behavior (i.e., height and mass kinetics), and (3) establishing accurate one-to-one correlation between the CNT diameter and the measured growth behavior.

In fact, there is currently no characterization methodology capable of monitoring the size evolution of nanostructures with accurate spatial and temporal correlation between the nanostructure size and the growth process. Measurement of CNT diameters and number of walls for both single-wall (SWCNT) or multi-wall (MWCNT) nanotubes is typically done using transmission electron microscopy (TEM) imaging.[40, 132, 133] However, high resolution spatial mapping of the CNT diameter distribution within a forest by TEM has proven difficult due to challenges of sample preparation. In addition, due to the low throughput of TEM measurements, it is practically impossible to get accurate descriptive statistics and probability density functions of size distributions within CNT populations, which are necessary to determine the evolution of CNT polydispersity during growth.

On the other hand, *in situ* monitoring of the growth process by measuring forest height kinetics has been achieved by many methods such as optical interference,[48] single-slit laser diffractography,[63] time-resolved reflectivity,[49] optical photography and videography,[50, 53] and laser triangulation.[51, 54] Although real-time TEM imaging has been used to measure CNT growth kinetics *in situ*,[89] these measurements are for

isolated individual-CNT growth in a low-pressure growth environment that is significantly different from the typical atmospheric pressure growth of CNT forests. Hence, using known methods, it is not possible to track the growth kinetics of an individual CNT within a growing population such as a film or forest. Raman spectroscopy has also been used to quantify CNT growth kinetics by integrating the area under the G-band *in situ*.[67-70] However, this technique is only applicable to the study of single CNTs or thin films and can only give diameter and chirality information for small SWCNTs (typically smaller than 2.5 nm in diameter) that fall within the measurement range for the frequency shift of radial breathing mode (RBM) peaks (about 100-500 cm^{-1}).[71] For such small SWCNTs, *in situ* Raman spectroscopy has also been recently used to identify chirality-dependent growth rates;[138, 139] however, this technique fails to give size-dependent growth kinetics of any CNT that does not exhibit RBM peaks in the aforementioned range (including larger-diameter CNTs like MWCNTs).

In this chapter, the first technique for metrology of diameter-dependent CNT population growth behavior is presented, and this technique is applied to quantify the diameter-dependent activation and deactivation kinetics of CNT population growth. This technique combines real-time measurement of forest height during growth, with spatially resolved small-angle X-ray scattering (SAXS) and X-ray attenuation measurements of a CNT forest after growth. This builds on the methodology presented in the previous chapter, including the use of SAXS to

quantify CNT diameter distribution and alignment,[35, 54, 74] as well as the utilization of X-ray attenuation to measure forest mass-kinetics of growth.[35] The CNT population within a forest is now discretized into CNT subpopulations each having different diameters and the growth kinetics of each subpopulation is tracked within the total population. The time evolution of number density and total mass per unit area are accurately mapped as a function of CNT diameter in the growing CNT forest. Results show that growth of smaller diameter CNTs activates more slowly and exhibits a longer lifetime than larger diameter CNTs. It is suggested here that attraction forces from van der Waals (VDW) interactions between CNTs are sufficiently strong to cause CNTs to adopt a collective average growth rate by preventing slip between neighboring CNTs, in spite of diameter-dependent growth rates that are predicted by analytical models of individual CNT growth. It is concluded that the scaling of these mechanical constraints, along with the diameter-dependent growth behavior, is responsible for the tortuosity of CNTs within forests.

3.3. Experimental Section

CNT forests were grown by CVD from substrate-bound Fe catalyst nanoparticles, which were made by dewetting a multilayer thin film (1 nm Fe/ 10 nm Al_2O_3/300 nm SiO_2/ 675 μm Si) by thermal annealing in a reducing atmosphere. For processing, a cold-wall reactor (modified SabreTube, Absolute Nano) was operated according to the recipe shown in Figure 12 in the previous chapter.[50] The input feedstock was a mixture of hydrogen (310 sccm H_2) and helium (180 sccm He) for

dewetting, and ethylene (120 sccm C_2H_4) was added during the CNT growth step. Real-time height kinetics were measured by a non-contact laser probe (LK-G152, Keyence), as described previously.[51, 54]

Synchrotron X-ray characterization was performed *ex situ* in the G1 beamline at Cornell High Energy Synchrotron Source (CHESS), with a monochromatic beam (energy =10+/- 0.1 keV and wavelength ≈0.13 nm), having a height of ≈10 μm focused using a single-bounce monocapillary). The sample was moved vertically using a motorized stage so that forest height was scanned (from top to bottom) at an increment of 10 μm. Simultaneously, scattering patterns were collected on a 2D area detector (Flicam CCD) as well as the intensity values upstream and downstream of the forest (Figure 35a).

Scattering patterns were utilized to calculate the integrated intensity of line scans between +/- 10° of the maximum intensity direction of the inverse space parameter *q*, and the mathematical model adopted for fitting these line scans considers the scattering intensity of hollow cylinders. As in the previous chapter, the probability density function (PDF) of a log-normal distribution of diameters[35, 54] is used to accurately represent the polydispersity in CNT diameters.

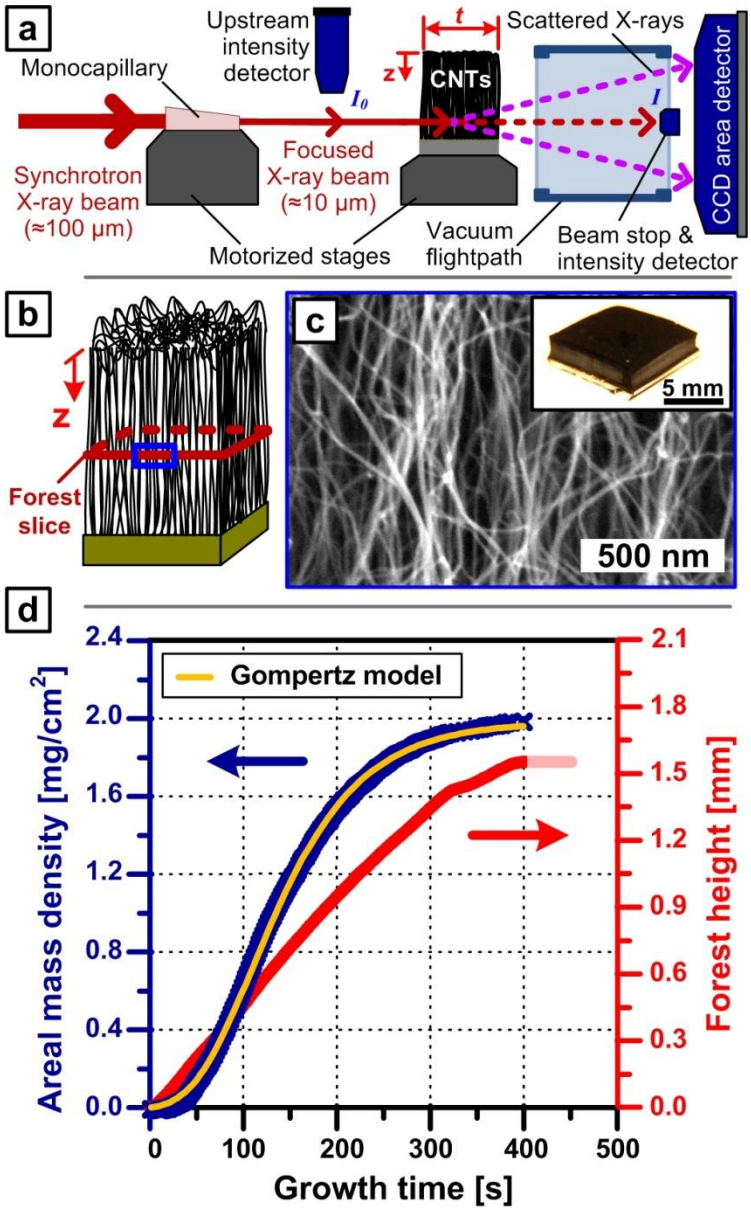

Figure 35. (a) Schematic of the setup for collecting simultaneous X-ray scattering and attenuation data. (b) Schematic of a typical forest and placement of a discrete slice parallel to the substrate. (c) SEM of CNT forest morphology (Inset: photograph of a CNT forest). (d) Forest growth kinetics showing the time evolution of both the collective forest height and total mass per unit area. The Gompertz model of population growth is used to fit the mass-based growth kinetics.

3.4. Methodology and Results

In order to determine the population dynamics of forest growth, we use synchrotron X-rays (Figure 35a) and discretize a representative CNT forest into 10-μm-thick horizontal slices parallel to the substrate, as shown in Figure 35b. Because of the accuracy of sample alignment procedure and the small size of the X-ray beam,[35] it was possible to apply this characterization methodology to tens of different CNT forest samples, some of them as short as 100 μm, and sample dimensions ranged from 1 to 10 mm. The typical morphology of tortuous CNTs within a forest is shown in Figure 35c. Probing the forest with X-rays and fitting mathematical models to SAXS data allow us to quantify (within each slice) the diameter distribution[35, 74] and the average orientation, which is expressed by the orientation parameter (based on the mean square cosine of the angle with the vertical axis).[35, 36, 38, 74] For each slice, the mass density is calculated based on the Beer-Lambert-Bouguer law of mass attenuation of X-rays.[35] Combining these results with real-time forest height measurements uniquely enables calculating the time evolution of the total mass of the growing CNT population (Figure 35d), which is a more accurate representation of the reaction progress than the height kinetics because the alignment and number density of the growing CNTs change with time.[35, 36] Importantly, the S-shaped population kinetics (i.e., the time evolution of population size), which was shown in the previous chapter to follow the Gompertz model of population growth (Figure 35d), represents a polydisperse population of CNT sizes

within each slice. As in the previous chapter, the CNT outer diameter (D), the ratio of inner to outer diameter (i), and the probability density function (PDF) of diameter distribution (Figure 36a) are obtained from fitting SAXS patterns using a model for log-normally distributed core-shell cylinders.[35, 36, 54]

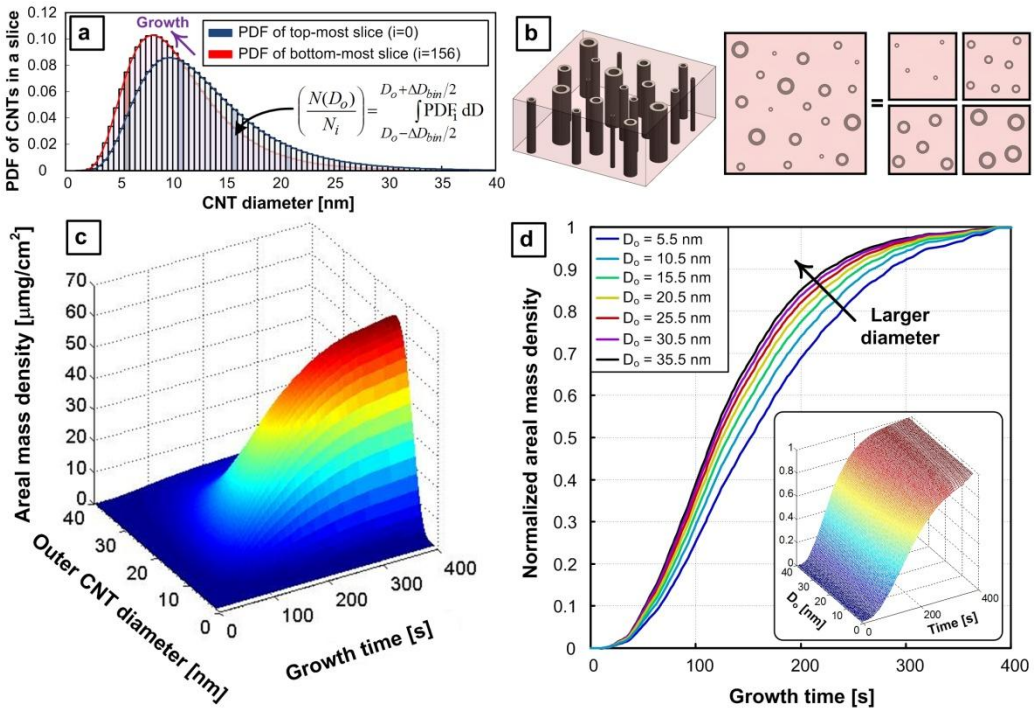

Figure 36. Measured diameter-dependent CNT population growth kinetics based on analysis of X-ray scattering, absorption, and height kinetics data. (a) PDFs for the lognormal distribution of outer CNT diameters, shown for the top and bottom slices, illustrating the division into subpopulations within each forest slice. (b) Schematic of the CNT population in a slice, which is broken into a summation of subpopulations with discrete diameter values. (c) Time evolution of the cumulative areal mass density of each CNT diameter bin within the forest. (d) Time evolution of the normalized cumulative areal mass density of each CNT diameter (Inset: 3D-plot of the same data).

The size-dependent growth behavior is then analyzed for subpopulations of CNTs via spatiotemporal mapping of the CNT number density and diameter distribution throughout the forest. For each slice, the CNT population is divided into a series of discrete "bins" with 0.5 nm range, and then the time evolution of mass and number density for each subpopulation is determined. Based on the measured diameter PDFs for a forest grown according to the recipe shown in Figure 12, approximately 90% of the population (by number) comprises CNTs having diameters within the 5-20 nm range (calculated by numerical integration of the PDFs and plotted in Figure S3). Hence, for our analysis, we consider that a diameter range from 1-40 nm completely represents the population.

Each quantity, such as mass density or number density, is designated two subscript indices i and j. The first index, i, is the slice number, where i=1 corresponds to the top-most forest slice and i=156 corresponds to the bottom-most slice (forest height = 156 × 10 μm = 1.56 mm). The second index, j, is the bin number, where j=1 is the first bin having CNT diameters in the 1-1.5 nm range and j=78 is the last bin having CNT diameters in the 39.5-40 nm range.

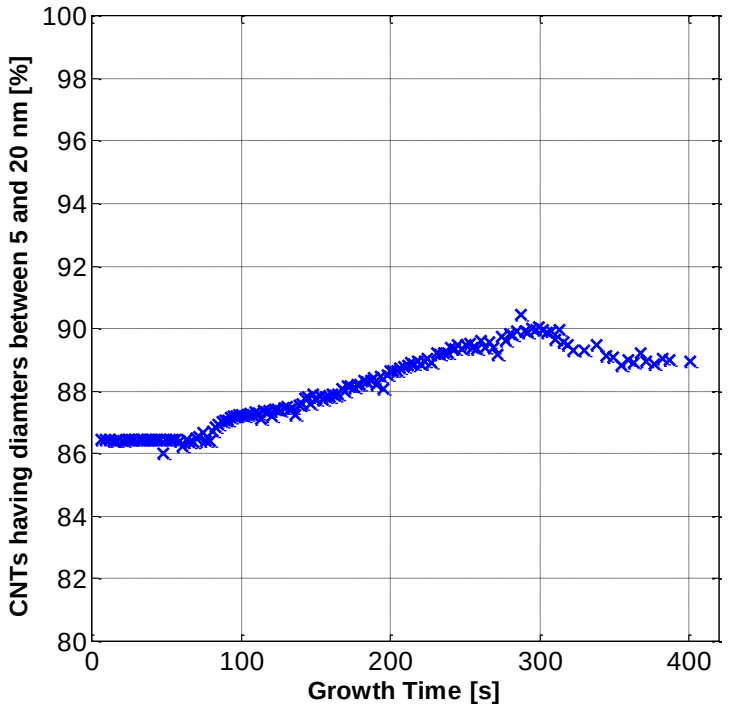

Figure 37. Evolution of the percentage of CNTs within the growing population that have diameters in the 5-20 nm range, calculated by numerical integration of the PDFs.

The mass density of each slice is calculated using the Beer-Lambert-Bouguer law of mass attenuation (Eq. 3.1), which relates the mass density of the slice (ρ_i) to the X-ray intensity upstream of the CNT forest (I_0), the X-ray intensity downstream of the CNT forest (I_i), and the CNT forest thickness in the direction of the X-ray beam (t) (as shown in Figure 35a). This equation uses the total mass attenuation coefficient of atomic carbon (μ/ρ), taking both scattering and absorption into account.[78] By integration with respect to slice thickness in the vertical direction

(z-direction), the mass per unit substrate area, or areal density (m_i) for each slice is calculated (Eq. 3.2). Then, the cumulative areal density of the forest (M_i) at a certain position across forest height is calculated by summation over all slices above that position (Eq. 3.3),

$$\rho_i = \frac{\ln\left(I_0 / I_i\right)}{t\left(\mu / \rho\right)} \qquad \text{Eq. 3.1}$$

$$m_i = \rho_i dz, \qquad \text{Eq. 3.2}$$

$$M_i = \sum_{i=1}^{i} \rho_i dz. \qquad \text{Eq. 3.3}$$

Now, the ratio between the number of CNTs that belong to each subpopulation (N_{ij}) and the total number of CNTs in a slice (N_i) is calculated (Eq. 3.4), based on the PDF shown in Figure 36a,

$$\left(\frac{N_{ij}}{N_i}\right) = \int_{\text{slice i}} \text{PDF}_i \text{dD}. \qquad \text{Eq. 3.4}$$

Combining the calculated areal density (mass per unit substrate area) and the corrected average CNT length (Δl_i) of each slice[35, 38] with the CNT size distribution, we calculate the total number of CNTs (N_i) within each slice (Eq. 3.5). This total number can be used to calculate the number of CNTs (N_{ij}) belonging to each

diameter bin (Eq. 3.6), which is in turn used to calculate the effective areal density (m_{ij}) represented by the CNT subpopulation within each diameter bin (Eq. 3.7), as well as the cumulative areal density (M_j) of each bin (Eq. 3.8).

$$N_i(z) = \frac{m_i(z)}{\sum_{j=1}^{j}\left(\frac{N_{ij}}{N_j}\right)\rho_g \frac{\pi}{4}\left(D_j{}^2 - \left(D_j c(z)\right)^2\right)\Delta l_i(z)}, \quad \text{Eq. 3.5}$$

$$N_{ij} = N_i\left(\frac{N_{ij}}{N_i}\right), \quad \text{Eq. 3.6}$$

$$m_{ij} = N_{ij}\rho_g \frac{\pi}{4}\left(D_j{}^2 - \left(D_j c\right)^2\right)\Delta l_i, \quad \text{Eq. 3.7}$$

$$M_j(z) = \sum_{i=1}^{i} m_{ij}\ . \quad \text{Eq. 3.8}$$

The spatial maps of these quantities across the forest height are then converted into the time domain via the real-time height kinetics measurements $\left(\frac{dz}{dt}\right)_i$. Hence, the time evolution of the areal and number density kinetics of CNTs is calculated for the total population, as well as the subpopulations in each diameter bin, according to Eqs. 9 10, 11, and 12.

$$M(t) = \int_{t=0}^{t=t_i} \frac{dm_i}{dz_i}\left(\frac{dz}{dt}\right)_i dt, \quad \text{Eq. 3.9}$$

$$\frac{dN(t_i)}{dt} = \left(\frac{dN(z_i)}{dz}\right)\left(\frac{dz}{dt}\right), \qquad \text{Eq. 3.10}$$

$$M_j(t) = \int_{t=0}^{t=t_i} \frac{dm_{ij}}{dz_i}\left(\frac{dz}{dt}\right)_i dt\,, \qquad \text{Eq. 3.11}$$

$$\frac{dN_{ij}(t)}{dt} = \left(\frac{dN_{ij}(z)}{dz_i}\right)\left(\frac{dz}{dt}\right)_i. \qquad \text{Eq. 3.12}$$

By discretizing the CNT population within each slice, the diameter-dependent time-resolved kinetics of cumulative areal density is then calculate, as shown in Figure 36. More results for the evolution of both the number density and the cumulative areal mass density versus forest height (Figure 38) and versus growth time (Figure 39) are shown below. Number density results show that the distribution tends to focus during growth towards a narrower distribution before reaching the bottom-most 10% of the forest, at which point the distribution starts to widen again. This could be explained by the continued growth of some CNTs even after the forest collectively stops increasing its height.

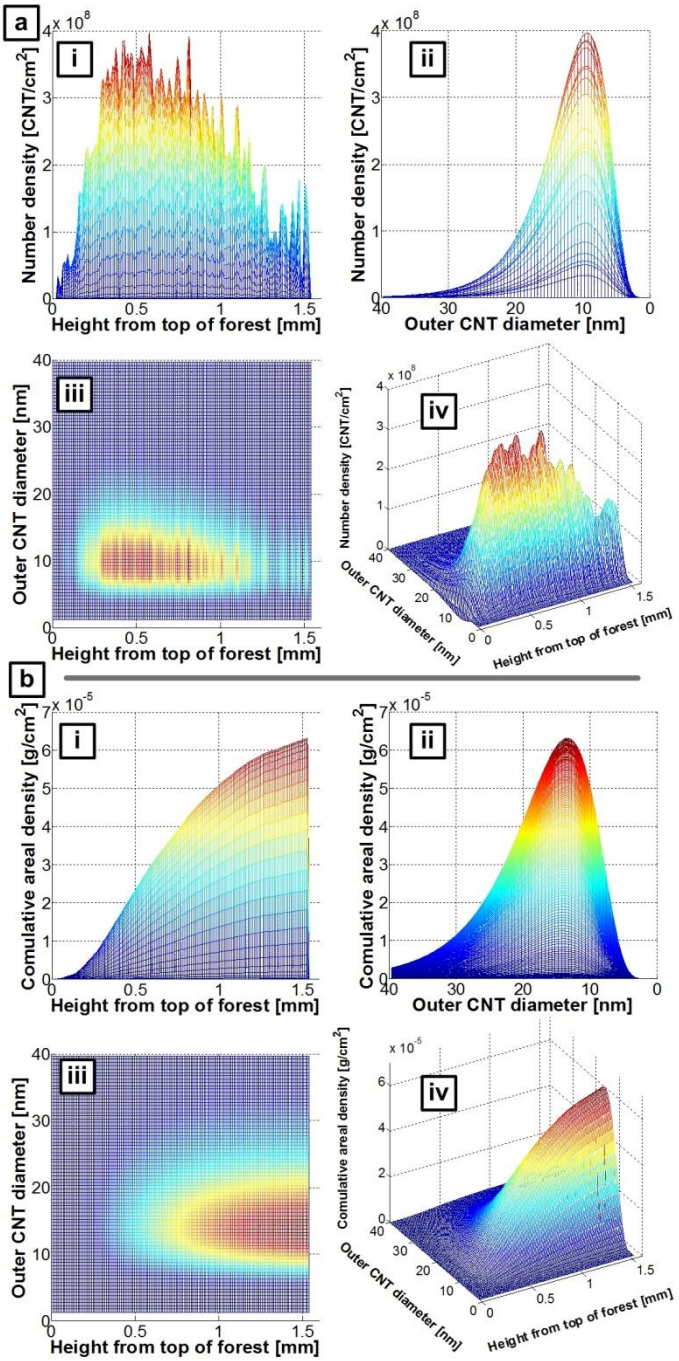

Figure 38. Diameter-dependent population growth as a function of forest height: (a) Evolution of CNT number belonging to different diameter bins as a function of height. (b) Evolution of the cumulative areal density belonging to different diameter bins as a function of height.

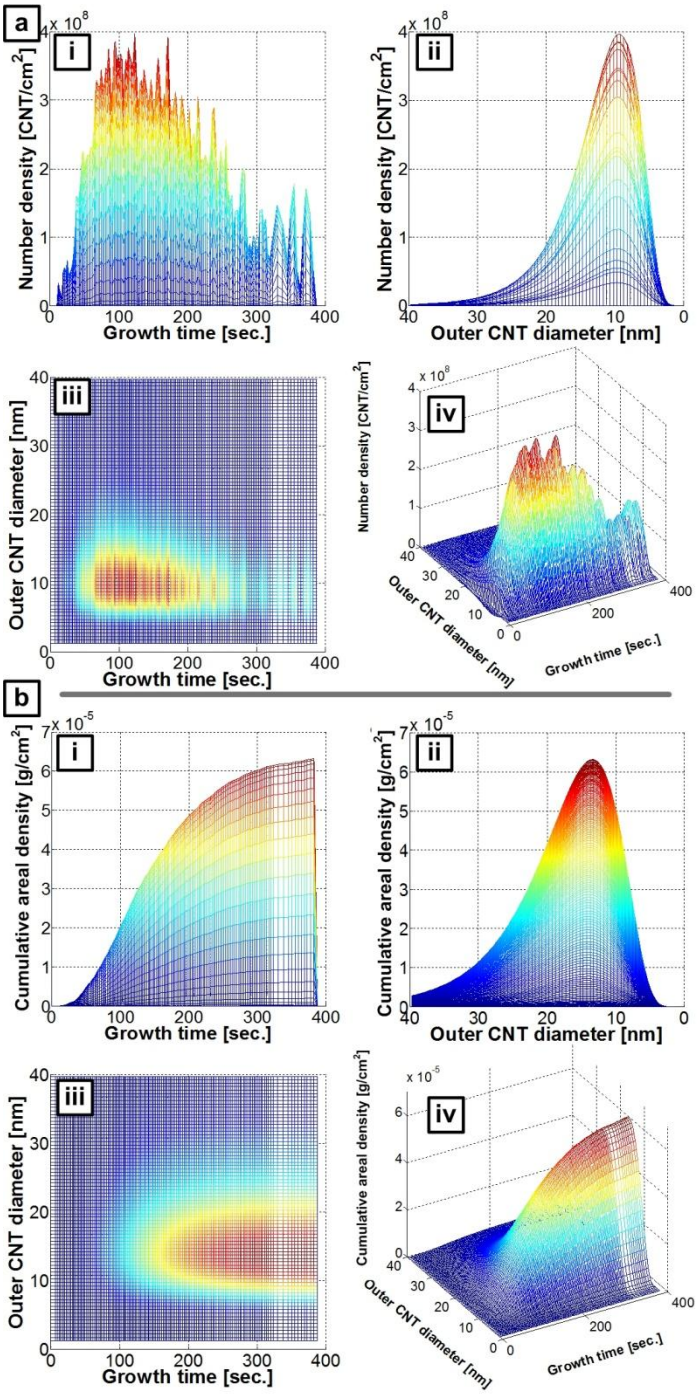

Figure 39. Diameter-dependent population growth kinetics: (a) Time-evolution of the CNT number belonging to different diameter bins. (b) Time-evolution of the cumulative areal density belonging to different diameter bins.

The diameter-dependent kinetics of cumulative areal mass density, shown in Figure 36c, are normalized as shown in Figure 36d. All curves have the characteristic S shape; however, the slope at the end of forest growth (the time of collective forest growth termination[36]) is generally larger for smaller CNTs. This indicates that larger diameter CNTs terminate first and that smaller CNTs may still be growing when the forest terminates, though these subpopulations do not have sufficient number density to maintain the self-supporting structure of the forest.

We find that, like the whole CNT population (Figure 35d), the population kinetics of each CNT subpopulation follows an S-shaped curve and can be represented by the Gompertz model[94] of population growth (Eq. 3.13),

$$m_a(t) = \alpha e^{\left(-e^{-k(t-\tau)}\right)}. \qquad \text{Eq. 3.13}$$

In this equation, α is the asymptotic final cumulative mass of growth, k is a population rate parameter, and τ is the time offset of the inflection point. The inflection point is the time at which the rate of change of slope of the curve stops increasing and starts decreasing, and the location of this point relative to the final value is an inherent property of the Gompertz curve (37% of its final value). Figure 40a and b show that good fits for our experimental results are obtained using Gompertz curves, indicating that the population growth dynamics for all subpopulations follow an asymmetric sigmoid function.

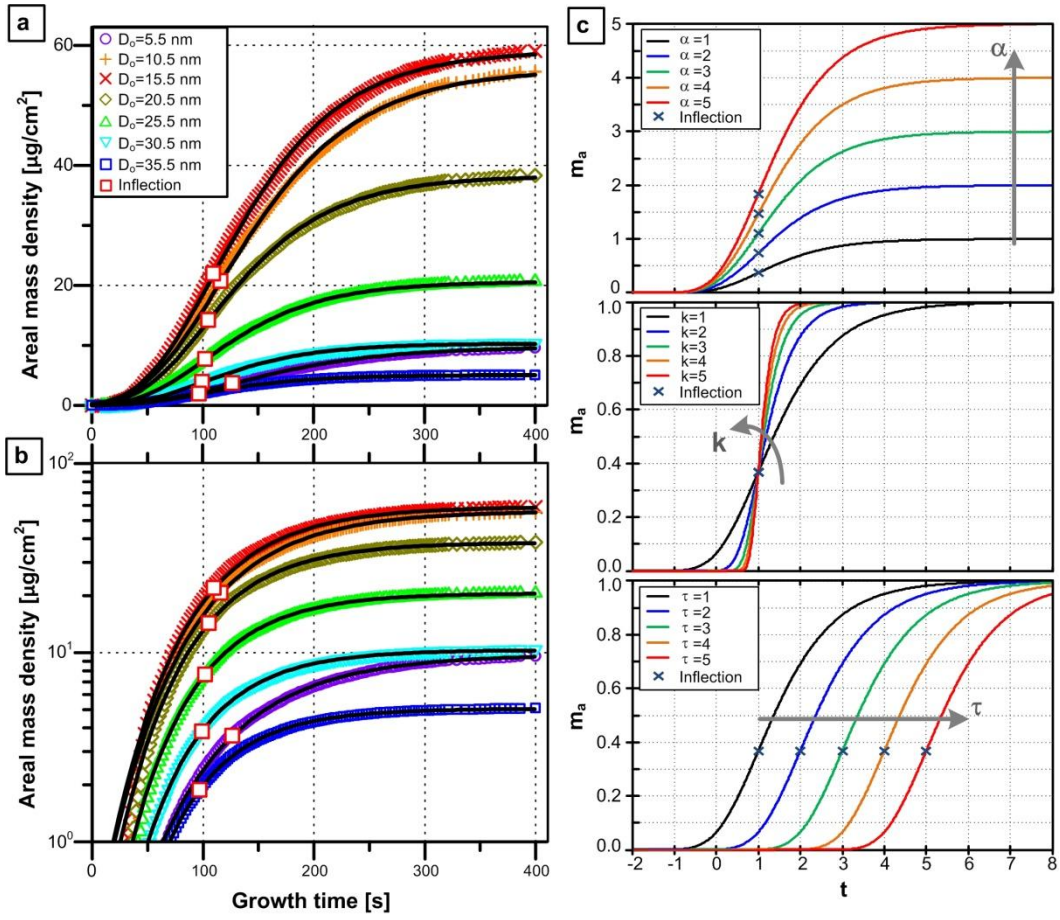

Figure 40. Measured mass kinetics for selected CNT diameters, and corresponding fits of the Gompertz model, plotted on linear scale (a), and logarithmic scale (b). Box markers indicate the location of the inflection point on each curve in (a). (c) Calculated Gompertz curves illustrating the effect of each parameter on the curve shape. The equation is $m_a(t) = \alpha . e^{\left(-e^{-k.(t-\tau)}\right)}$.

3.5. Discussion

Although the size evolution of catalyst nanoparticles during growth such as by diffusion through the catalyst support layers[39] could explain the shift in diameter distribution towards a smaller diameter (Figure 36a), the significant change in CNT

number density (first increasing rapidly, then decreasing gradually) shown in Figure 38 and Figure 39 indicates that catalyst activation and deactivation are inherently diameter-dependent. These findings also highlight the asymmetry of CNT activation and deactivation kinetics, and their importance to overall growth of the population. It is important here to define *activation* as the stage of growth during which the number of actively growing CNTs within each diameter bin (0.5 nm range) increases with time. Conversely, the *deactivation* stage is when the opposite happens, i.e., the number of growing CNTs decreases with time due to termination of individual CNTs within the subpopulation (see Figure 39a). In other words, activation is when the rate of change of the slope for cumulative mass kinetics is positive (acceleration), and deactivation is when the second derivative of cumulative mass kinetics is negative (deceleration). The inflection of the mass versus time occurs when the maximum density has been reached, and this is an early indication of the onset of growth termination.

The effect of changing each of the three equation parameters (α, k and τ) on the shape of the curve is shown in Figure 40c. The value of the asymptote (α) is directly proportional to the final mass of a given population. A low value of the population rate parameter (k) means that the slope of the population kinetics at inflection is small, i.e. a lower value of k indicates that the population growth is more spread on the time axis. A higher time parameter (τ) means that it takes longer for the population to reach its maximum density, i.e., to reach the inflection point.

Because the Gompertz model has only three parameters, the degree of asymmetry is fixed. As a result, the location of the inflection point is always at 37% of the population asymptote (α). Nevertheless, the goodness of the Gompertz fits shown in Figure 40 indicates that this attribute is reflected in our data as well.

We plot the parameters of the Gompertz model fits versus CNT diameter (Figure 41). Both the asymptote (α) and the maximum population growth rate ($\frac{k\alpha}{e}$) at inflection increase with diameter, reach a maximum (representing the mode of the complete CNT population), and decrease again (Figure 41a). This non-monotonic trend is determined by the relative sizes of the CNT diameter subpopulations, as described by the lognormal diameter distribution of the whole CNT population (Figure 36a). Even though the asymptote and the maximum growth rate each have a maximum value, the monotonic variation of the parameters τ and k (Figure 41b) indicates diameter-dependent scaling of CNT growth behavior. The time of inflection (τ) is inversely related to CNT diameter, so it takes longer for the subpopulations that have small diameters to reach 37% of their total mass at termination. Conversely, the population rate constant k increases with diameter, demonstrating that populations of larger CNTs grow at a faster rate.

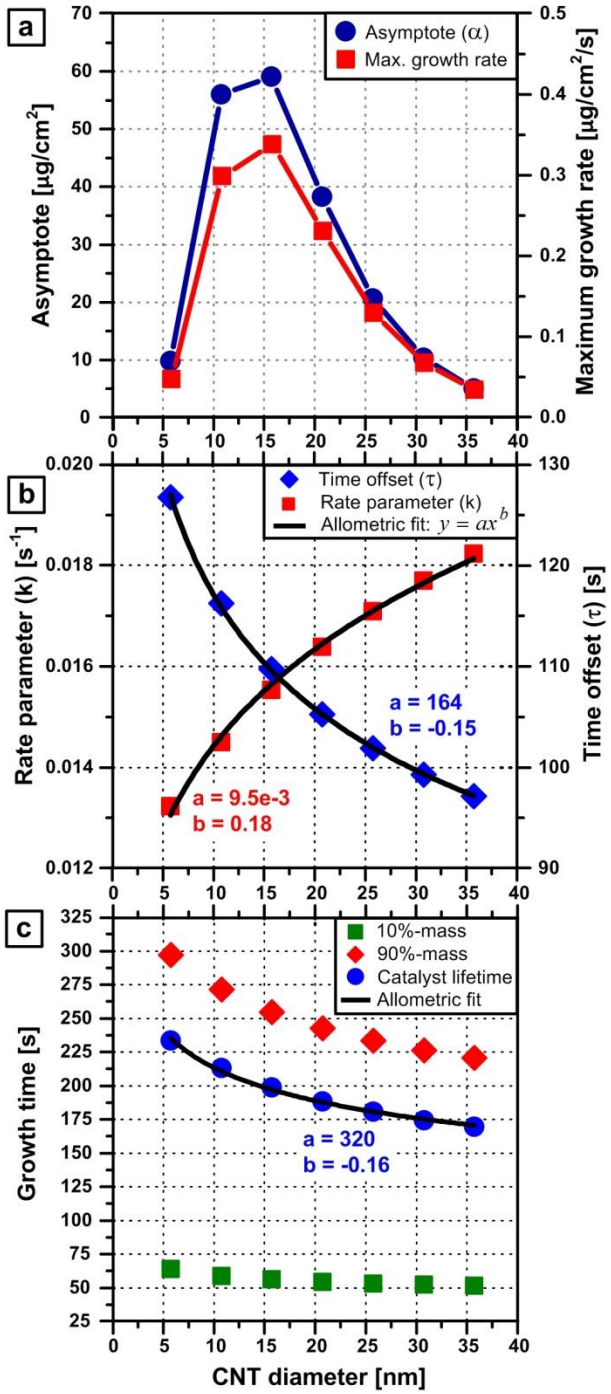

Figure 41. Diameter dependence of the kinetic parameters extracted from the Gompertz model using the curve fits in Figure 3: (a) Change of the asymptote and

the maximum growth rate (at inflection). (b) Change of the time offset (τ) and the rate parameter (k). (c) Change of the growth time needed for achieving 10% and 90% of the final mass of each subpopulation (see Figure 42), as well as the change of the catalyst lifetime, defined as the difference between the aforementioned two growth times.

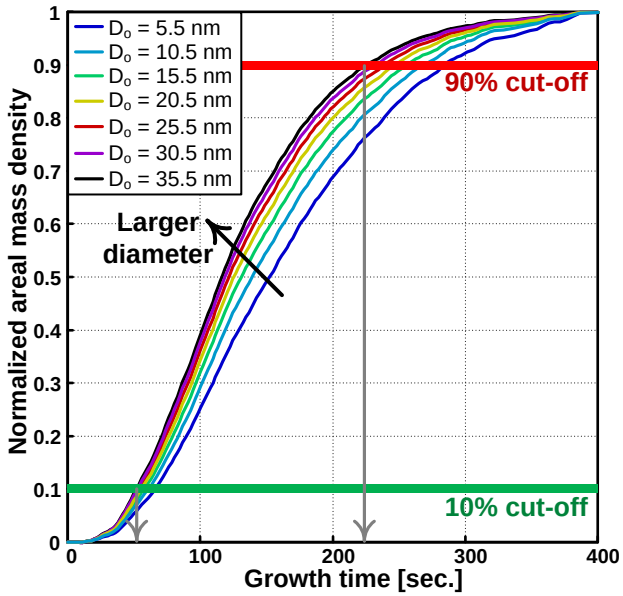

Figure 42. Method for calculating the growth-time for 10%-mass and the 90%-mass for different diameters (plotted in Figure 4c).

As a guide, both sets of data in Figure 41b were fit with allometric curves ($y = ax^b$), which is a flexible and versatile scaling formula and has been used to describe size-dependent behavior of chemical systems such as catalytic activity of nanoparticles[140, 141] and hydriding and dehydriding kinetics of nanoparticles.[142] Fitting results give exponent (b) values of -0.15 and 0.18 for the τ and the k curves, respectively. These scaling results demonstrate that the balance between the

activation-deactivation competition is dependent on diameter, and that the average catalyst lifetimes vary monotonically with diameter as well.

It is also important to note that the diameter-dependent growth parameters plotted in Figure 41 describe population behavior (i.e., the mass kinetics of a subpopulation of CNTs) rather than the height (or length) kinetics of individual CNTs. For example, the rate population constant (k) is considered a normalized population growth rate (with respect to α that represents the quantity of CNTs), so that it can be used to compare the growth dynamics of different subpopulations accumulating different final quantities of CNTs by the end of growth. The rate constant is not an indication of the growth kinetics of individual CNTs, because it represents the collective dynamics of activation and deactivation of many CNTs belonging to a given subpopulation. In fact, this methodology assumes that both the apparent forest height kinetics and the tortuosity-corrected CNT length kinetics do not depend on CNT diameter. Rather, it is suggested here that the lengthening kinetics are the same for all individual CNTs, which is explained later in the context of mechanical coupling of CNTs during collective growth.

Because a direct correlation between the size of the catalyst nanoparticle and CNT diameter has been widely established,[89, 113, 121, 143-145] these findings can be used to further understand the diameter-dependence of catalytic activity of nanoparticles for CNT growth. The catalyst lifetime is herein defined as the time it takes for the cumulative areal mass density to increase from 10% to 90% of its final value (Figure

41c). This is considered to be the region for steady-state growth, where the slope (rate of mass increase) does not significantly change, thus excluding both the rapid increase of slope during the early activation period and the rapid decrease of slope during the final deactivation period. Figure 41c thus demonstrates that populations of smaller CNTs have a longer catalyst lifetime, while larger CNTs deactivate (stop growing) first.

Because the catalyst thin film dewets rapidly into a population of particles with a well-defined size distribution,[113] it is suggested here that the slower activation kinetics of smaller CNTs are not likely to arise from formation dynamics that are diameter-dependent. Further, it has been discussed that the deceleration and final termination of growing CNTs are caused by catalyst poisoning,[55, 146] overcoating with carbon,[58] diffusion of catalyst through underlying support layer (e.g., Al_2O_3),[36, 39] particle coarsening by Ostwald ripening,[37] and buildup of stresses at the catalyst-CNT interface due to mechanical coupling within the forest.[147] To the author's knowledge, this measurement of diameter-dependent catalytic lifetimes is the first experimental proof that the CNT deactivation mechanism is size-dependent.

Moreover, while all the CNTs in the population are assumed to grow at a collective (average) rate that represents the increase of forest height, the growth rate (lengthening kinetics) of individual isolated CNTs has been shown to depend on the CNT diameter, based on theory and experiments. For instance, it was reported that smaller CNTs grow faster than larger CNTs due to enhanced diffusion in smaller

catalyst particles, resulting from the presence of a viscous state around the melting point.[137] Nevertheless, this work focused on small Fe clusters having diameters smaller than 3 nm, where straight CNTs were grown at low densities on quartz to favor a horizontal orientation (parallel to the substrate). In contrast, it has been predicted theoretically that smaller CNTs should have slower growth rates as a result of having smaller surface-area-to-circumference ratio.[49, 133] The diameter dependence of CNT growth rate predicted by analytical models depends on assumed values of constants such as reaction rates and activation energies. These predictions may be inconclusive because the constant values themselves could be diameter-dependent, as has been proposed recently.[133] And, importantly, mechanical interactions among neighboring CNTs that arise during the typical coordinated growth of ensembles have not been taken into consideration.

In principle, the discrepancy between the expected individual diameter-dependent CNT growth rates and the single average growth rate of the population can be explained in two ways. First, individual CNTs could slide axially with respect to one another to compensate for the possible variation in rates. However, if slip occurred, the forest-top surface would not be uniform and flat, and there would be a significant gradient in average diameter throughout the forest. Larger diameter CNTs would dominate the upper portion of the forest, and the number density of CNTs would increase from top to bottom, which is opposite to the observed trend. The second case is where the resultant growth rates of individual CNTs are not

significantly diameter-dependent, i.e., all CNTs grow at almost the same lengthening rate. As a result, the CNT forest grows upward as a unified solid body, and individual CNTs that terminate are pulled from the catalyst interface. It is suggested here that this is more plausible, due to the strong mechanical coupling between neighboring CNTs.

Therefore, the difference between size-dependent growth behavior of individual CNTs and the collective behavior of a forest is explained by considering the strength of mechanical coupling between CNTs within the forest. Indeed, mechanical coupling between neighboring CNTs is responsible for the self-supporting aligned morphology of forests. This occurs once the CNT number density reaches a critical value for self-organization, after which the CNTs grow collectively at the same average rate.[36] This claim is supported by calculating the attractive VDW force between two CNTs. CNTs are considered to be parallel cylinders having diameters of D_1 an D_2, length L, and separation δ (Figure 43a), according to Eq. 3.14:[148, 149]

$$F_{VDW} = -\frac{\pi C \rho_1 \rho_2}{(8\sqrt{2})\delta^{5/2}} L \sqrt{\left(\frac{D_1 D_2}{D_1 + D_2}\right)} \qquad \text{Eq. 3.14}$$

where,

$$A = \pi C \rho_1 \rho_2 , \qquad \text{Eq. 3.15}$$

is the Hamaker constant ($\approx 10^{-19}$ J for condensed phases).

In Figure 43b, the diameter-dependent values of the VDW attractive force are plotted per unit contact length L between two CNTs in contact (δ = 0.335 nm) having diameters of D_1 = 5, 10 and 15 nm and D_2 = 2-40 nm. The results of the model are considered an upper bound because the CNT is modeled as a solid cylinder, as opposed to the hollow CNT geometry, and also because the model considers the case of perfectly parallel CNTs. Also, these VDW force estimations are calculated based on a simple two-body model, which might underestimate the actual collective multi-body interactions present within a forest.[150] These values show that VDW interactions could apply lateral forces in the range of 10s of nN on CNTs, for any appreciable contact length (>100 nm). The interfacial shear strength between CNTs due to VDW interactions was previously estimated to be in the range of 0.05-0.25 GPa,[151] and the static coefficient of friction between two CNTs was experimentally measured to be 0.2, which is two orders of magnitude higher than the kinetic coefficient of friction.[152] Hence, it is concluded that VDW forces are large enough to prevent slip between CNTs in contact.

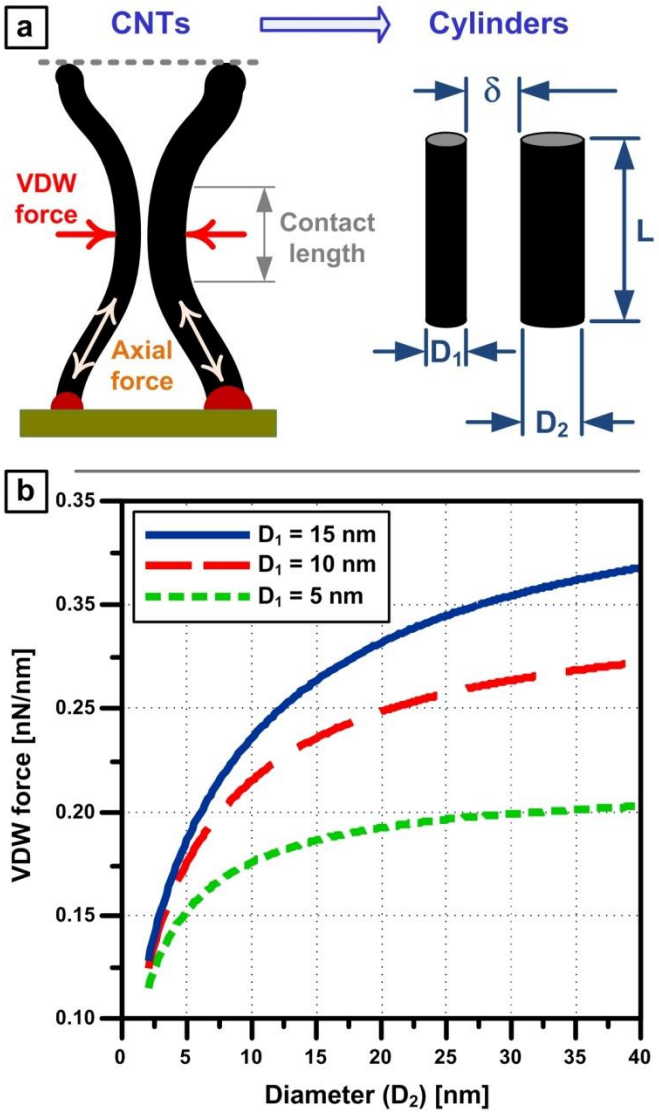

Figure 43. Analysis of van der Waals attractive forces between a pair of CNTs within a forest. (a) Schematic showing two bent CNTs in contact, modeled as parallel cylinders having diameters D_1 and D_2 and length L, separated by distance δ (the graphene layer spacing 0.335 nm is chosen). (b) Scaling of the calculated VDW force per unit contact length L as a function of CNT diameter D_2 for different CNT diameters D_1.

As a result of these lateral interactions, axial forces that are one order of magnitude less (~nN) could arise due to static friction. This is comparable to the force output of 0.16 nN per CNT that was approximated by measurements of how much weight could be lifted by a growing CNT forest.[153] And, in this previous study, the applied pressure resulted in significantly more defective CNTs.[153] These findings indicate that the inherent collective effects dictate the hierarchical forest morphology comprising of tortuous CNT bundles, typically observed by electron microscopy.[154]

Although, the alignment might slightly depend on diameter, this has never been demonstrated and is difficult to experimentally ascertain. Even if tortuosity is diameter-dependent, this dependence is likely to be minor (if any) because of the complex organization of CNTs and mechanics of bundling. Hence, the inherent assumption in this methodology that the alignment (tortuosity) of CNTs within the forest is not diameter-dependent is justified; as a result, it is assumed that all CNTs have the same alignment-based correction function[35, 38] for inferring lengthening kinetics. This assumption is also supported by morphological studies for CNT forests, using electron microscopy[35, 36, 38] and ultra-small angle X-ray scattering,[75] which showed that the bundling behavior is dominant and that the same bundle, which is held together by VDW interactions, could include CNTs of any diameters, as long as they are in proximity.

The longest CNTs reported have been grown individually under alignment by gas flows, without effects of mechanical coupling, and interestingly these CNTs are

of high structural quality.[155] Hence, the overall role of mechanical competition in collective CNT growth, and the effect of forces on CNT formation, may be a limiting aspect of CNT forest growth. Forces may also have an important influence on the properties of CNT forests, such as electrical and thermal conductivity. Notably, the properties of CNT forests are typically far below predictions based on the scaling of properties of individual CNTs.[9, 156-158] Hence, further study is required to elucidate the dynamic forces applied on CNTs during growth and understanding their effects on structural defects and resultant properties.

3.6. Conclusions

Quantification of the size-dependence of CNT growth kinetics is essential to build a mechanistic understanding of the growth process. This chapter presents the first experimental technique that enables the study of diameter-dependent activation and deactivation kinetics of CNT populations. The technique is non-destructive and can be implemented *in situ* during growth, as it is based on combining SAXS measurements, with mass attenuation and real-time forest height measurements. Results show that CNT subpopulations with smaller diameters have slow activation rates and long catalyst lifetimes compared to subpopulations with larger CNTs and that the S-shaped Gompertz model can accurately represent all stages of population growth. Further, interactions due to attractive VDW forces pin neighboring CNTs in contact, preventing slip among CNTs that grow at different rates. The combination of diameter-dependent growth behavior and mechanical coupling causes the typical

tortuous CNT morphology in dense forests, and may cause structural defects in the CNTs. This complex interplay must be taken into account in CNT growth models and in developing growth recipes for CNT forests with improved organization and properties.

CHAPTER 4: CHEMICAL COUPLING IN CARBON NANOTUBE FOREST GROWTH[3]

4.1. Summary

Control of the uniformity of as-grown aligned carbon nanotube (CNT) structures, in terms of both geometry and nanoscale morphology (density, diameter and alignment), is crucial for many applications exploiting their unique properties in a repeatable manner. However, many studies report complex and sometimes unexplained variations of the shape of macroscopic CNT forests, as well as variations among micron-sized CNT pillars (micropillars) in arrays. This chapter presents a mathematical model that describes the origins of synergetic CNT growth effects based on the chemical coupling between catalyst regions in proximity. It is proposed herein that during chemical vapor deposition (CVD) growth of CNTs from substrate-bound catalyst nanoparticles, the catalytic decomposition of the feedstock hydrocarbon at the catalyst surface produces active species that promote CNT growth. The local concentration of these active species modulates the growth rate of CNTs in the vicinity as they diffuse to the surroundings, creating an evolving spatial distribution of concentration. Through experiments and numerical

[3] Significant portions of this chapter are under publication in a journal article. See reference 159.Bedewy, M.; Farmer, B.; Hart, J., Synergetic chemical coupling controls the uniformity of carbon nanotube microstructure growth. Submitted.

simulations, a better understanding of this mechanism is achieved, which allow for the prediction of variations among CNT micropillar arrays. Results provide insights into the manufacturing of higher quality, more uniform arrays of CNT microstructures, as well as some design principles to tailor the structure of as-grown individual CNT micropillars.

4.2. Introduction and Literature Review

CNTs are potentially useful for many applications,[18] especially those that depend on the utilization of the properties of a large number of CNTs in parallel, as in filtration,[21] sensing,[22-24] and composites[11]. In fact, functional vertically aligned CNT "forests" have been incorporated into different material systems including thin films, interface layers, and structured 3D geometries such as micropillars or on the surfaces of fibers. The complex hierarchical morphology of aligned CNT microstructures gives rise to superior collective mechanical properties,[10] as well as enhanced electrical transport[7, 9] and thermal transport,[20] when compared to conventional counterparts. In all these cases, uniformity in the geometry, density, and diameter of the CNTs within the microforest is needed for tuning their collective properties. However, in several published reports as well as in previous work by the author, it is apparent that widely used growth recipes by CVD produce CNT micropillars having substantial spatial non-uniformities.

Different types of geometric and dimensional variations can be observed for typical CNT micropillar arrays. In the case of extended growth (30 minutes) producing high aspect-ratio structures, Figure 44 shows the variations in the micropillar orientation and curvature for the peripheral micropillars compared to the rest of the micropillars inside an array. Even in the case of experiments where the growth time was limited to 3 minutes producing low aspect-ratio micropillars, height variations can be observed within an array, with no lift-off of corner micropillars (Figure 44c). In addition, variations to the micropillar diameter and top-surface geometry are commonplace, indicating that such peripheral micropillars have a significantly different density as well, which limits the applicability of these micropillars in functional devices. All these variations are common, and the continued work of the author on CNT growth has shown that the presence of large catalyst features in the vicinity of such areas always boosts the growth. Variations of geometry/morphology among neighboring as-grown CNT microstructures have also been exploited to promote the growth of small horizontally aligned CNT structures in the vicinity of larger structures.[160] Similar "synergetic" growth effects have also been documented for individual nanowire growth.[161]

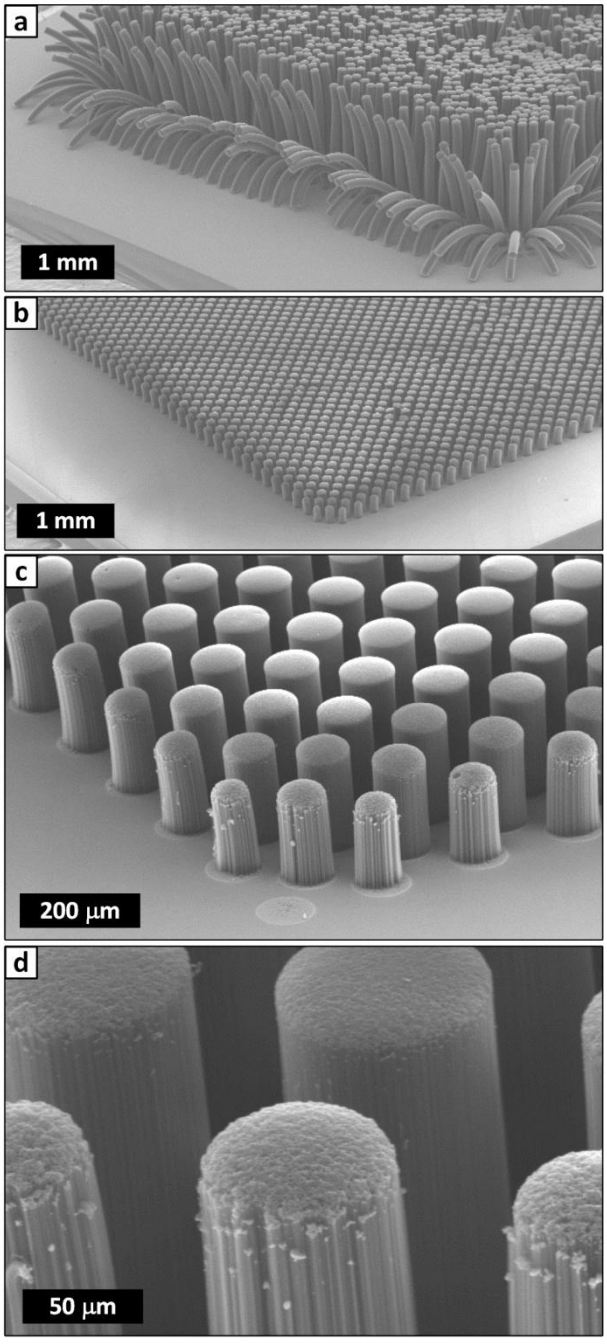

Figure 44. Non-uniformities in the geometry and dimensions of cylindrical CNT forest micropillars (100 μm diameter, 100 μm spacing in a square lattice). (a) Outward bending of peripheral micropillars in a large array, after growth time of 30

minutes. (b, c, d) Variations of height, diameter, and top surface geometry among CNT micropillars grown for only 3 minutes. Also note in (c) that the corner micropillar does not lift off into the forest morphology, and that the outer edges of the nearby micropillars also fail to lift off.

In CNT growth by CVD, these proximity effects have been previously explained as resulting from the variation of local partial pressures of carbon-containing active gaseous precursors,[162, 163] or the mechanical constraint of the topmost tangled crust.[147] Nevertheless, a complete mechanistic understanding of the various mechanical and chemical interactions between growing CNTs is yet to be reached. The difficulty in understanding growth variations is due to the multi-component nature of the CNT growth atmosphere, and the existence of possibly multiple chemical species having varying potency for promoting/deactivating the growth process. During a typical CVD process, the hydrocarbon feedstock gas (or other carbon-containing precursor species that result from the thermal decomposition of the feedstock in the reactor) catalytically decomposes at the surface of the catalyst nanoparticles producing active species that promote the CNT growth process. Literature abounds with studies aiming at determining the activity of different carbon-containing species,[164] and among the hydrocarbon molecules that have been previously identified as the key active molecules in the CVD growth of CNTs are acetylene,[165] or alkynes in general,[109] and polycyclic aromatic hydrocarbons (PAHs).[166] The efficiency of different hydrocarbon precursors is likely dependent on other growth conditions such as temperature, pressure, humidity, or the cooperative effects among multiple

hydrocarbon precursors. In fact, it has also been proposed that polyaromatic intermediate fragments form first on the surface of the support layer in the vicinity of the catalyst before getting incorporated into the growing CNT.[167] These complex mechanisms are not fully understood, but they strongly suggest that chemical coupling is a fundamental component of growth.

Despite these qualitative descriptions of the process, quantititive insights are still lacking. In order to be able to fabricate uniform CNT microstructures, and fully understand the effects governing their non-uniformity, a mathematical model is needed for describing the chemical process that involves local reactions at the nanoscale catalyst sites, and their diffusion-induced coupling among the growing patterned structures at the microscale. An analogy can be drawn between non-uniformity of as-grown CNT microstructures and other microfabrication processes such as thickness variations in chemical-mechanical polishing,[168] or the variations of etch rates in plasma etching,[169] both of which present significant concern for semiconductor manufacturing due to their pattern dependence. In these cases, developing mathematical models capable of predicting/analyzing the spatial distribution of expected geometry has enabled designing around the spatial coupling effects.

In this chapter, a holistic approach is adopted by focusing on developing a mathematical model describing the synergetic effect of chemical coupling between growing CNT micropillars in proximity. The spatial distribution of active species,

which are generated at catalyst sites and diffuse to the surroundings, is first modeled. Owing to the autocatalytic nature of growth,[35, 70] the activation energy of CNT growth is inversely related to the concentration of these active species, leading to a spatial correlation between concentration of active species and the modulation of CNT growth rates. Through experiments and computer simulations, the factors affecting the successive stages of CNT micropillar lift-off in arrays are revealed. This understanding allows for the fabrication of higher quality, more uniform CNT micropillars, by utilizing the model to design catalyst patterns having predictable growth behavior. At the end of this chapter, it is demonstrated that the mathematical model presented herein can be used to design the inter-pillar spacing and/or pillar size in an array in order to enhance uniformity.

4.3. Methodology

4.3.1. Mathematical Modeling

A mathematical model that describes the synergetic growth effects of CNT micropillars in arrays was developed by the author in collaboration with Brittan Farmer from the Department of Mathematics at the University of Michigan. This model is based on calculating the spatial distribution of active species that are locally produced at the catalyst surface and then diffuse to the surroundings (Figure 45a). As the used feedstock gas ethylene (C_2H_4) catalytically decomposes, a plethora of gaseous species are produced,[54] many of which contribute to promoting growth activity. In fact, it is most likely that a combination of multiple gases, in addition to

short-lived radicals, cooperatively boost the efficiency of CNT growth at a particular temperature and pressure from a catalyst nanoparticle having a particular chemical composition, size, and shape. Since we are focused on studying the spatially-varying growth activity, we collectively label the unique combination of growth promoters/precursors as "active species" in our mathematical framework, without specifying a specific hydrocarbon molecule/radical. The spatially varying concentration of these active species is utilized as a quantitative measure of chemical coupling, as it modulates the CNT growth rate by shifting the activation energy of CNT growth. As these active species diffuse to the surroundings (Figure 45b), a time-evolving spatial distribution of their concentration ensues, which leads to a distribution of activation energies. In this chapter, growth rate (height kinetics) is adopted as a quantitative measure of the efficiency of the CVD process, and all CNTs within a micropillar are assumed to be mechanically coupled and therefore collectively grow at the same rate.[170] This assumption underlies the straight vertical growth direction of the simulated micropillar growth shown later. The spatial variations of CNT growth rate within each micropillar and the resulting bending behavior are topics of ongoing research by the author and collaborators, and modeling these effects is beyond the scope of the present dissertation .

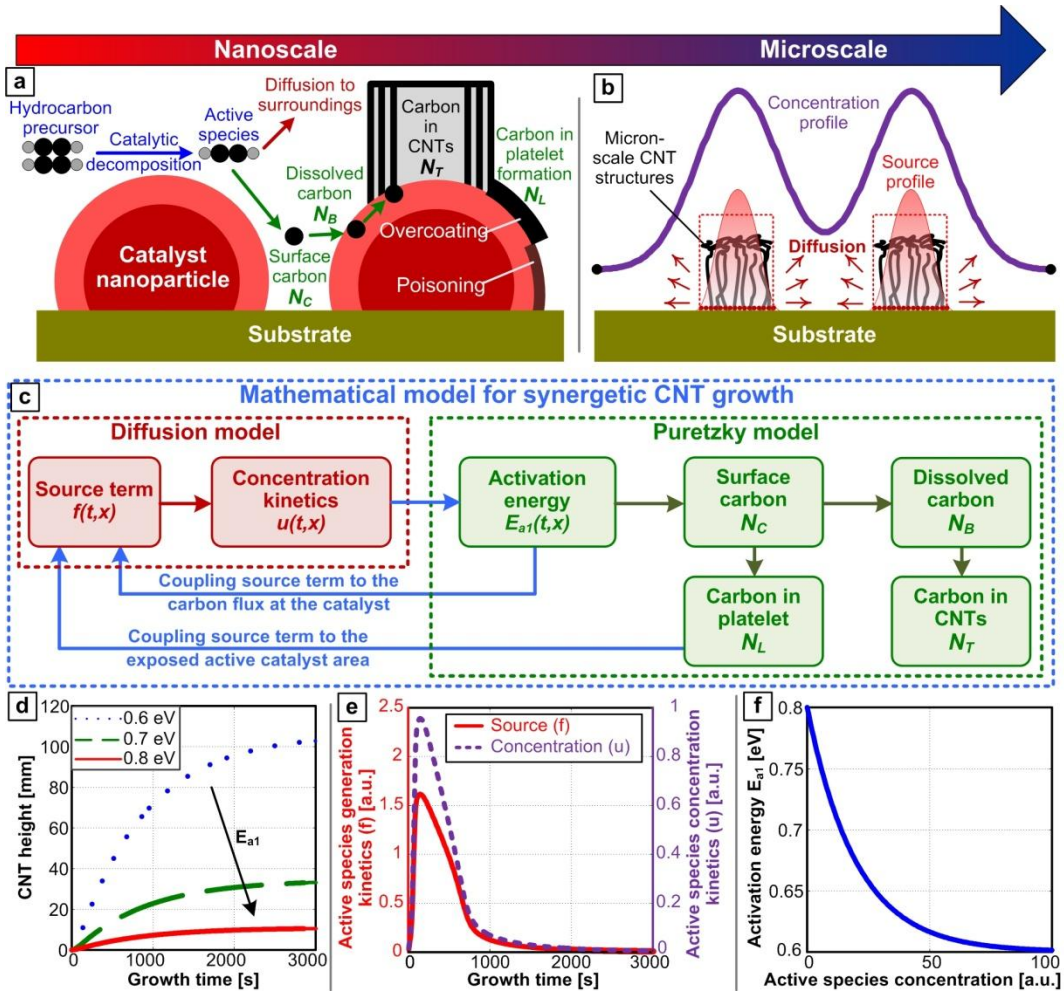

Figure 45. Model of synergetic CNT growth from the nanoscale to the microscale: (a) Schematic showing the chain of successive physicochemical steps that leads to individual CNT growth from a catalyst nanoparticle (adopted from Puretzky et al. [49]). (b) Schematic showing the diffusion-caused concentration profile of active species, which are being generated at the micron-scale catalyst regions. (c) Block diagram showing the architecture of the chemically coupled synergetic CNT growth model. (d) Time-evolution of height for a 10 nm diameter CNT with different activation energies E_{a1}, without chemical coupling. (e) Kinetics of the source term and the ensuing concentration increase on the catalyst region, according to Eqs. 8, 9 and 10. The spatial step size is $\Delta x = 0.004$ mm and the time step is $\Delta t = 7.5$ s. (f) The dependence of activation energy (E_{a1}) on the concentration of active species (u).

To model the chemical coupling between growing CNT micropillars a model of gas diffusion is combined with a widely accepted model of CNT growth from a catalyst particle, which was developed by Puretzky *et al.* [49] The Puretzky model is an example of mathematical models in literature that explain CVD growth kinetics of one CNT growing from one catalyst nanoparticle. In fact, the synergetic growth framework proposed herein (Figure 45c) is equally applicable with adopting any model of CNT growth that has an appropriate formulation of activation energy. The Puretzky model explains the different successive stages of the physicochemical growth steps: the chemisorption and catalytic decomposition of feedstock gas, the dissolution and diffusion of carbon on the nanoparticle surface, and finally, the precipitation of carbon atoms into a growing CNT at the CNT-catalyst interface (Figure 45a). The spread of the chemical byproducts is modeled using a gas diffusion equation, and hence the time-evolving spatial distribution of their concentration is calculated. Each micron-scale catalyst area acts as a time-varying source of these active species, the kinetics of which is coupled to growth deactivation kinetics.

First, the Puretzky model is used to calculate the growth rate of an individual CNT using a system of coupled ordinary differential equations to determine the evolution of the number of carbon atoms on the surface of the catalyst, denoted N_C; in a poisoning/carbonaceous layer, N_L; in a disordered layer of the catalyst, N_B; and in the growing nanotube, N_T. Growth occurs from a metal catalyst nanoparticle

(Figure 45a), which is surrounded by carbon-containing gas feedstock as well as the products of thermal decomposition thereof. These hydrocarbons catalytically decompose on the catalyst surface to atomic carbon and/or bonded carbon. The surface carbon then dissolves into a molten/disordered layer of the catalyst and precipitates into the CNT. On the other hand, some gas pyrolysis products directly contribute to the formation of a carbonaceous platelet layer on the catalyst surface, which effectively deactivates it. Eventually, this platelet grows to completely surround the catalyst nanoparticle causing complete cessation of growth. The surface carbon can also incorporate into the carbonaceous layer, and the carbonaceous layer can dissolve into the molten layer. In the model used here, the catalyst deactivation by poisoning, described by Puretzky *et al.*[49] as N_{L2} is neglected, and the only growth deactivation mechanism considered is catalyst overcoating with a carbonaceous layer N_{L1} (denoted here as N_L).

The carbon kinetics is given by a system of ordinary differential equations (ODEs):

$$\frac{dN_C}{dt} = \widetilde{F_{c1}} n \left(1 - \frac{N_L}{\alpha S_0 n_m}\right) - (k_{sb} + k_{cl}) N_C, \qquad \text{Eq. 4.1}$$

$$\frac{dN_L}{dt} = \widetilde{F_{c2}} n_p \left(1 - \frac{N_L}{\alpha S_0 n_m}\right) + k_{cl} N_C - k_{d1} N_L, \qquad \text{Eq. 4.2}$$

$$\frac{dN_B}{dt} = k_{sb} N_C - k_t N_B + k_{d1} N_{L1}, \qquad \text{Eq. 4.3}$$

$$\frac{dN_T}{dt} = k_t N_B. \quad \text{Eq. 4.4}$$

$$N_C(0) = N_L(0) = N_B(0) = N_T(0) = 0. \quad \text{Eq. 4.5}$$

Here, n is the concentration of feedstock molecules and n_p is the concentration of gas phase pyrolysis products. α is the number of monolayers coating the catalyst, $n_m$is the surface density of a monolayer of carbon atoms, and S_0 is the surface area of the catalyst. k_{sb} is the rate constant of dissolution of carbon atoms, k_{cl} is the rate constant of formation of the carbonaceous layer, k_{d1} is the dissolution rate constant of the poisoning carbonaceous layer, and k_t is the rate constant of precipitation of carbon atoms into the nanotube.

The fluxes in the first two equations are given by the following:

$$\widetilde{F_{c1}} = \frac{F_{c1}}{n}, \widetilde{F_{c2}} = \frac{F_{c2}}{n_p}, \quad \text{Eq. 4.6}$$

$$F_{c1} = F_{b1} p_1 \exp\left(-\frac{E_{a1}}{k_B T}\right), F_{c2} = F_{b2} p_2 \exp\left(-\frac{E_{a2}}{k_B T}\right), \quad \text{Eq. 4.7}$$

$$F_{b1} = \frac{1}{4} S_0 n \left(\frac{k_B T}{2\pi m}\right)^{1/2}, F_{b2} = \frac{1}{4} S_0 n \left(\frac{k_B T}{2\pi M}\right)^{1/2}. \quad \text{Eq. 4.8}$$

Here, p_1 and p_2 are pre-exponential factors. k_B is Boltzmann's constant and T is the gas temperature. E_{a1} and E_{a2} are the activation barriers for sticking and catalytic decomposition of the feedstock molecules and their gas-phase products, respectively. m and M are the masses of the feedstock molecule and the main pyrolysis product,

respectively. Values for these constants were selected to match experimental results.[49, 133] This system of ODEs is solved using Matlab's ode23s function.

Figure 45d shows the time evolution of CNT height and growth rate for a 10 nm diameter CNT grown at 1000 K from acetylene (C_2H_2). The height kinetics is typically sublinear and the growth rate decays after reaching a maximum early in the growth process. The model predicts that the growth rate reaches its maximum value very quickly (after a brief initial incubation period) and then gradually decays to zero (eventual growth self-termination). Importantly, lower activation energy leads to faster growth kinetics and higher terminal height (Figure 46).

Now, in order to describe the rate of production of active species (source term kinetics shown in Figure 45b) on the catalyst surface, it is coupled to the kinetics of surface carbon (N_C), which evolves with time owing to the evolution of the overcoating layer (N_L), as shown in the block diagram (Figure 45c). The source term is modeled in Eq. 4.9 as being proportional to the positive term of the rate of change in surface carbon $\frac{dN_c}{dt}$ (Eq. 4.1). This source term (*f*) now represents the catalytic activity of the exposed part (uncoated) of the catalyst nanoparticle, which describes the kinetics of the generation of active species at the catalyst. Thus, the rate of active species production is given as a function of position on the substrate x and time t by

$$f = \sum_i k_2 F_{c1,i}(t)\left(1 - \frac{N_{L,i}(t)}{\alpha S_0 n_m}\right)\chi_i(x) \qquad \text{Eq. 4.9}$$

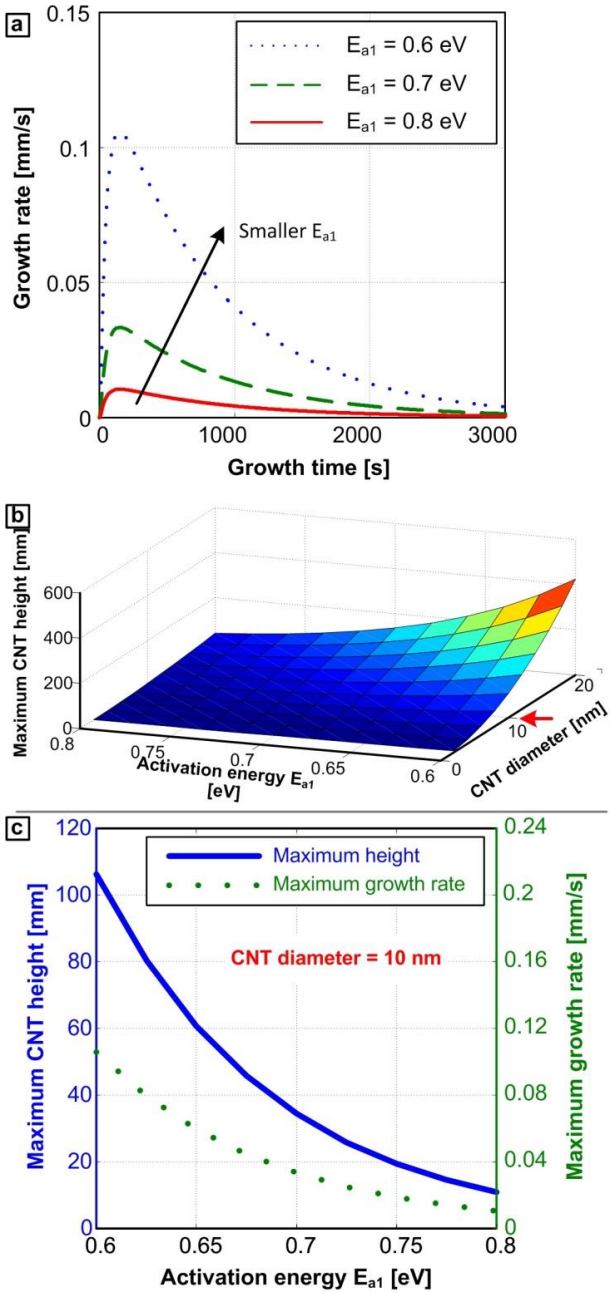

Figure 46. (a) The time evolution of growth rate of a 10 nm CNT growing at different activation energies (E_{a1}). (b) 3D plot of the effect of both the CNT diameter and the activation energy (E_{a1}) on the maximum CNT height at self-termination. (c) 2D plot of the effect of activation energy on the maximum CNT height and the maximum growth rate.

Here, χ_i represents the indicator function of the i-th catalyst region. The index i in $F_{c1,i}$ and $N_{L,i}$ specifies that these quantities are associated with the i-th catalyst region. The constant k_2 is a scaling factor that is determined empirically by comparing simulations to experimental results. The time-dependent evolution of the source is shown in Figure 45e, where the source kinetics (f) at a single micropillar in a catalyst pattern eventually decays to zero at growth termination. This source term is nonzero only on the catalyst regions and is zero elsewhere on the substrate. Two important assumptions are made to simplify the model. The first is the assumption that the distribution of the generated species over each macroscopic catalyst region is uniform, neglecting the synergetic growth effects between nano-scale catalyst particles within each micron-scale catalyst region. The second assumption is that the concentration of the active species equals zero at the edge of the simulation space. In reality, the concentration on the boundary is non-zero due to the bulk concentration of precursor in the CVD system. In order to minimize the effect of this boundary condition on our simulation results, a domain size of 1 mm is used, which is 10-times larger than the largest inter-pillar spacing simulated (100 μm), so that the boundary condition is far enough from the simulated micropillar growth.

After the active species is produced at a catalyst region, it diffuses through the surrounding area. The concentration of the active species u is given by the diffusion

equation, which is a partial differential equation that involves the source term f and the diffusion coefficient D:

$$\frac{\partial}{\partial t}u(x,t) = D\Delta u(x,t) + f(x,t). \quad \text{Eq. 4.10}$$

$$u(x,0) = 0. \quad \text{Eq. 4.11}$$

$u(x,t) = 0$ on the boundary. Eq. 4.12

The diffusion equation is numerically solved by discretizing the spatial domain into a regular square lattice with step size Δx and discretizing time into equal time steps Δt. The Laplacian is discretized with a five-point stencil, and the equation is evolved using an implicit scheme with a conjugate gradient solver. At each time step, the source term f is calculated from the concentration N_L, which is found by solving Eqs. 4.1-4.5 on the time interval $[t, t + \Delta t]$ with Matlab's ode23s solver. The step size Δx is chosen small enough that each catalyst region is several grid points wide, and the time step Δt is chosen small enough to resolve the dynamics of N_L. Figure 45e shows the kinetics of the active species concentration closely follows the source kinetics for the same CNT micropillar. This occurs because the diffusion of the gas is relatively fast in comparison to the time-scale of CNT micropillar growth.

As the concentration of the active species increases, the growth rate of the CNTs also increases, i.e. the activation energy E_{a1} in the Puretzky model decreases. Hence,

this model is based on modulating this activation energy E_{a1} by mathematically coupling it to the local average concentration $\bar{u}$ of active gaseous species, as shown in Eq. 4.14,

$$\overline{u_i}(t) = \frac{\int u(x,t)\,\chi_i(x)dx}{\int \chi_i(x)dx}, \qquad \text{Eq. 4.13}$$

$$E_{a1,i}(t) = E_{min} - (E_{max} - E_{min})\exp\,(k_1\,\overline{u_i}(t)). \qquad \text{Eq. 4.14}$$

Here, $\chi_i$represents the indicator function of the i-th catalyst region. When the concentration is zero, $E_{a1} = E_{max}$, and for large concentrations, E_{a1} approaches the asymptote E_{min}. The constants E_{min}, E_{max} are chosen based on typical values from the Puretzky model,[49, 133] while the constant k_1 is chosen by comparing the simulations to experimental results. Figure 45f shows a plot for the dependence of E_{a1} on u when $E_{max} = 0.8$, $E_{min} = 0.6$, and $k = 0.05$. This mathematical formulation captures the three main features of such dependence. First feature is the inverse relation between concentration and activation energy. Second feature is having a numerical maximum for activation energy at zero concentration, i.e. in the absence of catalytically produced active species. In this case, this value of maximum activation energy is dependent on only the active species produced by thermal decomposition of the hydrocarbon feedstock, which are generated by the thermal profile and location of the sample inside the furnace and are independent of the catalyst pattern. Third feature is the presence of a minimum bound for the

activation energy that cannot be surpassed no matter how high the concentration of the active species gets. This is mathematically described as an asymptote of the exponential function. This phenomenological relationship is also consistent with the experimental observations obtained for the dependence of growth rate of nanowires on the spacing.[161]

6.3.2. Experimental

Micron-scale patterning of the catalyst film was achieved by photolithography on a (100) silicon wafer with 300 nm SiO_2 layer (obtained by thermal oxidation). After spin-coating the photoresist (SPR220), a patterned mask was used during contact exposure of UV light (Karl Suss MA/BA-6) at 30 mJ/s for 6 seconds. After development of the patterned photoresist, the supported catalyst (1 nm Fe on 10 nm Al2O3) is deposited by sputtering (Lab 18 by Kurt J. Lesker). The wafer is diced manually by a diamond-tip scribe. The remaining photoresist is then lifted off the wafer by placing samples in an ultrasonic bath of acetone, before loading the catalyst-coated Si chips into the tube furnace. Micropillars of vertically aligned CNTs were grown in a custom-built hot-wall CVD reactor. First, the substrate is annealed to induce catalyst film dewetting and nanoparticle formation in a reducing atmosphere of hydrogen and helium (400 sccm H_2 / 100 sccm He) at 775 °C. After the annealing step, the substrate is retracted from the reactor to be held in an adjacent cold chamber, while the growth gases are introduced into the reactor. After 7 minutes, during which the growth atmosphere and the humidity inside the tube

furnace stabilize, the samples are returned inside the reactor. The feedstock gas used was ethylene (C_2H_4), and it was flowed to the reactor along with helium and hydrogen (100 sccm C_2H_4 / 400 sccm He / 100 sccm H_2) during growth at 775 °C. This recipe was chosen because it has shown to produce consistent high density CNTs. More details about this growth recipe can be found elsewhere.[171] CNT structures are characterized by scanning electron microscopy (SEM), using a Philips XL30FEG.

4.4. Results

Experiments of CNT micropillar growth by CVD produces arrays of spatially non-uniform micropillars with respect to their orientation, size, geometry and surface texture (Figure 44), in addition to the inherent polydispersity of CNT diameter, number of walls and alignment. In order to gain insights into understanding the origins of synergetic growth effects, and devise novel means of enhancing the uniformity of as-grown CNT forest structures, a comprehensive mathematical model is developed, which bridges the CVD reactions at the nanoscale and the diffusion-induced chemical coupling between catalyst regions at the microscale (Figure 45 and Figure 47). In the subsections that follow, it is shown that the chemically coupled growth model predicts spatial non-uniformities in CNT growth rate among micropillar arrays (Figure 49 and Figure 50). It is also demonstrated that the "digital" change in CNT growth from tangled horizontal mat to vertically aligned forest can be explained based on a threshold concentration of active species (Figure 50 and

Figure 51). Moreover, the insights gained by the simulation and experimental results are exploited to design more uniform individual CNT micropillars (Figure 52), as well as more uniform micropillar arrays (Figure 53).

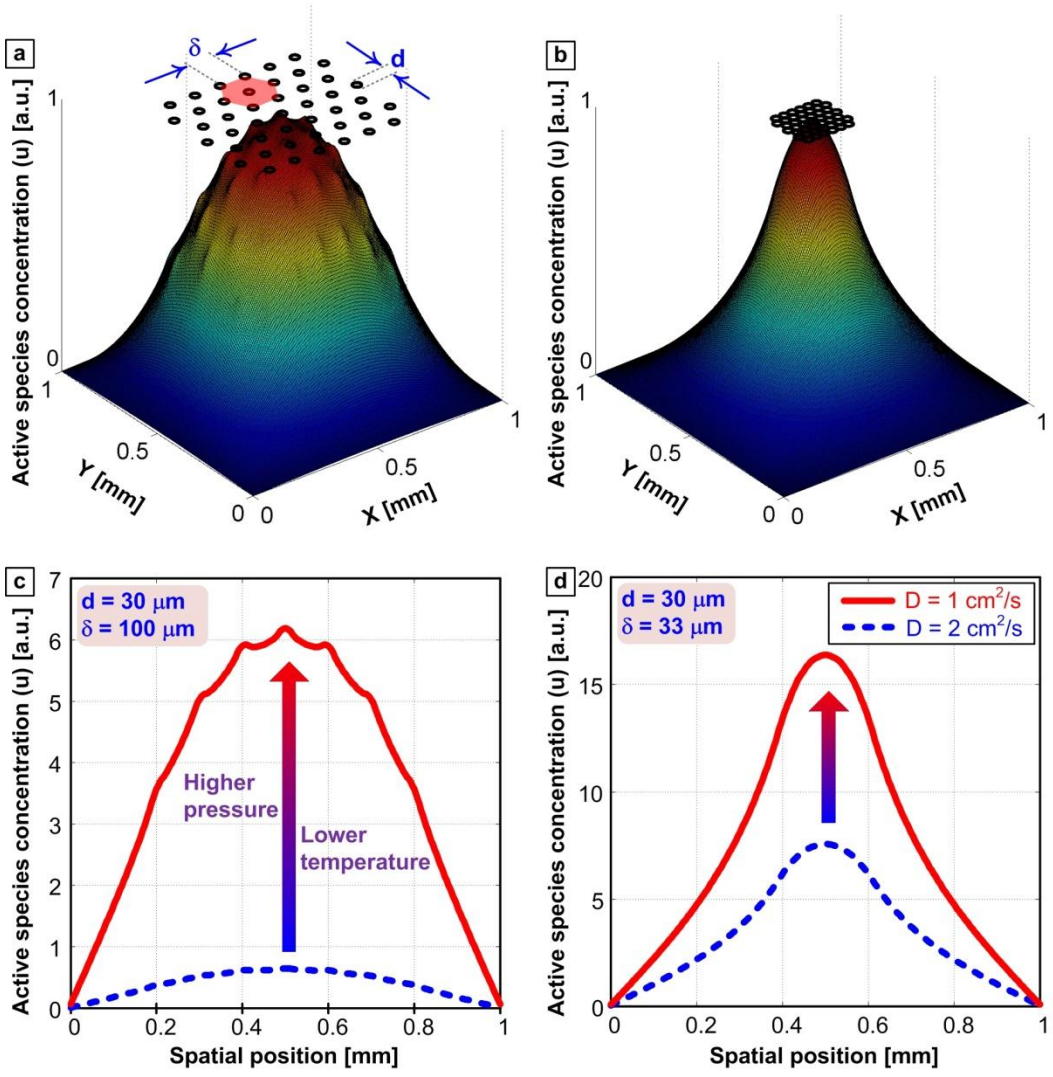

Figure 47. Effect of different model parameters. The spatial step size is $\Delta x = 0.004$ mm and the time step is $\Delta t = 7.5$ s. (a,b) 3D surface plot of concentration profile of active species generated at micron-scale catalyst patches (d = 30 μm) that are

arranged in a hexagonal array with different spacing δ of 100 and 33 μm, respectively (diffusion coefficient D=100 mm^2/s). (c, d) The 2D spatial distribution of active species concentration (u) for the same two catalyst arrays, plotted after 750 s of growth for two different temperatures of 600 and 1000 K, which correspond to two different values of diffusion coefficient of 1 and 2 cm^2/s, respectively. The solid red curve is the profile for a diffusion coefficient of 1 cm^2/s, and the blue dashed curve is the profile for a diffusion coefficient of 2 cm^2/s.

4.4.1. Diffusion-driven active species concentration profiles within micropillar arrays

The diffusion coefficient (D) in Eq. 4.10 is dependent on temperature, pressure and the gases. For example, the diffusion coefficient of C_2H_4 in He at 1 atm was calculated to be 1 cm^2/s at 600 K and 2 cm^2/s at 1000 K, according to an empirical relation (Eq. 15).[172]

$$D = 2.6280 \times 10^{-3} \frac{\sqrt{\frac{T^3(M_1+M_2)}{2M_1M_2}}}{p\sigma_{12}^2} \quad \text{Eq. 4.15}$$

$$\sigma_{12} = \frac{1}{2}(\sigma_1 + \sigma_2) \quad \text{Eq. 4.16}$$

Here, M is the molecular weight in grams per mole, T is the temperature in Kelvin, p is the pressure in atmospheres, and σ is the molecular diameter in Å. As temperature increases or pressure decreases, the diffusion coefficient increases.

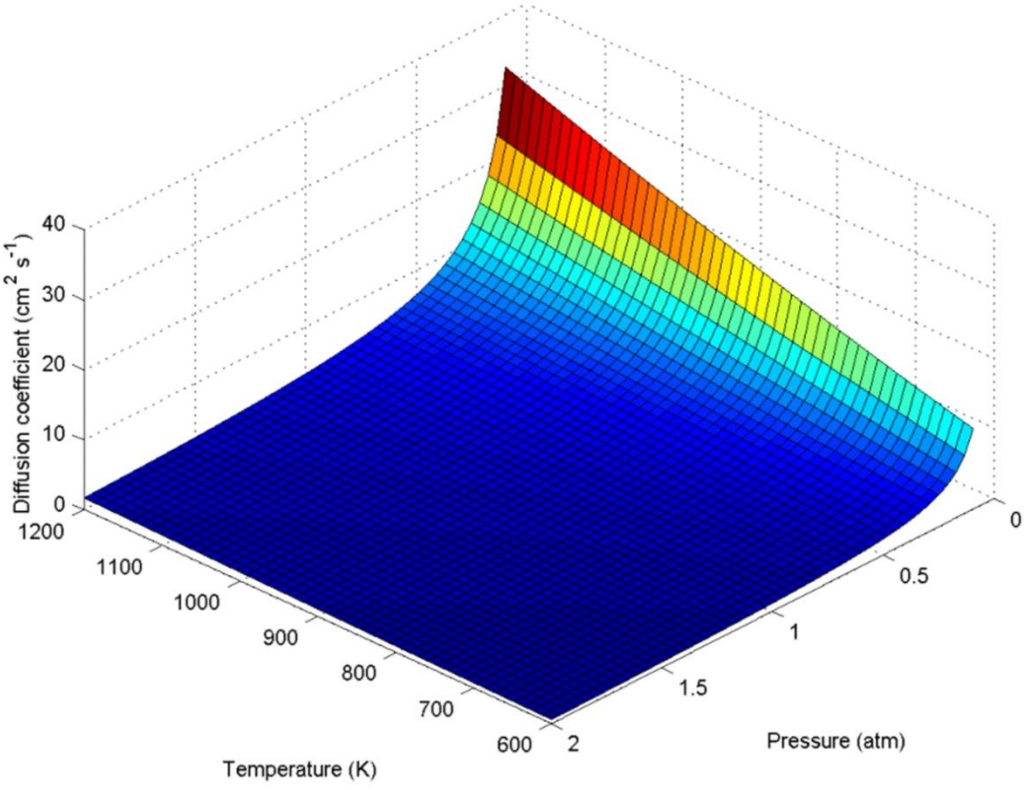

Figure 48. 3D plot showing the effect of pressure and temperature on the diffusion coefficient of C_2H_4 in He.

The effect of process temperature on gas diffusion and the resulting spatial distribution of active species concentration is first shown. 2D concentration profiles are plotted in Figure 47 after 750 seconds of growth at two different temperatures of 600 and 1000 K, which correspond to the values of diffusion coefficient of 1 and 2 cm^2/s, respectively. As shown in this figure, the maximum concentration occurs at the center micropillar in a hexagonal array, because at this location the maximum number of micropillars contributes to the overall concentration. Higher pressures

and lower temperatures significantly hinder gas diffusion to the surroundings, resulting in a much higher local concentration of active species. Larger inter-pillar spacing (δ) also contributes to having more discernible local maxima in the concentration profile of active species around each catalyst region, in contrast to the smooth concentration profiles observed for closely packed micropillar arrays.

4.4.2. Predicting spatially modulated growth kinetics of CNT micropillars in arrays

Now, it is demonstrated that the spatial distribution of active species governs the growth kinetics of CNT micropillars in arrays, predicting the observed spatial dependence of CNT growth rate and terminal height. Figure 49a shows a 3D plot of the simulation results of the terminal height distribution in an array of CNT micropillars grown by CVD according to our model. Here, heights are normalized to the tallest micropillar in the array (the central micropillar), in order to account for the scaling required to correct for process dependence on CVD conditions in the Puretzky model. The array has a domed shape with taller micropillars toward the center and shorter micropillars at the edges. Figure 49b shows the height kinetics of the central micropillar and the corner micropillar, showing that the final height of the corner micropillar is about 60% of the final height of the central micropillar. This height variation is due to the modulation of activation energy based on the spatial

distribution of active species concentration, which is lower at the edges (leading to higher activation energy and shorter terminal height).

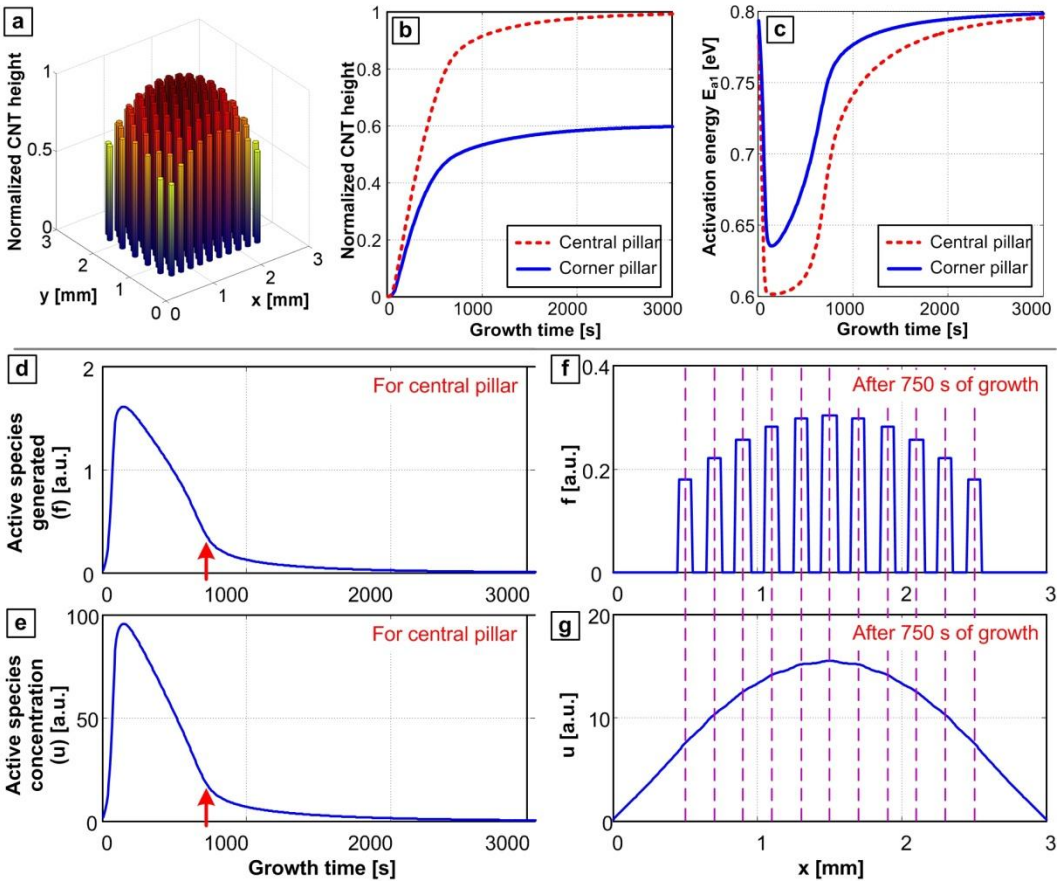

Figure 49. Simulation results for a hexagonal array of CNT micropillars having 100 micron diameters and 200 micron center-to-center spacing. The spatial step size is $\Delta x = 0.012$ mm and the time step is $\Delta t = 7.5$ s. (a) 3D plot of the spatial distribution of normalized micropillar heights. (b) Height kinetics for the central micropillar and a corner micropillar. (c) Time-evolution of activation energy (E_{a1}). (d, e) Time evolution of the active species generation term (source term) and the ensuing concentration for the same central micropillar. (f, g) Spatial distribution of the active species generation term (source term) and the concentration distribution after 750 seconds of growth (at y = 1.5 mm).

The kinetics of the activation energy is shown in Figure 49c. The minimum activation energy of the central micropillar is about 0.6 eV whereas the minimum activation energy of the corner micropillar is 0.64 eV. This difference arises from variation of active species concentration obtained by the continuous generation and diffusion of these gaseous molecules/radicals. The kinetics of the active species generation at the central micropillar in Figure 49d, and the kinetics of active species concentration are shown in Figure 49e. After a rapid increase in the production rate, it decreases almost linearly and then decays exponentially to zero. The spatial profiles of the active species generation and the ensuing concentration after 750 s of growth are shown in Figure 49f,g. The growth rate is typically lower at the edge of the pattern since the higher activation energy there causes carbon to decompose at a lower rate and therefore active species to be produced at a lower rate. The profile of the active species concentration in Figure 49g is a somewhat smooth curve, but small peaks at the catalyst site locations can be observed. Its maximum occurs at the center and it decays to zero at the endpoints (boundary conditions).

With the juxtaposition of simulations and experimental results, the spacing-dependent synergetic growth effects of 30 μm diameter CNT micropillars in a hexagonal array are elucidated. Figure 50a, b, c show that for small spacing (center-to-center distance of 33 μm), all CNT micropillars in the array grow vertically upward. On the other hand, in the case of large spacing (centre-to-centre distance of 100 μm), all of the CNT micropillars do not lift off to grow vertically. In the case of

medium spacing (center-to-center distance of 60 μm), however, only the CNT micropillars towards the centre of the array grow, while micropillars towards the edges/corners of the array does not grow. In fact, this consistent observation can be explained by the spatial variation of concentration-modulated growth that gives rise to the height variation shown in Figure 49.

4.4.3. Predicting CNT micropillar vertical lift-off via a chemical concentration threshold

Although the concentration of active species is non-zero at the locations that don't grow micropillars, lift-off and vertical growth does not take place. This phenomenon (Figure 50d, e, f) is explained by the presence of a threshold concentration of active species that is necessary for growing CNTs that are dense enough to self-organize into vertically aligned forest morphology, shown in Figure 50g, h, i. The threshold density required for vertical lift-off has been previously shown to exist experimentally, and was used to explain the successive growth stages.[35, 36, 124] Although some CNTs can start growing into a randomly oriented mat as soon as the hydrocarbon feedstock is introduced into the chamber (see inset in Figure 50i), micropillar lift-off is delayed until the threshold concentration is reached, as shown in Figure 50j, k, l.

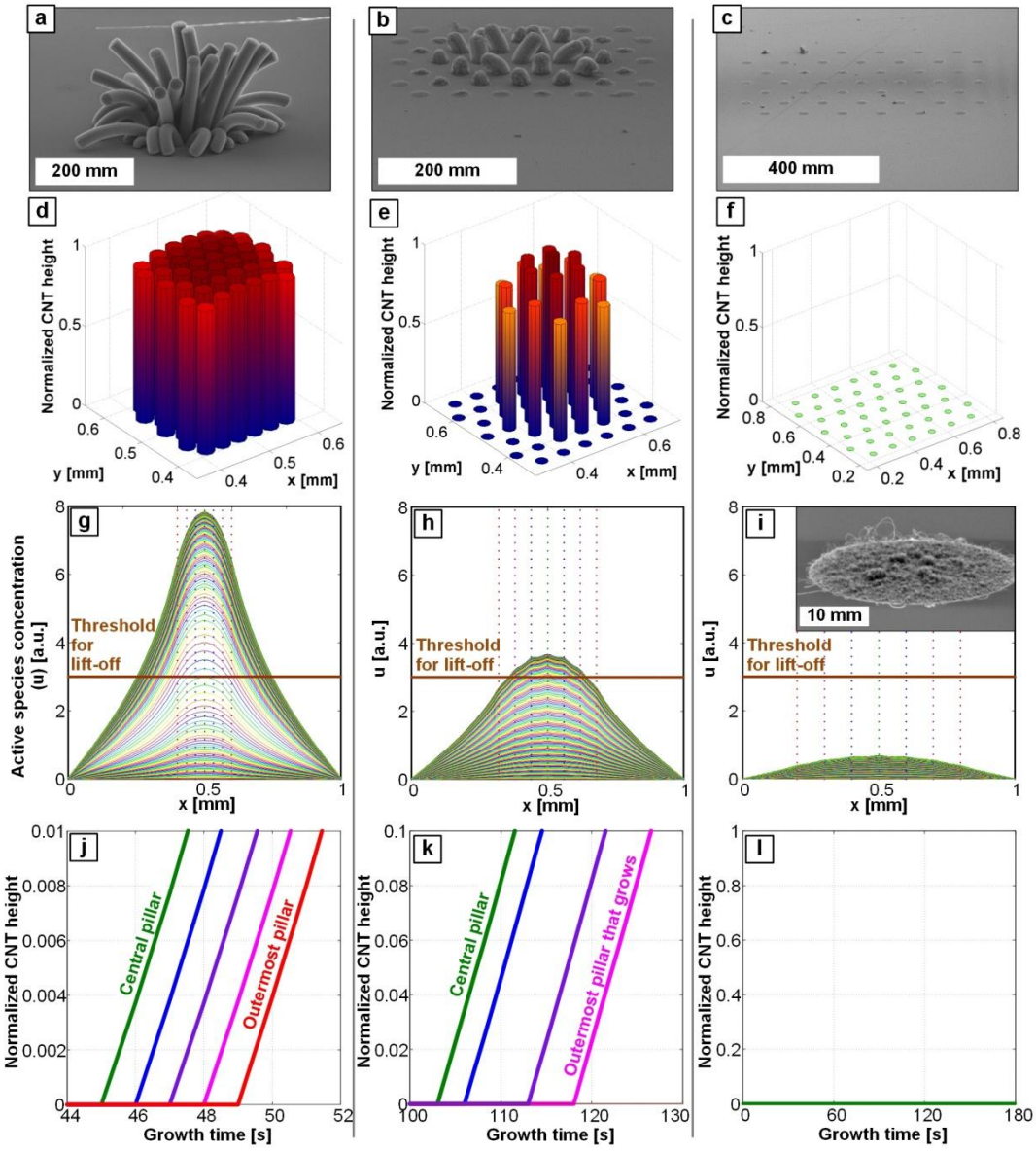

Figure 50. Effect of micropillar spacing in arrays on lift-off and growth. SEMs of CNT micropillar arrays having different spacing are shown in (a, b, c). Simulation results showing relative heights for these different CNT spacings are plotted in (d, e, f). The spatial step size is $\Delta x = 0.004$ mm and the time step is $\Delta t = 1.0$ s. Time-evolution of the spatial distribution of active species concentration for different spacings is plotted in (g, h, i), showing the threshold for lift-off. (Inset in i) SEM showing the growth of a tangled mat of CNTs in cases when micropillars do not lift

off. A zoomed-in plot of the height kinetics for each spacing is plotted in (j, k, l), showing the delayed onset of lift-off for outer micropillars compared to central micropillar.

Close-up electron micrographs of the CNT micropillar array with medium spacing (Figure 51a) shows that the geometry of each micropillar can be non-uniform as well, i.e. the top surface of the micropillar can be curved and the pillar could have a varying cross-sectional area from top to bottom. This non-uniformity, which is a typical indication of low-density CNT micropillars, can be attributed to density profiles across the height of each micropillar.[35, 36, 173] Although these density variations are not captured by the mathematical model, the introduction of the chemical threshold, shown in Figure 50g, h, i, adequately predicts the transition from horizontal randomly oriented growth of CNT mats to the vertical self-supported aligned growth of CNT forest morphology.

These experimental results also furnish a unique opportunity to observe the successive stages of vertical micropillar growth, by capturing different micropillars at varying stages of growth depending on their spatial position in the array. Figure 51b shows a schematic of the successive stages that are needed for CNT micropillar lift-off. First, CNT nucleation starts as soon as the hydrocarbon gas feedstock is introduced to the reactor, albeit at this stage CNTs grow in random orientations (mostly in the planar direction parallel to the substrate owing to the Van der Waal's

interactions between these CNTs and the substrate.) Due to the activation kinetics of CNTs,[124] this in-plane crowding proceeds until the density of actively growing CNTs reaches a threshold value (which has been identified in previous chapters to be about 10^9 CNTs/cm^2).[35, 36] This threshold density represents the density at which the total upward force overcomes the van der Waal's attraction forces pulling the CNTs to the substrate.

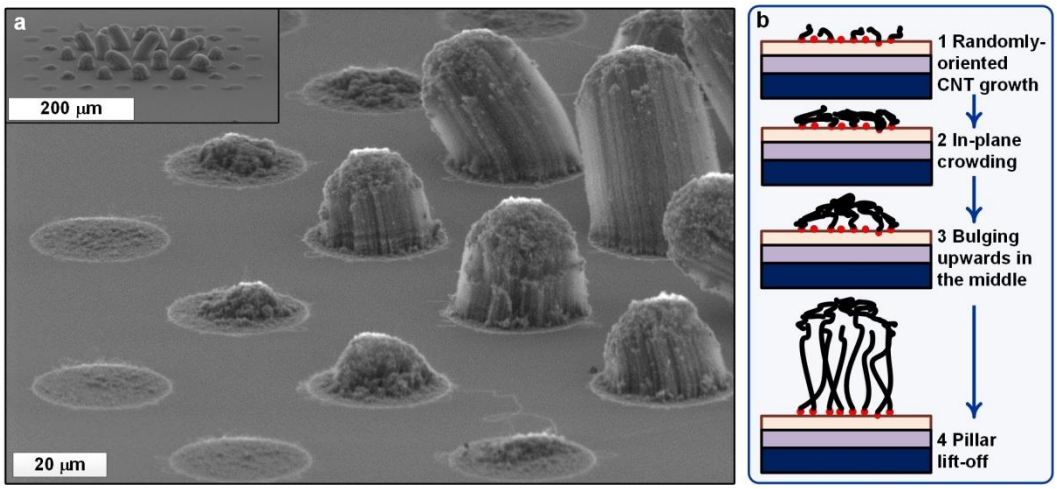

Figure 51. Successive stages of micropillar lift-off. (a) SEM of the medium spacing array (with 60 μm spacing), showing that micropillars are at different stages of lift-off depending on their position in the array. (b) Schematic showing the progression of stages leading to CNT micropillar lift-off.

Although the mathematical model presented in this chapter considers that the rate of active species generation is constant across each micron-sized catalyst area (Figure 45b), actual distribution is likely bell-shaped due to the chemical coupling

between individual catalyst nanoparticles within the catalyst area. Hence, CNT activation kinetics is expected to be maximal towards the middle of the catalyst area for each micropillar. Accordingly, the threshold density is reached in the middle of the micropillar area first, and lift-off starts to develop from the center of the micropillar, until eventually, the whole micropillar lifts off. It is worth noting here that this delay between the lift-off of the middle portion of the micropillar and the lift-off of the whole micropillar (micropillar lift-off dynamics) leave a print on the shape of the top surface of the grown micropillar. For instance, a more curved dome-shaped micropillar top is an indication to the slow micropillar kinetics of CNT activation, i.e. is an indication to the delay between the point at which the peripheral part of the micropillar reaches the threshold and the point at which the central part of the micropillar reaches the threshold. The mathematical model currently does not describe the curvature of the top-surface of the pillar, since the height kinetics is assumed to be similar for all CNTs within each micropillar. Nevertheless, the explanation above, which can be mathematically modeled in the future, provides insights into explaining why some micropillars don't lift off in large arrays, and why those that do, have different top-surface geometries. Hence, this modeling approach can be utilized to inform micropillar array design to achieve a desired outcome.

Because the concentration of generated active species is also dependent on the area of each CNT micropillar, there exists a minimum micropillar size for a given set of growth condition, below which micropillars don't grow vertically aligned

structures. From the previous work of the author and colleagues, it has experimentally demonstrated that this minimum size is related inversely to the CNT density.[173] Considering run-to-run variations of the CVD process,[174] the runs in which CNT nucleation density is higher resulted in a smaller minimum micropillar diameter for vertical lift-off.[173]

4.4.4. Design of uniform CNT micropillars

This model can also provide insights into understanding the effect of engineering the surroundings to an individual CNT micropillar, in order to improve its density, geometric uniformity and/or height. Although it has been shown before that having an outer surrounding border does improve the straightness and alignment of CNT microstructures grown for microelectromechanical systems (MEMS) applications,[175] this effect was never quantified, and the effect of the size and spacing of the border on the resulting micropillar was never investigated. Figure 52 shows the effect of having a surrounding border of CNTs around a square micropillar. For a small spacing of 100 μm between the central micropillar and the border, the resulting central micropillar is straighter than in the case of the larger spacing (300 μm), which indicated higher CNT density in the case of smaller spacing. Also, geometry of the top surface of the micropillar is more uniform and square in the case of the smaller spacing, compared to a more curved top in the case of the larger spacing. This is attributed to the faster kinetics of CNT activation that result from the higher concentration of active species in the case of smaller spacing (Figure 52b).

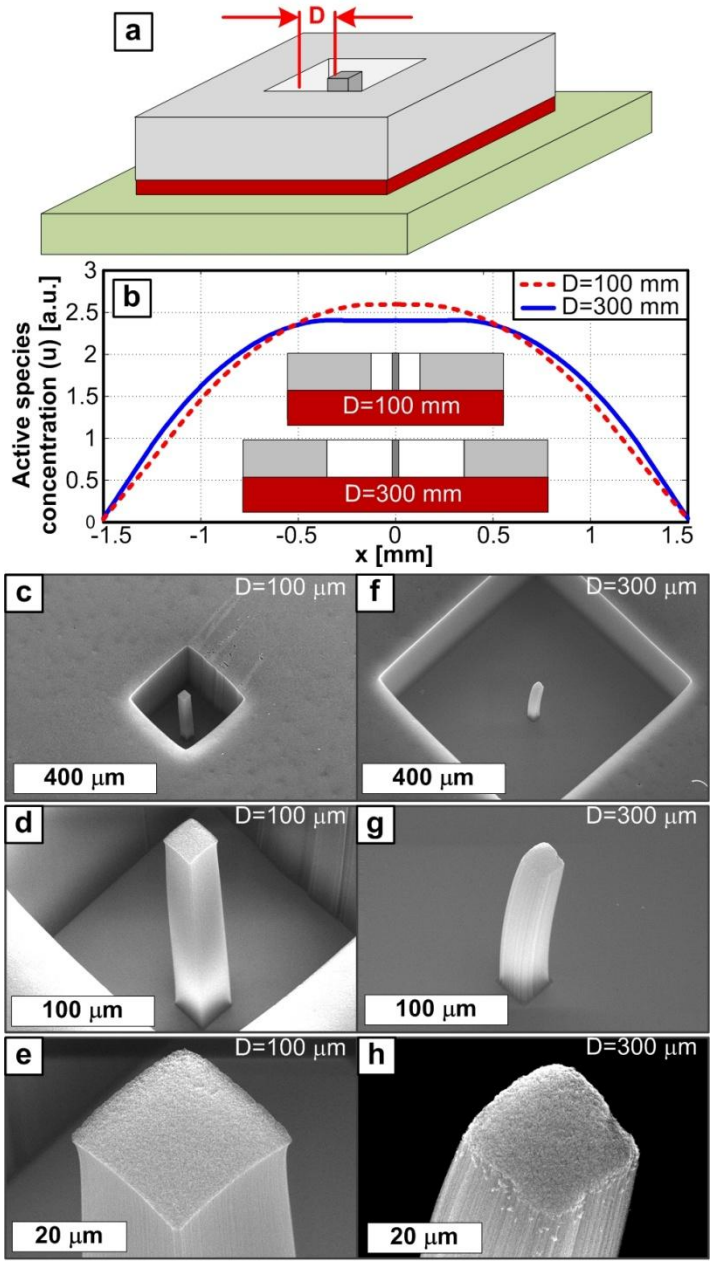

Figure 52. (a) Schematic showing the bordered design of single micropillar. (b) Concentration profile of active species showing two cases with different spacing D (100 and 300 μm). The spatial step size is $\Delta x = 0.012$ mm and the time step is $\Delta t = 7.5$ s. SEM images at different magnifications for the 100 μm spacing (c-e) and the 300 μm spacing (f-h).

Now, applying the insights from these simulations and experiments, CNT micropillar uniformity can be engineered by designing the array patterns. Tailoring the spacing between micropillars and/or the size of individual micropillars, results in a more uniform distribution of active species concentration, which eventually leads to growing large number of uniform CNT micropillars in arrays. This design principle will have an impact on the microfabrication of uniform CNT microstructures for applications where uniformity of CNT morphology and density are key determinants of device performance. Since arrays of CNT micropillars having tailored geometries are sought after for the scaled manufacturing of commercialized CNT-based devices with enhanced electrical, thermal, and mass transport properties, this chapter presents some design rules that enables unprecedented control on the outcome of the as-grown CNT micropillar arrays.

Figure 53 shows two different strategies that can greatly enhance the uniformity among arrayed CNT micropillars. The first strategy (Figure 53b, e) depends on designing a spatially varying spacing, wherein the distance between micropillars is largest in the middle of the array and smallest at the periphery of the array. This strategy is helpful for those applications that require similar diameter micropillars with no requirement that the positions of micropillars are equispaced. Example applications are those cases where the already grown CNT micropillars are harvested from the substrate. The second strategy (Figure 53c, f) relies on changing the size of the micropillars across the array, wherein pillars towards the centre of the pattern are

smallest and micropillars towards the periphery of the pattern are largest. This strategy is suitable for applications in which the position, or the center-line, of each micropillar is pre-specified by the device design, such as in the case of growing CNT micropillars as interconnects on microelectronic devices. In both strategies, the concentration profile becomes more uniform, as compared to the case of uniformly spaced same-sized micropillar array. It is worth noting here that for the second strategy the total catalyst area is increased, which results in an increase in the magnitude of the produced active species and is, hence, likely to be accompanied by an increase in CNT activation rate and density. Simulation results show that the ratio between the shortest (outermost) micropillar and the tallest (central) micropillar has increase from 86% in the case of uniformly spaced same-sized micropillars to 92% by applying the first strategy (varying the spacing only), and to 93% by applying the second strategy (varying the micropillar size only). Hence, employing a combination of similar strategies in pattern design will lead to both homogenizing the typically nonuniform concentration profile of active species, and boost the density activation kinetics of CNT micropillars. It is also worth noting here that the more uniform distribution of chemical concentration also leads to more uniform CNT activation kinetics, which in turn leads to more uniform CNT density distribution among micropillars in the same array.

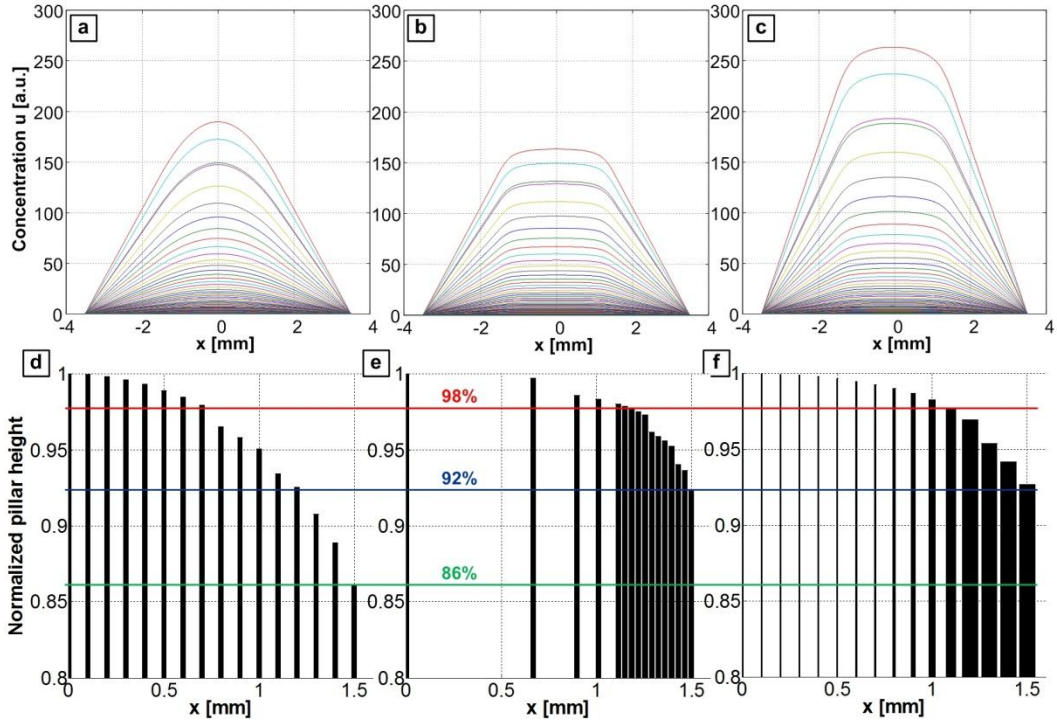

Figure 53. Array design to achieve uniform CNT micropillars. The spatial step size is $\Delta x = 0.004$ mm and the time step is $\Delta t = 7.5$ s. Evolution of the spatial distribution of active species concentration is shown for (a) uniformly spaced (60 μm spacing) micropillars having similar size (30 μm), (b) non-uniformly spaced micropillars having similar size (30 μm), and (c) uniformly spaced micropillars having varying sizes. Relative height distribution for only right-side half of the micropillar array for (a), (b), and (c) are shown in (d), (e), and (f) respectively. Green line indicates 92% bar and the red line indicated 98% bar.

4.5. Discussions

The comprehensive modeling framework presented in this chapter consolidates into a single metric the various gaseous species that actively promote the growth and modulate the reaction activation energy. The family of actual growth promoters

likely consists of multiple hydrocarbon gas molecules/radicals, which have varying potency in promoting the growth. Further research is required to enable a mathematical description of the relative proportions of each of these species, and designed experiments are needed to investigate their isolated, as well as cooperative, effects on modulating growth. In addition, the effects of other additives such as oxygen,[100] hydrogen,[100] water vapor,[34] and carbon dioxide[101, 102] on mediating CVD growth of CNTs, can be taken into consideration by empirically adding multiplying factors to the concentration parameter, for instance. On the other hand, other gaseous species probably have an opposite effect on growth, and some species might play either an activating or deactivating role depending on their partial pressure, total pressure, temperature, and/or gas composition in the reactor. These "harmful" effects on growth can also be captured phenomenologically by using an adequate multiplier to the concentration of active species (u).

Also, the exact mechanism(s) through which the activation energy shifts during CNT growth is yet to be fully understood, but mounting evidence from literature points to a competition between activation and deactivation mechanisms.[124] For instance, species that promote growth and reduce the activation energy of growth could do so by counteracting/neutralizing the effects of "harmful" species. This activation/deactivation competition is not solely controlled by the byproducts of local catalytic reaction or even gas-phase reaction in the vicinity of the catalyst

particle, but are also affected by the desorption of various species from the reactor wall.[111]

Despite such complexities that are not fully captured in the current model, this mathematical approach provides important quantitative insights into the effects of different process parameters on spatially-varying synergetic CNT growth, such as temperature and pressure. For instance, lower temperature and higher pressure growth recipes result in an amplified effect of chemical coupling, owing to the increased concentration of active species resulting from the reduced diffusion coefficient (See Figure 47). On the other hand, high temperature growth in vacuum conditions causes the synergetic growth effects to fade out due to the high diffusion coefficient and mean free path. Hence, one way to improve the uniformity of CNT micropillar growth in arrays is to employ high temperature and low pressure growth recipes. In other words, the relative ratio between the gas mean free path and the inter-pillar spacing in an array determine the extent of synergetic effects.

These findings not only quantitatively explain the typical observation that CNT micropillars in the center of an array grow taller than micropillars on the edges/corners, but also shed light on the reasons behind the different mechanical properties of CNT micropillars recently observed when comparing compression tests of micropillars grown at the edge of an array to micropillars grown in the centre of the array.[176] In that study, which was carried out as a collaboration between the author and Dr. Siddhartha Pathak from Prof. Julia Greer's group at the California

Institute of Technology, buckling of CNTs started at the bottom of the pillar for edge pillars, and started in the middle of the pillar for central pillars (Figure 54). This can be attributed to the spatially modulated activation/deactivation kinetics, which leads to spatial variations in density and density profiles.

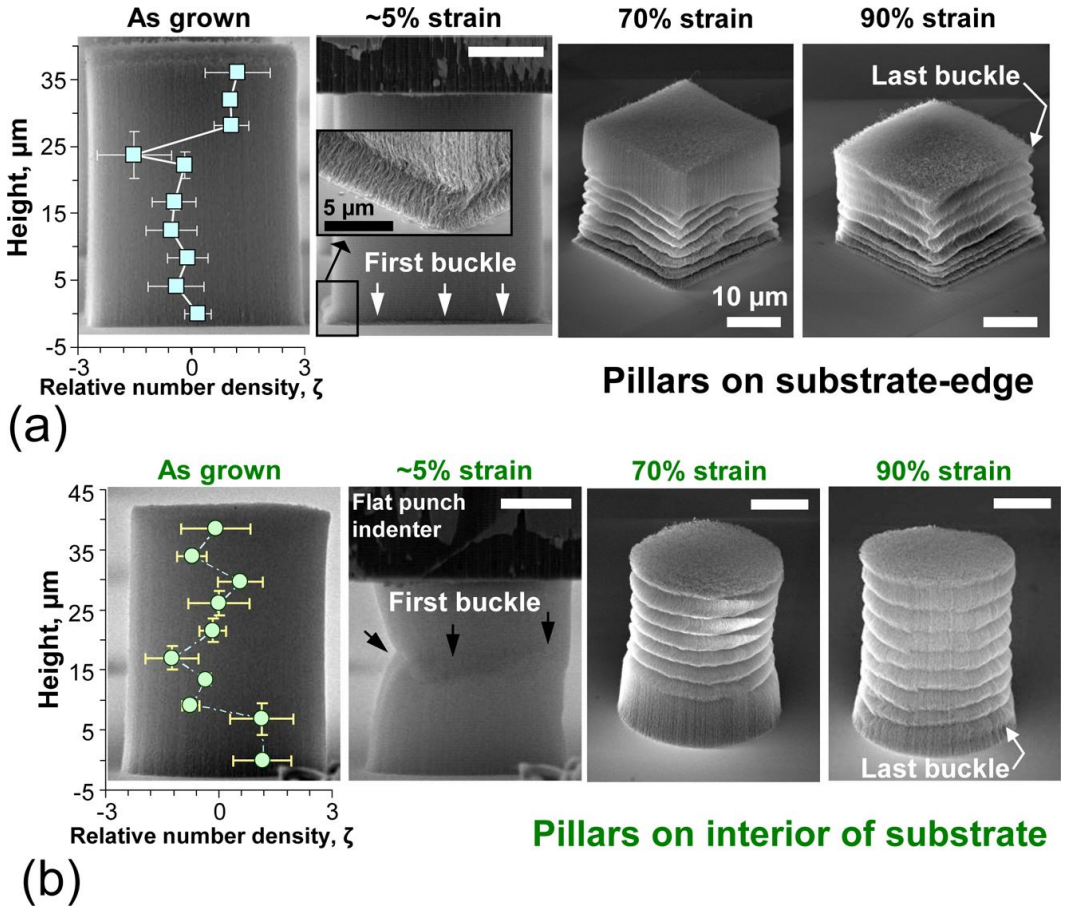

Figure 54. CNT buckling behavior during mechanical testing of CNT micropillars that were grown by the author according to the growth recipe in Figure 12, and were tested in Prof. Greer's group at Caltech. Results show that pillars located on the edge of the micropillar array behave differently from interior micropillars. Reprinted with permission from Reference 176. Copyright 2013 American Chemical Society.

4.6. Conclusions

From a manufacturing perspective, variations among as-grown CNT microstructures are sources of non-repeatability that hinder performance prediction of CNT-based devices such as electric interconnects, thermal interfaces, filtration membranes, and sensors. Hence, developing a better understanding of the origins of geometric/morphological non-uniformity helps overcome an important roadblock towards the scaled commercial production of nanodevices having tailored properties. This chapter enables prediction and control of non-uniformities in as-grown CNT micropillars by developing a holistic mathematical model that describes the origins of synergetic CNT growth effects based on the chemical coupling between catalyst regions in proximity. The model is based on chemical coupling arising from the generation of active species at the catalyst locations and their subsequent diffusion into the surroundings, leading to a spatial distribution thereof. The growth rates are modulated by coupling the activation energy of growth to the concentration of active species. Results show that higher pressure and lower temperature promote these synergetic growth effects, which are more prominent for arrays with small inter-pillar spacing. Combining experiments and simulations reveals that a threshold concentration of active species is needed for lift-off of CNT micropillars and enables the elucidation of successive stage of micropillar growth. These findings also provide insights into the design of more uniform micropillar arrays and can be implemented to achieve designed non-uniformities within CNT micropillar arrays if

needed. The mathematical formulation presented herein can be used in the future as the basis for a more mathematically intensive optimization algorithms that enables micropillar array design to maximize the shortest-to-tallest ratio as an objective function.

CHAPTER 5: MECHANICAL COUPLING IN CARBON NANOTUBE FOREST GROWTH[4]

5.1. Summary

Aligned carbon nanotube (CNT) structures are promising for many applications; however, as-grown CNT "forests" synthesized by chemical vapor deposition (CVD) are typically low-density and mostly comprise tortuous defective CNTs. This chapter presents evidence that the density and alignment of self-organized CNT growth is limited by mechanical coupling among CNTs in contact, in combination with their diameter-dependent growth rates. This study is enabled by the comprehensive X-ray characterization of the spatially and temporally-varying internal morphology of CNT forests (discussed in chapters 2 and 3). Based on this data, the time evolution and diameter-dependent scaling of the ensuing mechanical forces on catalyst nanoparticles during CNT growth are modeled. These mechanical loads arise from the mismatch between the collective lengthening rate of the forest and the diameter-dependent growth rates of individual CNTs. In addition to enabling self-organization of CNTs into forests, time-varying forces between CNTs in contact

[4] Significant portions of this chapter were reproduced with permission from The Royal Society of Chemistry from Reference 170. Bedewy, M.; Hart, A. J., Mechanical coupling limits the density and quality of self-organized carbon nanotube growth. *Nanoscale* 2013, 5, 2928-2937.

dictate the hierarchical tortuous morphology of CNT forests, and may be sufficient to influence the structural quality of CNTs. These forces reach a maximum that is coincident with the maximum density observed in our growth process, and are proportional to CNT diameter. Therefore, it is proposed that improved manufacturing strategies for self-organized CNTs should consider both chemical and mechanical effects. This may be especially necessary to achieve high density CNT forests with low defect density, such as for improved thermal interfaces and high-permeability membranes.

5.2. Introduction and Literature Review

Simultaneous growth and self-assembly of CNTs into aligned structures, such as yarns[10] and vertically aligned "forests",[177] offers significant opportunity to scale-up the exceptional properties of individual CNTs. Achieving a high packing density of long, well-aligned CNTs in these forms is critical for various applications including structural composites,[11] electrical interconnects,[7, 9] thermal interfaces,[20] filtration membranes,[21] gas sensors,[22-24] and oil-sorbent materials.[25] Moreover, from a nanomanufacturing standpoint, self-assembled growth of CNTs by CVD can potentially be scaled-up in a production process aimed at making CNT ensembles with application-tailored morphology and properties. Although CVD of CNTs has been extensively studied, relatively little attention has been paid to the influence of CNT-CNT interactions on this hierarchical organization process, which significantly

influences, and in some cases limits, the bulk properties of functional CNT-based materials/devices.

In the case of vertically aligned CNT growth from substrate-bound catalyst nanoparticles, a large population of CNTs grows simultaneously, and eventual growth self-termination is inevitable and abrupt.[35, 36, 38, 49, 51, 52, 55, 58] Using X-ray techniques, the evolution of CNT diameter, alignment, and density during forest growth has been elucidated in previous chapters. These findings were used to build a collective model of the growth process, which describes the successive stages of growth.[35, 36] These chapters also demonstrated that the number density of growing CNTs increases during the initial "crowding stage", which is followed by a "density decay stage" leading to eventual termination of growth. The CNT alignment was also shown to correlate with this density trend, i.e. higher density forests are generally characterized by having straighter CNTs.[35, 36, 38] The existence of self-organized CNT growth suggests that mechanical coupling among CNTs in contact plays a significant role in the collective evolution of the CNT population. Nevertheless, to the author's knowledge, there are no studies of how mechanical coupling among CNTs can influence growth and how mechanical-coupling-induced forces correlate with the evolution of CNT straightness and forest density.

On the other hand, experimental results as well as theoretical models have shown that CNT growth rates are diameter-dependent,[49, 54, 133, 137, 138] and it is well established that a CNT forest contains a distribution of CNT diameters.[35, 40, 54, 124, 132, 133

However, the van der Waals (VDW) attraction and mechanical entanglement among CNTs in contact causes the forest to grow upward as a single block, wherein all CNTs have the same collectively averaged growth rate. Therefore, while analyses have typically treated the CNT forest as a continuous body, the discrepancy between the different diameter-dependent growth rates of individual CNTs and the single collective growth rate of the forest, abstracts the complex behavior that gives rise to the tortuosity of individual CNTs.

In this chapter, mechanical coupling among CNTs growing in concert is shown to present a significant limitation to the density and quality of CNTs grown in self-assembled forest configuration. The mismatch between the measured apparent forest height kinetics and the calculated diameter-dependent growth kinetics is analyzed in order to estimate the axial load applied on catalyst nanoparticles by tortuous CNTs in contact. This is based on modeling of the CNTs as curved beams under axial deflection, with geometry derived from X-ray mapping of CNT forests. Forces are shown to be proportional to the CNT diameter and correlate with alignment/density. Therefore, forces due to mechanical coupling may influence the maximum density and alignment found in CNT forests, and relate to the observation that the density starts decreasing due to the "death" of individual CNTs after a threshold maximum force is reached. The potential influence of mechanical forces on the kinetics and quality of growing CNTs suggests that strategies to improved

manufacturing of organized CNTs should consider both chemical and mechanical effects.

5.3. Methodology

CNT forests were grown in a modified cold-wall CVD reactor shown in Figure 12 with resistive heating of the substrate (SabreTube, Absolute Nano), while monitoring the forest height using a non-contact laser displacement-sensor (LK-G152, Keyence). The hydrocarbon gas used for the CVD process was ethylene (C_2H_4), and it was introduced after annealing the thin film catalyst (1 nm Fe / 10 nm Al_2O_3 / 300 nm SiO_2 / 500 μm Si) in a mixture of hydrogen (H_2) and helium (He).[113]

After growth, CNT forests where placed in the beamline of a Synchrotron X-ray source (energy of 10 +/- 0.1 keV) for collecting both 2D small angle X-ray scattering (SAXS) patterns and measurements of the beam intensity upstream and downstream to the sample. A focused X-ray beam was used (10 μm) to achieve high resolution profiling across the forest height. More details of the growth process and the X-ray characterization methodology can be found in chapters 2 and 3.[35, 38, 124]

As shown in Figure 55a, CNTs in vertically aligned forests have a complex bundled morphology of highly intertwined CNTs. The mechanical coupling of a pair of CNTs that are in contact is considered at a point small distance above the substrate (Figure 55b).

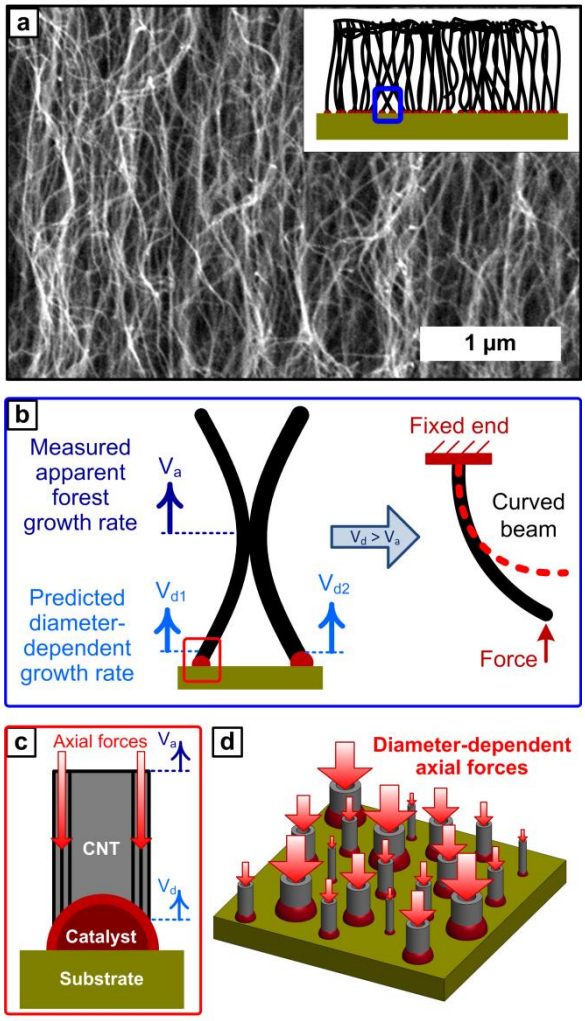

Figure 55. (a) Scanning electron micrograph a sidewall of a typical CNT forest. (Inset) Schematic of the intertwined morphology of the forest. (b) Schematic showing two CNTs in contact, where each CNT is modelled as a curved beam fixed at one end due. Axial forces arise due to the mismatch between the measured apparent forest growth rate (V_a) and the predicted diameter-dependent growth rate (V_d). (c, d) Schematic of the concept of diameter-dependent axial forces that are transmitted to the catalyst particles on the substrate, as a result of the growth rate mismatch and the mechanical coupling between contacting CNTs within the growing forest.

We estimate that the strength of VDW forces between CNTs in contact is sufficient to resist relative slip during growth. This is supported by measurements of CNT-CNT friction[152] and by *in situ* scanning electron microscopy (SEM) observation of CNT-CNT contacts during mechanical deformation of CNT forests.[178] Specifically, the VDW-induced interfacial shear strength between CNTs, was estimated to be in the range of 0.05-0.25 GPa.[151] Also, a static friction force of about 10 nN was measured between two overlapping CNTs, where the overlap distance was about 150 nm.[179] The non-slip assumption is also supported by the high values of VDW attraction forces calculated in the chapter 3 for CNTs in proximity, which can exceed 20 nN for 100 nm contact length.[124, 149]

Due to the polydispersity of CNT diameters within the forest, the two CNTs in our contact model, shown in Figure 55b, have different diameters, which are determined by the diameters of the corresponding catalyst particles on the substrate. Models describing the growth of individual CNTs predict that growth rate depends on CNT diameter.[49] Thus, assuming there is no slip between the CNTs in contact (as discussed above), there is a mismatch between the collective forest growth rate (V_a) and the predicted diameter-dependent growth rate (V_d). This mismatch leads to axial forces along the CNTs that are transmitted to the catalyst-CNT interface (Figure 55c). Because the growth rates are diameter-dependent, the ensuing axial forces are diameter-dependent as well (Figure 55d).

Building upon the no-slip assumption, we model the CNT-CNT contact as a constraint (i.e., a fixed end), and decouple the deformation of each CNT due to the differential growth behavior of the contacting pair. As shown in Figure 56a, the axial force (P) is calculated based on an analytical expression of the stiffness of a curved inextensible elastic beam. Each CNT is assumed to have the curved shape and is fixed at the point of interaction with a neighboring CNT. The load-displacement relationship for the curved shape is based on the Bernouilli–Euler hypothesis, taking into account large displacement,[180]

$$\frac{P}{\hat{P}} = \left(\frac{\xi}{2\alpha}\right)\left(\frac{1-\beta\xi^2}{(1-\xi)^{2/3}}\right). \qquad \text{Eq. 5.1}$$

Here, $P/\hat{P}$ is the non-dimensional load calculated based on the modulus of elasticity (E) and the area moment of inertia (I) of the beam, and ξ is the non-dimensional displacement,

$$\hat{P} = \frac{2EI\delta_{\max}}{R_0^3}, \qquad \text{Eq. 5.2}$$

$$\xi = \frac{\delta}{\delta_{\max}}. \qquad \text{Eq. 5.3}$$

The maximum value of displacement when the CNT is fully straightened (δ_{max}) is calculated considering the length of the CNT portion being modeled (l_0) and the measured value of b,

$$\delta_{\max} = l_0 - b. \qquad \text{Eq. 5.4}$$

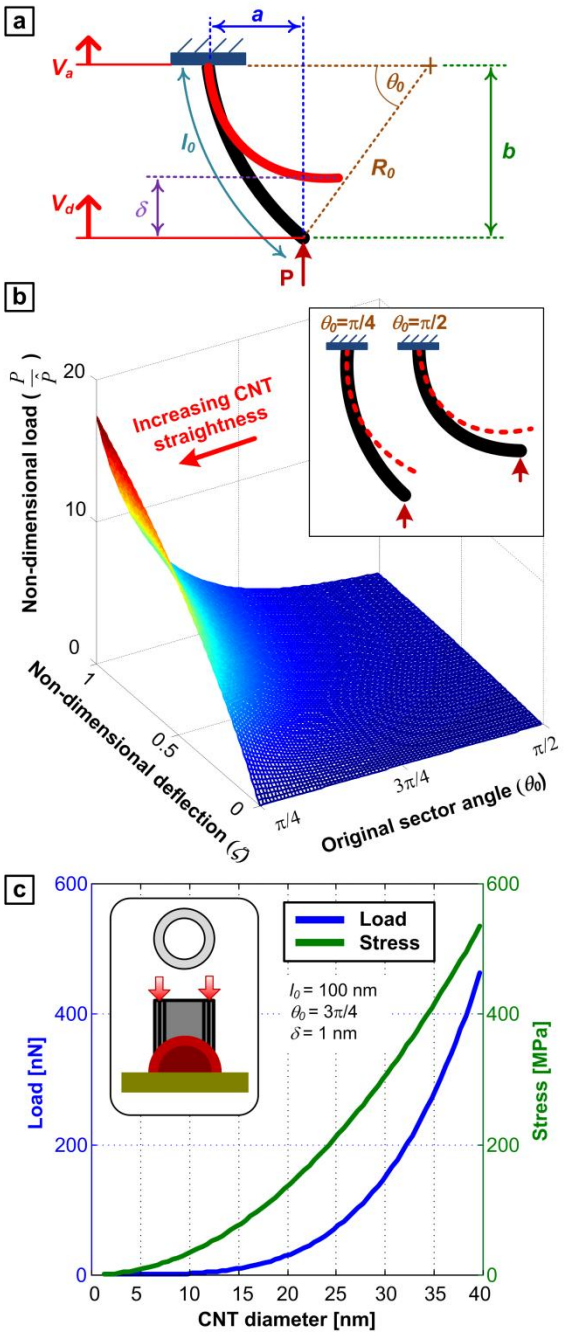

Figure 56. (a) Schematic showing a CNT as a curved beam, where the deflection is calculated based on the mismatch between the measured forest growth rate and the predicted diameter-dependent growth rate. (b) Non-dimensional load-deflection relationship of a curved beam as a function of the initial curvature of the beam. (c)

Diameter-dependent compressive load and stress predicted for a single 100 nm long CNT curved with a sector angle of $3\pi/4$, as a result of axial deflection (δ) of 1 nm (ζ=0.0071).

Non-dimensional parameters α and β in Eq. (1) are defined as

$$\beta = 1 - 2^{1/3}\alpha\left(\frac{R_0}{\delta_{\max}}\right)^{5/3}, \quad \text{Eq. 5.5}$$

$$\alpha = \theta_0 + \frac{\theta_0}{2}\cos 2\theta_0 - \frac{3}{4}\sin 2\theta_0, \quad \text{Eq. 5.6}$$

where R_0 is the radius of curvature of this portion of CNT being modeled, and θ_0 is the original sector angle before displacement. As will be shown later, the experimentally measured values of *a* and *b* will be used, throughout the forest, to calculate the instantaneous values of these dimensions, assuming the curvature of the CNT can be approximated as a circular arc, such that

$$R_0 = \frac{b^2 - a^2}{2a}, \quad \text{Eq. 5.7}$$

$$\theta_0 = \sin^{-1}\frac{b}{R_0}. \quad \text{Eq. 5.8}$$

In Figure 56b, the non-dimensional load-deflection relationship is plotted for a 100 nm long CNT with different initial curvatures, i.e., different original sector angles. Straighter CNTs are significantly stiffer than more curved ones, and therefore bear greater loads given equal curvature. Also, given equal curvature and deflection, larger diameter CNTs bear greater loads due to their greater stiffness.

Calculated values for this diameter-dependent load and the equivalent stress (load per unit projected area) for a 100 nm long CNT with an original sector angle of $3\pi/4$ and an axial deflection of 1 nm are plotted in Figure 56c.

To relate the curved beam model to the real morphology of the CNT forests, the tortuosity of CNTs is quantified from SAXS, by calculating the Hermans orientation parameter (H).[35, 36, 38, 74]

$$H = \frac{1}{2}\left(3\left\langle \cos^2\phi \right\rangle - 1\right) \qquad \text{Eq. 5.9}$$

Here, the average orientation angle (ϕ) is calculated by azimuthally integrating the scattering intensity $I(\phi)$ within a annulus on the 2D intensity map,

$$\left\langle \cos^2\phi \right\rangle = \frac{\int_0^{\frac{\pi}{2}} \left(I(\phi)\sin\phi\cos^2\phi\right)d\phi}{\int_0^{\frac{\pi}{2}} \left(I(\phi)\sin\phi\right)d\phi}. \qquad \text{Eq. 5.10}$$

5.4. Results

In order to apply this model to estimate the forces exerted on the CNT-catalyst interface during growth, the diameter-dependent growth rate of individual CNTs within the forest must be derived, and related to the experimentally measured collective growth rate of the mechanically-coupled CNTs (i.e., the whole forest).

For this, V_a (Fig. 3a,b) is defined as the collective lengthening rate of the forest, which is independent of CNT diameter. This is obtained by transforming measurements of the real-time forest height kinetics to an estimate of the true CNT length, correcting for the tortuosity of the CNTs. This correction is made by multiplying the differential change in CNT height with time, by a transformation factor that is calculated from the orientation parameter measured from the SAXS pattern obtained at each differential position of the CNT forest.[35, 38]

Next, V_d (Figure 57c,d) is defined as the diameter-dependent growth rate of individual CNTs during the CVD process. The rate V_d is calculated by adopting the theoretical model developed by Puretzky *et al.* This model predicts that the growth rate of an individual CNT seeded by an individual nanoparticle is dependent on CNT diameter, and specifically that larger diameter CNTs grow faster.[49, 133] The Puretzky model breaks down the reaction pathway during CNT growth into successive stages, starting with the chemisorption and catalytic decomposition of feedstock, followed by the dissolution and diffusion on the nanoparticle surface, and concluding with the precipitation of carbon at the CNT-catalyst interface. For illustration, the diameter-dependent CNT lengthening rates predicted by this model for growth in 0.5 sccm C_2H_2 at 1000 K are plotted in Figure 57c. It can be seen that the predicted shape of the growth kinetics curves for different diameters are self-similar, starting with an initially linear ramp followed by a gradual decay of growth rate until self-deactivation. Moreover, it is clear that the differences in growth rate between CNTs having

diameters that could be typically sampled from the same population of a single forest are significant, and therefore can be used to inform this model of growth rate mismatch.

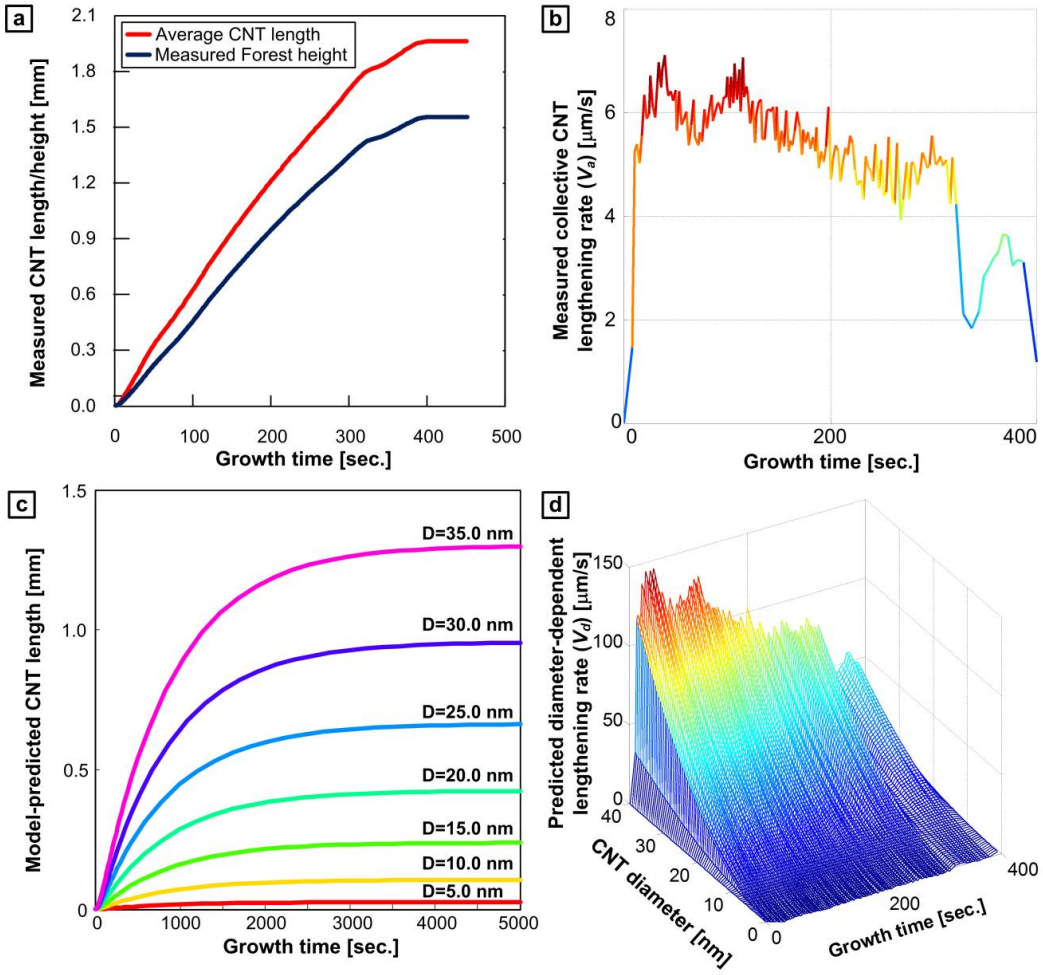

Figure 57. Analysis of CNT forest height kinetics compared to individual CNT lengthening kinetics. (a) Tortuosity-corrected diameter-independent CNT lengthening kinetics, obtained by SAXS mapping in combination with real-time forest height measurement.[38] (b) The slope of the collective lengthening kinetics (V_a). (c) Model prediction of diameter-dependent growth kinetics, adapted from Puretzky *et al,*[49] for CNT growth from Fe nanoparticles using 0.5 sccm C_2H_2 as the

hydrocarbon precursor at 1000 K. (d) The slope of the diameter-dependent kinetics, after normalization of the data obtained from (c) with respect to the collective rate in (b) at the diameter value equal to the mode of the CNT diameter distribution measured for the forest (see Figure 58).

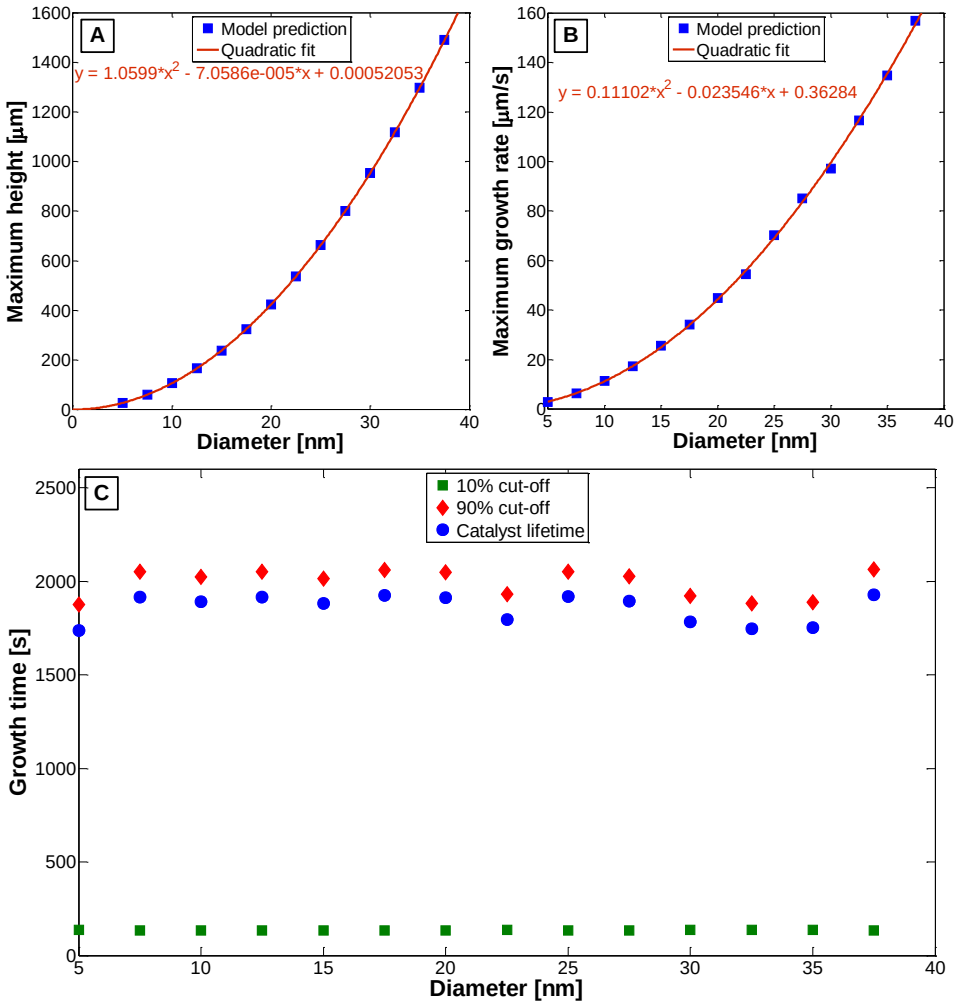

Figure 58. Results from the mathematical model developed by Puretzky *et al.* [49] for CNT growth from Fe nanoparticles using 0.5 sccm C_2H_2 as the hydrocarbon precursor at 1000 K. Diameter-dependent change in maximum height (A), growth rate (B), and lifetime (C).

However, because the model by Puretzky *et al.*[49] assumes CNT growth from a single carbon source, whereas a plethora of hydrocarbons exist in a typical CVD process,[181] it is necessary to scale the model predictions to fit our experimental data. The hydrocarbon population, as well as the characteristics of the catalyst, influences the CNT growth rate and the deactivation kinetics that lead to eventual growth termination. To adapt the model to our data, the maximum slope (i.e., the maximum CNT growth rate) of the kinetics curves shown in Figure 57c is first fitted using a quadratic function of the outer CNT diameter (*d*), and a normalized value for V_d is calculated (Figure 57d),

$$V_d = f\left(0.11d^2 - 0.02d + 0.36\right). \qquad \text{Eq. 5.11}$$

This quadratic relationship is shown in Figure 58. The time-dependent scaling factor (*f*) is computed using the experimentally obtained collective growth rate (V_a). For each point in time (*t*), which corresponds to a single scattering image, the values V_a and the mode of the CNT diameter distribution (d_m) are substituted in Eq. 5.11,

$$f(t) = \frac{V_a(t)}{0.11(d_m(t))^2 - 0.02(d_m(t)) + 0.36}. \qquad \text{Eq. 5.12}$$

This allows predicting the mismatch between the lengthening rate of a CNT of any diameter within the forest, and the collective growth rate imposed by the no-slip condition. Actually, the mismatch would occur between any pair of CNTs with different rates, and hence the growth rate difference between the two CNTs would

be more relevant; however, here the average lengthening rate is used as a reference rate.

Next, as a representation of the tortuous CNTs observed from SEM imaging (Figure 55a), the curve of neighboring CNTs in contact is assumed to follow a half sinusoidal wave shape known for the first buckling mode of slender columns (Figure 59). In order to accurately define the dimensions of this simplified model (*a* and *b*), the local alignment of the CNTs is related to their average orientation angle (ϕ), and their average spacing within the forest.

The spatial mapping of both the CNT orientation angle and the total number of CNTs-per-unit-area (*N*) are plotted in Figure 59d.

The total CNT number density (*N*) is calculated based on combining the mass density measurement from applying the Beer-Lambert-Bouguer law of mass-attenuation with the tortuosity-corrected lengthening kinetics, as described in previous chapters.[35]

Based on this data, *a* is calculated as half the average spacing between the CNTs,

$$a = \frac{1}{2\sqrt{N}}, \qquad \text{Eq. 5.13}$$

and *b* is approximated based on both *a* and ϕ,

$$b = \frac{a}{\tan(\phi)}. \qquad \text{Eq. 5.14}$$

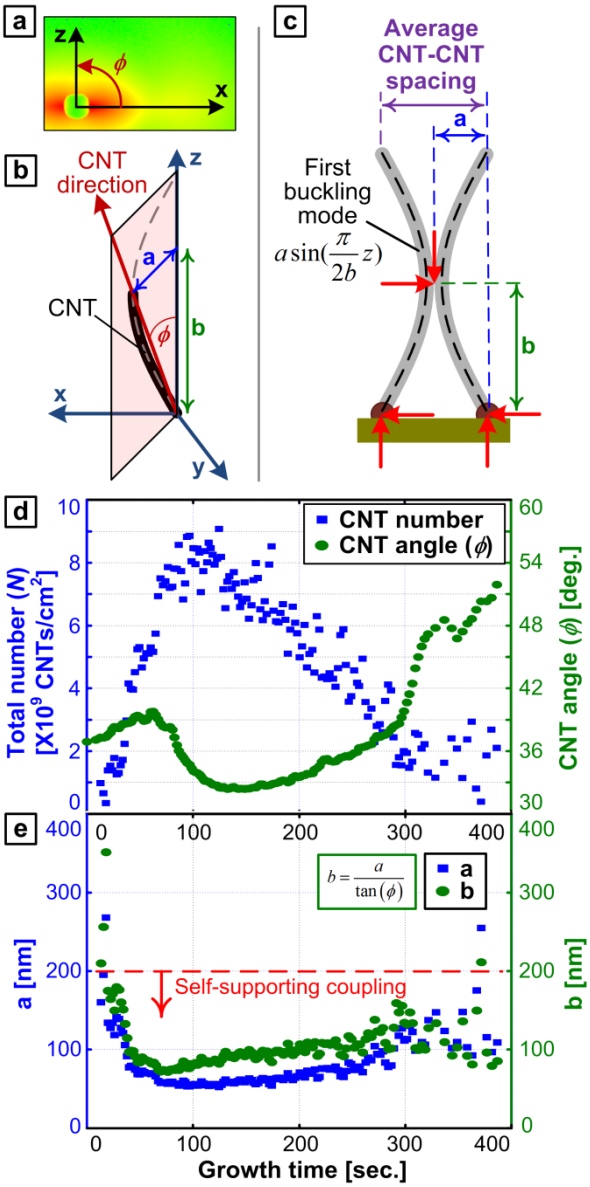

Figure 59. (a) Representative SAXS image used to calculate the average angle of CNT alignment (ϕ) by azimuthally scanning and integration (Eq. 5.10). (b) Adaptation of average angle to calculate geometric parameters of individual CNTs, according to the curved beam approximation; (c) Assumed geometry for a pair CNTs in contact close to the catalyst, simplified as harmonic curve representing the first buckling mode, where red arrows denote horizontal and vertical components of

contact and reaction forces. (d, e) Calculated time evolution of the total number of CNTs, representative orientation angle (ϕ), and geometric parameters *a* and *b*.

Accordingly, the evolution of both *a* and *b* during growth is plotted in Figure 59e. As shown in this figure, the value of *a*, and accordingly the value of *b* drop during the initial crowding stage as CNTs become closer to one another. When CNTs are close-enough, self-supporting mechanical coupling is achieved. When CNT density decays, both *a* and *b* increase, and eventually surpass the self-supporting threshold causing loss of alignment which results in abrupt termination of forest growth. Although the evolution of the CNT number density exhibits a well-defined peak, the evolution of both *a* and *b* show a flat valley because of the inverse square root in Eq. 5.13.

Now, the relative displacement (δ) of an exemplary CNT can be calculated from the mismatch of growth rates,

$$\delta = (V_a - V_d)t_{inc}, \qquad \text{Eq. 5.15}$$

where t_{inc} is a short time increment. The force applied to the catalyst particle is then estimated by multiplying the displacement by the stiffness of the CNT calculated from the numerical expression of a curved beam model. Here, t_{inc} = 1 μs is used in Eq. 5.15, in order to calculate relevant values for the displacement (δ) that are

smaller than the value of δ_{max}, considering the values of V_a and V_d shown in Figure 57.

Using this approach, Figure 60a shows the time evolution of the diameter-dependent compressive force applied on the catalyst nanoparticles. Here, the diameter range of 1-40 nm is assumed to completely represent the CNT population within the forest.[124] The instance (t = 115 s) when the predicted forces are maximum is highlighted, and the relationships between both force, as well as stress, and outer CNT diameter are plotted in Figure 60b,c. Owing to the sign of the growth rate mismatch in Eq. 5.14, the loads change from slightly tensile for diameters smaller than the mode of the diameter distribution (d_m) to highly compressive for larger diameter CNTs. The compressive stresses applied on the catalyst nanoparticles are then calculated as the force per unit projected area of CNT (Figure 61), based on the measured values for the outer and inner CNT diameters obtained from fitting SAXS linescans.[35] In this figure, positive force or stress means that CNTs are pushing on the catalyst, and negative means the CNT is pulling on the catalyst.

Now, using the calculated distribution of CNT number densities as a function of diameter and growth time (as in Figure 39 of chapter 3), the evolution of the total load applied on the substrate per unit area is calculated as a function of CNT diameter (Figure 62a). This plot shows the summation of loads applied by all CNTs

belonging to subpopulations having a narrow diameter range. With integration over all CNT subpopulations having different diameters, the time-evolution of the total net value for the compressive load on substrate is calculated as shown in Figure 62b.

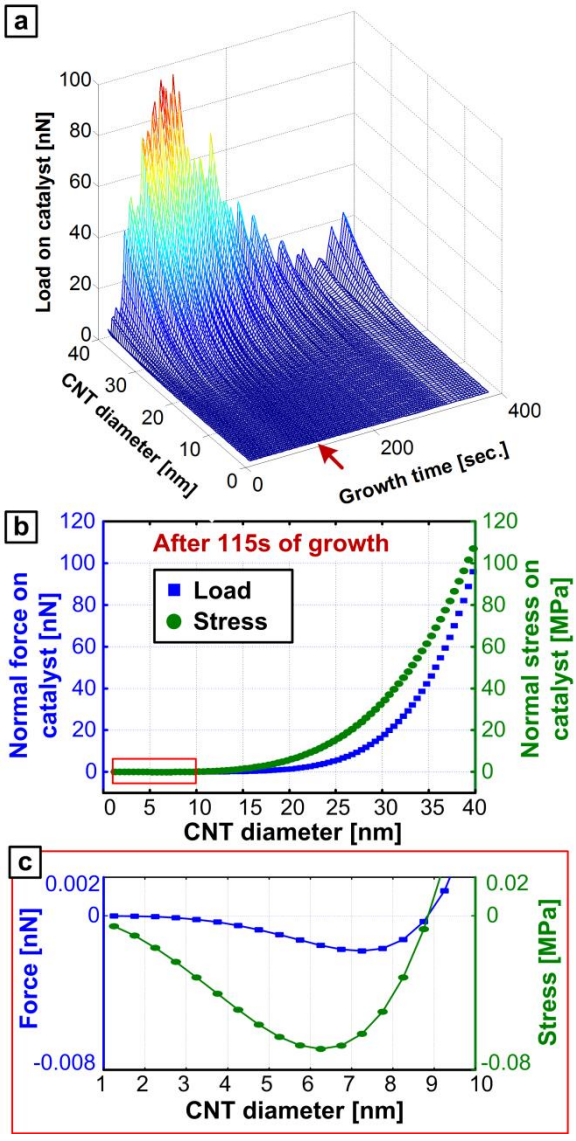

Figure 60. (a) Time evolution of the diameter-dependent load exerted by the CNTs on corresponding catalyst particles. (b) Diameter-dependent load and stress that are

applied to the catalysts after 115 seconds of growth, which is the time at which the CNT density and ensuing forces are at a maximum. (c) Diameter-dependent load on a semilog scale for CNT diameters between 1 and 10 nm, showing that CNTs growing slower than the collective rate experience tensile forces and therefore pull upward on the catalyst particles.

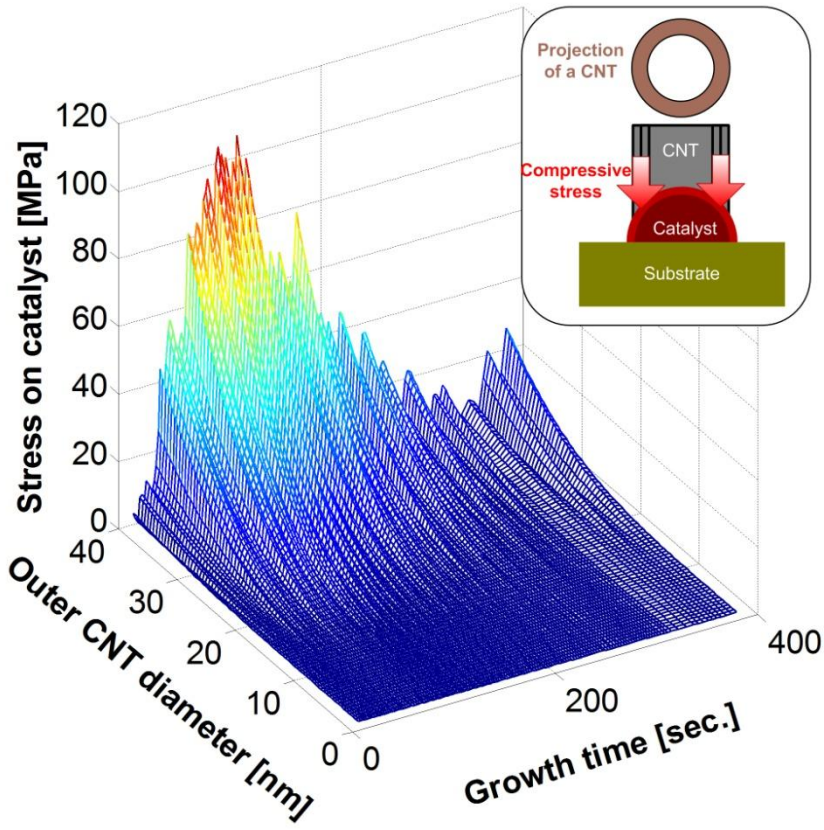

Figure 61. The time evolution of compressive stresses on the catalyst nanoparticles as a function of diameter , relative to the collective forest growth rate. Here, the stress is calculated by dividing the force by the projected area of a CNT considering their outer and inner diameters calculated based on fitting the SAXS linescans.

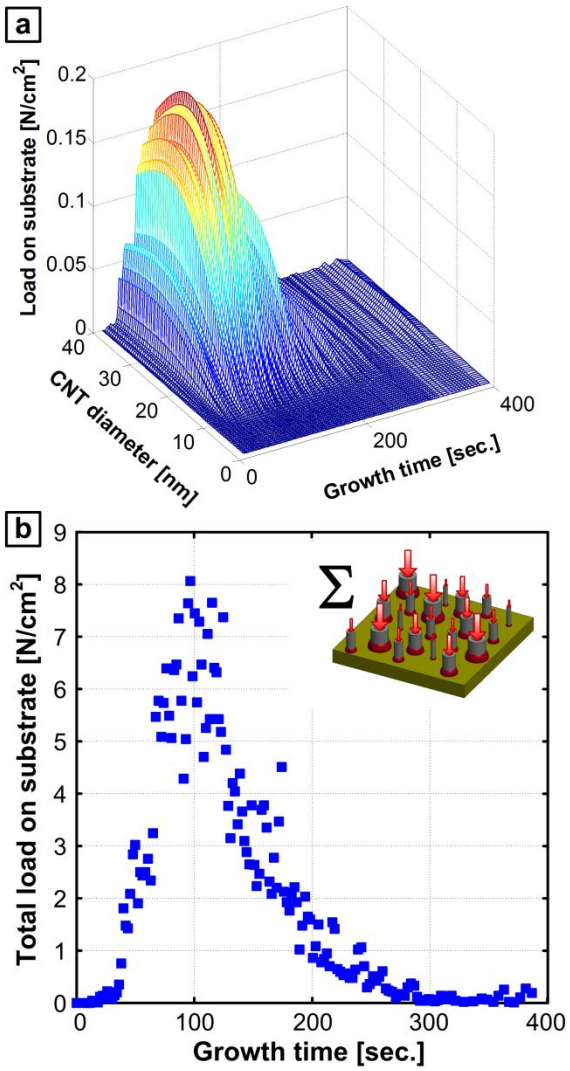

Figure 62. (a) Force distribution based on the probability density function of the CNT diameter distribution, obtained by multiplying the number density of each diameter bin by the predicted normal load on the catalyst particle. (b) Time evolution of the total normal force applied per unit area of the substrate, obtained by summing the forces on all CNTs at each time increment.

This methodology predicts that forces significantly increase with diameter, and this is because the stiffness of larger CNTs is much higher than that for smaller ones, considering the experimentally measured values of inner and outer diameters. Combining that with the fact that the diameter distribution is skewed (Figure 39 of chapter 3), the resulting magnitudes for tensile stress on CNTs that are smaller than the mean diameter are much smaller than the magnitudes of the compressive stresses on larger CNTs. While it has been assumed that CNT-CNT contacts are rigid (i.e., no slip), the propensity for slip will be determined by the complex and interdependent relationship between the deformation of the CNTs and the resultant force. The CNT diameter will influence the axial force, deflection, and the strength of the coupling due to van der Waals forces. These are expected to vary rapidly, and cyclically, as growth proceeds; therefore, in what follows as attempt is made to build a generalized picture of how forces may influence growth, regardless of the time-dependent trends that may exist and depend on the exact CNT dimensions, morphology, and growth conditions.

5.5. Discussion

The competition between the elastic properties of CNTs and their adhesion have recently been studied with respect to the deformation of CNT forests under mechanical compression[182-184] and the mechanics of CNT yarn spinning.[46] However, the effects of this energetic competition on CNT growth behavior has not been previously discussed or modeled mathematically. Despite the highly complex nature

of the mechanical/chemical coupling among simultaneously growing CNTs in proximity, the simplified mechanical model presented herein captures the dynamicity of axial forces and successfully derives a relationship between mechanical forces, CNT density, and alignment (Figure 63).

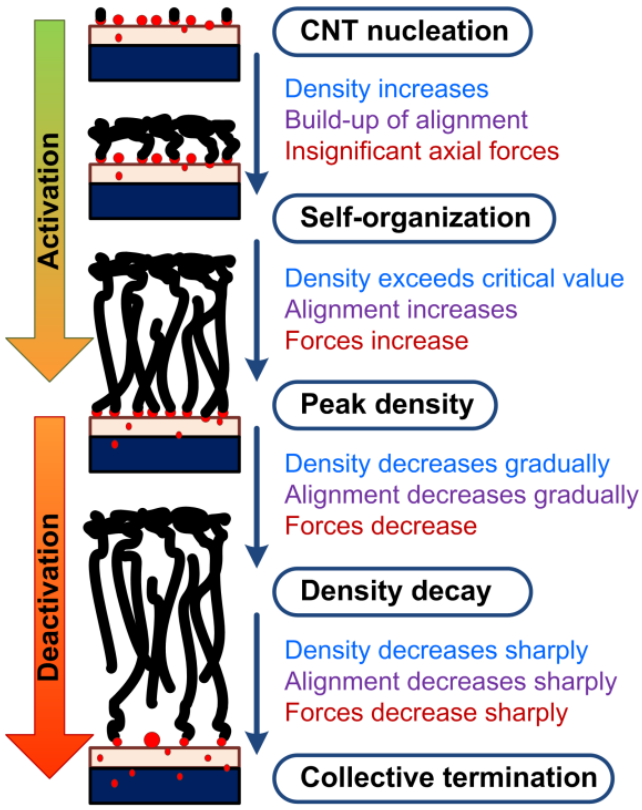

Figure 63. Schematic of the successive stages of CNT forest growth showing the evolution of density, alignment and forces along with the competition between CNT activation and deactivation, starting with CNT nucleation and ending with collective growth self-termination.

The finding in this chapter that significant forces exist due to mechanical competition among differentially-growing CNTs has several implications for understanding CNT forest growth, which are discussed in this section. While the description below relies largely on qualitative interpretation of findings, it is hoped that it provides a more complete framework for interpreting the complex population behaviour of CNT forest growth, and for designing quantitative studies of mechanical influences on CNT growth behaviour in the future.

CNT population growth dynamics

A perspective on the evolution of mechanical forces during CNT growth complements the existing picture of CNT population dynamics. As shown previously in chapters 2 and 3,[35, 36] the CVD process starts with CNT nucleation, followed by continued activation of nanoparticles until the seeded CNTs are dense enough to self-organize into the vertically aligned forest morphology. This is dependent on the attainment of the critical density for CNT self-organization, indicated in Figure 59e. The initiation of CNT-CNT contact due to crowding, which is necessary for self-organization, also represents the initiation of force transmission between CNTs that grow at different rates due to the polydispersity of the population. As self-organization proceeds, and nucleation of new CNTs continues, the density and alignment (i.e., orientation factor) of the CNTs increase. According to the geometric interpretation of force transmission, this crowding stage is accompanied by an increase in the magnitude of axial forces exerted on each CNT.

Later, a peak density is reached; and, because the peak density is coincident with the highest alignment, the force is also highest at this instant. After this, the catalytic deactivation kinetics overcomes the activation kinetics, leading to a decrease in density, a loss of alignment and decay in axial forces, until eventual termination of forest growth when the density falls below the critical threshold for self-alignment. It is important to emphasize that the rate of force increase would be related to the rate of crowding (density increase) at the start of the growth process. In other words, if the nucleation of CNTs is uniform and CNT crowding is rapid, the maximum force will be reached almost instantaneously as a result of the abrupt increase in density and alignment.

Figure 60 and Figure 62 illustrate the spatiotemporal evolution forces and stresses during this coordinated process; and Figure 63 places this information into the collective picture of CNT population growth. Importantly, CNT-CNT interactions are necessary for self-organization of CNTs at low density, and may be detrimental to the growth process due to the significant loads exerted on the catalyst nanoparticles. These loads not only cause the typical kinking morphology observed from transmission electron microscopy (TEM) imaging (Figure 64) of as-grown CNTs, but they may also instigate catalytic deactivation as explained below. The magnitudes of these forces and stresses will depend on the exact relationship between CNT diameter, growth rate, and other process conditions, including the

strength of the mechanical coupling. Nevertheless, our current force estimates are already several orders of magnitude larger than the weight of CNTs (Figure 65).

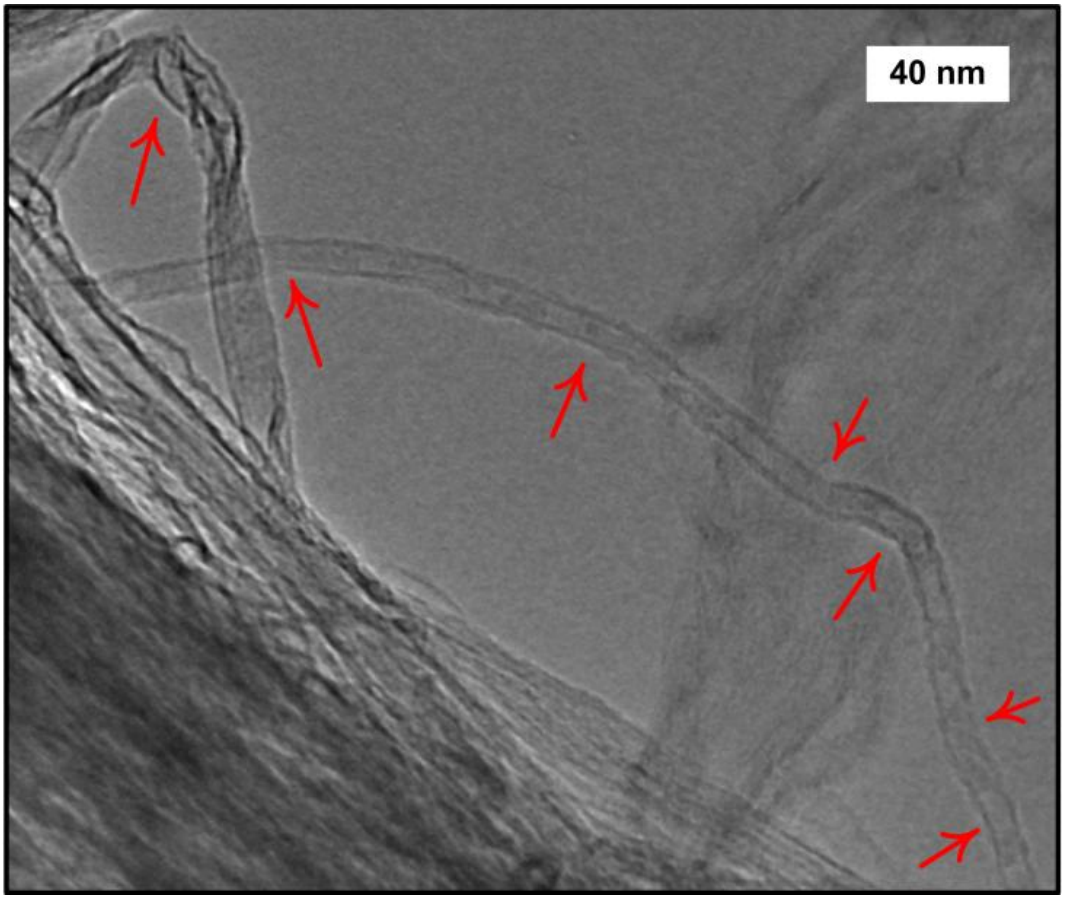

Figure 64. TEM image of a CNT from the same forest studied in this paper; arrows indicate flaws arising from mechanical forces during growth.

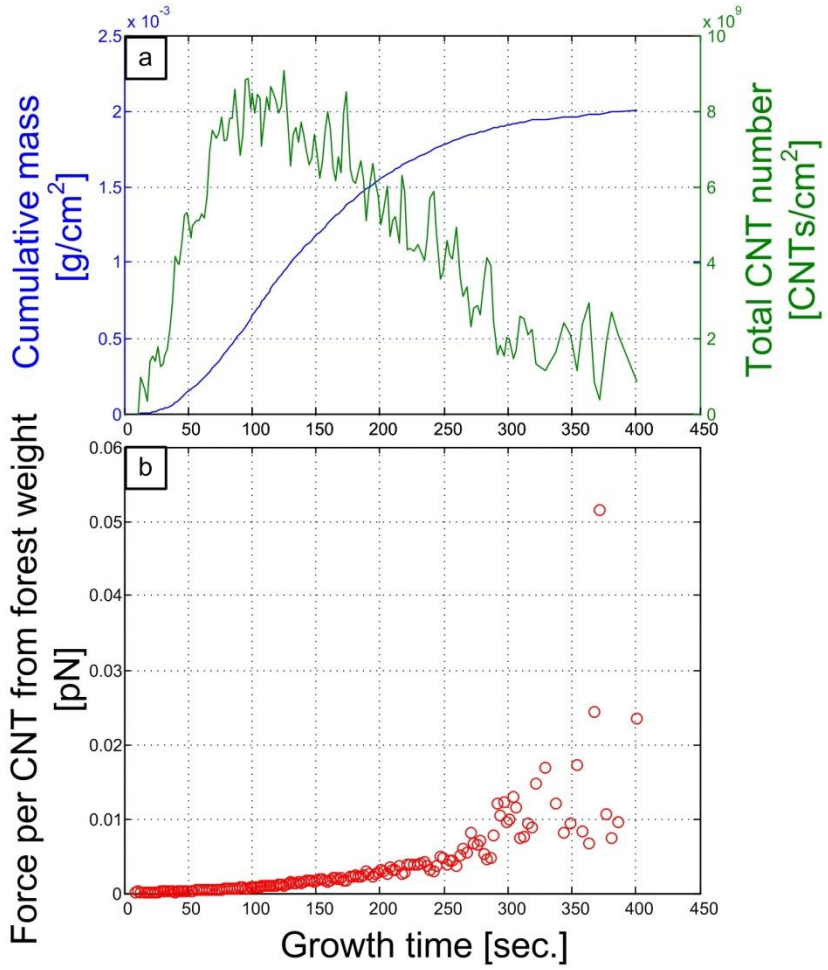

Figure 65. (A) Time evolution if the cumulative forest mass and total CNT number density. (B) Force per CNT from forest weight calculated by dividing the blue curve by the green curve.

Mechanochemistry of CNT growth

There is emerging precedence regarding mechanical effects on chemical reactions because displacing atoms from their equilibrium position alters the potential energy landscape.[185, 186] Recent and ongoing work focuses on "covalent

mechanochemistry",[187] as it was shown that mechanical forces can bias reaction pathways in polymeric materials,[188-190] as well as activate catalytic reactions.[191] Enhanced crystal growth rates were also reported for solid phase epitaxial growth (SPEG) of B_2O_3,[192] Si,[193] and Ge[193] crystals under applied hydrostatic pressure.

Therefore, it is hypothesized here that the forces exerted on the substrate-bound catalyst particles can influence the growth rate and structural quality of CNTs. Along these lines, a previous study showed that application of a static force (by placing a weight on top of the catalyst before the CVD process began) to a CNT forest decreased the growth rate.[153] Moreover, the highest loads caused the CNTs to adopt a corrugated arrangement with a very high density of defects. However, the force exerted by each CNT to balance the applied compressive weight was calculated to be significantly less than the force needed to deform (i.e., buckle) CNTs after growth, and was also significantly less than the equivalent activation energy of carbon diffusion on the catalyst. Therefore, relatively small forces could influence the quality of growing CNTs, by activating defect formation mechanisms that allow the CNTs to deform in response to the applied forces.

Importantly, the growth rate mismatch discussed in this chapter shows that high forces are intrinsic in a normal CNT growth process. Forces can shift the energetic barriers in the CVD process. Hence, ensuing mechanical loads could be affecting the growth rate, i.e. the stresses at catalyst-CNT interface could raise or reduce the interfacial chemical potential difference, leading to variations in activation energies.

This variation of activation energy could partially homogenize the growth rates among CNTs with different diameters, i.e. larger CNTs having fast growth rates would have their activation energy raised to reduce the growth rate to a value closer to the collective rate. This mechanism could be acting like a feedback system that spontaneously reduces the mismatch of growth rates, while in turn creating defects and bends in CNTs to accommodate for the applied forces. Moreover, the dynamicity of forces, and force-modulated activation energies, in concert with the physical configuration of the CNTs held together by VDW forces, is the source of the highly tangled hierarchical morphology of the forest. The potential effects of mechanical coupling on the CVD process, which may result in modulation of CNT growth rate, quality, and/or diameter, are not considered in the present model, but this is subject of ongoing research by the author and his colleagues.

Forces may also influence termination of growth. Previously, a mechanochemical model of growth termination was proposed, which considered the stiffness of "springs" connecting the top surface of neighboring CNTs that are assumed to be all straight and sliding with respect to one another.[147] This model states that the effects of mechanical coupling are digital, e.g., a force above threshold causes termination. However, the author believes that the origin of the abrupt termination is the density decay below the threshold density necessary for maintaining a self-supporting structure.[36] Work in this dissertation demonstrates

that this density decay is gradual, and that the deactivation starts long before the apparent sudden growth cessation.[35]

The importance of forces throughout the growth process is supported by the previously mentioned observation that taller CNT forests grown at the same growth recipe tend to have a lower density (Figure 29 in chapter 2).[35] This inverse relationship indicates that the denser forests terminated faster than less dense ones, for the same growth conditions. This hypothesis is also supported by the previous findings of diameter-dependent lifetime wherein larger diameter CNTs were shown to have shorter lifetime (Figure 41 in chapter 3).[124] This agrees with the finding in this chapter that larger diameter CNTs experience higher forces.

Reflection on model assumptions

In future work, the nanomechanical model presented herein can be improved to represent a more realistic picture of both the individual CNT and collective CNT growth processes. For example, in this study a mathematical treatment of the growth rate dependence on CNT diameter was adopted. This treatment is based on a model by Puretzky *et al.* that describes the physico-chemical processes involved in the growth of an individual CNT from an individual catalyst nanoparticle.[49] Although various models have been proposed in literature to mathematically describe growth, the main findings of the mechanical model developed in this chapter would not change had a different equation been used to describe the

diameter dependence of growth rate. Moreover, because diameter affects the CNT growth rate, additional insight could arise if the constants in this model used to describe surface processes such as chemisorption and diffusion, are replaced with diameter dependent relationships instead of constants. In addition, the mathematical description of the geometry and dimensions for the curved portions of CNTs can be rendered more realistic by resolving the possible diameter dependent tortuosity within forests using more in-depth SAXS analysis. Instead, a single value of average orientation is used now to represent all CNTs within a thin slice of the forest at a specific point in time. These are all areas of continued investigation that are beyond the scope of this dissertation .

Implications for high-performance CNT materials

Importantly, the lack of understanding of how CNT-CNT interactions affect collective growth may be a reason why the bulk properties of well-organized CNT assemblies are significantly less than predictions based on scaling of the properties of individual CNTs. For example, theory and measurements of CNT thermal and electrical conductivities show exceptional values;[20, 194, 195] however measurements of CNT assemblies such as forests remain 1-2 orders of magnitude lower, even when normalized according to volume fraction.[9, 196] Thus, it is hypothesized here that CNT-CNT interactions during growth, in combination with size-dependent catalytic activity, lead to mechanical stresses that limit the collective growth process and influence the hierarchical structure and functional properties of the final assembly.

Because the root-cause for these loads and stresses is the mismatch of diameter-dependent growth rates, a strategy toward growth of mutually dense and high-quality is to engineer catalyst populations that are monodisperse in size and shape, in order to reduce the mismatch in growth rates within the growing CNT population. Understanding how mechanical forces govern CNT properties may enable the design and fabrication of electrical and thermal interfaces having significantly improved properties.

5.6. Conclusions

This chapter investigates the discrepancy between the coordinated nature of CNT growth into a self-supporting forest morphology, which dictates that the whole forest structure grows at the same rate, and the diameter-dependent growth rate expected from individual CNTs. This growth rate mismatch leads to significant mechanical stresses on individual CNTs that are coupled due to van der Waals forces at contact points. Spatiotemporal mapping of these forces correlates with the successive stages of CNT forest growth, indicating that the maximum density achieved in a forest may be limited by the axial forces acting on the CNT-catalyst interface. Moreover, it is possible that these loads can influence the kinetics and perfection of individual CNTs; it is therefore concluded that mechanical coupling not only enables self-organized CNT growth, but also contributed to the origin of tortuosity and defects typically observed in CNT forests. Consideration of both mechanical and chemical effects is essential to improving the coordinated growth of

CNTs, such as to achieve highly uniform diameter distributions, and ultra-dense forests comprising high quality CNTs.

CHAPTER 6: FORCE-MODULATED CHEMICAL VAPOR DEPOSITION OF CARBON NANOTUBES

6.1. Summary

This chapter builds on the previously demonstrated importance of mechanical coupling among CNTs on the CVD growth process of CNTs. In this chapter, a custom-built CVD reactor is used to apply forces to CNT micropillars during growth. Using this cold wall reactor, experiments are performed where a controlled force in the 0.08 - 0.7 gram range (0.8 mN - 70 mN) is applied to CNTs growing on a heated substrate through a contact probe. The growth kinetics are measured in real-time by matching the forest height increase using a feedback loop controlled actuator that moves the probe vertically upwards to maintain a constant force during growth. Results show that a mechanical force influences the growth kinetics, and that the maximum growth rate is inversely related to applied force. These findings highlight the importance of studying mechanochemistry of CVD, in which the process activation energy at the catalyst is modulated by the compressive/tensile load acting on it. Collectively, this results in an internal feedback within the growing forest, wherein the kinetics of CNTs subjected to compressive forces is slowed down, while the kinetics of those CNTs subjected to tensile loads is accelerated. This homogenizing effect on the growth rate mismatch, eventually leads to reducing

the growth rate mismatch and contribute towards the coordinated forest growth at a single collective growth rate.

6.2. Introduction and Literature Review

Literature abounds with various examples, in which chemical reactions are shown to be influenced by mechanical loads acting on the reacting surfaces/volumes. Among those examples is the ongoing work focuses on "covalent mechanochemistry",[187, 197] wherein mechanical forces have been shown to bias reaction pathways in polymeric materials,[188-190] as well as activate catalytic reactions.[191] As in the case of electrochemistry and photochemistry, in which chemical reactions are activated by means of supplying electric energy, similarly mechanochemistry refers to those reactions which are activated by mechanical energy.

Physical processes such as diffusion, in which atoms are displaced/reorganized, have also been shown to respond to mechanical loads. For instance, hydrostatic pressure was shown to modulate the growth rates in solid phase epitaxial growth (SPEG) of B_2O_3,[192] Si,[193] and Ge[193] crystals. At the atomic scale, this can be explained by the alteration of the potential energy landscape, which result from displacing atoms from their equilibrium position by force.[185, 186] Hence, such physico-chemical process that make up the CVD growth of CNTs is likely to be also affected by mechanical forces.

Previous work on carbon nanotube growth under mechanical pressure has studied the effect of applying a static compressive force on CNT growth by CVD, simply by placing a weight on top of the catalyst before the CVD process began (Figure 66).[153] That study showed that the growth rate of CNT forests decreased with applying the compressive force. This decrease started at a pressure of about 400 N/m^2, until the final forest height reached about tenth of its initial height at a pressure of 60 000 N/m^2. At the highest loads, it was observed that CNTs that grow under pressure were more structurally defective and corrugated.

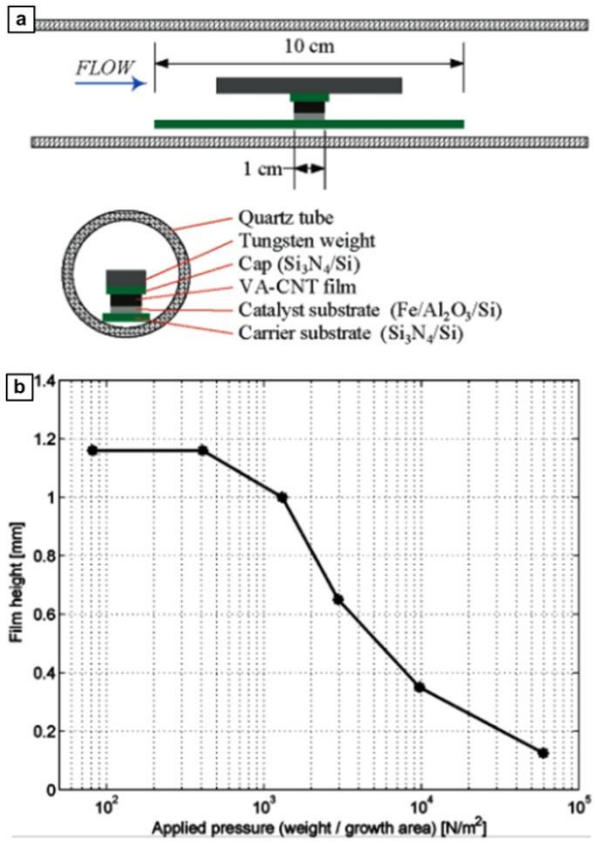

Figure 66. (a) Schematic showing the experimental setup for the growth under load from a previous study. Adapted from reference [153].

As was shown in the previous chapter, a significant mismatch exists between the diameter-dependent growth rate of each CNT in a large population and the homogenized rate of collected forest height increase.[170] As a result of this mismatch mechanical loads ensue, wherein CNTs that are growing at a rate slower than the collective forest height increase are subjected to tensile forces, while those CNTs that are growing at a rate faster than the collective height kinetics are subjected to compressive forces. Hence, intrinsic mechanical forces are transmitted through the tangled forest morphology down to the CNT-catalyst interface at each growth CNT. These diameter-dependent forces acting at the catalyst nanoparticles are likely to shift the reaction kinetics towards either acceleration or deceleration, depending on whether the force is tensile or compressive. Hence, the key towards overcoming the challenges that currently face the manufacturing of tailored CNT forests having uniform morphology lies in understanding the effect of mechanical forces on CNT growth. This understanding will pave the way for controlling the performance of CNT-based structures and devices.[18]

Despite these previous findings hinting at the importance of external/internal mechanical forces on the CVD growth behavior of VACNT forests, *in situ* studies of CNT growth under mechanical stimulation have not been carried out before. This can be attributed to the lack of CVD reactors that enable this and the need for designing and building specialized instruments with such capabilities. In this chapter,

a custom-built CVD reactor is described, which enables experimentally varying compressive loads on growing CNTs, while recording the height kinetics in real-time.

6.3. CVD System for Mechanically-Controlled CNT Growth

A new cold-wall CVD reactor was designed and fabricated to enables *in situ* mechanical manipulation of growing CNTs, shown in Figure 67. The design, construction, and installation of this system was a group effort in which the author contributed with colleagues (J. Beroz, K. Teichert, T. Serbowicz, and others) towards various aspects of the design. However, all the experiments and the data analysis were carried out by the author of this thesis. The system is composed of three main modules: the manipulator tower, the reaction chamber and the substrate stage.

Module 1 (the manipulator tower) comprises a linear motion system, coupled to a flat probe that gets in contact with the growing CNTs, by means of a load cell. The linear motion system consists of a central shaft which is actuated vertically by a voice coil motor and constrained by a pair of flexure bearings (Figure 67). Position and velocity of the shaft are controlled via a closed loop feedback control based on readings from the optical encoder. This design allows frictionless translation of the shaft, which enables very smooth motion with 20 nm resolution.

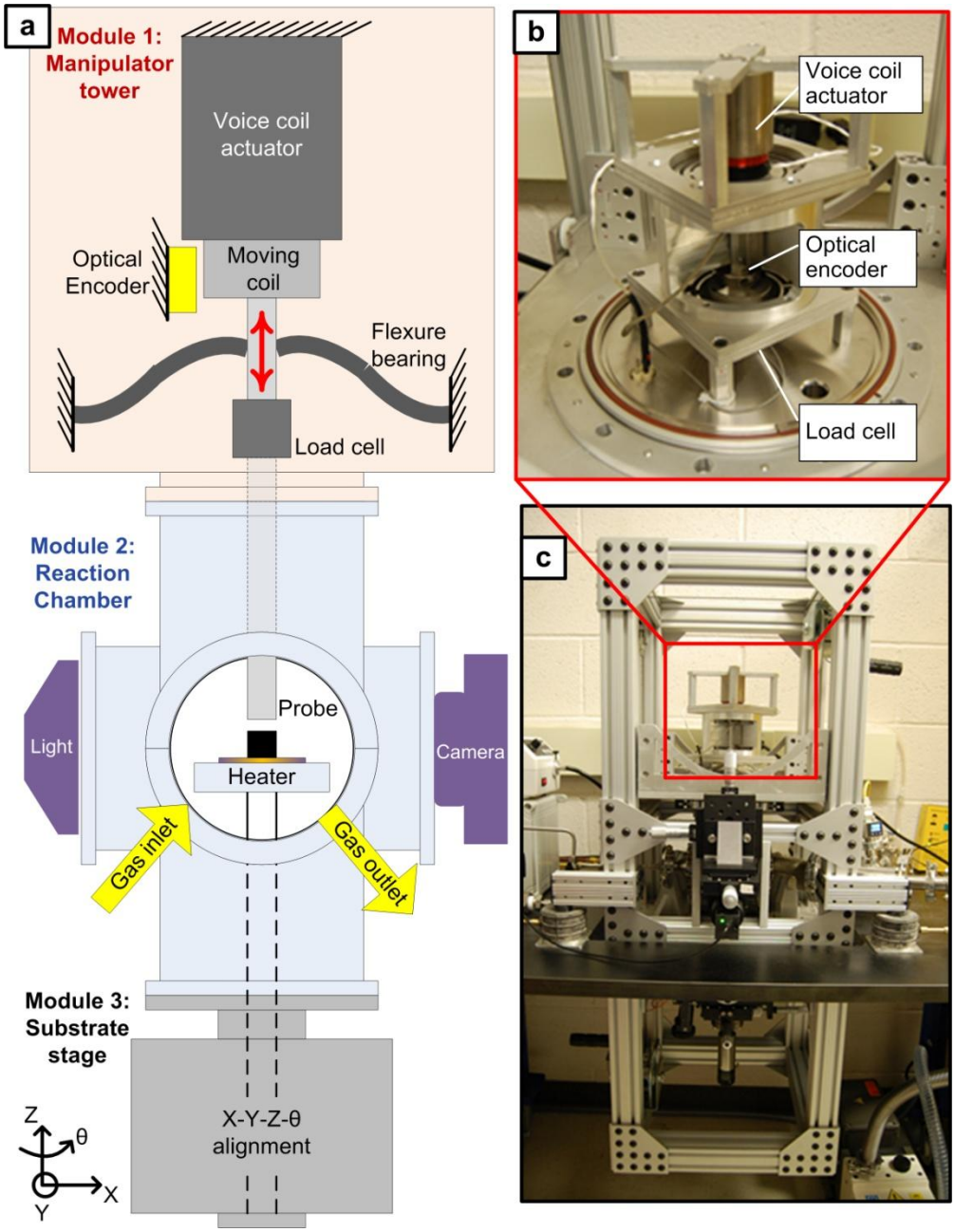

Figure 67. (a) Schematic of the CVD system for *in situ* growth manipulation: (b) a photograph of the manipulator tower. (c) a photograph of the complete system.

The two linear flexure bearings have been designed to be compliant only in the vertical direction and stiff along the other 5 degrees of freedom. Principles of symmetry have been employed to allow vertical displacement without parasitic rotation. Flexure beam dimensions have been optimized to provide a force-displacement curve tailored to the voice-coil actuator and to the strain limits of the flexure bearing material.

Module 2 (the reaction chamber) consists of a six-port cross, for which the top flange is connected to the tower system (Module 1), the bottom flange is connecter to the lower substrate stage (Module 3), and the four flanges whose axes lie on the horizontal plane are connected as follows. Two opposing flanges are connected to the gas plumbing for the inlet line (coming from the mass flow controllers), and for the outlet line (going to the exhaust), respectively. The other two opposing flanges however, are fitted with transparent windows, in such a way that a light source is mounted on one side and a camera is mounted on the other side for *in situ* viewing of CNT growth.

Module 3 (the substrate stage) consists of a heater platform mounted on a four degree-of-freedom (X-Y-Z-θ) alignment stage, as shown in Figure 67. The resistive heater system is mounted on a translation/rotation alignment stage. The resistive heater is made of Inconel, which is an oxidation and corrosion resistant alloy that has better resistance to thermal shocks as compared to ceramic heaters, although a ceramic heater was also used for some experiments. This heater is shielded and has

an integrated K-type thermocouple 0.05" away from the substrate for temperature measurement. The sample is then placed on the heater and held in place by three clips. This heater has a maximum operating temperature of about 850-1200°C in a reactive environment. The four degree-of-freedom (4-DOF) motion stage provides means for alignment of CNT pillar to the required position and/or orientation with respect to the manipulator probe. The heater assembly is supported by a rod that is coupled to a rotary feed-through shaft, an X-Y-Z manipulator is mounted in-series between the 6-way cross and the rotary feed-through.

6.4. Results

The system was used to perform experiments of mechanically controlled CNT growth. Before starting the experiment, the catalyst-coated Si wafer sample is loaded onto the stage, then the system is sealed, evacuated, and flushed with Helium 3 times. Next, the probe is actuated to come in contact with catalyst coated silicon chip (1 nm Fe / 10 nm Al_2O_3 / 300 nm SiO2 / 500 μm Si). A set point for the force is specified to the control system, and the actuator moves the probe towards the substrate until the compressive load is reached, as shown in Figure 68a. This load is maintained throughout the experiment. After that, the system is operated according to the recipe in Figure 68b. During the annealing step, the substrate is heated in an atmosphere of Hydrogen (H_2) and Helium (He), then temperature is held for 30 minutes. After that, the growth gases are introduced (100 sccm Ethylene and 10 sccm Acetylene) until growth termination

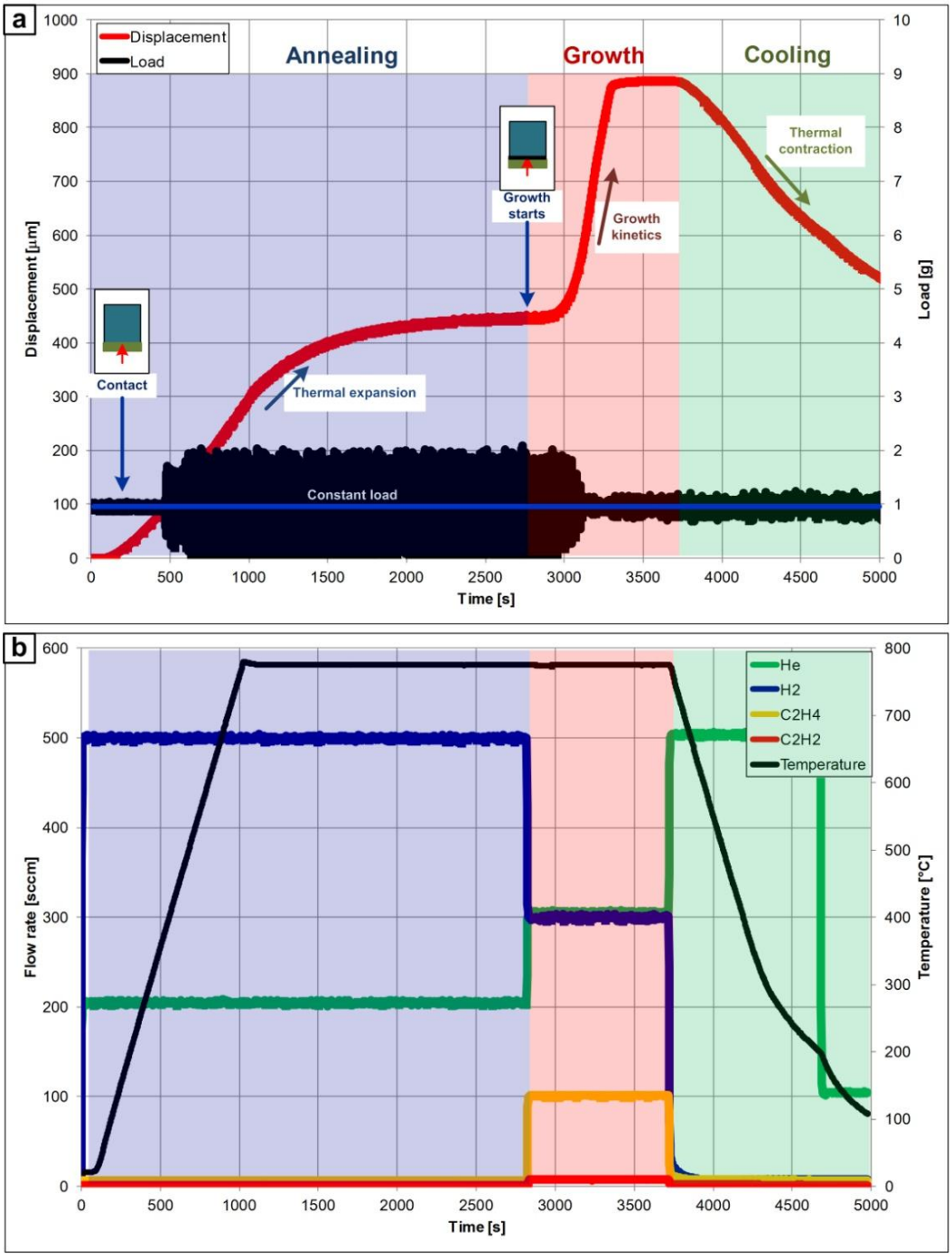

Figure 68. (a) Vertical displacement and load sensed by the probe during the experiment. (b) Growth recipe including gas flow rates and temperature.

The initial increase vertical displacement of the substrate that can be seen in Figure 68a results from the thermal expansion of the heater system components. Therefore it is necessary that growth gases are not introduced until this thermal-induced drifts are stabilized. It was found in these experiments that a 30 minute dwell time at the annealing conditions is enough to reach a steady state of thermal equilibrium.

After the 25 minutes, the displacement curve exhibits a plateau, so the hydrocarbon gas mixture of Ethylene (C_2H_4) and Acetylene (C_2H_2) is introduced after 30 minutes from the beginning of annealing. Following a brief delay period, CNTs start to grow, and push upward on the probe. Because the feedback control circuit is designed to maintain a constant static load on the substrate, a signal is sent to the actuator to move the probe upward in order to match the growth rate of CNTs. Hence, by monitoring the probe displacement under constant force, the real-time height kinetics of CNT forests growing under mechanical forces are obtained.

The same procedure is repeated several times while changing the magnitude of the static force setpoint to range from about 0.08 to 0.7 g (0.8 to 7 mN). The CNT growth kinetics under the applied force are measured in each case and is plotted in Figure 69. The pressure acting on the forest can be calculated by dividing these force figures by the cross-sectional area of the probe, to range from about 64 to 560 N/m^2. Assuming that the CNT number density is similar to the values of 5 x 10^9

CNTs/cm^2, which we obtained in chapter 2, and is constant throughout the forest, the average force per CNT is calculated to range from 1.3 to 11.1 pN/CNT.

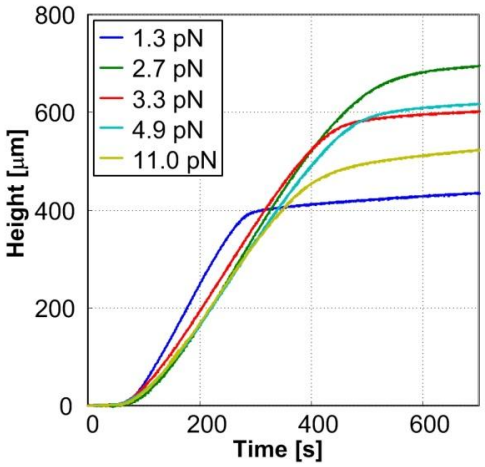

Figure 69. Forest height kinetics for different calculated forces per CNT.

Further analysis of the CNT forest height kinetics is provided by plotting the derivative to obtain the growth rate, as shown Figure 70. In these plots, a low-pass filter is used to remove high frequency noise. After that, a Gaussian equation (Eq. 6.1) is used to fit these results in order to quantify the force-induced changes to the reaction rates. As seen from the Gaussian equation, there are three fitting parameters: (a) is the maximum the height of the Gaussian peak, i.e., the maximum growth rate; (b) is the position of the peak, i.e. ,the point in time when growth rate reaches a maximum; and (c) is a measure of the peak width, i.e., the catalytic lifetime.

$$f(x) = a\left(e^{-\left(\frac{x-b}{c}\right)^2}\right) \qquad \text{Eq. 6.1}$$

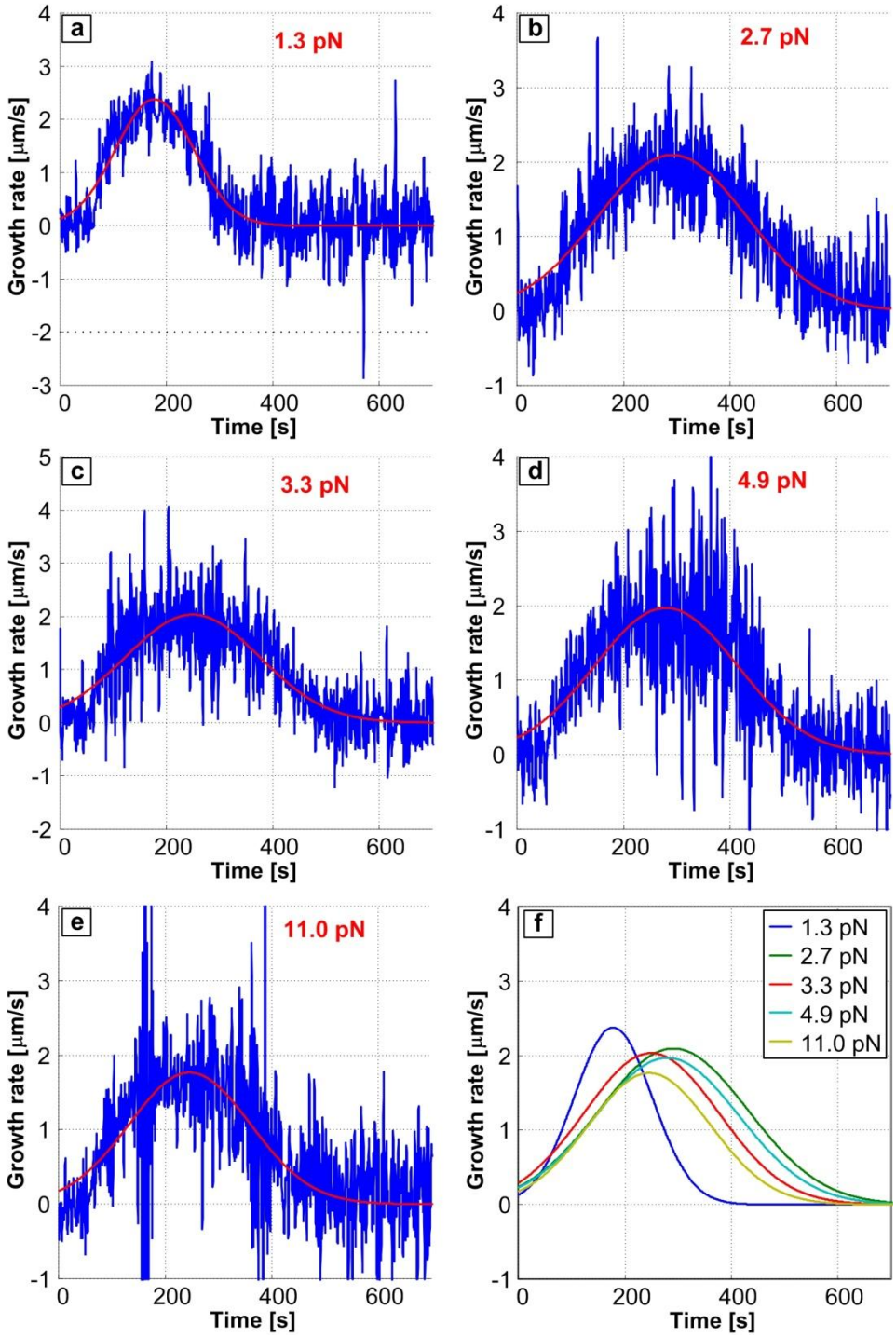

Figure 70. (a-e) Low-pass-filtered growth rates with Gaussian fit. (f) Superimposing all Gaussian fits for all forces.

The dependence of the Gaussian fitting parameters on normalized force is plotted in Figure 71. As seen in this figure, the fitting parameter a, which represents the maximum growth rate reached in each experiment, monotonically decreases as a function of the compressive force. On the other hand, the other two parameters b, which represents the point in time at which the maximum rate is reached, and c, which is a measure of peak broadness, both reach a maximum before decaying.

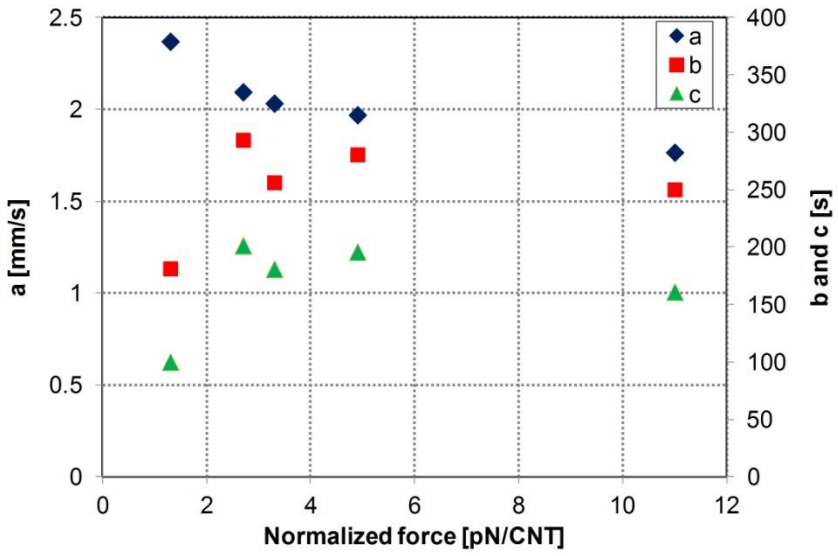

Figure 71. Dependence of Gaussian fit parameters on the normalized force.

In view of the small number of points and considering the typical run-to-run variations of growth, it is difficult to assign a mathematical description to the trends plotted in Figure 71. Nevertheless, a continued decrease of the maximum growth

rate as a function of compressive force was observed. This is consistent with other example from polymer mechanochemistry.[197]

6.5. Discussion

It was observed here that CNTs can exert significant forces, up to 15 pN each. This compares to the previous study by Hart and Slocum, cited in the introduction,[153] in which forces as high as 160 pN were measured. This discrepancy may be attributed to the variation of CNT density used to normalize the force values, or to differences between the growth system (hot wall vs. cold wall reactor), as well as to differences in growth recipe. In the current work, the probe is made of quartz, while a silicon chip was used to interface with the catalyst in the previous study.[153]

Owing to imperfection of the flatness of the probe, results have shown that a localized high pressure region exists in the center of the probe (Figure 72), which would affect the force distribution across the catalyst nanoparticles on the substrate. These results indicate that the localized central region stimulates the growth in this region, as compared to the global growth on the substrate. At this point, it is difficult to speculate whether this localized effect stems from the effect of mechanical pressure on particle formation/activation, or whether it is a gas flow effect. For future work, a flat probe design needs to be incorporated along with some accurate means of aligning the probe to the substrate.

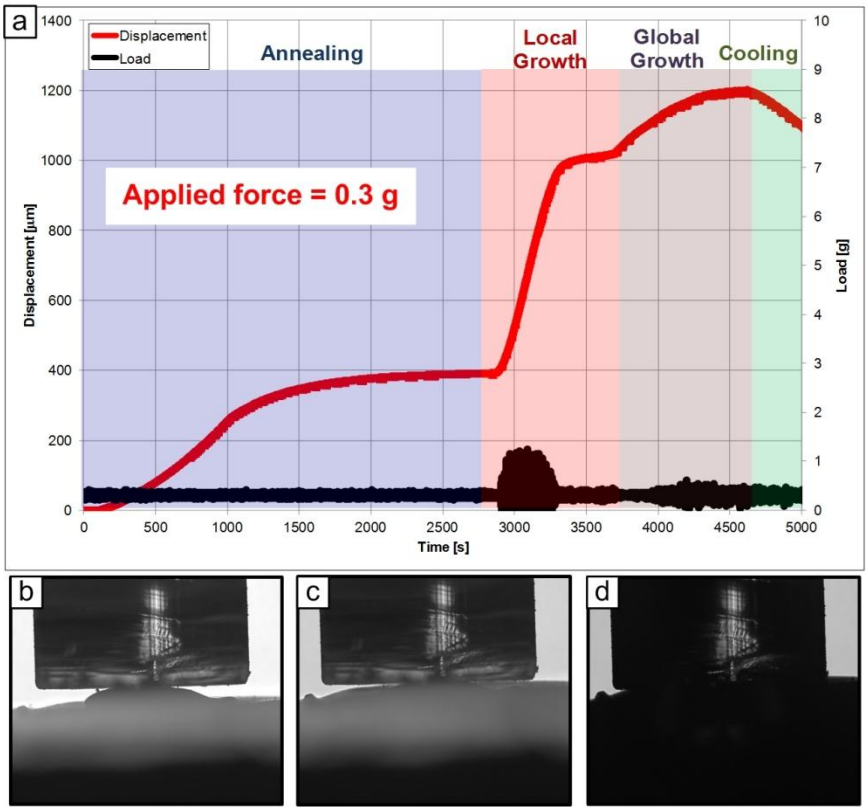

Figure 72. Effect of localized pressure under the probe on the growth kinetics.

As the probe is pushed by the CNTs, and the actuator moved upwards to match the forest growth kinetics, the gas flow between the probe and the substrate continuously changes, which certainly also affects the growth reaction at the catalyst. In order to mitigate this issue in the future, non-contact means of applying a force is needed, such as by means of electrostatic forces using an electrode hovering above the growth forest. In that case however, the growth kinetics needs also to be measured by a non-contact methods such as by using a capacitance proximity sensor.

Designs are currently underway to achieve this, and the author of this thesis will contribute towards that effort in the future.

In all the results shown in the chapter, the normalized force per CNT is calculated based on a number density of CNTs observed earlier in chapter 2 (10^9 CNT/scm^2), and it is also assumed that the density is the same for all the experiments, which is yet to be confirmed from further detailed studies.

Both in the results of this chapter, and previous work,[153] confirm that the force exerted by each CNT to balance the applied compressive weight is significantly less than the force needed to deform (i.e., buckle) CNTs after growth, and is also significantly less than the equivalent activation energy of carbon diffusion on the catalyst.[153] These forces are also smaller than the force needed to break a single covalent C – C bond, which was previously estimated to be 5-6 nN.[198] Hence, it is conclude here that although the applied forces are much smaller than those that would break covalent bonds, they can still shift the kinetics of the growth reaction, indicating mechanochemical behavior. Therefore, relatively small forces could influence both the quality of growing CNTs, by activating defect formation mechanisms, and the reaction kinetics by shifting the activation energy landscape.

Comparing the magnitudes of the normalized force per CNT to the calculated forces in the previous chapter, reveals that the simple mechanical coupling model grossly overestimated the force per CNT. This is explained here based on the

feedback mechanism within a growing CNT forest, in which the growth rate is locally modulated at each active catalyst nanoparticle based on the force transmitted to this particle. In other words, those CNTs that grow at a faster rate than the acollectve growth rate, or even locally faster than its neighbors, will be subjected to compressive forces, which leads to increasing the activation energy of growth and effectively slows down the growth rate of this particle. In contrast, if a CNT is growing at a rate that is slower than the collective rate, it is subjected to tension, which eventually leads to lowering the activation energy of growth and effectively accelerates the growth. This "feedback" scenario is expected to homogenize the growth rates within a growing forest, and would proceed until those forces reach a limit that would terminate the growth. Shows a schematic representation of the relationship between force and growth rate, but further research into mathematically modeling the mechanochemisty of such reaction are needed to reveal the nature of this relationship. For a certain threshold force, growth termination could proceed as a result of an energy barrier, as was previously proposed.[147] In the case of tensile stress, this termination mechanism could be detachment of CNTs from the seeding catalyst nanoparticles.

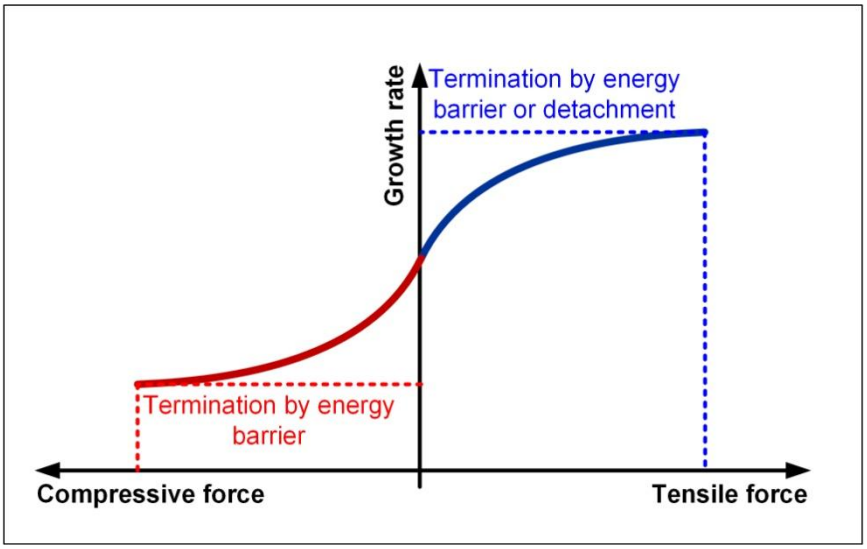

Figure 73. Schematic representation of the relationship between tensile/compressive force on the growth rate. The threshold forces on both sides represent the termination mechanisms when the force is too tensile or too compressive.

6.6. Conclusions

In this chapter, a custom-built CVD chamber was used to perform preliminary experiments to elucidate the effect of applying external forces to growing CNTs. Results show that although the applied forces are much smaller than the values for breaking covalent bonds, these values (1-11 pN) are enough to shift the reaction kinetics. In general, the maximum growth rate continuously decreased as a function of compressive force. These findings support the notion that CNT growth by CVD involves mechanochemical reactions that can be influenced by applying external mechanical energy. Further research into mathematically modeling the relationship between force and reaction rate is needed for building a comprehensive

understanding on the mechanical feedback within a growing CNT population, wherein growth rate is modulated at each growth CNT based on the force transmitted to the catalyst-CNT interface.

CHAPTER 7: IN-SITU TRANSMISSION ELECTRON MICROSCOPY OF CARBON NANOTUBE NUCLEATION AND SELF-ORGANIZATION

7.1. Summary

In previous chapters, it was shown that Synchrotron X-ray scattering and absorption can provide valuable quantitative information about the morphological evolution of carbon nanotubes (CNTs) within a forest. However, the initial stages of nanoparticle formation and CNT nucleation are more elusive and cannot be inferred directly from X-ray characterization. In this chapter, *in situ* and *operando* experimental studies of CNT growth are carried out inside an environmental transmission electron microscope (TEM). Real-time imaging of particle formation and CNT nucleation shows a characteristic S-shaped kinetics. Although further studies are needed to identify the differences between active nanoparticles and inactive nanoparticles, results show that inactive nanoparticles that do not bear CNTs are generally encapsulated inside a graphitic coating. *In situ* TEM images also show evidence of the pinning at contact between CNTs, where CNTs were observed to snap together to form a bundle when they are growing in proximity. As a results of this mechanical coupling, a pair of CNTs in contact shows evidence of mechanical competition, wherein one CNT is under compression, while the other CNTs in contact exhibit signs of tensile loading. Results in this chapter complement the

previously presented suite of characterization techniques employed to study CNT growth and will inform more accurate mechanical modeling of mechanical coupling among CNTs.

7.2. Introduction and Literature Review

In Chapters 2 and 3, small angle X-ray scattering (SAXS) was used to accurately map CNT diameter distribution and quantified alignment across growing forests. Also, X-ray mass attenuation was used to infer mass density evolution. However, when studying the activation percentage of the catalyst particles, *ex situ* Atomic Force Microcopy (AFM) was done post-annealing in order to count the number of particles that exists after dewetting of the thin catalyst film. By comparing this to the measured number of CNTs, the number of active catalyst particles (number of CNTs) was seen to increase during the initial crowding stage, and decay after than until self-termination (Figure 30). However, this information is obtained from converting the spatial density map to the time domain (using the real-time height kinetics). As a result, it does not provide information about the earliest stages of CNT growth, in which randomly-oriented CNT nucleate and grow to self-organize during the crowding stage. Moreover, the results in chapter 2 are only limited to information about the forest evolution after lift-off of the forest has already started. Another limitation of the X-ray method is the size of the X-ray beam, which was focused down to a 10 μm spot. Although this is very small when compared to the typical millimeter-scale overall forest height, it is about three orders of magnitude

larger than the size of the nanoparticles. Hence, information about the earliest stage of nucleation within a 100-1000 nm distance from the substrate is still largely missing.

To bridge this cap, grazing incidence small angle X-ray scattering (GI-SAXS) was previously used by researchers from Prof. A. John Hart's group at the University of Michigan (including the author) and Prof. Sol Gruner's group at Cornell University (Figure 74). This enabled studying the dynamics of particle dewetting and initial CNT nucleation/growth.[113] Results of that study revealed that when annealing in a He-H_2 atmosphere, the dynamics of particle formation are fairly sudden, even if the heating rate was slow. Another observation is that when heating the sample in the growth atmosphere (He + H2 + C_2H_4), the particle formation is also abrupt, with the emergence of some larger particles. Although GI-SAXS is very suited to studying the formation and size/shape evolution of nanoparticles, data analysis become more subtle once CNTs start growing because the scattering patterns collected on the 2D area detector represent both scattering from the C atoms and from Fe atoms. Owing to the difference in scattering cross-section between C is different from that of Fe, and because CNTs start to crowd at high densities quickly, the signal coming for the nanoparticles becomes very difficult to decouple from the carbon scattering signal. As a result, the CNT nucleation kinetics can only be qualitatively inferred from the time-evolution of the integrated scattering readings.

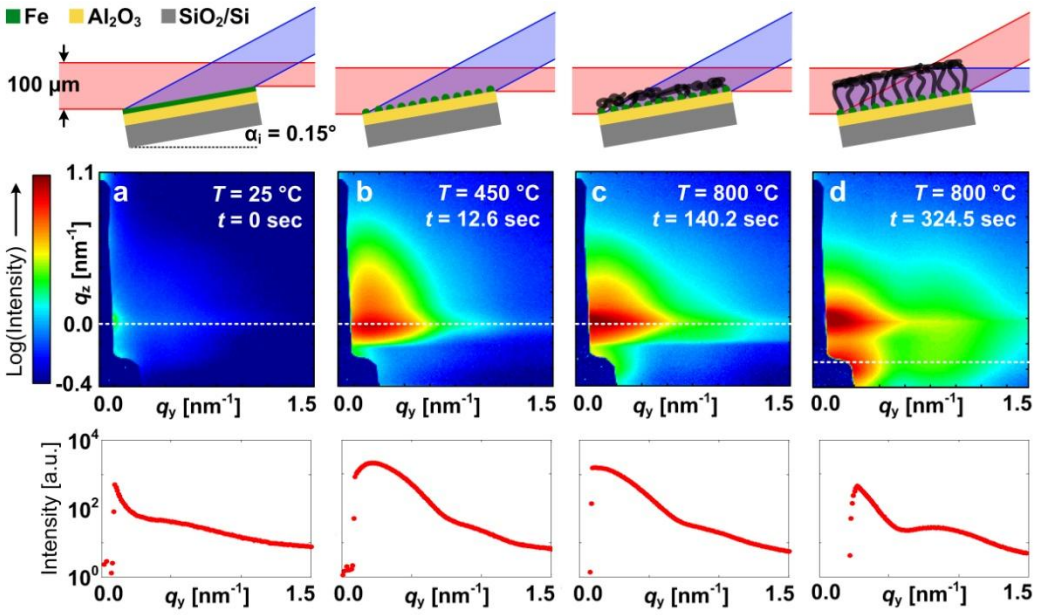

Figure 74. GI-SAXS results, showing the dynamics of thin-film dewetting into nanoparticles, followed by the nucleation and growth of CNTs.

Moreover, because X-ray characterization typically interrogate millions of particles/CNTs simultaneously, it is virtually impossible to get a clear picture of the mechanical coupling and the bundling behavior at the scale of individual CNTs. Thus, E-TEM studies of CNT growth would provide unprecedented insights into the early stages of nanoparticle formation, catalyst activation and CNT nucleation.

Although there are examples in literature of *in situ* E-TEM studies of CNT growth, those have focused on revealing the growth kinetics of individually growing CNTs,[89] and have not been applied to study the collective growth of a small population of CNTs growing in proximity. In this chapter, *in situ* E-TEM

characterization of small populations of growing CNTs is presented. Results show that the kinetics particle formation upon introducing the hydrocarbon gas (C_2H_2) (number of particles versus time) exhibits S-shaped kinetics. This indicates that further reduction of the catalyst proceeds in the presence of C_2H_2. Results also showed the coupling-induced "snapping" of CNTs together to form bundles when they are growing in proximity, and showed evidence that some CNTs are subjected to tensile forces, while others are compressed.

7.3. Methods

The author designed and carried out experiments at the Center for Functional Nanopmaterials (CFN) at the Brookhaven National Laboratory (BNL), in collaboration with Dr. Eric Meshot (Lawrence Livermore National Laboratory), Dr. Dmitri Zakharov (Brookhaven National Laboratory) and Dr. Eric Stach (Electron Microscopy group leader at BNL). All experiments were carried out inside the FEI Titan 80-300, shown in Figure 75, which is a field-emission environmental transmission electron microscope (E-TEM) with an objective-lens aberration corrector. In all experiments, a 300 kV beam was used for imaging. With a spatial resolution of 0.08 nm, even at unusually high pressures, this system is ideal for *in situ* and *operando* studies of CNT growth from catalyst nanoparticles. Mass-flow of process gases can be controlled to provide accurate partial pressures. For this study, a partial pressure of 40 mtorr of Hydrogen (H_2) and 10 mtorr of Acetylene (C_2H_2) were selected. Sample annealing and growth temperatures were controlled by means

of single-tilt heating holder, operated at 750 °C. Before starting the growth experiments, a base pressure of below 10^{-5} torr was reached.

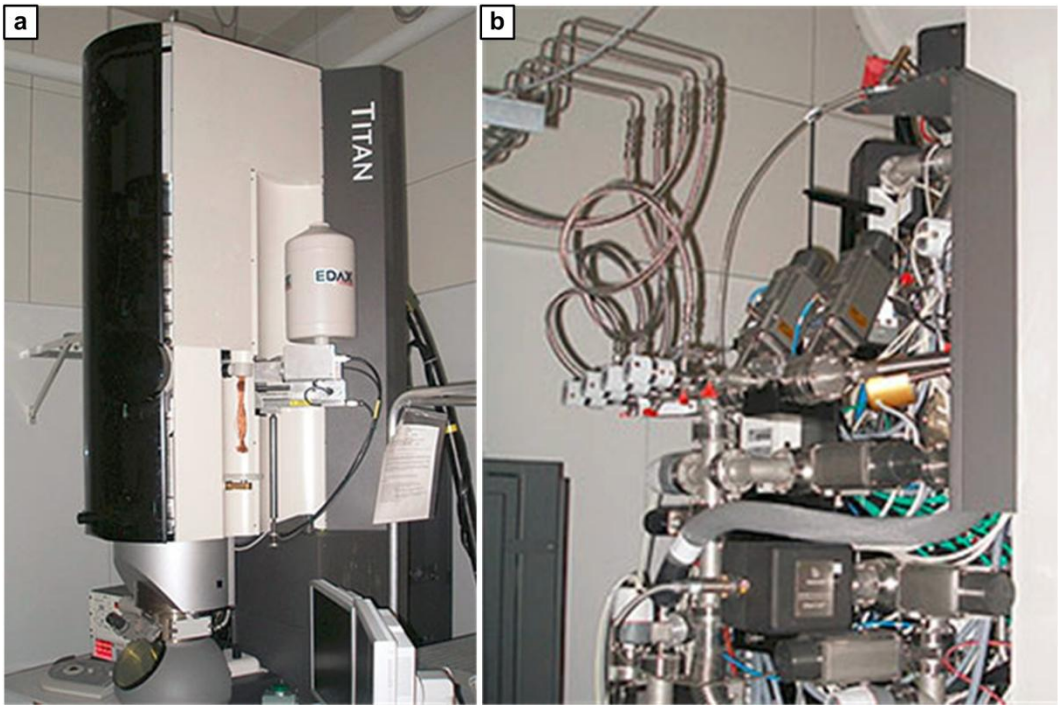

Figure 75. Titan E-TEM. (a) Image of the front of Titan with cover. (b) Image of the rear of Titan microscope showing the gas plumping [images from the BNL website http://www.bnl.gov].

Two types of 3 mm diameter TEM grids were used in this study (Norcada), as shown in Figure 76. The first is 30 nm thick membrane having an array of nine 100 x 100 μm windows. The other type of samples is the Holey grid samples that have an array of 2 μm diameter holes on a 200 nm thick membrane. In all cases,

samples have a silicon nitride membranes (Si_3N_4), with sputtered catalyst multilayer on it (1 nm Fe on top of 10 nm Al_2O_3).

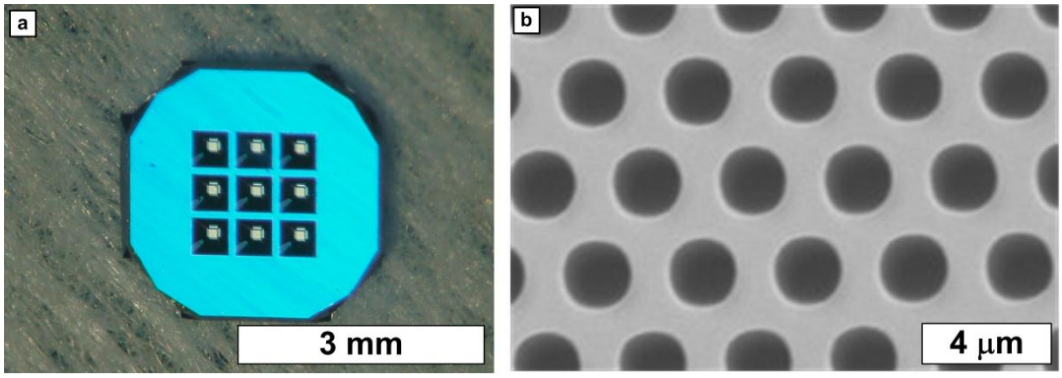

Figure 76. (a) 9 window TEM grids with 30 nm thick Si_3N_4 membranes. (b) Holey grid with 2 µm diameter holes in a 200 µm thick Si_3N_4 membrane (images from the Norcada website http://www.norcada.com].

The sample is first loaded inside the E-TEM reactor (Figure 77), and the temperature is raised to the 750 °C in 40 mtorr of H_2, at rate of 100 °C per minute. After waiting at this temperature for 15 minutes (to allow for the thermal stabilization of substrate and avoid sample drift during imaging), C_2H_2 is introduced so that the total pressure reaches 50 mtorr. This enables imaging during the initial nucleation stage that starts with introducing the hydrocarbon gas. Figure 78 shows a schematic of the catalyst annealing and growth steps. During annealing in the reducing environment (H_2), the thin catalyst film is reduced and breaks up into nanoparticles. Upon introducing the hydrocarbon gas (C_2H_2), nucleation and growth of CNTs proceeds until termination.

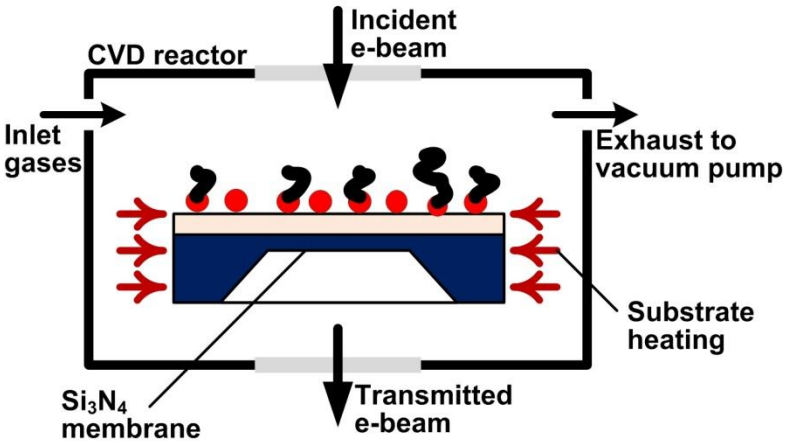

Figure 77. Schematic showing the CVD reactor inside E-TEM.

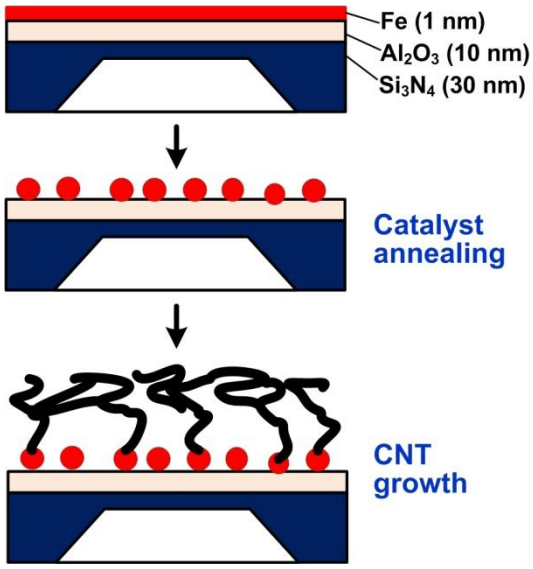

Figure 78. Schematic showing both the catalyst annealing step, in which the thin film catalyst layer is breaks up into nanoparticles, and the growth step, in which the hydrocarbon gas decomposes at the surface of the nanoparticles and then precipitates to form a growing CNTs.

7.4. Results and Discussion

The growth conditions are different from the typical growth conditions inside either a cold wall or hot wall reactors discussed in previous chapters. Both the composition of the gas atmosphere and the pressures, which are likely to shift the kinetics of the process and may explain the slower rates of particle evolution and CNT growth that are observed in previous work.[35, 113] Nevertheless, results in this chapter provide insights into various fundamental processes that are likely to be similar in all CVD reactors growing CNTs, such as particle formation by dewetting, CNT nucleation, and mechanical coupling/bundling.

7.4.1. Nucleation kinetics

Before introducing C_2H_2, some fully-formed nanoparticles were observed (see Figure 79). In this figure, time 0 is the point at which the hydrocarbon gas (C_2H_2) is introduced to the system. Results show that the introduction of C_2H_2 leads to the emergence of high contrast nanoparticles. The kinetics of this particle "popping" phenomenon were observed to follow an S-shaped curve, as seen in Figure 80. This behavior can be explained by the reducing effect of C_2H_2 on the catalyst layer that is likely to be not fully reduced by the 10 minute anneal in H_2. Figure 81 shows schematically how the annealing step in H_2 may leave a large portion of the catalyst not fully reduced, in the form of broken and flat islands, which are not very easily visible in the early images at such low magnification. It is also likely that small particles are also fully formed, but are too small to have significant contrast. The

effect of adding C_2H_2, not only facilitates the reduction of iron oxide into iron, but also greatly boosts the surface mobility of Fe atoms, and hence accelerates the particle formation (dewetting process).

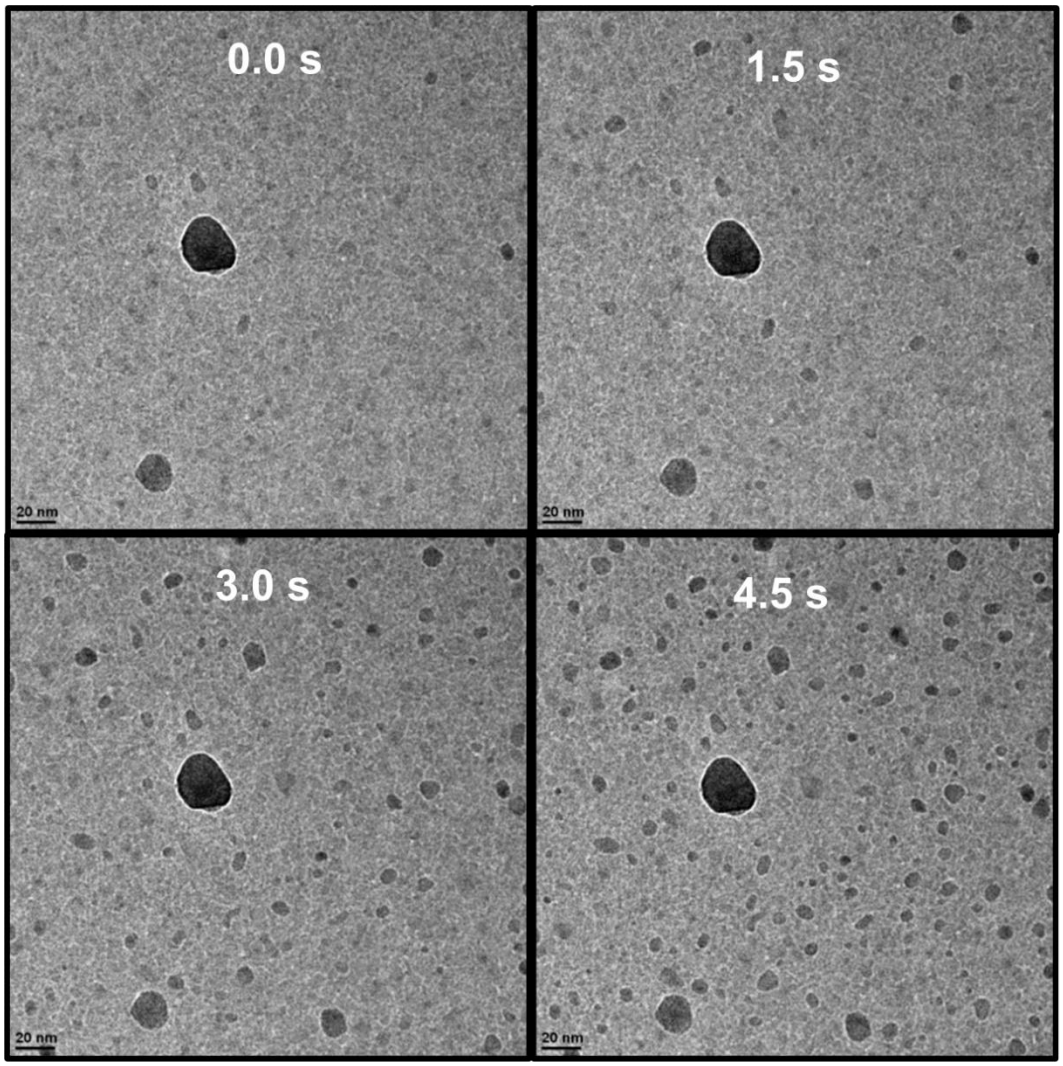

Figure 79. TEM images at different time-steps, showing the kinetics of particle formation upon introducing C_2H_2.

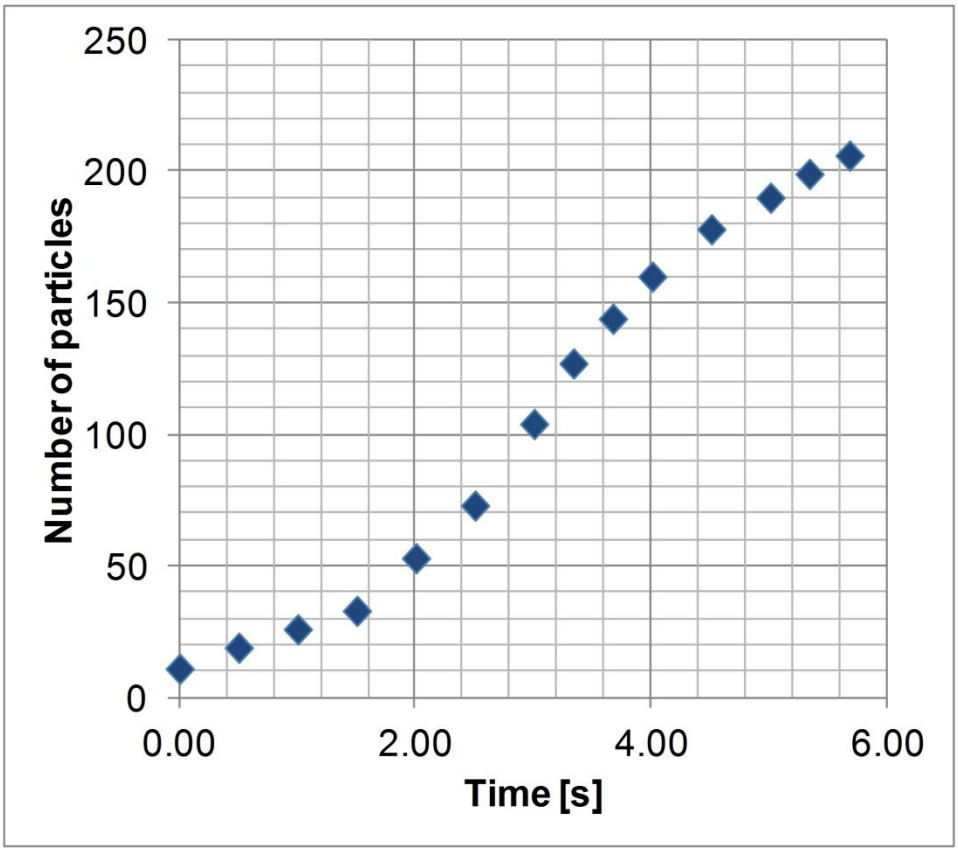

Figure 80. Kinetics of particle formation upon introducing C_2H_2.

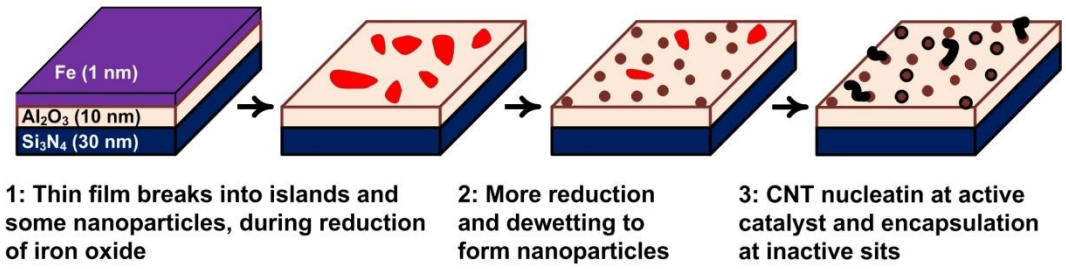

Figure 81. Interpretation of the nanoparticle popping kinetics that follow the introduction of C_2H_2 to the system.

Within 6 seconds, the particle "popping" dynamics have already reached a plateau, indicating that full reduction of iron oxide and complete dewetting has been accomplished. CNTs start to nucleate immediately after particles are formed.

As time proceeds, more randomly oriented CNTs nucleate and those that nucleated earlier gets longer, as seen in Figure 82, after 54 seconds of growth.

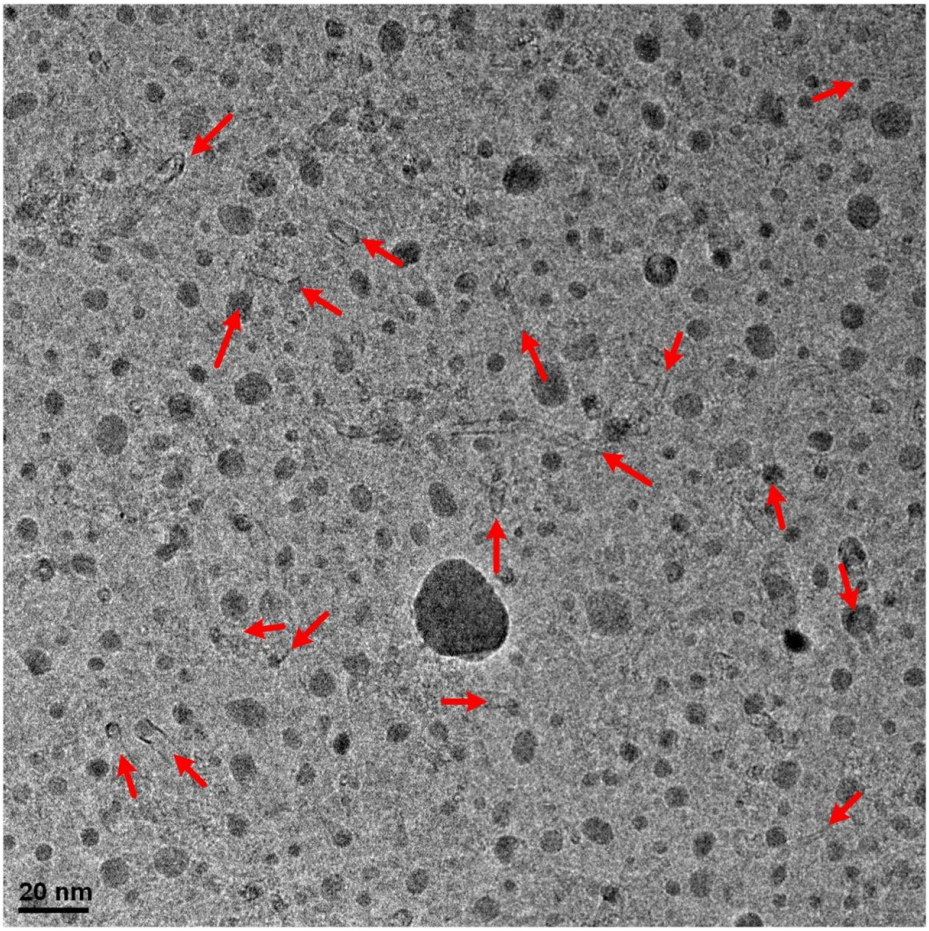

Figure 82. TEM image after 54 seconds from introducing C_2H_2., showing the increase in density of randomly oriented CNTs, with no evidence of alignment.

Further into the growth, the density of growing CNTs increases significantly, leading to crowding-induced self-organization into the vertical orientation, as seen below in Figure 83, after 5 minutes and 45 seconds of growth. The importance of this observation is that it confirms the collective model proposed in Figure 33.

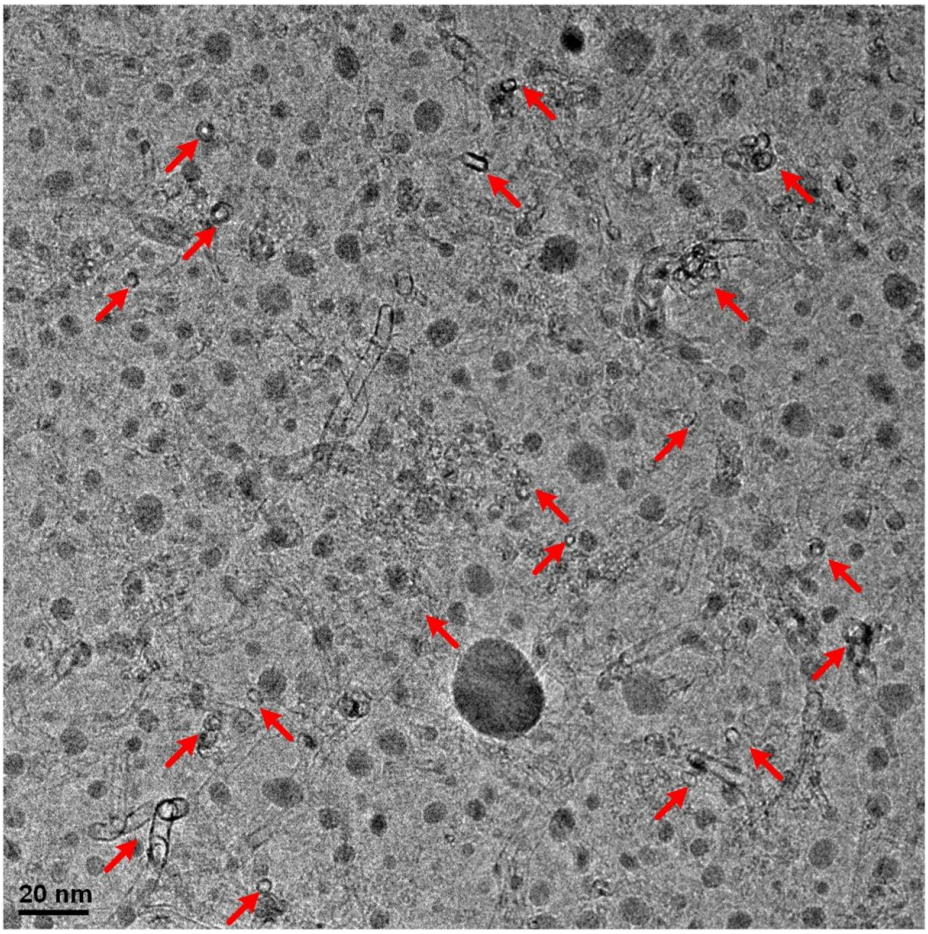

Figure 83. TEM image after 5 minutes and 45 seconds from introducing C_2H_2., showing further density increase accompanied by build-up of alignment, as evidenced by vertically pointing CNTs (pointing towards the line of sight).

Importantly, only a fraction of nanoparticles become active and bear CNTs, and by taking high magnification TEM images of inactive particles (after a few minutes of introducing C_2H_2), it was observed that they are typically encapsulated inside a graphitic overcoating layer, as seen in Figure 84. This provides insights into the deactivation mechanism that is dominant here.

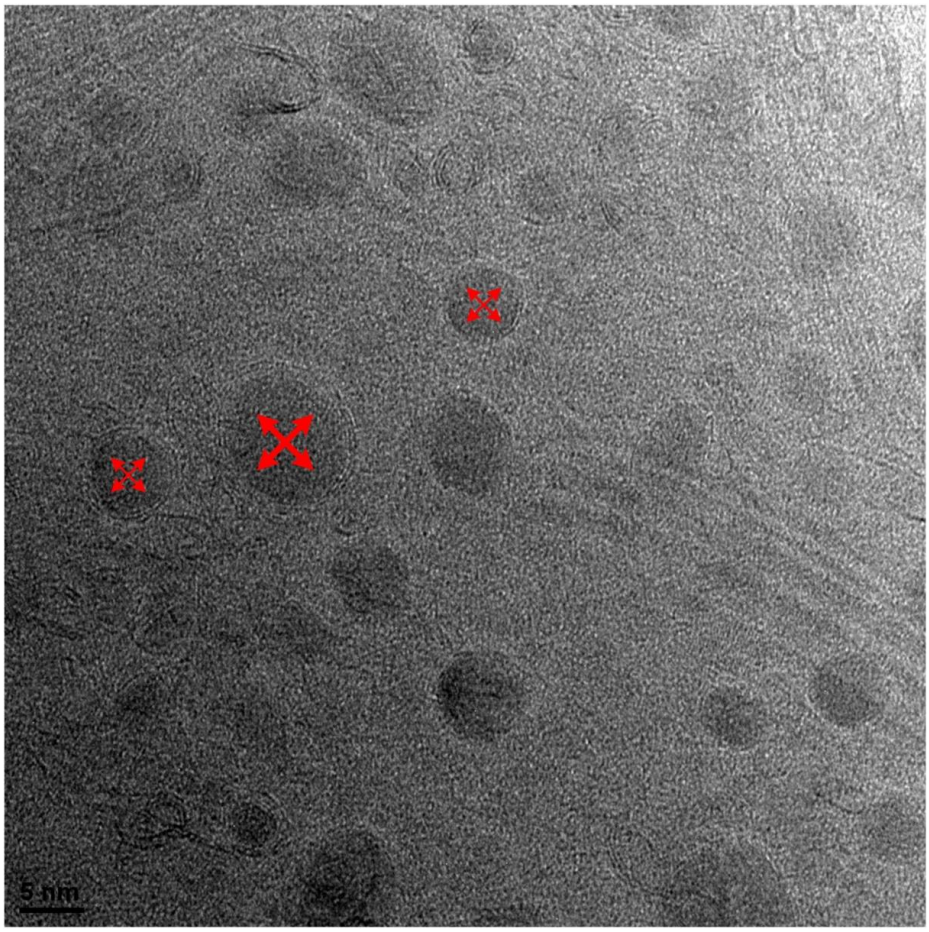

Figure 84. Higher magnification TEM image after 8 minutes and 9 seconds from introducing C_2H_2., showing that the inactive catalyst nanoparticles are generally encapsulated in graphitic overcoating.

It is worth noting here that as soon as particles popped, they either formed a cap that lifted into a growth CNT, or they became fully encapsulated with graphitic overcoating layers. As seen in Figure 85, iron-oxide planar islands form more spherical nanoparticles as a result of introducing C_2H_2. Those newly formed particles become either seeds for CNT growth (activation), or fully encapsulated by graphitic coating (deactivation). Further research is required to fully understand the critical factors controlling the fate of each nanoparticles. One hypothesis is that a certain phase is more active such as body-centered cubic metallic iron for instance, and by mere probabilistic chance, the nanoparticle population has a distribution of activity, owing to the polydispersity of sizes, shapes, and possible phases as well. It is also worth noting here that additives, such as oxidizing agents, have been proposed before to reactivate or prevent deactivation of catalytic nanoparticles by etching away the overcoating carbon.[37, 106]

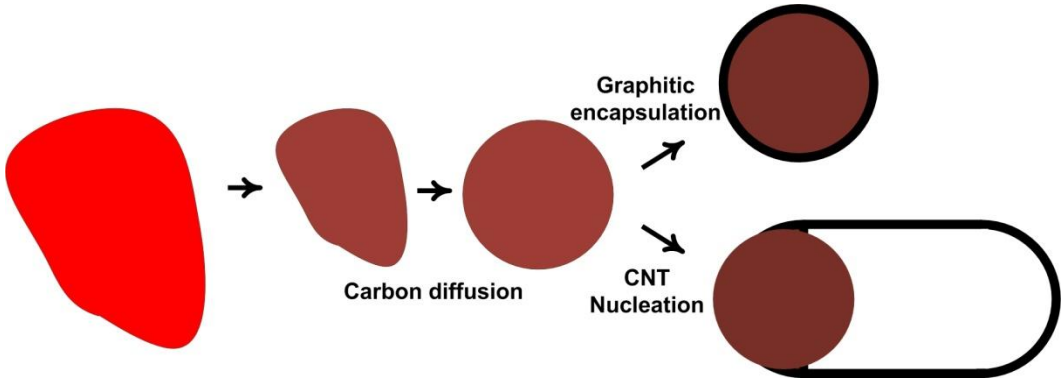

Figure 85. Schematic showing the reduction/dewetting that results from introducing C2H2 to the system, which is followed by a split path of activation vs. deactivation.

To further characterize the early stages of growth, a similar experiment was repeated, but with collecting Electron Energy Loss Spectroscopy (EELS), instead of TEM imaging. Results showed that upon heating, the K-edge peak of carbon increases, as shown in Figure 86. This is attributed to desorption of carbonaceous species from the walls of the sample holder/heater. This observation highlights the importance of waiting for the base-pressure to drop before 10^{-6} before starting the experiment. Also, the order of shutting down an experiment can greatly impact the effect of these carbonaceous species on growth. For instance, it is proposed here that shutting down the gas flow valves for C_2H_2 before ramping the temperature down is important for ensuring that the partial pressure of C_2H_2 is as low as possible during cooling. In general a wait of 5 minutes at high temperature after shutting the hydrocarbon gas flow was deemed enough to rid the system of the residual species.

As soon as the C_2H_2 gas was introduced, new peaks started to emerge on the EELS spectrum. The peak at around 284 eV is in agreement with the expected position for the 1s-π^* transformation, while the multiple peaks in the range of 290 - 310 eV agree with the peaks for the 1s-σ^* transformation. These peaks are typical for graphitic materials and are strong evidence of the formation of graphene-like structures (CNTs and particle encapsulation).[199, 200] The spectra shown below are plotted after background subtraction using a power law. However, the peak strength of the raw data for the carbon K-edge peaks can be considered an indication of the

growth kinetics of in other words the graphitization kinetics after introducing C_2H_2. However, this has proved to be challenging to quantify without involved processing.

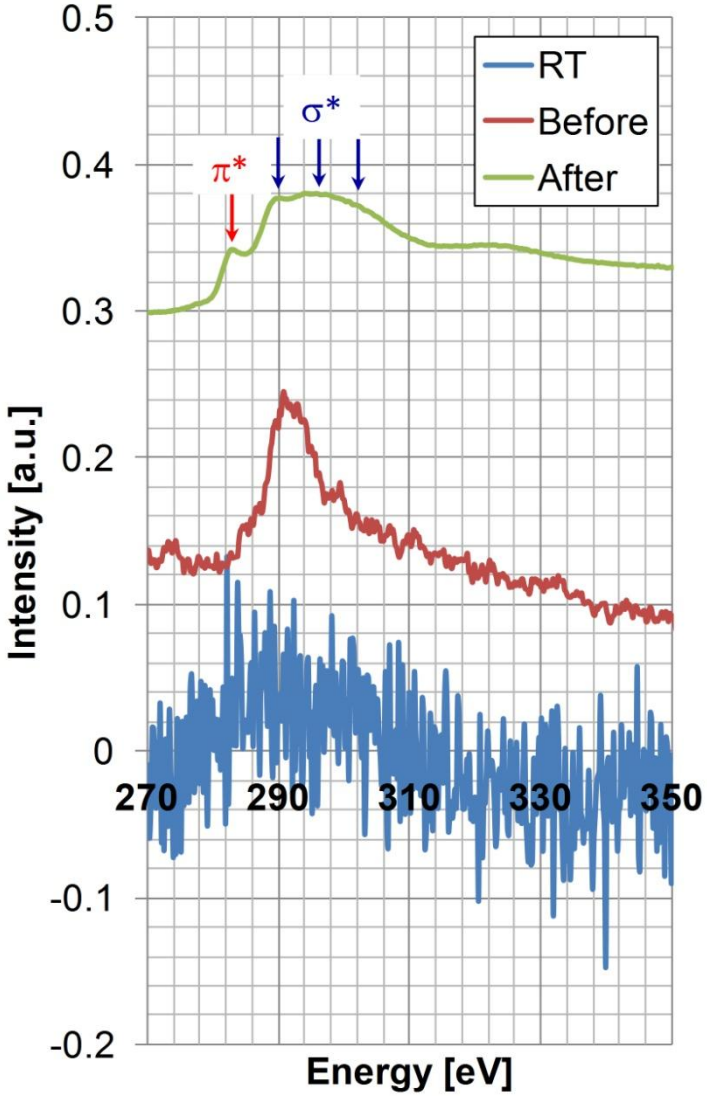

Figure 86. Comparing EELS spectra for carbon K-edge at room temperature (RT), at growth temperature before introducing C_2H_2, and after introducing (C_2H_2), showing the characteristic 1s-π* and 1s-σ* peaks of graphitic structures.

7.4.2. Mechanical coupling

In situ E-TEM also provided insights to the role of mechanics during the early stages of CNT forest nucleation and self-organization. Most importantly, understanding the development of CNT bundles that are coupled by VDW forces and how neighboring CNTs interact with each other would provide more insights in the force-modulated nature of growth. In order to study this, 200 nm thick Si_3N_4 membranes with patterned holes were used, called Holey grids, which have an array of 2 μm diameter holes. Glancing angle sputtering was used to deposit the catalyst, in order to ensure deposition on the lateral surfaces of the holes, as shown in Figure 87. During growth, only CNTs that are growing laterally outward from the rim of the holes are imaged, in order to have a side-view of mechanically coupled CNTs in focus of the electron beam.

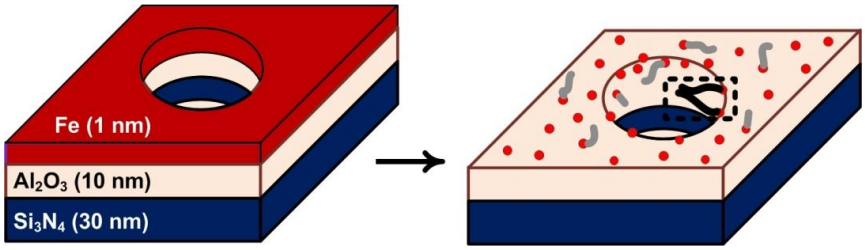

Figure 87. Schematic showing the Holey nitride membranes, before and after annealing.

Examples of newly formed CNT bundles are shown in Figure 88, which appear to have caused bends/kinks in some of CNTs that are part of the bundle. This

figure also shows how the contact length between bundled CNTs can be extend to tens and sometimes hundreds of nanometers. Figure 88e shows a bundle with CNTs separated at a close distance to the catalyst, indicating that forces can be transmitted through the bundle to act on each CNT-catalyst interface.

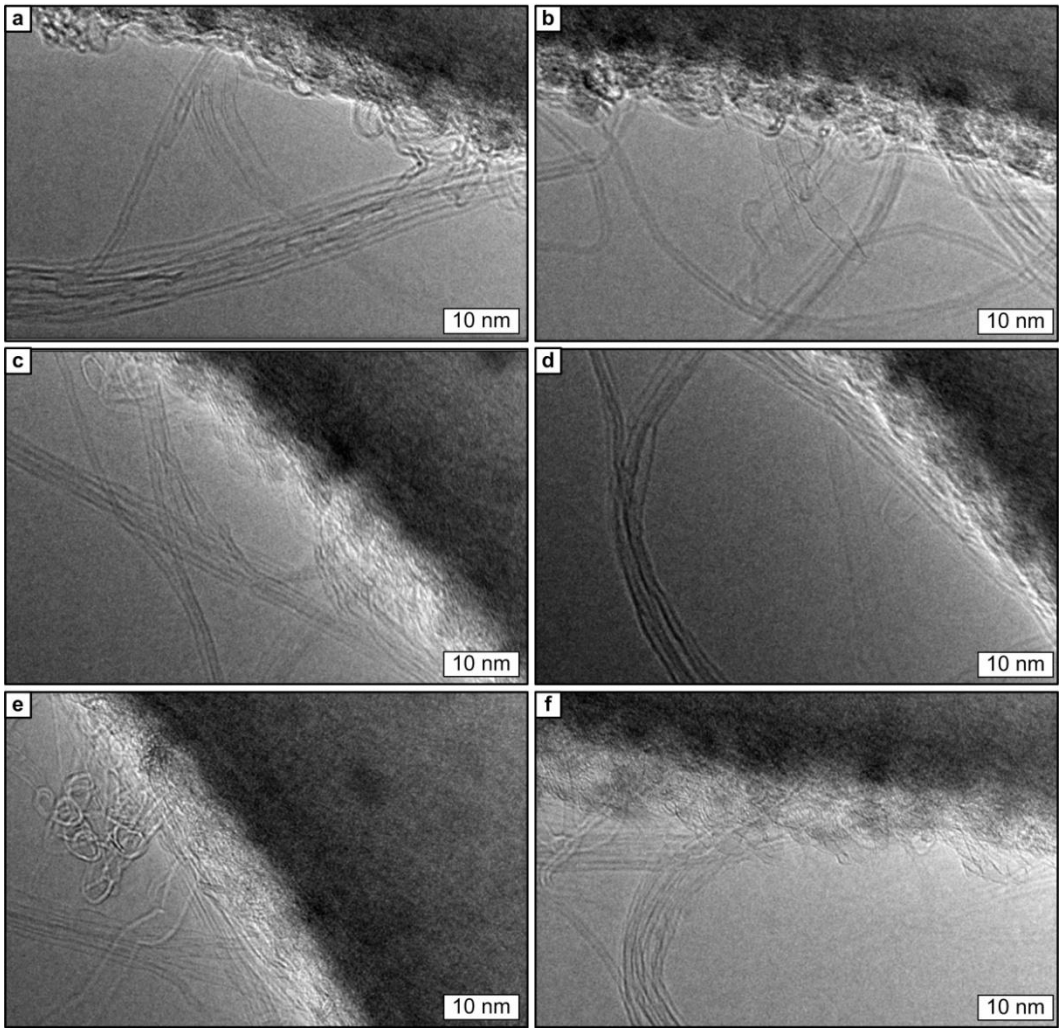

Figure 88. TEM of mechanical coupling and bundling among CNTs in proximity.

Higher resolution TEMs revealed evidence of mechanical competition between two CNTs in contact (Figure 89). It is hypothesized here that because each of the two CNT have different diameters and different numbers of walls, they do not grow at the same rate, i.e., the CNT lengthening rate for each one of them is different. However, because of the strength of the VDW attraction at the contact length between CNTs, internal forces ensue depending on the inherent growth rate at the catalyst-CNT interface. The CNT that is growing faster, presumably the one on the right, is subjected to compressive forces (highlighted in red), as evidenced by the bending geometry and the outer buckles/ripples in Figure 89a, and by the inner buckle/ripple in Figure 89b. On the other hand, the other CNT (highlighted in blue) grows at an inherently slower rate, leading to tensile forces that maintain the CNT more taut and slightly stretches.

Based on the mechanical feedback arguments made in the previous chapter, in which shifts in the growth rates were shown to be force-modulated, it is conceivable that such growth rate mismatch could lead to termination of the individual CNTs either by being subjected to an extremely high tensile or compressive load. Because the seeding catalyst nanoparticles is not included in TEM images obtained, it is more difficult to provide a single explanation to the hypothesis of mechanical frustration of detachment. Hence, more research in the future is needed to capture high resolution and high speed TEM videos showing the updated geometry of each CNT

and how the elastic forces (inferred from geometry), affect the lengthening rate (reaction kinetics).

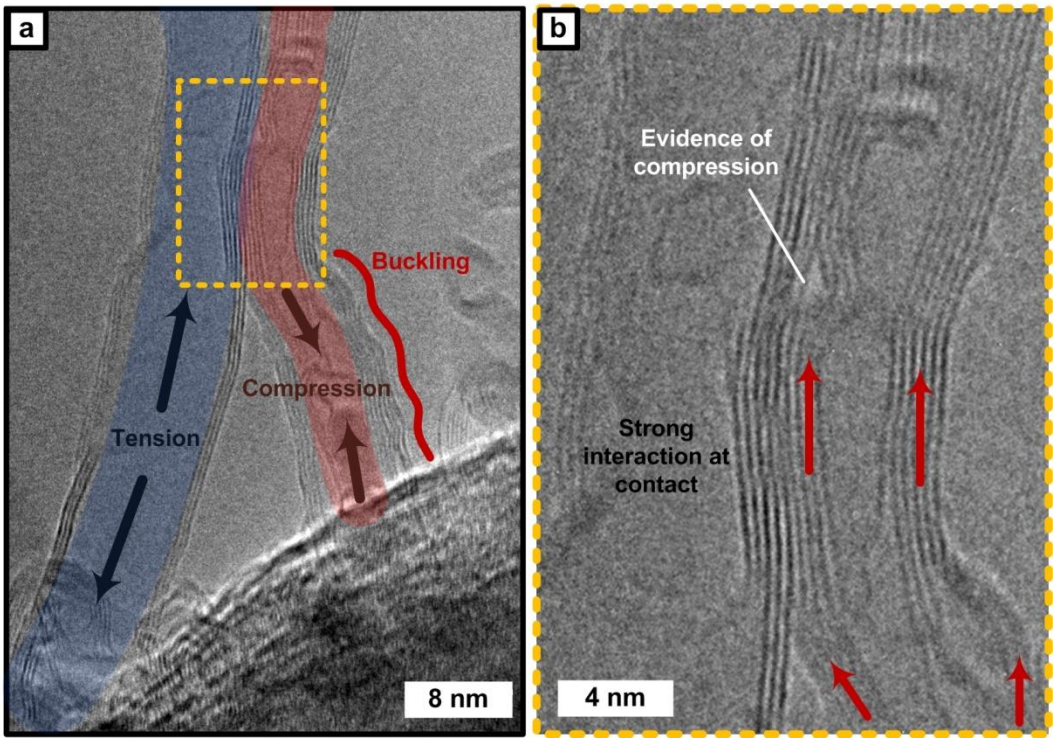

Figure 89. Evidence of mechanical competition between two CNT in contact, wherein, on CNT is growing a faster rate and is subjected to compression, while the other grow at a slower rate and is subjected to tension.

7.5. Conclusions

In situ E-TEM is a powerful technique that enables a deeper mechanistic understanding of the fundamental physical and chemical processes that are involved in the early stages of CNT nucleation and self-organization. Results show that upon introduction of the acetylene gas, high-contrast spherical-looking catalyst nanoparticles start to pop into existence, following an S-shaped kinetics. This is attributed to the reduction and dewetting of the iron oxide thin film (or partially reduced Fe_xO_y islands). As soon as each particle appears, it is either activated by forming a graphitic cap that grows into a CNT, or deactivated immediately by becoming encapsulated in graphitic overcoating layers. EELS spectra confirm the immediate graphitic formation by analyzing the characteristic fine-structure at the K-edge of carbon, which is typically exhibited for graphitic material such as CNTs or graphene-like material. E-TEM studies of the lateral growth of interacting CNTs demonstrated that building the bundled morphology lead to kinks/bends that are indicative of mechanical straining of CNTs pinned to the bundle by VDW forces. Results also show evidence for a mechanical competition between two neighboring CNTs, one of them is under tension, while the other is under compression.

CHAPTER 8: CONTRIBUTIONS AND OUTLOOK

8.1. Contributions of this Dissertation

The synthesis methods, characterization techniques, and mathematical models developed in this dissertation may be considered a paradigm shift in the CNT community, since the more traditional view of a CNT forest assumed that each CNT is identical and that the growth behavior of a forest can be simplified as a single CNT growing from a single catalyst nanoparticle. This assumption has been proven invalid throughout this dissertation, as the effects of mechanical and chemical interactions between neighboring CNTs and CNT microstructures have been revealed.

A summary of the contributions of this dissertation towards revealing the collective aspects of CNT population growth is illustrated in Figure 90. This categorizes the work with respect to two main axes: (1) the resolution of spatial mapping of CNT features, and (2) the capability of inferring diameter dependence of CNT growth kinetics and population behavior.

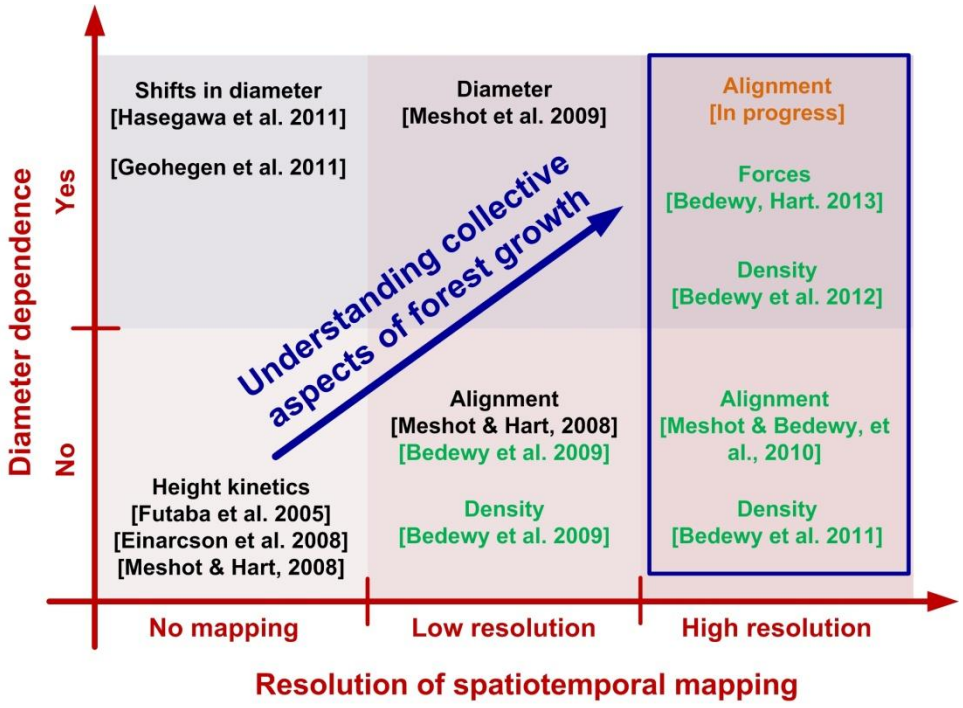

Figure 90. Chart showing where the contributions of this dissertation research on the study of the collective aspects of CNT growth and self-organization are positioned with respect to two axes: the resolution of spatiotemporal mapping and the diameter dependence. (black: literature; green: finished; orange: underway).

A list of contributions of the present dissertation towards revealing the collective mechanochemical aspects of CNT population growth is given below.

1. Discovered significant density gradients in CNT forests grown by CVD, and developed a model of collective CNT growth.[36] This new paradigm of population growth behavior replaced the traditional single-CNT-single-nanoparticle paradigm. My collective model identified the successive stages

of the CNT forest growth process and correlated the evolution of CNT alignment, density, diameter, and forces within a large CNT population growing simultaneously.[35, 36, 170]

2. Developed a comprehensive characterization methodology for CNT materials, by combining Synchrotron X-ray scattering with mass attenuation and non-contact laser sensing of real-time height kinetics.[35, 36, 38, 124, 170] This method quantifies the distribution of carbon nanotube diameters in a forest and the forest mass kinetics. The mass kinetics is inferred from a high resolution technique for calculating CNT mass density from X-ray intensity attenuation measurements, according to the Beer-Lambert law of mass-attenuation.[35]

3. Developed an approach for inferring a tortuosity-corrected lengthening kinetics of CNT forests by correlating the spatial distribution of CNT orientation and real-time height kinetics. In collaboration with Dr. Eric Meshot, this method was applied to reveal the true lengthening kinetics of CNTs grown in a cold-wall reactor. [35, 38]

4. Elucidated the diameter-dependent population growth dynamics of CNTs growing simultaneously inside high-density forests. This study showed that the competition between activation and deactivation kinetics is indeed

diameter-dependent, and that subpopulations of larger CNT have faster activation behavior compared to subpopulations of smaller CNTs.[124]

5. Worked closely with Brittan Farmer (Applied Mathematics PhD student) to develop a computational framework that models that spatially dependent growth rates of CNT patterns based on chemical coupling.[159] This model enabled design of patterns to achieve improved morphological uniformity.

6. Quantified the mechanical coupling among CNTs, and calculated the diameter-dependence and time-evolution of internal forces applied axially through individual CNTs, based on a model of elastic curved beams.[170] Results highlighted the importance of mechanical coupling to coordinated forest growth, in which significant forces could arise from a combination of mechanical coupling and diameter-dependent growth rate at individual CNTs.

7. Worked with a team on designing and building a CVD reactor that enables mechanical and electrical manipulation of CNT growth, for improved process control.

8. Carried out experimental studies using that CVD reactor that revealed how mechanical forces modulate the kinetics of chemical reactions. Results showed that compressive forces reduce the maximum growth rate of a CNT forest.

9. In collaboration with Dr. Eric Stach and Dr. Dmitri Zakharov, I studied the catalyst nanoparticle popping kinetics during the early stages of CNT growth by CVD *in situ* inside an environmental transmission electron microscope (E-TEM), at the Center for Functional Nanomaterials (CFN) at the Brookhaven National Laboratory (BNL). Results showed that the introduction of C_2H_2 gas accelerated the reduction and dewetting of catalyst islands into spherical particles, which either grew CNTs or were completely encapsulated by graphitic layers of carbon. This popping kinetics was shown to follow an S-shaped curve.

10. As part of the same collaboration, I used *in situ* TEM to study the evolution of mechanical coupling and CNT bundling during the earliest stage of growth. Results showed the snapping of neighboring CNTs together to form bundles, when they are close enough, contributing to the self-organization and build-up of alignment during the crowding stage of growth. Individual CNTs in contact also showed signs of competition between tensile and compressive stresses, which indicate the predicted straining resulting from growth rate mismatch of neighboring CNTs having different diameters.

8.2. Complementary Contributions

In addition to the contributions listed above, which are directly based on chapters of this dissertation, I have contributed to the following collaborative efforts during the course my PhD studies at the University of Michigan:

1. In collaboration with PhD student Jinjing Li, I applied the same SAXS-based characterization methodology developed/used in this dissertation to spatially map the morphology of CNT-clay nanocomposites prepared by CVD growth of CNTs within a layer-by-layer deposited catalyst-clay stack.[201]

2. In collaboration with former postdoctoral associate Sameh Tawfick, I used X-rays to quantify the wall-thickness of core-shell CNT-ceramic composites prepared by atomic layer deposition (ALD) of a conformal coating of aluminum oxide (Al_2O_3) around CNTs in a forest structure.[202]

3. In collaboration with former postdoctoral fellow Assaf Ya'akobovitz, I carried out an *in situ* characterization study of the morphological changes in CNT forests under electrostatic stimulation. I designed and carried out the SAXS experiment at the Synchrotron beamline and processed the data to show a quantified increase in CNT alignment towards the forest top.[203]

4. In collaboration with former PhD student Erik Polsen and current PhD student C. Ryan Oliver, I carried out SAXS characterization and contributed to data analysis and interpretation of results for CNT forests grown under

different humidity conditions, as part of a large study to control growth repeatability.[174]

5. In collaboration with former PhD student Eric Meshot, I developed a MATLAB code for processing atomic force microscopy (AFM) images to quantify the correlation between nanoparticle positions by triangulation. Moreover, I contributed to the design of experiments, set up, and data analysis of grazing incidence small angle X-ray scattering (GI-SAXS) study of thin film dewetting to form catalyst nanoparticles for CNT growth.[113]

6. I collaborated with PhD student Sei Jin Park on a study aimed at using laser extinction to measure the density of CNT microstructures.[173] This method is analogous to the method I developed using Synchrotron X-rays, in which intensity attenuation measurement are used to infer mass density of CNTs.

7. In collaboration with former postdoctoral researcher Siddhartha Pathak (from the California Institute of Technology), I grew low aspect ratio CNT micropillars with density variations in order to study how the mechanical properties of such microstructures varied accordingly, and developed interpretations of this data which led to a joint publication.[176]

8. In collaboration with graduate student Megan Roberts, I characterized nanoengineered substrates, used for growth of living motor neuron cells, by atomic force microscopy (AFM), and processed the images to quantify the

hierarchical topography and its periodicity. Then discussed the implications of this interface on multi-scale interactions with living cells.[204]

9. I proposed and led a ME450 project to design an instrument and develop a direct-write method for droplet printing and evaporative assembly via 4-degree-of-freedom meniscus manipulation. This was initially a ME450 project, and became a major part of the master's dissertation of Justin Beroz who was a member of the ME450 team.[205]

10. I designed and built an apparatus for blade casting of particle monolayers, and revealed the critical factors affecting the formation of defect-free large area monolayers of self-assembled nanoparticle crystals by a roll-to-roll compatible process.[206] This work is in preparation for publication with contributions of previous undergraduate researcher Jingjie Hu.

11. In collaboration with former PhD student Erik Polsen, I demonstrated that the same apparatus can be used for assembly of catalyst nanoparticles used for the growth of carbon nanotubes by chemical vapor deposition (CVD), leading to a joint publication.[207]

12. In collaboration with former PhD student Eric Meshot, I utilized the blade casting apparatus for self-assembly of fullerene crystals on flat and nanostructures surfaces.[208] This study compared the crystallization behavior of fullerenes on CNT templates and on bare silicon, and results showed that

the nanoscopic morphology of horizontally aligned CNTs directed the crystallization irrespective of the direction of meniscus motion (controlled by blade casting).

13. I surveyed a variety of methods for nanoparticle cluster assembly, and showed that large arrays of particle clusters can be fabricated by dynamic printing of pinned liquid bridges. A combination of surface energy patterning as well as topography pattering enabled breaking macroscopic droplets of particle solution to multiple femtoliter droplets.

8.3. Outlook

The following research directions are proposed to follow the work of this dissertation, in order to improve on the techniques and methods developed herein, apply them to other nanostructure systems, and/or built on the findings of this work to advance the manufacturing and metrology of CNT-based materials:

1. Based on the findings of this dissertation that typical CNT forests grown by CVD have inherently nonuniform distribution of density, diameter and alignment, new dynamic recipes need to be designed to minimize this non-uniformity. Preliminary results obtained by collaboration with PhD student Jinjing Li demonstrated the potential of using decoupled growth and annealing to grow more uniform, denser and taller CNT forests. In the

future, automated CVD reactors could be used to achieve more accurate control on the timing of each step in a dynamic recipe.

2. Although most of the SAXS characterization presented in this dissertation has been carried out *ex situ*, the same methodology can be based on *in situ*/ *operando* studies of catalytic CNT growth. In this case, integrating the processing of X-ray data into a feedback control system would enable regulation of process parameters based on updated real-time information about the forest morphology from X-ray characterization signal. This approach promises not only uniformity and repeatability, but also can achieve designed gradients of properties if needed.

3. Based on insights from this dissertation into the importance of mechanical coupling between CNTs growing simultaneously in a coordinated forest, new methods can be developed to relieve these internal stresses as they ensue during growth. For instance, chemical functionalization or electric charging of the outer walls of growing CNTs, could facilitate the slip between CNT, and hence would limit the transmitted loads within the forest to small magnitudes. This will eliminate, or reduce, the effect of mechanical forces on compromising CNT quality and straightness.

4. The mechanical model in chapter 5 of this dissertation highlights the correlation between the maximum CNT density and the highest calculated

forces, indicating that mechanical forces could be a key limiting mechanism halting and reversing the density increase during the crowding stage. Considering that the origin of these mechanical loads is the growth rate mismatch between different nanoparticles having varying sizes/shapes, a simple strategy to eliminate/ameliorate this issue would be to design the catalyst nanoparticles to have uniform sizes, shapes and spacing before starting growth. This could be achieved by self-assembly of stable preformed nanoparticles, instead of thin film dewetting.

5. Further work is needed to model the relationship governing the force-modulated growth kinetics of CNTs. Combined with a finite element model describing the elastic properties of CNTs, and adhesion interactions between them, this would enable developing accurate predictive models capable of more deterministic design and control on the resulting forest morphology/properties.

6. The mathematical framework presented in chapter 4 can be expanded to take into consideration internal mechanics of growing CNT micropillars, in order to predict and control the direction and degree of pillar bending and orientation within designed patterns.

7. Expanding the *in situ* E-TEM studies of CNT growth, by including *operando* characterization of the phase of active and inactive nanoparticles (using

electron diffraction for instance), would provide valuable insights into the chemical and physical factors that govern CNT growth activation. This understanding would enable engineering catalyst nanoparticles in the future to maximize CNT growth activation and achieve ultra-high density forests.

8. The density measurement technique presented here in chapter 2 suffered from a low signal-to-noise ratio. Preliminary work by the author indicated that the integration of scattering intensity from the 2D area detector also correlates to CNT mass density and can hence be used to provide an improved signal-to-noise ratio for CNT density measurements.

9. The collective forest growth model proposed in chapters 2 and 3 of this dissertation indicates that some CNTs (especially smaller diameter CNT) are still actively growing although the apparent forest height stops increasing (self-termination). These CNTs growing post-termination form a tangled mat at the forest-substrate interface. Preliminary results by the author found evidence of this mat from electron microscopy. Further work in studying this post-termination evolution of CNT forests, as well as correlating it to adhesion properties as well as to thermal and electrical transport properties could enable another method of tuning the interface between CNTs and device components.

10. The suite of characterization techniques developed/used in this dissertation could also be applied to other growing/self-organizing nanoscale filamentary structures such as inorganic nanotubes and nanowires, or biofilaments. For example, these techniques could enable designing uniform self-assembled forests of actin filaments for applications in tissue engineering.

11. Expanding the capability of these X-ray based techniques, it is possible to study the self-assembly of nanoparticle *in situ*, in order to reveal the crystallization dynamics and defect formation mechanisms. For example, GI-SAXS can be used to study the dynamics of the evaporative self-assembly of nanoparticles by blade casting.

12. Although a Synchrotron source was used for all the X-ray experiments discussed in this dissertation, it is possible to rely on desktop versions of X-ray equipment for SAXS characterization as long as the sample is dense enough. This is especially true for *ex situ* characterization, in which the collection time on the detector can be extended to compensate for the lower flux. From a manufacturing and metrology perspective, such desktop X-ray instruments could impact quality control on production lines of CNT materials.

13. The methodologies developed in this dissertation and the findings of spatiotemporal evolution of morphology during CNT forest growth can

reveal the structure-property relationships when combined with property measurements of CNT forests such as electric and thermal conductivities for instance. Recent publications have built on qualitative insights in this dissertation,[209] as well as quantitative modeling of density evolution[210] (Gompertz mode) to explain the thermal and electrical conductivities of CNT films having different thicknesses.

REFERENCES

1. Link, S.; Ei-Sayed, M. A., Optical properties and ultrafast dynamics of metallic nanocrystals. *Annual Review of Physical Chemistry* 2003, 54, 331-366.

2. Reibold, M.; Paufler, P.; Levin, A. A.; Kochmann, W.; Paetzke, N.; Meyer, D. C., Materials - Carbon nanotubes in an ancient Damascus sabre. *Nature* 2006, 444, 286-286.

3. Roduner, E., *Nanoscopic Materials: Size-Dependent Phenomena*. Royal Society of Chemistry.

4. Jensen, K.; Weldon, J.; Garcia, H.; Zettl, A., Nanotube radio. *Nano Letters* 2007, 7, 3508-3511.

5. Rutherglen, C.; Burke, P., Carbon nanotube radio. *Nano Letters* 2007, 7, 3296-3299.

6. Fan, J. A.; Wu, C.; Bao, K.; Bao, J.; Bardhan, R.; Halas, N. J.; Manoharan, V. N.; Nordlander, P.; Shvets, G.; Capasso, F., Self-assembled plasmonic nanoparticle clusters. *Science* 2010, 328, 1135-1138.

7. Wei, B. Q.; Vajtai, R.; Ajayan, P. M., Reliability and current carrying capacity of carbon nanotubes. *Applied Physics Letters* 2001, 79, 1172-1174.

8. Li, J.; Ye, Q.; Cassell, A.; Ng, H. T.; Stevens, R.; Han, J.; Meyyappan, M., Bottom-up approach for carbon nanotube interconnects. *Applied Physics Letters* 2003, 82, 2491-2493.

9. Tawfick, S.; O'Brien, K.; Hart, A. J., Flexible high-conductivity carbon-nanotube interconnects made by rolling and printing. *Small* 2009, 5, 2467-2473.

10. Li, Y. L.; Kinloch, I. A.; Windle, A. H., Direct spinning of carbon nanotube fibers from chemical vapor deposition synthesis. *Science* 2004, 304.

11. Qian, H.; Greenhalgh, E. S.; Shaffer, M. S. P.; Bismarck, A., Carbon nanotube-based hierarchical composites: a review. *Journal of Materials Chemistry* 2010, 20, 4751-4762.

12. Atwater, H. A.; Polman, A., Plasmonics for improved photovoltaic devices. *Nature Materials* 2010, 9, 205-213.

13. Chattopadhyay, S.; Huang, Y. F.; Jen, Y. J.; Ganguly, A.; Chen, K. H.; Chen, L. C., Anti-reflecting and photonic nanostructures. *Materials Science & Engineering R-Reports* 2010, 69, 1-35.

14. PCAST *Report to the President on Ensuring American Leadership in Advanced Manufacturing*; Executive Office of the President, June 2011.

15. Madou, M. J., *Fundamentals of microfabrication: the science of miniaturization*. 2nd ed.; CRC Press.

16. Boncheva, M.; Whitesides, G. M., Making things by self-assembly. *Mrs Bulletin* 2005, 30, 736-742.

17. Baughman, R. H.; Zakhidov, A. A.; de Heer, W. A., Carbon nanotubes - the route toward applications. *Science* 2002, 297, 787-792.

18. De Volder, M. F. L.; Tawfick, S. H.; Baughman, R. H.; Hart, A. J., Carbon nanotubes: present and future commercial applications. *Science* 2013, 339, 535-539.

19. Dresselhaus, M. S.; Lin, Y. M.; Rabin, O.; Jorio, A.; Souza, A. G.; Pimenta, M. A.; Saito, R.; Samsonidze, G. G.; Dresselhaus, G., Nanowires and nanotubes. *Materials Science & Engineering C-Biomimetic and Supramolecular Systems* 2003, 23, 129-140.

20. Berber, S.; Kwon, Y. K.; Tomanek, D., Unusually high thermal conductivity of carbon nanotubes. *Physical Review Letters* 2000, 84, 4613-4616.

21. Halonen, N.; Rautio, A.; Leino, A. R.; Kyllonen, T.; Toth, G.; Lappalainen, J.; Kordas, K.; Huuhtanen, M.; Keiski, R. L.; Sapi, A.; Szabo, M.; Kukovecz, A.; Konya, Z.; Kiricsi, I.; Ajayan, P. M.; Vajtai, R., Three-dimensional carbon nanotube scaffolds as particulate filters and catalyst support membranes. *ACS Nano* 2010, 4, 2003-2008.

22. Valentini, L.; Armentano, I.; Kenny, J. M.; Cantalini, C.; Lozzi, L.; Santucci, S., Sensors for sub-ppm NO2 gas detection based on carbon nanotube thin films. *Applied Physics Letters* 2003, 82, 961-963.

23. Li, J.; Lu, Y. J.; Ye, Q.; Cinke, M.; Han, J.; Meyyappan, M., Carbon nanotube sensors for gas and organic vapor detection. *Nano Letters* 2003, 3, 929-933.

24. Modi, A.; Koratkar, N.; Lass, E.; Wei, B. Q.; Ajayan, P. M., Miniaturized gas ionization sensors using carbon nanotubes. *Nature* 2003, 424, 171-174.

25. Hashim, D. P.; Narayanan, N. T.; Romo-Herrera, J. M.; Cullen, D. A.; Hahm, M. G.; Lezzi, P.; Suttle, J. R.; Kelkhoff, D.; Munoz-Sandoval, E.; Ganguli, S.; Roy, A. K.;

Smith, D. J.; Vajtai, R.; Sumpter, B. G.; Meunier, V.; Terrones, H.; Terrones, M.; Ajayan, P. M., Covalently bonded three-dimensional carbon nanotube solids via boron induced nanojunctions. *Scientific Reports* 2012, 2.

26. van der Veen, M. H.; Vereecke, B.; Sugiura, M.; Kashiwagi, Y.; Ke, X.; Cott, D. J.; Vanpaemel, J. K. M.; Vereecken, P. M.; De Gendt, S.; Huyghebaert, C.; Tokei, Z.; Electrical and structural characterization of 150 nm cnt contacts with cu damascene top metallization. *2012 IEEE International Interconnect Technology Conference (IITC)* 2012.

27. Holt, J. K.; Park, H. G.; Wang, Y. M.; Stadermann, M.; Artyukhin, A. B.; Grigoropoulos, C. P.; Noy, A.; Bakajin, O., Fast mass transport through sub-2-nanometer carbon nanotubes. *Science* 2006, 312, 1034-1037.

28. Vilatela, J. J.; Windle, A. H., Yarn-like carbon nanotube fibers. *Advanced Materials* 2010, 22, 4959-+.

29. Sinnott, S. B.; Andrews, R., Carbon nanotubes: Synthesis, properties, and applications. *Critical Reviews in Solid State and Materials Sciences* 2001, 26, 145-249.

30. Dresselhaus, M. S.; Dresselhaus, G.; Avouris, P., *Carbon nanotubes : synthesis, structure, properties, and applications*. Springer: Berlin ; New York, 2001; p xv, 447 p.

31. Terranova, M. L.; Sessa, V.; Rossi, M., The world of carbon nanotubes: An overview of CVD growth methodologies. *Chemical Vapor Deposition* 2006, 12, 315-325.

32. Jourdain, V.; Bichara, C., Current understanding of the growth of carbon nanotubes in catalytic chemical vapour deposition. *Carbon* 2013, 58, 2-39.

33. Zhang, Q.; Huang, J.-Q.; Qian, W.-Z.; Zhang, Y.-Y.; Wei, F., The road for nanomaterials industry: a review of carbon nanotube production, post-treatment, and bulk applications for composites and energy storage. *Small* 2013, 9, 1237-1265.

34. Hata, K.; Futaba, D. N.; Mizuno, K.; Namai, T.; Yumura, M.; Iijima, S., Water-assisted highly efficient synthesis of impurity-free single-waited carbon nanotubes. *Science* 2004, 306, 1362-1364.

35. Bedewy, M.; Meshot, E. R.; Reinker, M. J.; Hart, A. J., Population growth dynamics of carbon nanotubes. *ACS Nano* 2011, 5, 8974-8989.

36. Bedewy, M.; Meshot, E.; Guo, H.; Verploegen, E.; Lu, W.; Hart, A., Collective mechanism for the evolution and self-termination of vertically aligned carbon nanotube growth. *Journal of Physical Chemistry C* 2009, 113, 20576-20582.

37. Amama, P. B.; Pint, C. L.; McJilton, L.; Kim, S. M.; Stach, E. A.; Murray, P. T.; Hauge, R. H.; Maruyama, B., Role of water in super growth of single-walled carbon nanotube carpets. *Nano Letters* 2009, 9, 44-49.

38. Meshot, E.; Bedewy, M.; Lyons, K.; Woll, A.; Juggernauth, K.; Tawfick, S.; Hart, A., Measuring the lengthening kinetics of aligned nanostructures by spatiotemporal correlation of height and orientation. *Nanoscale* 2010, 2, 896-900.

39. Kim, S. M.; Pint, C. L.; Amama, P. B.; Zakharov, D. N.; Hauge, R. H.; Maruyama, B.; Stach, E. A., Evolution in catalyst morphology leads to carbon nanotube growth termination. *Journal of Physical Chemistry Letters* 2010, 1, 918-922.

40. Hasegawa, K.; Noda, S., Millimeter-Tall Single-Walled Carbon Nanotubes rapidly grown with and without water. *ACS Nano* 2011, 5, 975-984.

41. Prasher, R. S.; Hu, X. J.; Chalopin, Y.; Mingo, N.; Lofgreen, K.; Volz, S.; Cleri, F.; Keblinski, P., Turning carbon nanotubes from exceptional heat conductors into insulators. *Physical Review Letters* 2009, 102.

42. Coleman, J. N.; Khan, U.; Blau, W. J.; Gun'ko, Y. K., Small but strong: A review of the mechanical properties of carbon nanotube-polymer composites. *Carbon* 2006, 44, 1624-1652.

43. Nirmalraj, P. N.; Lyons, P. E.; De, S.; Coleman, J. N.; Boland, J. J., Electrical connectivity in single-walled carbon nanotube networks. *Nano Letters* 2009, 9, 3890-3895.

44. Zhang, M.; Fang, S. L.; Zakhidov, A. A.; Lee, S. B.; Aliev, A. E.; Williams, C. D.; Atkinson, K. R.; Baughman, R. H., Strong, transparent, multifunctional, carbon nanotube sheets. *Science* 2005, 309, 1215-1219.

45. Zhang, M.; Atkinson, K. R.; Baughman, R. H., Multifunctional carbon nanotube yarns by downsizing an ancient technology. *Science* 2004, 306, 1358-1361.

46. Kuznetsov, A. A.; Fonseca, A. F.; Baughman, R. H.; Zakhidov, A. A., Structural model for dry-drawing of sheets and yarns from carbon nanotube forests. *ACS Nano* 2011, 5, 985-993.

47. Amama, P. B.; Pint, C. L.; Kim, S. M.; McJilton, L.; Eyink, K. G.; Stach, E. A.; Hauge, R. H.; Maruyama, B., Influence of alumina type on the evolution and activity of alumina-supported fe catalysts in single-walled carbon nanotube carpet growth. *ACS Nano* 2010, 4, 895-904.

48. Kim, D. H.; Jang, H. S.; Kim, C. D.; Cho, D. S.; Yang, H. S.; Kang, H. D.; Min, B. K.; Lee, H. R., Dynamic growth rate behavior of a carbon nanotube forest characterized by in situ optical growth monitoring. *Nano Letters* 2003, 3, 863-865.

49. Puretzky, A. A.; Geohegan, D. B.; Jesse, S.; Ivanov, I. N.; Eres, G., In situ measurements and modeling of carbon nanotube array growth kinetics during chemical vapor deposition. *Applied Physics a-Materials Science & Processing* 2005, 81, 223-240.

50. Hart, A. J.; van Laake, L.; Slocum, A. H., Desktop growth of carbon-nanotube monoliths with in situ optical Imaging. *Small* 2007, 3, 772-777.

51. Meshot, E. R.; Hart, A. J., Abrupt self-termination of vertically aligned carbon nanotube growth. *Applied Physics Letters* 2008, 92.

52. Einarsson, E.; Murakami, Y.; Kadowaki, M.; Maruyama, S., Growth dynamics of vertically aligned single-walled carbon nanotubes from in situ measurements. *Carbon* 2008, 46, 923-930.

53. Puretzky, A. A.; Eres, G.; Rouleau, C. M.; Ivanov, I. N.; Geohegan, D. B., Real-time imaging of vertically aligned carbon nanotube array growth kinetics. *Nanotechnology* 2008, 19.

54. Meshot, E. R.; Plata, D. L.; Tawfick, S.; Zhang, Y. Y.; Verploegen, E. A.; Hart, A. J., Engineering vertically aligned carbon nanotube growth by decoupled thermal treatment of precursor and catalyst. *ACS Nano* 2009, 3, 2477-2486.

55. Futaba, D. N.; Hata, K.; Yamada, T.; Mizuno, K.; Yumura, M.; Iijima, S., Kinetics of water-assisted single-walled carbon nanotube synthesis revealed by a time-evolution analysis. *Physical Review Letters* 2005, 95.

56. Zhu, L. B.; Hess, D. W.; Wong, C. P., Monitoring carbon nanotube growth by formation of nanotube stacks and investigation of the diffusion-controlled kinetics. *Journal of Physical Chemistry B* 2006, 110, 5445-5449.

57. Patole, S. P.; Park, J. H.; Lee, T. Y.; Lee, J. H.; Patole, A. S.; Yoo, J. B., Growth interruption studies on vertically aligned 2-3 wall carbon nanotubes by water assisted chemical vapor deposition. *Applied Physics Letters* 2008, 93.

58. Stadermann, M.; Sherlock, S. P.; In, J.-B.; Fornasiero, F.; Park, H. G.; Artyukhin, A. B.; Wang, Y.; De Yoreo, J. J.; Grigoropoulos, C. P.; Bakajin, O.; Chernov, A. A.; Noy, A., Mechanism and kinetics of growth termination in controlled chemical vapor deposition growth of multiwall carbon nanotube arrays. *Nano Letters* 2009, 9, 738–744.

59. Shanov, V.; Mallik, N.; Chu, W.; Li, W.; Jayasinghe, C.; Yun, Y.; Schulz, M. J.; Yarmolenko, S.; Salunke, P.; Li, G., Advances in synthesis and application of carbon nanotube materials. Materials Science and Technology Conference, Pittsburgh, Pennsylvania, 2008.

60. Mattevi, C.; Wirth, C. T.; Hofmann, S.; Blume, R.; Cantoro, M.; Ducati, C.; Cepek, C.; Knop-Gericke, A.; Milne, S.; Castellarin-Cudia, C.; Dolafi, S.; Goldoni, A.; Schloegl, R.; Robertson, J., In-situ X-ray photoelectron spectroscopy study of catalyst-support interactions and growth of carbon nanotube forests. *Journal of Physical Chemistry C* 2008, 112, 12207-12213.

61. Patole, S. P.; Alegaonkar, P. S.; Lee, H. C.; Yoo, J. B., Optimization of water assisted chemical vapor deposition parameters for super growth of carbon nanotubes. *Carbon* 2008, 46, 1987-1993.

62. Wu, J.; Huang, Q. W.; Ma, Y. F.; Huang, Y.; Liu, Z. F.; Yang, X. Y.; Chen, Y. S.; Chen, D. P., Distortion of carbon nanotube array and its influence on carbon nanotube growth and termination. *Colloids and Surfaces a-Physicochemical and Engineering Aspects* 2008, 313, 13-17.

63. Dell'Acqua-Bellavitis, L.; Ballard, J.; Ajayan, P.; Siegel, R., Kinetics for the synthesis reaction of aligned carbon nanotubes: A study based on in situ diffractography. *Nano Letters* 2004, 4, 1613-1620.

64. Valiente, A. M.; Lopez, P. N.; Ramos, I. R.; Ruiz, A. G.; Li, C.; Xin, Q., In situ study of carbon nanotube formation by C_2H_2 decomposition on an iron-based catalyst. *Carbon* 2000, 38, 2003-2006.

65. Yasuda, S.; Hiraoka, T.; Futaba, D. N.; Yamada, T.; Yumura, M.; Hata, K., Existence and kinetics of graphitic carbonaceous impurities in carbon nanotube forests to assess the absolute purity. *Nano Letters* 2009, 9, 769-773.

66. Jackson, J. J.; Puretzky, A. A.; More, K. L.; Rouleau, C. M.; Eres, G.; Geohegan, D. B., Pulsed growth of vertically aligned nanotube arrays with variable density. *ACS Nano* 2010, 4, 7573-7581.

67. Picher, M.; Anglaret, E.; Arenal, R.; Jourdain, V., Self-Deactivation of single-walled carbon nanotube growth studied by in situ raman measurements. *Nano Letters* 2009, 9, 542-547.

68. Chiashi, S.; Kohno, M.; Takata, Y.; Maruyama, S., Localized synthesis of single-walled carbon nanotubes on silicon substrates by a laser heating catalytic CVD. In *Cola'05: 8th International Conference on Laser Ablation*, Hess, W. P.; Herman, P. R.; Bauerle, D.; Koinuma, H., Eds. 2007; Vol. 59, pp 155-158.

69. Li-Pook-Than, A.; Lefebvre, J.; Finnie, P., Phases of carbon nanotube growth and population evolution from in situ raman spectroscopy during chemical vapor deposition. *Journal of Physical Chemistry C* 2010, 114, 11018-11025.

70. Latorre, N.; Romeo, E.; Cazana, F.; Ubieto, T.; Royo, C.; Villacampa, J. J.; Monzon, A., Carbon nanotube growth by catalytic chemical vapor deposition: a phenomenological kinetic model. *Journal of Physical Chemistry C* 2010, 114, 4773-4782.

71. Dresselhaus, M. S.; Dresselhaus, G.; Saito, R.; Jorio, A., Raman spectroscopy of carbon nanotubes. *Physics Reports-Review Section of Physics Letters* 2005, 409, 47-99.

72. Kim, Y. A.; Kakegawa, H.; Fujisawa, K.; Shimamoto, D.; Muramatsu, H.; Kim, J. H.; Jung, Y. C.; Hayashi, T.; Endo, M.; Terrones, M.; Dresselhaus, M. S., Sensitive G-band raman features for the electrical conductivity of multi-walled carbon nanotubes. *Journal of Nanoscience and Nanotechnology* 2010, 10, 3940-3944.

73. Wang, B. N.; Bennett, R. D.; Verploegen, E.; Hart, A. J.; Cohen, R. E., Characterizing the morphologies of mechanically manipulated multiwall carbon nanotube films by small-angle X-ray scattering. *Journal of Physical Chemistry C* 2007, 111, 17933-17940.

74. Wang, B. N.; Bennett, R. D.; Verploegen, E.; Hart, A. J.; Cohen, R. E., Quantitative characterization of the morphology of multiwall carbon nanotube films by small-angle X-ray scattering. *Journal of Physical Chemistry C* 2007, 111, 5859-5865.

75. Verploegen, E.; Hart, A. J.; De Volder, M.; Tawfick, S.; Chia, K.-K.; Cohen, R. E., Non-destructive characterization of structural hierarchy within aligned carbon nanotube assemblies. *Journal of Applied Physics* 2011, 109, 094316-5.

76. Louchev, O. A.; Laude, T.; Sato, Y.; Kanda, H., Diffusion-controlled kinetics of carbon nanotube forest growth by chemical vapor deposition. *Journal of Chemical Physics* 2003, 118, 7622-7634.

77. Wood, R. F.; Pannala, S.; Wells, J. C.; Puretzky, A. A.; Geohegan, D. B., Simple model of the interrelation between single- and multiwall carbon nanotube growth rates for the CVD process. *Physical Review B* 2007, 75.

78. Hubbell, J. H.; Seltzer, S. M., Tables of X-ray mass attenuation coefficients and mass energy-absorption coefficients from 1 kev to 20 mev for elements z = 1 to 92 and 48 additional substances of dosimetric interest. NIST Standard Reference Database 126, 2004.

79. Horcas, I.; Fernandez, R.; Gomez-Rodriguez, J. M.; Colchero, J.; Gomez-Herrero, J.; Baro, A. M., WSXM: A software for scanning probe microscopy and a tool for nanotechnology. *Review of Scientific Instruments* 2007, 78.

80. Hubbell, J. H., Compilation of photon cross-sections: Some historical remarks and current status. *X-Ray Spectrometry* 1999, 28, 215-223.

81. Hubbell, J. H., Review and history of photon cross section calculations. *Physics in Medicine and Biology* 2006, 51, R245-R262.

82. Arcos, T. D. L.; Oelhafen, P.; Thommen, V.; Mathys, D., The influence of catalyst's oxidation degree on carbon nanotube growth as a substrate-independent parameter. *Journal of Physical Chemistry C* 2007, 111, 16392-16396.

83. Okita, A.; Ozeki, A.; Suda, Y.; Nakamura, J.; Oda, A.; Bhattacharyya, K.; Sugawara, H.; Sakai, Y., Analysis of oxidation state of multilayered catalyst thin films for carbon nanotube growth using plasma-enhanced chemical vapor deposition. *Japanese Journal of Applied Physics Part 1-Regular Papers Brief Communications & Review Papers* 2006, 45, 8323-8329.

84. Picher, M.; Anglaret, E.; Arenal, R.; Jourdain, V., Processes controlling the diameter distribution of single-walled carbon nanotubes during catalytic chemical vapor deposition. *ACS Nano* 2011, 5, 2118-2125.

85. Wang, H.; Xu, Z.; Eres, G., Order in vertically aligned carbon nanotube arrays. *Applied Physics Letters* 2006, 88.

86. Bedewy, M.; Meshot, E. R.; Aitkaliyeva, A.; Shao, L.; Hart, A. J., Post-termination evolution of carbon nanotube forest-substrate interface in chemical vapor deposition reactors. In preparation.

87. Hofmann, S.; Sharma, R.; Ducati, C.; Du, G.; Mattevi, C.; Cepek, C.; Cantoro, M.; Pisana, S.; Parvez, A.; Cervantes-Sodi, F.; Ferrari, A. C.; Dunin-Borkowski, R.; Lizzit, S.; Petaccia, L.; Goldoni, A.; Robertson, J., In situ observations of catalyst dynamics during surface-bound carbon nanotube nucleation. *Nano Letters* 2007, 7, 602-608.

88. Hermans, P. H., *Contribution to the physics of cellulose fibres; a study in sorption, density, refractive power and orientation*. Elsevier Pub. Co.: Amsterdam, 1946; p xvi, 221 p.-xvi, 221 p.

89. Lin, M.; Tan, J. P. Y.; Boothroyd, C.; Loh, K. P.; Tok, E. S.; Foo, Y. L., Direct observation of single-walled carbon nanotube growth at the atomistic scale. *Nano Letters* 2006, 6, 449-452.

90. Yasuda, S.; Futaba, D. N.; Yamada, T.; Satou, J.; Shibuya, A.; Takai, H.; Arakawa, K.; Yumura, M.; Hata, K., Improved and large area single-walled carbon nanotube forest growth by controlling the gas flow direction. *ACS Nano* 2009, 3, 4164-4170.

91. Vinten, P.; Lefebvre, J.; Finnie, P., Kinetic critical temperature and optimized chemical vapor deposition growth of carbon nanotubes. *Chemical Physics Letters* 2009, 469, 293-297.

92. Lacava, A. I.; Bernardo, C. A.; Trimm, D. L., Studies of deactivation of metals by carbon deposition. *Carbon* 1982, 20, 219-223.

93. Richards, F. J., A Flexible growth function for empirical use. *Journal of Experimental Botany* 1959, 10, 290-300.

94. Winsor, C. P., The Gompertz curve as a growth curve. *Proceedings of the National Academy of Sciences of the United States of America* 1932, 18, 1-8.

95. Laird, A. K., Dynamics of tumor growth. *British Journal of Cancer* 1964, 18, 490-&.

96. Zwietering, M. H.; Jongenburger, I.; Rombouts, F. M.; Vantriet, K., Modeling of the bacterial-growth curve. *Applied and Environmental Microbiology* 1990, 56, 1875-1881.

97. Necula, M.; Kuret, J., A static laser light scattering assay for surfactant-induced tau fibrillization. *Analytical Biochemistry* 2004, 333, 205-215.

98. Xiang, R.; Yang, Z.; Zhang, Q.; Luo, G.; Qian, W.; Wei, F.; Kadowaki, M.; Einarsson, E.; Maruyama, S., Growth deceleration of vertically aligned carbon nanotube arrays: Catalyst deactivation or feedstock diffusion controlled? *Journal of Physical Chemistry C* 2008, 112, 4892-4896.

99. Zhu, L. B.; Xu, J. W.; Xiao, F.; Jiang, H. J.; Hess, D. W.; Wong, C. P., The growth of carbon nanotube stacks in the kinetics-controlled regime. *Carbon* 2007, 45, 344-348.

100. Zhang, G. Y.; Mann, D.; Zhang, L.; Javey, A.; Li, Y. M.; Yenilmez, E.; Wang, Q.; McVittie, J. P.; Nishi, Y.; Gibbons, J.; Dai, H. J., Ultra-high-yield growth of vertical single-walled carbon nanotubes: Hidden roles of hydrogen and oxygen. *Proceedings of the National Academy of Sciences of the United States of America* 2005, 102, 16141-16145.

101. Magrez, A.; Seo, J. W.; Kuznetsov, V. L.; Forro, L., Evidence of an equimolar C_2H_2-CO_2 reaction in the synthesis of carbon nanotubes. *Angewandte Chemie-International Edition* 2007, 46, 441-444.

102. Nasibulin, A. G.; Brown, D. P.; Queipo, P.; Gonzalez, D.; Jiang, H.; Kauppinen, E. I., An essential role of CO_2 and H_2O during single-walled CNT synthesis from carbon monoxide. *Chemical Physics Letters* 2006, 417, 179-184.

103. Futaba, D. N.; Hata, K.; Namai, T.; Yamada, T.; Mizuno, K.; Hayamizu, Y.; Yumura, M.; Iijima, S., 84% Catalyst activity of water-assisted growth of single walled carbon nanotube forest characterization by a statistical and macroscopic approach. *Journal of Physical Chemistry B* 2006, 110, 8035-8038.

104. Pint, C. L.; Pheasant, S. T.; Parra-Vasquez, A. N. G.; Horton, C.; Xu, Y. Q.; Hauge, R. H., Investigation of optimal parameters for oxide-assisted growth of vertically aligned single-walled carbon nanotubes. *Journal of Physical Chemistry C* 2009, 113, 4125-4133.

105. Nishino, H.; Yasuda, S.; Namai, T.; Futaba, D. N.; Yamada, T.; Yumura, M.; Iijima, S.; Hata, K., Water-assisted highly efficient synthesis of single-walled carbon nanotubes forests from colloidal nanoparticle catalysts. *Journal of Physical Chemistry C* 2007, 111, 17961-17965.

106. Zhang, Y. Y.; Gregoire, J. M.; van Dover, R. B.; Hart, A. J., Ethanol-Promoted high-yield growth of few-walled carbon nanotubes. *Journal of Physical Chemistry C* 2010, 114, 6389-6395.

107. Frenklach, M.; Clary, D., Aspects of Autocatalytic Reaction-Kinetics. *Industrial & Engineering Chemistry Fundamentals* 1983, 22, 433-436.

108. Eres, G.; Rouleau, C. M.; Yoon, M.; Puretzky, A. A.; Jackson, J. J.; Geohegan, D. B., Model for self-assembly of carbon nanotubes from acetylene based on real-time studies of vertically aligned growth kinetics. *The Journal of Physical Chemistry C* 2009, 113, 15484-15491.

109. Plata, D. e. L.; Meshot, E. R.; Reddy, C. M.; Hart, A. J.; Gschwend, P. M., Multiple alkynes react with ethylene to enhance carbon nanotube synthesis, suggesting a polymerization-like formation mechanism. *ACS Nano* 2010, 4, 7185-7192.

110. Plata, D. e. L.; Hart, A. J.; Reddy, C. M.; Gschwend, P. M., Early evaluation of potential environmental impacts of carbon nanotube synthesis by chemical vapor deposition. *Environmental Science & Technology* 2009, 43, 8367-8373.

111. Liu, K.; Liu, P.; Jiang, K.; Fan, S. S., Effect of carbon deposits on the reactor wall during the growth of multi-walled carbon nanotube arrays. *Carbon* 2007, 45, 2379-2387.

112. Monzon, A.; Lolli, G.; Cosma, S.; Mohamed, S. B.; Resasco, D. E., Kinetic modeling of the swnt growth by co disproportionation on como catalysts. *Journal of Nanoscience and Nanotechnology* 2008, 8, 6141-6152.

113. Meshot, E. R.; Verploegen, E.; Bedewy, M.; Tawfick, S.; Woll, A. R.; Green, K. S.; Hromalik, M.; Koerner, L. J.; Philipp, H. T.; Tate, M. W.; Gruner, S. M.; Hart, A. J., High-speed in situ x-ray scattering of carbon nanotube film nucleation and self-organization. *ACS Nano* 2012, 6, 5091-5101.

114. Sushumna, I.; Ruckenstein, E., Role of physical and chemical interactions in the behavior of supported metal-catalysts - iron on alumina - a case-study. *Journal of Catalysis* 1985, 94, 239-288.

115. de los Arcos, T.; Vonau, F.; Garnier, M. G.; Thommen, V.; Boyen, H. G.; Oelhafen, P.; Duggelin, M.; Mathis, D.; Guggenheim, R., Influence of iron-silicon interaction on the growth of carbon nanotubes produced by chemical vapor deposition. *Applied Physics Letters* 2002, 80, 2383-2385.

116. Paparazzo, E., XPS analysis of iron aluminum-oxide systems. *Applied Surface Science* 1986, 25, 1-12.

117. Byrd, J. E.; Perona, M. J., Kinetics of popping of popcorn. *Cereal Chemistry* 2005, 82, 53-59.

118. Kim, D. H.; Lipke, E. A.; Kim, P.; Cheong, R.; Thompson, S.; Delannoy, M.; Suh, K. Y.; Tung, L.; Levchenko, A., Nanoscale cues regulate the structure and function of macroscopic cardiac tissue constructs. *Proceedings of the National Academy of Sciences of the United States of America* 2010, 107, 565-570.

119. Kukovitsky, E. F.; L'Vov, S. G.; Sainov, N. A.; Shustov, V. A.; Chernozatonskii, L. A., Correlation between metal catalyst particle size and carbon nanotube growth. *Chemical Physics Letters* 2002, 355, 497-503.

120. Nerushev, O. A.; Dittmar, S.; Morjan, R. E.; Rohmund, F.; Campbell, E. E. B., Particle size dependence and model for iron-catalyzed growth of carbon nanotubes by thermal chemical vapor deposition. *Journal of Applied Physics* 2003, 93, 4185-4190.

121. Helveg, S.; Lopez-Cartes, C.; Sehested, J.; Hansen, P. L.; Clausen, B. S.; Rostrup-Nielsen, J. R.; Abild-Pedersen, F.; Norskov, J. K., Atomic-scale imaging of carbon nanofibre growth. *Nature* 2004, 427, 426-429.

122. Pint, C. L.; Xu, Y. Q.; Moghazy, S.; Cherukuri, T.; Alvarez, N. T.; Haroz, E. H.; Mahzooni, S.; Doorn, S. K.; Kono, J.; Pasquali, M.; Hauge, R. H., Dry contact transfer printing of aligned carbon nanotube patterns and characterization of their optical properties for diameter distribution and alignment. *ACS Nano* 2010, 4, 1131-1145.

123. Reymann, A. C.; Martiel, J. L.; Cambier, T.; Blanchoin, L.; Boujemaa-Paterski, R.; Thery, M., Nucleation geometry governs ordered actin networks structures. *Nature Materials* 2010, 9, 827-832.

124. Bedewy, M.; Meshot, E. R.; Hart, A. J., Diameter-dependent kinetics of activation and deactivation in carbon nanotube population growth. *Carbon* 2012, 50, 5106-5116.

125. Campbell, C. T.; Parker, S. C.; Starr, D. E., The effect of size-dependent nanoparticle energetics on catalyst sintering. *Science* 2002, 298, 811-814.

126. Rioux, R. M.; Song, H.; Hoefelmeyer, J. D.; Yang, P.; Somorjai, G. A., High-surface-area catalyst design: Synthesis, characterization, and reaction studies of platinum nanoparticles in mesoporous SBA-15 silica. *Journal of Physical Chemistry B* 2005, 109, 2192-2202.

127. Jones, G.; Jakobsen, J. G.; Shim, S. S.; Kleis, J.; Andersson, M. P.; Rossmeisl, J.; Abild-Pedersen, F.; Bligaard, T.; Helveg, S.; Hinnemann, B.; Rostrup-Nielsen, J. R.; Chorkendorff, I.; Sehested, J.; Norskov, J. K., First principles calculations and experimental insight into methane steam reforming over transition metal catalysts. *Journal of Catalysis* 2008, 259, 147-160.

128. Moisala, A.; Nasibulin, A. G.; Kauppinen, E. I., The role of metal nanoparticles in the catalytic production of single-walled carbon nanotubes - a review. *Journal of Physics-Condensed Matter* 2003, 15, S3011-S3035.

129. Schmidt, V.; Wittemann, J. V.; Senz, S.; Goesele, U., Silicon Nanowires: A Review on Aspects of their Growth and their Electrical Properties. *Advanced Materials* 2009, 21, 2681-2702.

130. Wu, Y. Y.; Fan, R.; Yang, P. D., Block-by-block growth of single-crystalline Si/SiGe superlattice nanowires. *Nano Letters* 2002, 2, 83-86.

131. Kikkawa, J.; Ohno, Y.; Takeda, S., Growth rate of silicon nanowires. *Applied Physics Letters* 2005, 86.

132. Hasegawa, K.; Noda, S., Diameter increase in millimeter-tall vertically aligned single-walled carbon nanotubes during growth. *Applied Physics Express* 2010, 3.

133. Geohegan, D. B.; Puretzky, A. A.; Jackson, J. J.; Rouleau, C. M.; Eres, G.; More, K. L., Flux-dependent growth kinetics and diameter selectivity in single-wall carbon nanotube arrays. *ACS Nano* 2011, 5, 8311-8321.

134. Sazonova, V.; Yaish, Y.; Ustunel, H.; Roundy, D.; Arias, T. A.; McEuen, P. L., A tunable carbon nanotube electromechanical oscillator. *Nature* 2004, 431, 284-287.

135. Majumder, M.; Chopra, N.; Andrews, R.; Hinds, B. J., Nanoscale hydrodynamics - enhanced flow in carbon nanotubes. *Nature* 2005, 438, 44-44.

136. Fam, D. W. H.; Palaniappan, A.; Tok, A. I. Y.; Liedberg, B.; Moochhala, S. M., A review on technological aspects influencing commercialization of carbon nanotube sensors. *Sensors and Actuators B-Chemical* 2011, 157, 1-7.

137. Cervantes-Sodi, F.; McNicholas, T. P.; Simmons, J. G.; Liu, J.; Csanyi, G.; Ferrari, A. C.; Curtarolo, S., Viscous state effect on the activity of Fe nanocatalysts. *ACS Nano* 2010, 4, 6950-6956.

138. Rao, R.; Liptak, D.; Cherukuri, T.; Yakobson, B. I.; Maruyama, B., In situ evidence for chirality-dependent growth rates of individual carbon nanotubes. *Nature Materials* 2012, 11, 213-216.

139. Ding, F.; Harutyunyan, A. R.; Yakobson, B. I., Dislocation theory of chirality-controlled nanotube growth. *Proceedings of the National Academy of Sciences of the United States of America* 2009, 106, 2506-2509.

140. Lopez, N.; Janssens, T. V. W.; Clausen, B. S.; Xu, Y.; Mavrikakis, M.; Bligaard, T.; Norskov, J. K., On the origin of the catalytic activity of gold nanoparticles for low-temperature CO oxidation. *Journal of Catalysis* 2004, 223, 232-235.

141. Saint-Lager, M. C.; Laoufi, I.; Bailly, A.; Robach, O.; Garaudee, S.; Dolle, P., Catalytic properties of supported gold nanoparticles: new insights into the size-activity relationship gained from in operando measurements. *Faraday Discussions* 2011, 152, 253-265.

142. Langhammer, C.; Zhdanov, V. P.; Zoric, I.; Kasemo, B., Size-dependent kinetics of hydriding and dehydriding of Pd nanoparticles. *Physical Review Letters* 2010, 104, 4.

143. Ding, F.; Bolton, K.; Rosen, A., Nucleation and growth of single-walled carbon nanotubes: A molecular dynamics study. *Journal of Physical Chemistry B* 2004, 108, 17369-17377.

144. Raty, J. Y.; Gygi, F.; Galli, G., Growth of carbon nanotubes on metal nanoparticles: A microscopic mechanism from ab initio molecular dynamics simulations. *Physical Review Letters* 2005, 95.

145. Zhu, H. W.; Suenaga, K.; Hashimoto, A.; Urita, K.; Hata, K.; Iijima, S., Atomic-resolution imaging of the nucleation points of single-walled carbon nanotubes. *Small* 2005, 1, 1180-1183.

146. Harutyunyan, A. R.; Mora, E.; Tokune, T.; Bolton, K.; Rosen, A.; Jiang, A.; Awasthi, N.; Curtarolo, S., Hidden features of the catalyst nanoparticles favorable for single-walled carbon nanotube growth. *Applied Physics Letters* 2007, 90.

147. Han, J. H.; Graff, R. A.; Welch, B.; Marsh, C. P.; Franks, R.; Strano, M. S., A mechanochemical model of growth termination in vertical carbon nanotube forests. *Acs Nano* 2008, 2, 53-60.

148. Israelachvili, J. N., *Intermolecular and Surface Forces*. Second ed.; Academic Press: 1992.

149. De Volder, M. F. L.; Vidaud, D. O.; Meshot, E. R.; Tawfick, S.; Hart, A. J., Self-similar organization of arrays of individual carbon nanotubes and carbon nanotube micropillars. *Microelectronic Engineering* 2010, 87, 1233-1238.

150. Shtogun, Y. V.; Woods, L. M., Many-body van der Waals interactions between graphitic nanostructures. *Journal of Physical Chemistry Letters* 2010, 1, 1356-1362.

151. Li, C. X.; Liu, Y. L.; Yao, X. F.; Ito, M.; Noguchi, T.; Zheng, Q. S., Interfacial shear strengths between carbon nanotubes. *Nanotechnology* 2010, 21.

152. Bhushan, B.; Ling, X., Adhesion and friction between individual carbon nanotubes measured using force-versus-distance curves in atomic force microscopy. *Physical Review B* 2008, 78, 9.

153. Hart, A. J.; Slocum, A. H., Force output, control of film structure, and microscale shape transfer by carbon nanotube growth under mechanical pressure. *Nano Letters* 2006, 6, 1254-1260.

154. Einarsson, E.; Shiozawa, H.; Kramberger, C.; Rümmeli, M. H.; Grüneis, A.; Pichler, T.; Maruyama, S., Revealing the small-bundle internal structure of vertically aligned single-walled carbon nanotube films. *The Journal of Physical Chemistry C* 2007, 111, 17861-17864.

155. Zhang, R. F.; Wen, Q.; Qian, W. Z.; Su, D. S.; Zhang, Q.; Wei, F., Superstrong ultra long carbon nanotubes for mechanical energy storage. *Advanced Materials* 2011, 23, 3387-+.

156. Akoshima, M.; Hata, K.; Futaba, D.; Mizuno, K.; Baba, T.; Yumura, M., Thermal diffusivity of single-walled carbon nanotube forest measured by laser flash method. *Japanese Journal of Applied Physics* 2009, -.

157. Duong, H.; Yamamoto, N.; Papavassiliou, D.; Maruyama, S.; Wardle, B., Inter-carbon nanotube contact in thermal transport of controlled-morphology polymer nanocomposites. *Nanotechnology* 2009, -.

158. Tong, T.; Zhao, Y.; Delzeit, L.; Kashani, A.; Meyyappan, M.; Majumdar, A., Dense, vertically aligned multiwalled carbon nanotube arrays as thermal interface materials. *Ieee Transactions on Components and Packaging Technologies* 2007, 30, 92-100.

159. Bedewy, M.; Farmer, B.; Hart, J., Synergetic chemical coupling controls the uniformity of carbon nanotube microstructure growth. Submitted.

160. Parker, J. M.; Wong, H. S. P., Synergetic carbon nanotube growth. *Carbon* 2013, 62, 61-68.

161. Borgstrom, M. T.; Immink, G.; Ketelaars, B.; Algra, R.; Bakkers, E. P. A. M., Synergetic nanowire growth. *Nature Nanotechnology* 2007, 2, 541-544.

162. Bronikowski, M. J., CVD growth of carbon nanotube bundle arrays. *Carbon* 2006, 44, 2822-2832.

163. Jeong, G. H.; Olofsson, N.; Falk, L. K. L.; Campbell, E. E. B., Effect of catalyst pattern geometry on the growth of vertically aligned carbon nanotube arrays. *Carbon* 2009, 47, 696-704.

164. Kimura, H.; Goto, J.; Yasuda, S.; Sakurai, S.; Yumura, M.; Futaba, D. N.; Hata, K., Unexpectedly high yield carbon nanotube synthesis from low-activity carbon feedstocks at high concentrations. *ACS Nano* 2013, 7, 3150-3157.

165. Eres, G.; Kinkhabwala, A. A.; Cui, H. T.; Geohegan, D. B.; Puretzky, A. A.; Lowndes, D. H., Molecular beam-controlled nucleation and growth of vertically aligned single-wall carbon nanotube arrays. *Journal of Physical Chemistry B* 2005, 109, 16684-16694.

166. Nessim, G. D.; Seita, M.; Plata, D. L.; O'Brien, K. P.; Hart, A. J.; Meshot, E. R.; Reddy, C. M.; Gschwend, P. M.; Thompson, C. V., Precursor gas chemistry determines the crystallinity of carbon nanotubes synthesized at low temperature. *Carbon* 2011, 49, 804-810.

167. Magrez, A.; Smajda, R.; Seo, J. W.; Horvath, E.; Ribic, P. R.; Andresen, J. C.; Acquaviva, D.; Olariu, A.; Laurenczy, G.; Forro, L., Striking influence of the catalyst

support and its acid-base properties: new insight into the growth mechanism of carbon nanotubes. *ACS Nano* 2011, 5, 3428-3437.

168. Stine, B. E.; Ouma, D. O.; Divecha, R. R.; Boning, D. S.; Chung, J. E.; Hetherington, D. L.; Harwood, C. R.; Nakagawa, O. S.; Oh, S. Y., Rapid characterization and modeling of pattern-dependent variation in chemical-mechanical polishing. *Ieee Transactions on Semiconductor Manufacturing* 1998, 11, 129-140.

169. Abrokwah, K. O.; Chidambaram, P. R.; Boning, D. S., Pattern based prediction for plasma etch. *IEEE Transactions on Semiconductor Manufacturing* 2007, 20, 77-86.

170. Bedewy, M.; Hart, A. J., Mechanical coupling limits the density and quality of self-organized carbon nanotube growth. *Nanoscale* 2013, 5, 2928-2937.

171. Li, J.; Bedewy, M.; Tawfick, S.; Hart, A. J., Well aligned and high density CNT forests obtained by hydrocarbon deposition with decoupling of anneal and growth. In preparation.

172. Hirschfelder, J. O.; Curtiss, C. F.; Bird, R. B., The molecular theory of gases and liquids. Wiley: 1964.

173. Park, S. J.; Schmidt, A. J.; Bedewy, M.; Hart, A. J., Measurement of carbon nanotube microstructure relative density by optical attenuation and observation of size-dependent variations. *Physical Chemistry Chemical Physics* 2013, 15, 11511-11519.

174. Oliver, C. R.; Polsen, E. S.; Meshot, E. R.; Tawfick, S.; Park, S. J.; Bedewy, M.; Hart, A. J., Statistical analysis of variation in laboratory growth of carbon nanotube forests and recommendations for improved consistency. *ACS Nano* 2013, 7, 3565-3580.

175. Moulton, K.; Morrill, N. B.; Konneker, A. M.; Jensen, B. D.; Vanfleet, R. R.; Allred, D. D.; Davis, R. C., Effect of iron catalyst thickness on vertically aligned carbon nanotube forest straightness for CNT-MEMS. *Journal of Micromechanics and Microengineering* 2012, 22.

176. Pathak, S.; Mohan, N.; Decolvenaere, E.; Needleman, A.; Bedewy, M.; Hart, A. J.; Greer, J. R., Local relative density modulates failure and strength in vertically aligned carbon nanotubes. *ACS Nano* 2013.

177. Fan, S. S.; Chapline, M. G.; Franklin, N. R.; Tombler, T. W.; Cassell, A. M.; Dai, H. J., Self-oriented regular arrays of carbon nanotubes and their field emission properties. *Science* 1999, 283.

178. Maschmann, M. R.; Ehlert, G. J.; Park, S. J.; Mollenhauer, D.; Maruyama, B.; Hart, A. J.; Baur, J. W., Visualizing strain evolution and coordinated buckling within cnt arrays by in situ digital image correlation. *Advanced Functional Materials* 2012, 22, 4686-4695.

179. Suekane, O.; Nagataki, A.; Mori, H.; Nakayama, Y., Static friction force of carbon nanotube surfaces. *Applied Physics Express* 2008, 1.

180. Gonzalez, C.; Llorca, J., Stiffness of a curved beam subjected to axial load and large displacements. *International Journal of Solids and Structures* 2005, 42, 1537-1545.

181. Plata, D. L.; Hart, A. J.; Reddy, C. M.; Gschwend, P. M., Early evaluation of potential environmental impacts of carbon nanotube synthesis by chemical vapor deposition. *Environmental Science & Technology* 2009, 43.

182. Vinten, P.; Bond, J.; Marshall, P.; Lefebvre, J.; Finnie, P., Origin of periodic rippling during chemical vapor deposition growth of carbon nanotube forests. *Carbon* 2011, 49.

183. Hutchens, S. B.; Needleman, A.; Greer, J. R., A microstructurally motivated description of the deformation of vertically aligned carbon nanotube structures. *Applied Physics Letters* 2012, 100.

184. Yang, X.; He, P.; Gao, H., Competing elastic and adhesive interactions govern deformation behaviors of aligned carbon nanotube arrays. *Applied Physics Letters* 2012, 101.

185. Beyer, M. K.; Clausen-Schaumann, H., Mechanochemistry: The mechanical activation of covalent bonds. *Chemical Reviews* 2005, 105, 2921-2948.

186. Beyer, M. K., Coupling of mechanical and chemical energy: Proton affinity as a function of external force. *Angewandte Chemie-International Edition* 2003, 42, 4913-4915.

187. Ribas-Arino, J.; Shiga, M.; Marx, D., Understanding covalent mechanochemistry. *Angewandte Chemie-International Edition* 2009, 48, 4190-4193.

188. Hickenboth, C. R.; Moore, J. S.; White, S. R.; Sottos, N. R.; Baudry, J.; Wilson, S. R., Biasing reaction pathways with mechanical force. *Nature* 2007, 446.

189. Davis, D. A.; Hamilton, A.; Yang, J.; Cremar, L. D.; Van Gough, D.; Potisek, S. L.; Ong, M. T.; Braun, P. V.; Martinez, T. J.; White, S. R.; Moore, J. S.; Sottos, N. R., Force-induced activation of covalent bonds in mechanoresponsive polymeric materials. *Nature* 2009, 459.

190. Caruso, M. M.; Davis, D. A.; Shen, Q.; Odom, S. A.; Sottos, N. R.; White, S. R.; Moore, J. S., Mechanically-induced chemical changes in polymeric materials. *Chemical Reviews* 2009, 109.

191. Piermattei, A.; Karthikeyan, S.; Sijbesma, R. P., Activating catalysts with mechanical force. *Nature Chemistry* 2009, 1.

192. Aziz, M. J.; Nygren, E.; Hays, J. F.; Turnbull, D., Crystal-growth kinetics of boron-oxide under pressure. *Journal of Applied Physics* 1985, 57, 2233-2242.

193. Lu, G. Q.; Nygren, E.; Aziz, M. J.; Turnbull, D.; White, C. W., Pressure-enhanced solid-phase epitaxy of germanium. *Applied Physics Letters* 1990, 56, 137-139.

194. Pop, E.; Mann, D.; Wang, Q.; Goodson, K. E.; Dai, H. J., Thermal conductance of an individual single-wall carbon nanotube above room temperature. *Nano Letters* 2006, 6.

195. Li, H. J.; Lu, W. G.; Li, J. J.; Bai, X. D.; Gu, C. Z., Multichannel ballistic transport in multiwall carbon nanotubes. *Physical Review Letters* 2005, 95.

196. Marconnett, A. M.; Yamamoto, N.; Panzer, M. A.; Wardle, B. L.; Goodson, K. E., Thermal conduction in aligned carbon nanotube-polymer nanocomposites with high packing density. *ACS Nano* 2011, 5.

197. Ribas-Arino, J.; Marx, D., Covalent mechanochemistry: Theoretical concepts and computational tools with applications to molecular nanomechanics. *Chemical Reviews* 2012, 112, 5412-5487.

198. de Boer, J. H., The influence of van der waals' forces and primary bonds on binding energy, strength and orientation, with special reference to some artificial resins. *Transactions of the Faraday Society* 1936, 32, 0010-0036.

199. Ajayan, P. M.; Ebbesen, T. W., Nanometre-size tubes of carbon. *Reports on Progress in Physics* 1997, 60, 1025-1062.

200. Suenaga, K.; Sandre, E.; Colliex, C.; Pickard, C. J.; Kataura, H.; Iijima, S., Electron energy-loss spectroscopy of electron states in isolated carbon nanostructures. *Physical Review B* 2001, 63.

201. Li, J.; Srivastava, S.; Ok, J.; Zhang, Y.; Bedewy, M.; Kotov, N.; Hart, A., Multidirectional hierarchical nanocomposites made by carbon nanotube growth within layer-by-layer-assembled films. *Chemistry of Materials* 2011, 23, 1023-1031.

202. Brieland-Shoultz, A.; Tawfick, S.; Park, S. J.; Bedewy, M.; Maschmann, M.; Baur, J. W.; Hart, A. J., Carbon-ceramic nanocomposite foams with extremely tunable stiffness, strength, and toughness. Submitted.

203. Ya'akobovitz, A.; Bedewy, M.; Rao, A.; Hart, A. J., Electrostatic loading and resonance of carbon nanotube forests. In preparation.

204. Roberts, M. J.; Leach, M. K.; Bedewy, M.; Meshot, E. R.; Copic, D.; Corey, J. M.; Hart, A. J., Directed growth of primary motor neurons on horizontally aligned carbon nanotube films and striped patterns. Submitted.

205. Beroz, J.; Bedewy, M.; Reinker, M.; Chhajer, V.; Awtar, S.; Hart, A. J., Four degree of freedom liquid dispenser for direct write capillary self-assembly with sub-nanoliter precision. *The Review of scientific instruments* 2012, 83, 015104.

206. Bedewy, M.; Hu, J.; Hart, A. J., Critical Factors mediating crystal domain size of self-assembled nanoparticle monolayers by roll-to-roll compatible blade casting. In preparation.

207. Polsen, E. S.; Bedewy, M.; Hart, A. J., Decoupled control of carbon nanotube forest density and diameter by continuous-feed convective assembly of catalyst particles. *Small (Weinheim an der Bergstrasse, Germany)* 2013, 9, 2564-75.

208. Meshot, E. R.; Patel, K. D.; Tawfick, S.; Juggernauth, K. A.; Bedewy, M.; Verploegen, E. A.; De Volder, M. F. L.; Hart, A. J., Photoconductive hybrid films via directional self-assembly of C60 on aligned carbon nanotubes. *Advanced Functional Materials* 2012, 22, 577-584.

209. Yuan, G.; Marconnet, A. M.; Rong, X.; Maruyama, S.; Goodson, K. E., Heat Capacity, thermal conductivity, and interface resistance extraction for single-walled carbon nanotube films using frequency-domain thermoreflectance. *Components, Packaging and Manufacturing Technology, IEEE Transactions on* 2013, 3, 1524-1532.

210. Marschewski, J.; In, J. B.; Poulikakos, D.; Grigoropoulos, C. P., Synergistic integration of Ni and vertically aligned carbon nanotubes for enhanced transport properties on flexible substrates. *Carbon.* In press.